Alma Mater Studiorum - Università di Bologna

DIPARTIMENTO DI ASTRONOMIA
Corso di Dottorato di Ricerca in Astronomia
Ciclo XXII (2007-2009)
Esame finale anno 2010

Stellar relics of the hierarchical assembly of the Galaxy

Dottorando:
Matteo Correnti

Relatori:
Ch.mo Prof. F.R. Ferraro
Dott. M. Bellazzini

Coordinatore:
Ch.mo Prof. Lauro Moscardini

Scuola di Dottorato in Scienze Matematiche, Fisiche e Astronomiche
Settore Scientifico Disciplinare: Area 02 - Scienze Fisiche
FIS/05 Astronomia e Astrofisica

Contents

CHAPTER 1

Introduction

SECTION 1.1

Scientific goals and Thesis organization

This *Ph.D Thesis* has been carried out as part of a long-term wide research project of the *Osservatorio Astronomico di Bologna* that has as primary goal the comprehension and reconstruction of formation mechanism of galaxies and of their evolution history.

There is now substantial evidence, both from theoretical and observational point of view, in favor of the hypothesis that the halo of the Galaxy has been, at least partially, built up by the progressive accretion of small fragments, similar in nature to the present day dwarf galaxies of the Local Group.

In this framework, the photometric and spectroscopic study of systems which nature is already known, as for example the Sagittarius dwarf spheroidal galaxy (Sgr dSph, Ibata et al., 1994), the Magellanic Clouds (Large and Small, LMC and SMC, Olszewski et al., 1996; Bekki & Chiba, 2005) and the others dwarf galaxies of the Local Group, (see for instances Grebel, 2005, and references therein) or others that have been recently discovered (both galaxies and tidal streams, see for example Zucker et al., 2006a,b; Belokurov et al., 2007a,b; Irwin et al., 2007; Liu et al., 2008; Martin et al., 2008; Grillmair, 2009) permits to discover not only the origin and behaviour of these systems, but also the structure of our Galactic halo, combined with its formation history. In fact, the study of the population of these objects (from dwarf galaxies to tidally destroyed ones, from peculiar globular clusters to “simple” overdensities) and also of their chemical compositions, ages, metallicities and velocity dispersions, permit us, not only an improvement

in the understanding of the mechanisms that govern the galactic formation, but also a valid indirect test for the cosmological model itself.

In particular this Thesis has two main purposes:

1. To provide a complete characterization of the tidal Stream of Sagittarius dwarf spheroidal, using Red Clump stars extracted from the catalogue of the Sloan Digital Sky Survey (SDSS, Adelman-McCarthy et al., 2008), in the portion in the Northern emispehere sampled by this survey. With this technique we obtained an estimate of the distance, of the depth along the line of sight and of the local density for each detected portion of the Stream (and more in general for each detected structures along our lines of sight). Moreover, exploiting also Blue Horizontal Branch stars, we compared the ratio of the Sgr populations (Red Clump stars are associated with an intermediate-age metal rich population, while Blue Horizontal Branch stars with an old metal-poor one) in the main body of the galaxy and in the Stream, in order to verify the presence of an age-metallicity gradient along the Stream.

2. To provide an innovative and powerful method that permits to fully exploit the huge amount of informations present in wide field survey databases. Thanks to our approach, we detected a population of Red Clump stars probably associated to the recently discovered stellar system Boötes III. Furthermore, it can be applied in a general way to investigate regions of the halo, looking for new systems, also if the technique is best suited for the accurate localization of already detected structures.

In Chapter 2 we review and summarize the context in which this Thesis has been developed. We will also outline the main characteristic of the Sgr dSph and its tidal Stream, summarizing the principal literature related to it. In Chapter 3 and 4 we will show the results obtained in the study of Sgr Stream; in Chapter 5 we will discuss the *discovery* of Boötes III stellar system and, finally, in Chapter 6 we will show the results of a radial velocity survey in the external part of the globular cluster ω Cen, devoted to the study of the velocity dispersion profile of the cluster.

SECTION 1.2

Published Results

Some of the results presented in this Thesis have been already published in refereed journals and conference proceedings. These publications are listed in the following. Some papers, inherent to the general topic of my research, but for which the results are not presented here, are also listed.

Refereed Publications

1. *The formation of Palomar 1 in a Galactic merger event - Stellar abundances from HDS/Subaru Data*
   Monaco, L., **Correnti, M.**, Saviane, I., & Bellazzini, M.,
   in preparation

2. *The Northern wraps of the Sagittarius Stream as traced by Red Clump stars: distances, intrinsic widths and stellar densities*
   Correnti, M., Bellazzini, M., Ferraro, F.R., & Ibata, R.A.,
   to be submitted to ApJ

3. *Red Clump stars in the Boötes III stellar system*
   Correnti, M., Bellazzini, M., & Ferraro, F.R.,
   2009, MNRAS, 397, L26

4. *The non-peculiar velocity dispersion profile of the stellar system* ω *Centauri*
   Sollima, A., Bellazzini, M., Smart, R.L., **Correnti, M.**, Pancino, E., Ferraro, F.R., & Romano, D.,
   2009, MNRAS, 396, 2183

5. *Detection of a population gradient in the Sagittarius stream*
   Bellazzini, M., Newberg, H.J., **Correnti, M.**, Ferraro, F.R., & Monaco, L.,

2006, A&A 457, L21

6. *The age of the main population of the Sagittarius dwarf spheroidal galaxy - Solving the M giant conundrum*
   Bellazzini, M., **Correnti, M.**, Ferraro, F.R., Monaco, L., & Montegriffo, P.,
   2006, A&A 446, L1

Contributed Papers

1. *The relics of the Sagittarius dSph galaxy: stellar populations and distances in the Main Body and in the Stream*
   Correnti, M., Bellazzini, M., Ferraro, F.R., & Monaco, L.,
   2008, Mmsait, 79, 692

2. *A wide field survey of Sagittarius dSph. Data and Tools for the study of the Sgr Tidal Stream*
   Correnti, M., Bellazzini, M., Ferraro, F.R:, & Monaco, L.,
   2007, IAUS, 241, 329

CHAPTER 2

The remnants of the Galactic Building Blocks: dwarf spheroidal galaxies, tidal tails and massive globular clusters

This chapter aims at providing a brief overview of the scientific context of this work. We will describe the enormous progress in understading the mechanism of formation of galaxies, and the advantage in the comprehension of their structure given by the production of large-scale digital surveys of the sky like 2MASS and SDSS. Then we will discuss in detail the most striking example of an ongoign accretion event, i.e., the Sagittarius dwarf spheroidal galaxy.

In a seminal paper Eggen et al. (1962, herafter ELS) showed how dynamical and chemical information of stars in the Galactic halo can be used to study the formation of the Milky Way (MW). In particular, studying the motion of high velocity stars, they noted that as the metal abundance decreases, the orbit energy and eccentricities of the stars increase while their orbital angular momentum decreases. From this evidence, they inferred that the formation of the Galaxy began with a relatively rapid (a few 10^8 yr) radial collapse of the initial protogalactic cloud, followed by an equally rapid settling of gas into a rotating disc. This model readily explained the origin and general structural, kinematic, and metallicity correlations of observationally identified populations of field stars (Baade, 1944; O'Connell, 1958): low metallicity Population II stars formed during the initial collapse and populate the extended stellar halo; younger Population I and intermediate Population II stars formed after the gas had settled into the Galactic plane and constitute

the disc. The observationally determined distributions of disc stars is commonly described by exponential density laws (Bahcall & Soneira, 1980; Gilmore & Reid, 1983; Gilmore et al., 1989), while power laws of flattened De Vaucouleurs spheroids are usually used to describe the halo (e.g. Wyse & Gilmore, 1989; Larsen & Humphreys, 1996; Majewski, 1993, and references therein). In both the disc and the halo, the distribution of stars is expected to be a smooth function of position, perturbed only slightly by localized bursts of star formation or spiral structure induced shocks.

Later, Searle & Zinn (1978, hereafter SZ) showed that the Galactic globular clusters have a wide range of metal abundance which does not correlate with the distance from the Galactic center. Moreover, they tentatively interpreted the observed range of variations of the horizontal branch morphology at fixed metallicity as due to a range of cluster ages. In contrast to the ELS picture of an halo formed in a rapid free-fall collapse, SZ interpreted their results as evidence for a halo built up over an extended period. In particular, they wrote: "It is suggested that the halo clusters originated within transient protogalactic fragments that gradually lost gas while undergoing chemical evolution and continued to fall into the Galaxy after the collapse of its central regions had been completed".

In the same period the idea of galaxy formation via hierarchical aggregation of smaller elements from the early universe was emerging from theoretical studies of cosmology (Peebles, 1971; Press & Schechter, 1974).

Nowadays, the most recent results of the observative cosmology agree on a model of Universe with a geometry sustantially flat, dominated by a sort of unknown energy (i.e., *Dark Energy*) and in which the bulk of the matter is non-barionic and non-relativistic (Λ-Cold Dark Matter, Λ-CDM hereafter, see Tegmark et al., 2004, and references therein).

In such a model, the formation of cosmic structures is ruled by the process of hierarchical merging (see e.g. White & Rees, 1978; White & Frenk, 1991; Bullock et al., 2001; Madau et al., 2008, and references therein), that is the progressive assembly of the large scale structures by the union of sub-structures of minor mass (see Fig. 2.1 for an example of merger-tree history of a MW sized galaxy).

Indeed, the Λ-CDM model of structure formation predicts that the dark matter haloes of galaxies like the MW were formed by the continual accretion of lower-mass systems. While some fraction of the accreted dark haloes are expected to survive as sub-haloes, most of the extended dark halo is built up from merging systems that are tidally destroyed (Zentner & Bullock, 2003). Similarly, if the accreted systems contain dissipationless stars, for example in

the form of dwarf galaxies, then this process leads naturally to the formation of an extended stellar halo.

N-body simulations (an example is reported in Fig. 2.2, from Bullock & Johnston, 2005) predict that the survived relics of this process still exist (in various forms) in the halo of our Galaxy and in the last ten-fifteen years, it has been realized that they can be also observed and studied in detail. Moreover, the discovery of the Sgr dSph (Ibata et al., 1994) and of the Canis Major dwarf spheroidal galaxy (Martin et al., 2004) clearly demonstrates that the hierarchical merging process is still in progress in our Galaxy. Even clearer examples are observed in M31 (Ibata et al., 2007) and in some more distant galaxies (Martínez-Delgado et al., 2008, 2009), confirming the prediction of CDM simulations (e.g. Johnston et al., 2008) that a typical MW-like galaxy should presently contain on average about one large, high surface brightness ($\mu_0 < 30$ mag arcsec^{-2}) stream (for a complete review of the detections in nearby and external galaxies see for instance Majewski, 2010, and references therein).

Hence, it is evident that the MW and, more in general the Local Group (LG) offers an excellent laboratory for studies of galaxy formation and evolution at the highest possible resolution, thanks to the possibility of analyzing individual stars.

In this context, the Galactic halo probably offers the best opportunity to probe the details of the hierarchical scenario at $z = 0$. It is possible to identify groups of halo stars that originate from common progenitor satellites (see f.i. Navarro et al., 2004). The study of the stellar content, star formation history and chemical evolution of these disrupting systems is a fundamental step in order to reconstruct the evolutionary history of the MW. Dynamics and chemistry are two basic tools to identify these systems. Some objects can be identified by the coherence in the phase space (positions and velocities) of their stellar population, as happened in the case of Sgr dSph (Ibata et al., 1994). Some other objects could be identified by the presence of an unexpected (related to the halo) stellar population in a region of the sky: this is the case of the Boötes III stellar system, as we will see in chapter 5, and also of the large number of "ultra-faint" dwarf galaxies discovered in the last years (Zucker et al., 2006a,b; Belokurov et al., 2007a,b; Irwin et al., 2007; Liu et al., 2008; Martin et al., 2008; Grillmair, 2009).

Dynamics plays an important rôle in the contribution that stellar populations can give in the study of hierarchical galaxy formation. In fact, infall of DM subhaloes along filaments should leave rather specific fingerprints in terms of preferred shapes, orientations and coincidences of orbit of LG systems and

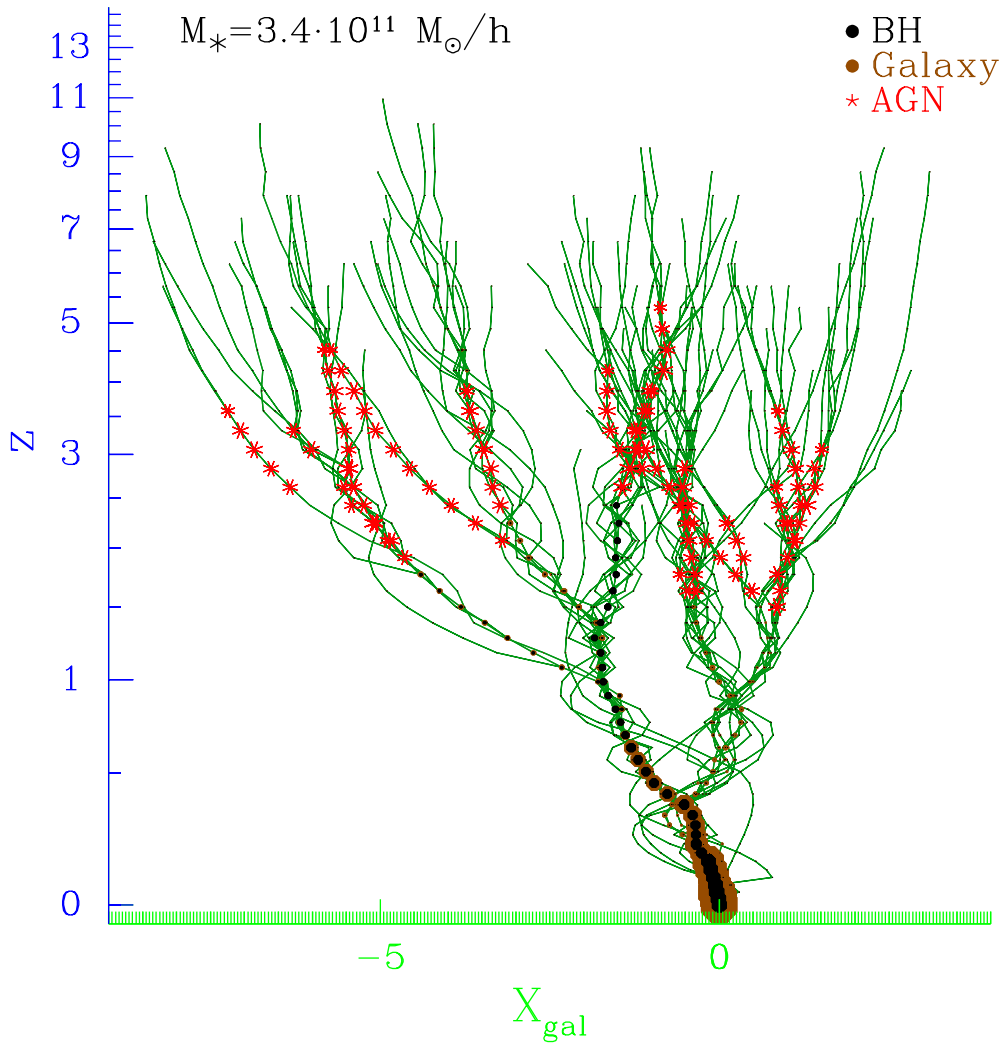

Figure 2.1: A typical MW like galaxy merging-tree model, from Marulli et al. (2009). The sizes of brown and black dots are proportional to the stellar mass of the galaxies and to the mass of the central black holes (BHs), respectively. The red stars indicate the presence of an AGN and their sizes are proportional to the AGN bolometric luminosities. In the example shown, the merging history of a parent galaxy with stellar mass $M_\star = 3.4 \cdot 10^{11} h^{-1} M_\odot$ is traced back in time from $z = 0$, at the bottom of the plot, out to $z \sim 10$. The variable on the horizontal axis represents the displacement between the parent galaxy and its progenitor, defined as $X_{gal} = \sum_{i=1}^{3} (x^i_{gal} - x^i_{par})$, where x^i_{gal} and x^i_{par} represent the three Cartesian comoving components of the progenitor and the parent galaxy, respectively, in unit of h^{-1} Mpc.

MW satellites, accreted globular cluster and (halo) stars (see e.g. Knebe et al., 2004). It has long been known that most of the "classical" MW satellites show a relatively strong planar alignment (see Fusi Pecci et al., 1995; Metz et al., 2009; Majewski, 2010, and references therein) almost perpendicular to Galactic plane. Analysis of the proper motions of these MW satellites has more or less supported the notion of dynamical kinship of at least some satellites, at least in that a number of these systems seem to share similar orbital poles, showing common direction of angular momentum. Dynamical correlations could reflect some relations occuring among the satellites: (1) through the break-up of once larger satellites, like a greater Magellanic or Fornax system (Kunkel, 1979; Lynden-Bell, 1982; Majewski, 1994; Metz et al., 2008); (2) through the formation of satellites as tidal dwarfs (see e.g. Kroupa et al., 2005); (3) through the infall of satellites onto the MW in groups (Li & Helmi, 2008; D'Onghia & Lake, 2008; Metz et al., 2009); or (4) through the preferential infall of satellites along CDM filaments (Kang et al., 2005; Zentner et al., 2005).

According to the simulations, the surviving galaxies of today reflect the most recent infall into the MW - of subhaloes now in the MW, those in current satellites were the most distant subhaloes at earlier times. Earlier material to fall in came from initially closer matter and is now spread out among the star and star cluster debris of the halo. Thus, comparing the orbits of the satellites to the orbits of halo stars is a comparison of how infall proceeded at these different epochs, and this translates to spatial variations in the dynamics. According to high-resolution numerical simulation (e.g. Diemand et al., 2005) the outermost Galactic halo stars and globular clusters should be on radially biased orbits while the inner regions should contain more isotropic orbits. The predicted kinematics for the late-infalling satellite dwarf galaxies is different, with small anisotropies even in the outer parts.

Also the study of the chemical properties of the stellar populations of these systems is fundamental. Different merger histories for galaxies will yeld different chemical patterns in their substructure. As shown by Johnston et al. (2008), $[Fe/H]$ is a tracer of accreted masses (because larger mass satellites typically have higher metallicity), while $[\alpha/Fe]$ more or less traces the accretion times of satellites (because in more recent mergers, satellites and tails tend to have lower $[\alpha/Fe]$). Thus, there are strong motivations to study the chemistry of galactic substructure, because it is possible to constrain the parent halo accretion history, to learn about the star formation histories and chemical enrichment histories of stream progenitors, to establish the connection between present, bound host satellites and stars lost in the halo,

to reconstruct the chemical distribution of the original satellite galaxies and finally, to check the chemical make-up of haloes against CDM model predictions (for a complete review on this topic see Freeman & Bland-Hawthorn, 2002, and references therein).

Moreover checks on the theory with resolved stellar populations are very important because, while ΛCDM has enjoyed great success in matching the observations of structures on the largest scales, several problems still remain in matching the theory to observations on galaxy scales. Among these problems on small scales we remind: (1) the "missing satellite problem", where the models predict a mass spectrum of galaxy subhaloes that are strongly in disagreement with that observed around the MW (e.g. Klypin et al., 1999); (2) the "central cusp problem", where ΛCDM predicts the mass density of galaxies to have steeply rising central cusp (e.g. Navarro et al., 1997) for which there is little observational evidence in the MW (see f.i. Merrifield, 2005) and which is belied by the flat central density profiles of dwarf galaxies; and (3) problems with the predicted angular momentum distributions in galaxies, wherein the models have difficulty making large, extended discs like that of the MW (e.g. Abadi et al., 2003).

For what concern the "missing satellite problem", another interesting possibility is that some of the missing satellites had already been discovered but not recongized as remnants of accreted dwarf galaxies. This could be the case of some massive Galactic globular clusters, like ω Centauri (ω Cen) and Terzan 5 (Ferraro et al., 2009).

ω Cen is the most massive and luminous globular cluster of the MW ($M_V \sim -10$ and $M \sim 2.5 \cdot 10^6 M_\odot$). It is the only known globular cluster which shows clear star-to-star variations in the abundance in the iron-peak elements (Freeman & Rodgers, 1975; Norris et al., 1996) and indications exist for possible helium abundance variations within its stellar population (Norris, 2004; Piotto et al., 2005). Together with a few other clusters (like M54 and NGC2419, for example) ω Cen fall well above the sharp upper envelope of the main distributions of globular clusters on the size-luminosity plane (Mackey & van den Bergh, 2005; Federici et al., 2007). These (and other) evidences suggest that ω Cen could be not a "genuine" globular cluster but more likely the nuclear remnant of a dwarf galaxy that merged in the past with the MW (see Bellazzini et al., 2008, for the discussion of the analogy with the case of M54 within the disrupting Sgr dSph).

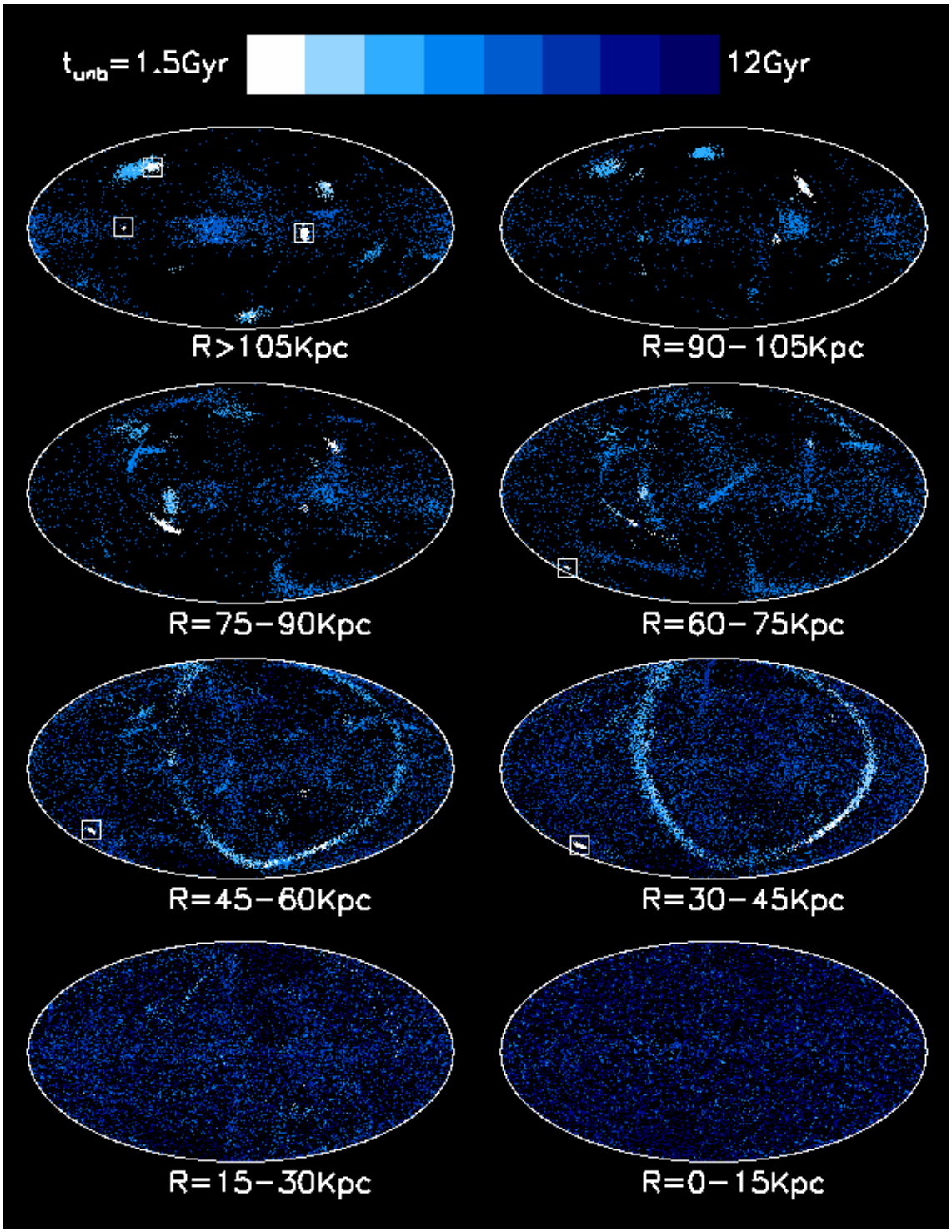

Figure 2.2: Stellar haloes model by Bullock & Johnston (2005) in all-sky projection whitin bins of 15 Kpc stepping out in Galacto-centric radius. Each point represents a tracer star of one per $500L_{\odot}$ in total V-band luminosity. The color code (shown at the top) represents the time the particle became unbound from its original satellite. Bound particles and recent disruptions are white. The boxes signify bound systems at $z = 0$. Substructure is apparent in this color space, which may provide a reasonable tracer how chemically evolved the stars should be.

SECTION 2.1

A tool to investigate the halo: wide field surveys

Another prediction of CDM models is that subhaloes infallling onto MW-like systems will face dynamical shredding and create a web of luminous (and dark) streams around these systems (i.e: satellites that undergo tidal disruption, see Fig. 2.2 from Bullock & Johnston, 2005). The vision of a MW halo networked by streams has been hinted at for several decades by small, pointed pencil-beam surveys, with the conclusion that the *entire* halo is made from accreted systems (see e.g. Majewski, 2004, and references therein), erasing the concept of a smooth halo with a density profile scaling as a simple power law.

However, this vision of the MW halo is finally came out in all its magnificence with the advent of wide field photometric (and spectroscopic) surveys like the Two Micron All Sky Survey (2MASS, Skrutskie et al., 2006) and the Sloan Digital Sky Survey (SDSS, Adelman-McCarthy et al., 2008, and references therein) which have enabled the construction of large portraits of the halo where many of these streams can be seen clearly.

The 2MASS is a photometric survey that covers all the entire celestial sphere in the H (1.25 μm), J (1.65 μm) and K_s (2.16 μm) near-infrared photometric bands. 2MASS produced a Point Source Catalogue of ~ 470 million sources and an Extended Source Catalogue of ~ 1.6 million sources. 2MASS revealed itself to be of great importance in the discovery and study of the Sgr Stream. In fact, Ibata et al. (2002), using M giants selected from the Second Incremental Data Release of 2MASS, obtained the first panoramic view of the Sgr Stream. Subsequently, Majewski et al. (2003), having at disposal the final All Sky Data Release of 2MASS, provided a clearer view of the whole complex, tracing very neatly the Sgr Stream all over the celestial sphere (see Fig. 2.3).

Instead, the SDSS is a digital photometric and spectroscopic survey which covers up to one quarter of the celestial sphere in the North Galactic Cap while a smaller area (~ 225 deg^2) but much deeper is sampled in the Southern Galactic hemisphere (York et al., 2000; Stoughton et al., 2002; Abazajian et al., 2003; Gunn et al., 2006; Tucker et al., 2006). The flux densities of detected objects are measured almost simultaneously in five bands, *u, g, r, i,* and *z* (Fukugita et al., 1996; Gunn et al., 1998; Smith et al., 2002; Hogg et al., 2001). The final survey sky coverage of about 8000 deg^2 results in photometric measurements to the above detection limits for about 80 million stars and a similar number of galaxies. Also the SDSS, as we will see in detail in the next

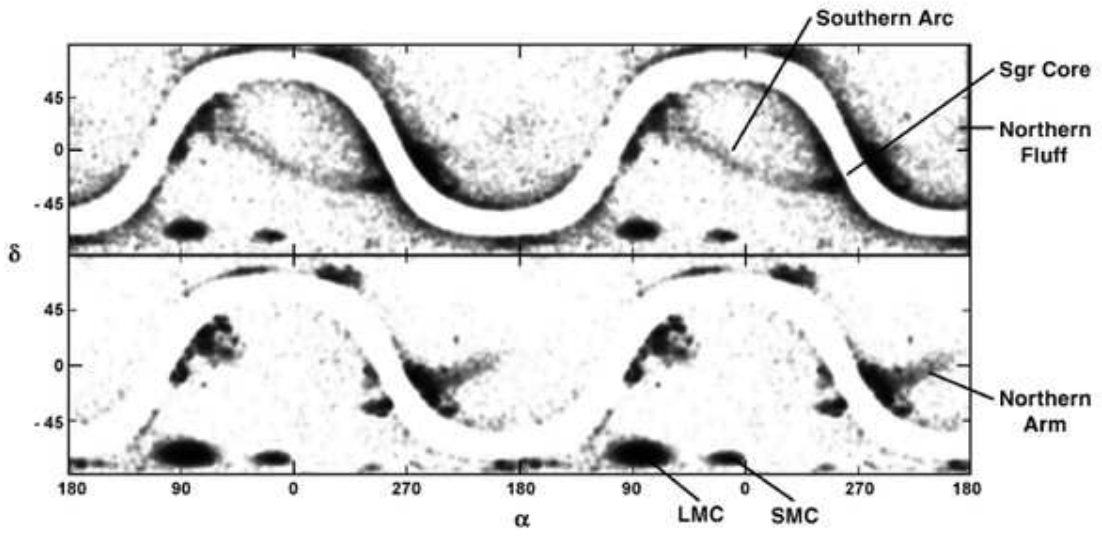

Figure 2.3: Smoothed maps of the sky in equatorial coordinates for two color-magnitude windows of the (nondereddened) 2MASS point-source catalogue filtered optimally to show the southern arc (top) and the northern arm (bottom), from Majewski et al. (2003): $11 \leq K_s \leq 12$ and $1.00 \leq J - K_s \leq 1.05$ (top), and $12 \leq K_s \leq 13$ and $1.05 \leq J - K_s \leq 1.15$ (bottom). They show two cycles around the sky to demonstrate the continuity of features.

chapters, played a fundamental rôle in this field of research. For example, Belokurov et al. (2006) exploiting the SDSS data release 5 (DR5) provided a picture of the leading arm of the Sgr Stream in the North Galactic Cap with remarkable clarity, together with a number of other notable stellar structures in the field, that for this reason was called "Field of Streams" (see Fig. 2.4).

Therefore, with the advent of these large surveys, our ability to detect stellar systems and/or structures in the halo and in the disc of the MW has incredibly increased and several large-scale likely relics of the build-up of the Galactic halo have been identified (Ibata et al., 2001; Newberg et al., 2002; Yanny et al., 2003; Majewski et al., 2003; Martin et al., 2004; Belokurov et al., 2006; Jurić et al., 2008). Also smaller tidal streams have been found around disrupting globular cluster (see, for example Rockosi et al., 2002; Grillmair & Johnson, 2006) or lacking an evident progenitor (Grillmair & Dionatos, 2006; Belokurov et al., 2006, hereafter Bel06). Furthermore a large number of new dSph galaxies of extremely low luminosities have been discovered (Willman et al., 2005; Zucker et al., 2006a,b; Belokurov et al., 2007a,b; Irwin et al., 2007; Liu et al., 2008; Martin et al., 2008; Grillmair, 2009), substantially doubling the number of dwarf galaxies previously known. In Fig. 2.5 these new detected dwarf galaxies are reported, together with the previously known ones: there is an evident increase (of a factor ~ 2) in the number of dwarf

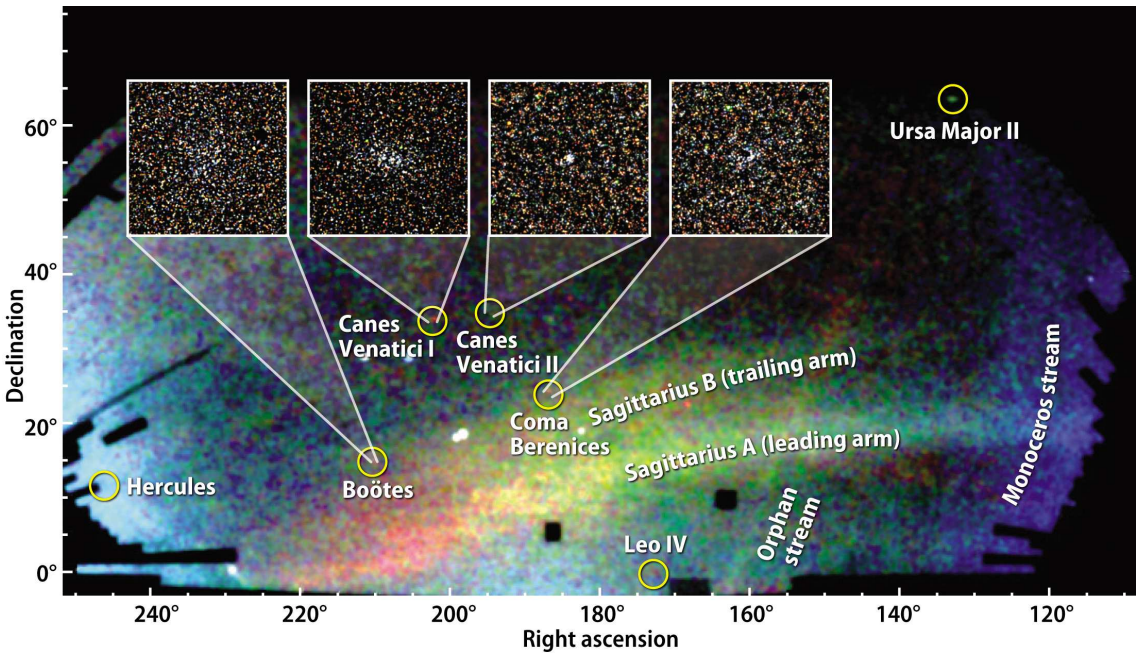

Figure 2.4: Spatial density of SDSS stars with $g-r<0.4$ around the North Galactic Cap in equatorial coordinates, binned $0.5^\circ \times 0.5^\circ$, from Belokurov et al. (2006). The color plot is an RGB composite with blue for the most nearby stars with $20.0<r\leq 20.66$, green for stars with $20.66<r\leq 21.33$ and red for the most distant stars with $21.33<r\leq 22.00$. Note the bifurcation in the Stream starting at $\alpha\approx 180^\circ$. Further structures that are visible are the Monoceros Ring at $\alpha\approx 120^\circ$ and the Orphan Stream at $150^\circ\leq\alpha\leq 160^\circ$ and $0^\circ\leq\delta\leq 10^\circ$. At $\alpha\approx 230^\circ$, near the left bottom margin of the figure, is also visible the globular cluster Palomar 5, with its tidal tails. Some dwarf satellites, discovered exploiting SDSS data, are also reported.

galaxies around the MW. These ultra-faints dSphs tend to have a very high M/L ratios (Muñoz et al., 2006; Simon & Geha, 2007) that point to a common dSph mass scale (Strigari et al., 2008), which may arise from some critical scale in the formation of galaxies or a characteristic scale for the clustering of Dark Matter.

The astounding pace of discovery and revolution in our understanding of the structure of the MW, that has occured as a result of these large-scale photometric surveys, can be expected to continue in the next years, with impending photometric surveys in various bands[1] that will cover a large fraction of the sky more deeply.

Not only these surveys will allow deep searches for streams and satellites through color-magnitude filtering for specific stellar tracers of these structures, but their inclusion of a time series dimension will enable the search for pulsational variables. In fact, these stars are high quality standard candles that have already proven to be quite powerful in the search for halo substructure - e.g. RR Lyrae variables from SDSS (e.g. Ivezić et al., 2004; Watkins et al., 2009) or the QUEST project (e.g. Duffau et al., 2006; Vivas & Zinn, 2006). The discovery and exploration of increasing numbers of tidal streams not only tell us about the assemblage of the *luminous* MW, but also the structure and size of the MW's dark halo, because the shapes and orbits of tidal streams are extremely sensitive probes of the overall mass distribution of the host galaxy (see Chapter. 4 for an exhaustive discussion of the fundamental rôle of Sgr Stream in this context). Also in the understanding of the chemical evolution of our Galaxy and its network of disrupted dSphs significant advances can be expexted in the next decade, where huge database of medium to high resolution spectroscopy of Galactic stars will be generated with a variety of instruments (e.g. *APOGEE*, *HERMES* and above all *Gaia*). Moreover, the accumulation of high quality radial velocities for many millions of stars will also shape a very detailed understanding of the dynamics of Galactic stellar populations. Not only the Galactic halo and its substructures will be thoroughly probed by these upcoming surveys, but also the populations of the inner Galaxy, including those typically hidden by dust obscuration, will be revealed by infrared spectroscopic surveys like for example *APOGEE*.

Therefore, the chance to take advantage of this large mine of information is of crucial importance becuase of handling with a huge amount of data that only wide field surveys can provide. They offer the opportunity to have a homogeneous and complete vision of the entire Galactic halo and of

[1] in the optical *Pan-STARSS* and *LSST* will cover the Northern hemisphere while *SkyMapper* the Southern one; in the near infrared *WISE* and other surveys will sample the Galactic midplane and region affected by strong extinction.

the objects that populate it. At the same time, to extract properly all this information and fully exploit the potentiality of these surveys, it is mandatory the developement of extremely powerful techniques aimed at investigating the fundamental properties of stellar populations composing the halo and its substructures.

SECTION 2.2

A striking example of accretion: Sagittarius dwarf spheroidal galaxy

The most spectacular example of the process of tidal disruption and accretion of a dwarf satellite into our Galaxy is the Sagittarius dwarf spheroidal galaxy (Sgr dSph), originally discovered by Ibata et al. (1994). The main body of the Sgr galaxy is located at ~ 26 kpc (Monaco et al., 2004) from the Sun, beyond the Galactic bulge (Galactic coordinates $l, b = +5.6^{\circ}, -14.0^{\circ}$), with an extension in the sky of $\sim 22^{\circ} \times 8^{\circ}$.
Furthermore Sgr it is remarkable among the other dSphs orbiting our Galaxy as (1) it is bright and massive ($M_V \simeq -13$ and $M \simeq 10^9\ M_{\odot}$, Majewski et al., 2003) and it was likely even more luminous in the past (Majewski et al., 2003; Bellazzini et al., 2003), (2) it currently hosts four globular clusters in the main body, but its GC system should have been significantly larger in the past (Bellazzini et al., 2003; Carraro et al., 2007); (3) it has a (double) stellar nucleus at its center (Bellazzini et al., 2008; Ibata et al., 2009). The stellar content in the main body of Sgr dSph is dominated by an intermediate age relatively metal-rich population, with distribution peaking at age $\sim 6-8$ Gyr and $[Fe/H] \sim -0.5$ (see Bellazzini et al., 2006, hereafter B06a, and references therein), but there is also clear evidence for the presence of an older (> 10 Gyr) and more metal-poor population as well (see Fig. 2.6), including Blue Horizontal Branch (BHB) (Ibata et al., 1997; Bellazzini et al., 1999a; Monaco et al., 2003) and RR Lyrae stars (Mateo et al., 1995; Alcock et al., 1997; Cseresnjes, 2001). All the available spectroscopic analyses indicates that the Metallicity Distribution (MD) of Sgr stars is characterized by a broad peak in the range $-1.0 \leq [Fe/H] \leq 0.0$, with a weak tail likely extending beyond $[Fe/H] < -2.0$ (see B06a, Cseresnjes, 2001; Monaco et al., 2005; Mc William & Smecker-Hane, 2006; Bonifacio et al., 2006; Sbordone et al., 2007; Bellazzini et al., 2008; Lagadec et al., 2009). $[\alpha/Fe]$ ratios appear to range from $[\alpha/Fe] \sim +0.3$ for $[Fe/H] \leq 1.2$, plunging deeply into the sub-solar

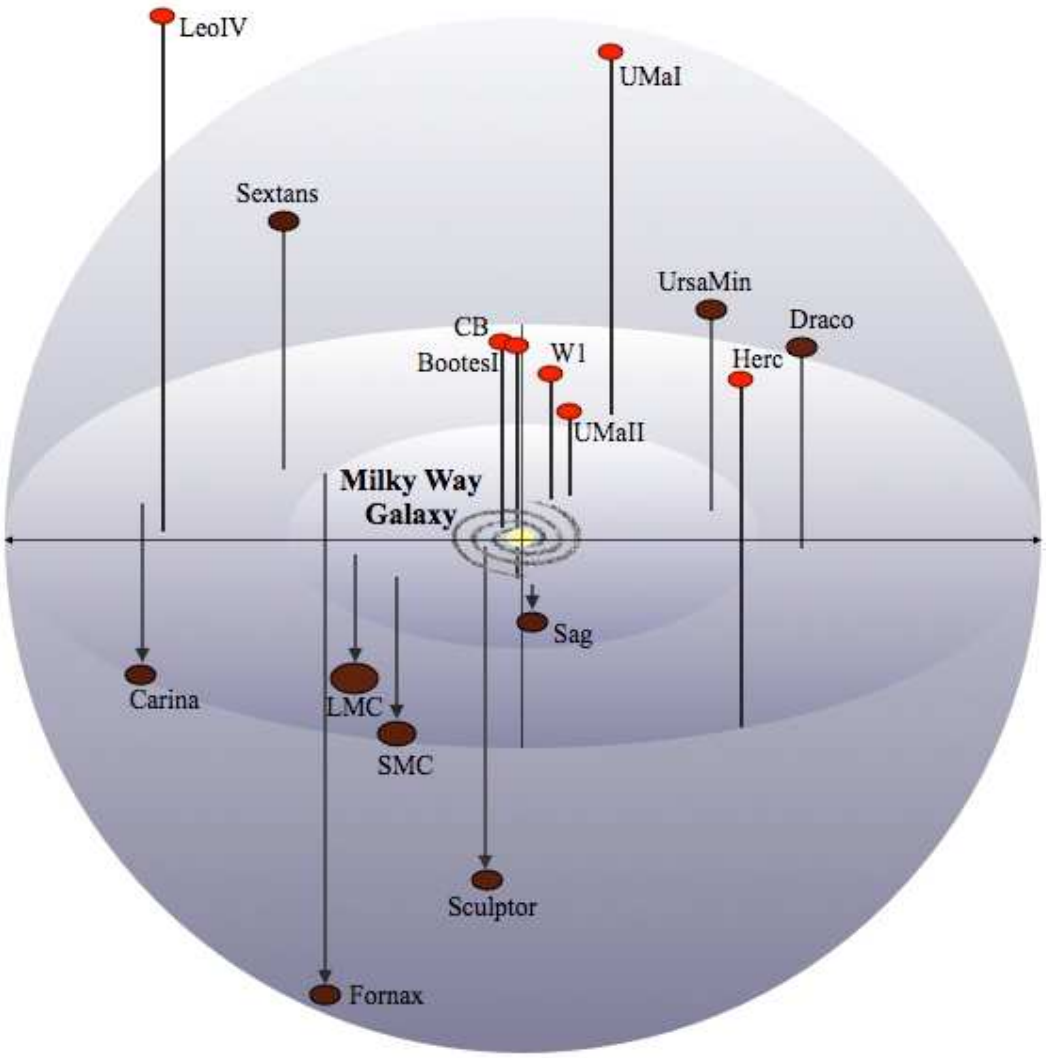

Figure 2.5: A schematic reproduction of the location of dwarf spheroidal galaxies in the neighbourhood of the MW. The ultra-faint dSphs, discovered by the SDSS are reproduced with filled red points, while the previously known dSphs are in brown. The ratio between the dimension of the points and of the MW is in scale, that is the different dimension of the points indicate the different size of the galaxies. Thanks to the SDSS, the number of dSphs galaxies of the LG is increased by a factor of ~ 2.

regime at high metallicity ($[\alpha/Fe] \sim -0.5$). s-process abundances are strongly enhanced and $[Cu/Fe]$ is deficient with respect to the trends observed in the Galactic disc/halo, indicating that Sgr followed a chemical evolutionary path remarkably different from the MW.

The body of Sgr dSph appears tidally disturbed (Ibata et al., 1995), and, soon after its discovery, it was realized that there was some tidal debris surrounding the galaxy (Mateo et al., 1996; Fahlman et al., 1996; Alard, 1996; Ibata et al., 1997; Majewski et al., 1999). Indeed, it has been subsequently established that there are two huge tidal tails promanating from the edges of the galaxy and approximately tracing its orbital path, as expected from N-body simulations (Johnston et al., 1995; Ibata & Lewis, 1998). These tails form a coherent and dynamically cold filamentary structure (hereafter Sgr Stream) that extend for tens of kpc from the parent galaxy and has been probed with many different tracers. Yanny et al. (2000) used SDSS first-year commissioning data to identify an overdensity of blue A-type stars in two stripes located at (l, b,D)= ($341^\circ, +57^\circ$,46 kpc) and ($157^\circ, -58^\circ$,33 kpc), which were subsequently found to match with the prediction of the available theoretical models of the Sgr Stream (Ibata et al., 2001). Similarly, (Ivezić et al., 2000) noticed that clumps of RR Lyrae stars in SDSS commissioning data lay along the Sgr orbit. The thorough study of the structure of the halo as traced by F stars from the SDSS, within a strip of $\pm 1.26^\circ$ around the celestial equator, by Newberg et al. (2002) provided the first examples of color Magnitude Diagrams (CMD) of the Stream population toward (l, b)= ($350^\circ, 50^\circ$) and (l, b)= ($167^\circ, -54^\circ$). Other detections toward specific directions were provided by Martínez-Delgado et al. (2001, 2004); Bellazzini et al. (2003); Vivas & Zinn (2006).

The first panoramic view of the Sgr Stream was presented by Ibata et al. (2002) using late M giants selected from the Second Incremental Data Release of 2MASS. Subsequently, Majewski et al. (2003), having at disposal the final All Sky Data Release of 2MASS, used a larger sample of M giants to provide a clearer view of the whole complex, tracing very neatly the trailing tidal tail all over the Southern Galactic hemisphere, as well as the part of the leading arm closer to the main body of the galaxy, up to $RA \simeq 190^\circ$ (see Fig. 2.3).

In a very recent analysis Yanny et al. (2009) showed that M and K giants can be successfully selected also from the SDSS and SEGUE datasets (Yanny et al., 2009) and used to trace the Stream; one main advantage of using giants as tracers is that they can be (relatively) easily followed-up spectroscopically, thus providing crucial kinematical and chemical information (Majewski et al., 2004; Monaco et al., 2007; Chou et al., 2007; Yanny et al., 2009).

Bel06 exploited the SDSS data release 5 (DR5) to provide a picture of the leading arm of the Sgr Stream in the vicinity of the North Galactic Cap with remarkable clarity, using tracers (A-F dwarfs) that are intrinsically more numerous than M giants, for a given space density and/or surface brightness[2]. In their Fig. 1 (i.e., Fig. 2.4), they show the density of (candidate) A-F dwarf stars (selected with a simple color cut, $g-r \leq 0.4$, corresponding to $\sim B-V \leq 0.6$) in the portion of the sky covered by the SDSS. The Sgr Stream emerges very clearly as a broad (and bifurcated) band going from (α, δ) $\simeq (220^{\circ}, 0^{\circ})$ to (α, δ) $\sim (125^{\circ}, 25^{\circ})$, where it plunges into the Galactic Disc. The color cut adopted by Bel06 is very successful in tracing the Stream structure as it takes advantage of the fact that Sgr stars are younger than typical halo stars, hence they have a bluer Turn Off (TO) color with respect to the halo population (see Unavane et al., 1996, for another application of the same principle). The density map by Bel06 puts in evidence a clear distance gradient along the Stream, from the nearest part crossing the Disc at $\alpha \approx 120$, to the the most distant part at $\alpha \approx 210$, toward the North Galactic Pole (NGP). More recently, in a pilot project limited to a subsample of the SDSS (the so called Stripe 82) Cole et al. (2008) described a more refined approach to the study of the spatial structure of the Stream, using the same tracers as Newberg et al. (2002). Very recent detections from different data and/or using different models can be found also in de Jong et al. (2009), Prior et al. (2009a), and Keller (2009a).

[2]In a stellar population of given age and chemical composition the number of stars per units of sampled (integrated) luminosity in a given evolutionary phase is proportional to the duration of the evolutionary phase (see Renzini & Buzzoni, 1986; Renzini & Fusi Pecci, 1988; Renzini, 1998, and references therein). A-F stars are evolving along the Main Sequence, a phase lasting several Gyr for these stars, while M giants are in the latest phases of their evolution along the Red Giant Branch, lasting $< 10^8$ yr. Hence in any given field, independently of the absolute density normalization, A-F dwarfs outnumber M giants by a factor of > 10.

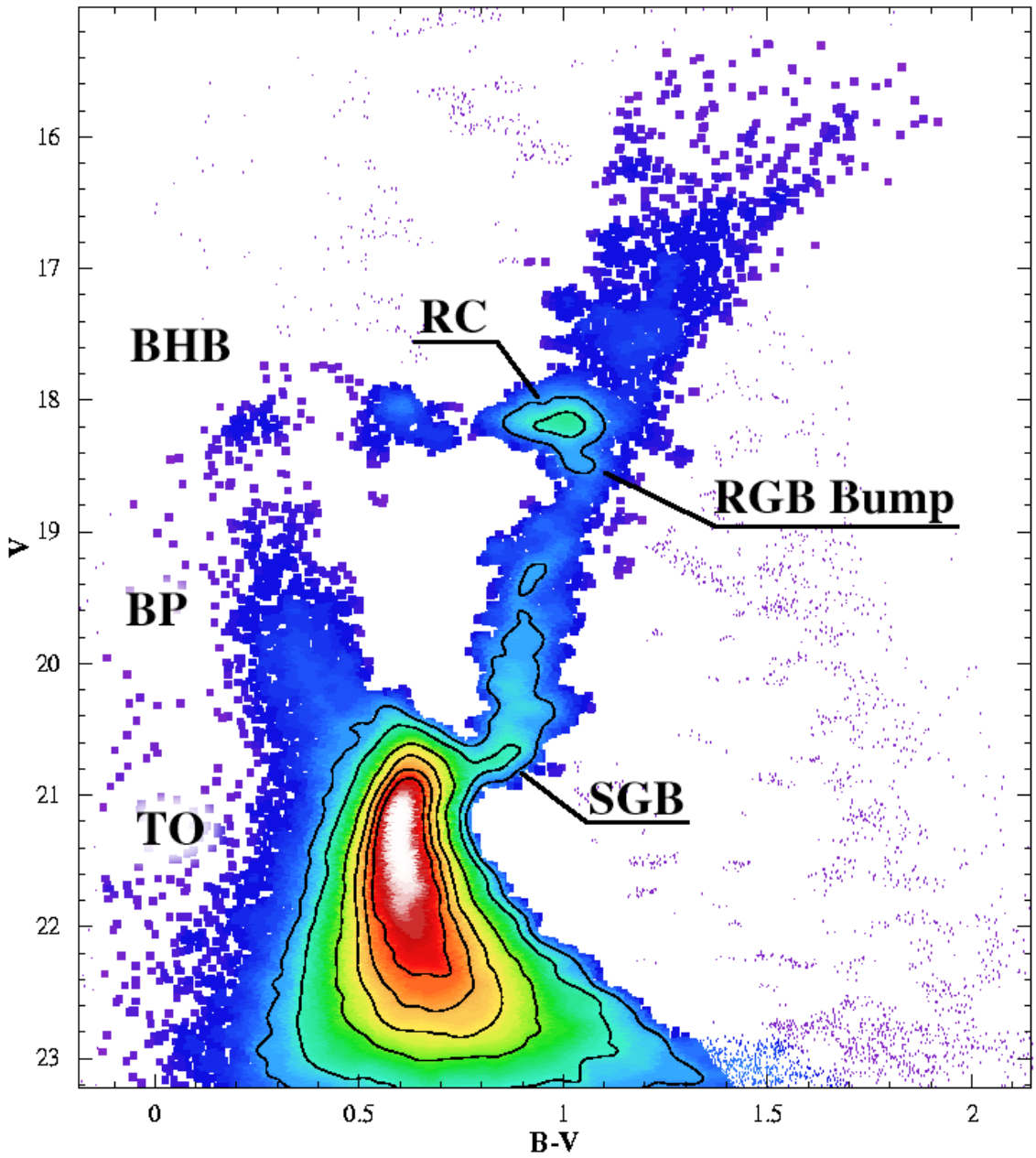

Figure 2.6: Statistically decontaminated CMD of the *Sgr34* Field, in the core of Sgr dSph, presented in B06a. The color of the stars is coded according to the local density of stars on the diagram. A few representative density contours are also overplotted. Some remarkable features of the CMD are labeled: the Red Clump (RC), the Blue Horizontal Branch (BHB), the RGB Bump, the Blue Plume (BP), the Main Sequence Turn Off point (TO) and the Sub Giant Branch (SGB). The spurious residuals of the statistic decontamination process (mainly due to edge effects) to the lower left and the upper right of the main locus of the Sgr populations in the CMD have been plotted as small points to provide a clearer view of the most significant parts of the diagram.

CHAPTER 3

Detection of a population gradient in the Sagittarius Stream

We present a quantitative comparison between the Horizontal Branch morphology in the core of the Sagittarius dwarf spheroidal galaxy (Sgr dSph) and in a wide field sampling a portion of its tidal stream (Sgr Stream), located tens of kpc away from the center of the parent galaxy. We find that the Blue Horizontal Branch (BHB) stars in that part of the Stream are five times more abundant than in the Sgr core, relative to Red Clump stars. The difference in the ratio of BHB to RC stars between the two fields is significant at the $\geq 4.8\sigma$ *level. This indicates that the old and metal-poor population of Sgr was preferentially stripped from the galaxy in past peri-Galactic passages with respect to the intermediate-age metal rich population that presently dominates the bound core of Sgr, probably due to a strong radial gradient that was settled within the galaxy before its disruption. The technique adopted in the present study allows to trace population gradients along the whole extension of the Stream.*

SECTION 3.1

Introduction

The Sagittarius dwarf spheroidal galaxy (Sgr dSph, Ibata et al., 1994) provides an excellent case for the study of the process of tidal disruption and accretion of a dwarf satellite into a large galaxy. Its huge tidal tails form a coherent and dynamically cold filamentary structure (hereafter Sgr Stream) extending for tens of kpc from the parent galaxy that has been probed with many different tracers (see, among the others Ibata et al., 2001; Newberg et al., 2002; Majewski et al., 2003; Martínez-Delgado et al., 2004; Vivas et al., 2005; Belokurov et al., 2006, and references therein).

It is quite clear that the progenitor of the presently observed Sgr remnant was a quite remarkable galaxy, possibly similar to the LMC (Monaco et al., 2005, hereafter M05). While the stellar content of the bound core of the galaxy is dominated by an intermediate-old metal-rich population, $[M/H] \sim -0.5$, (M05 Bellazzini et al., 2006, hereafter B06), the globular clusters possibly associated with the Stream are predominantly old and metal-poor (Bellazzini et al., 2003; Belokurov et al., 2006). Majewski et al. (2003, hereafter M03) and Martínez-Delgado et al. (2004, hereafter MD04) provided the first indications of the possible presence of a metallicity gradient along the Stream, suggesting that the stars lost in previous peri-Galactic passages, were, on average, more metal poor than those recently lost or still bound to the main body. Chou et al. (2007, hereafter C07), studying the chemical abundances of relatively nearby Stream stars, have shown that the metallicity distribution within the Stream is significantly different from that of the main body of Sgr, the former being skewed toward lower metallicities. These results strongly suggest that the stellar content of the Sgr progenitor could have been quite different from the present-day remnant, and indicates that it may be possible to trace the change of stellar content along the Stream (see C07). The Horizontal Branch (HB) morphology is a very powerful tool to study population gradients within galaxies (see Harbeck et al., 2001), since the color of HB stars depends very strongly on their age and metal content (see Fusi Pecci et al., 1993, for discussion and references).

In particular, HB stars can be located to the *blue* of the RR Lyrae instability strip (Blue HB stars) only if they are very old (age $>$ 10 Gyr) and (typically) metal-poor, while HB stars lying to the *red* of the instability strip (Red Clump stars) must be (comparatively) young or metal-rich, or both (see Monaco et al., 2003, and B06a for the interpretation of the HB morphology of Sgr in this context).

Monaco et al. (2003) noted that both the BHB and RC sequences observed at the center of Sgr have a clear counterpart in the Color-Magnitude Diagrams (CMDs) of Stream fields obtained by Newberg et al. (2002, hereafter N02) using data from the Early Data Release of the Sloan Digital Sky Survey (SDSS). Here we perform a direct comparison of the relative abundance of BHB and RC stars in the Sgr core and in one of the Stream fields studied by N02, to search for a population gradient. While the results we obtain are qualitatively similar to those of C07, they refer to a different and more distant portion of the Stream, and provide an on-field demonstration that the whole Sgr Stream can be studied with this technique.

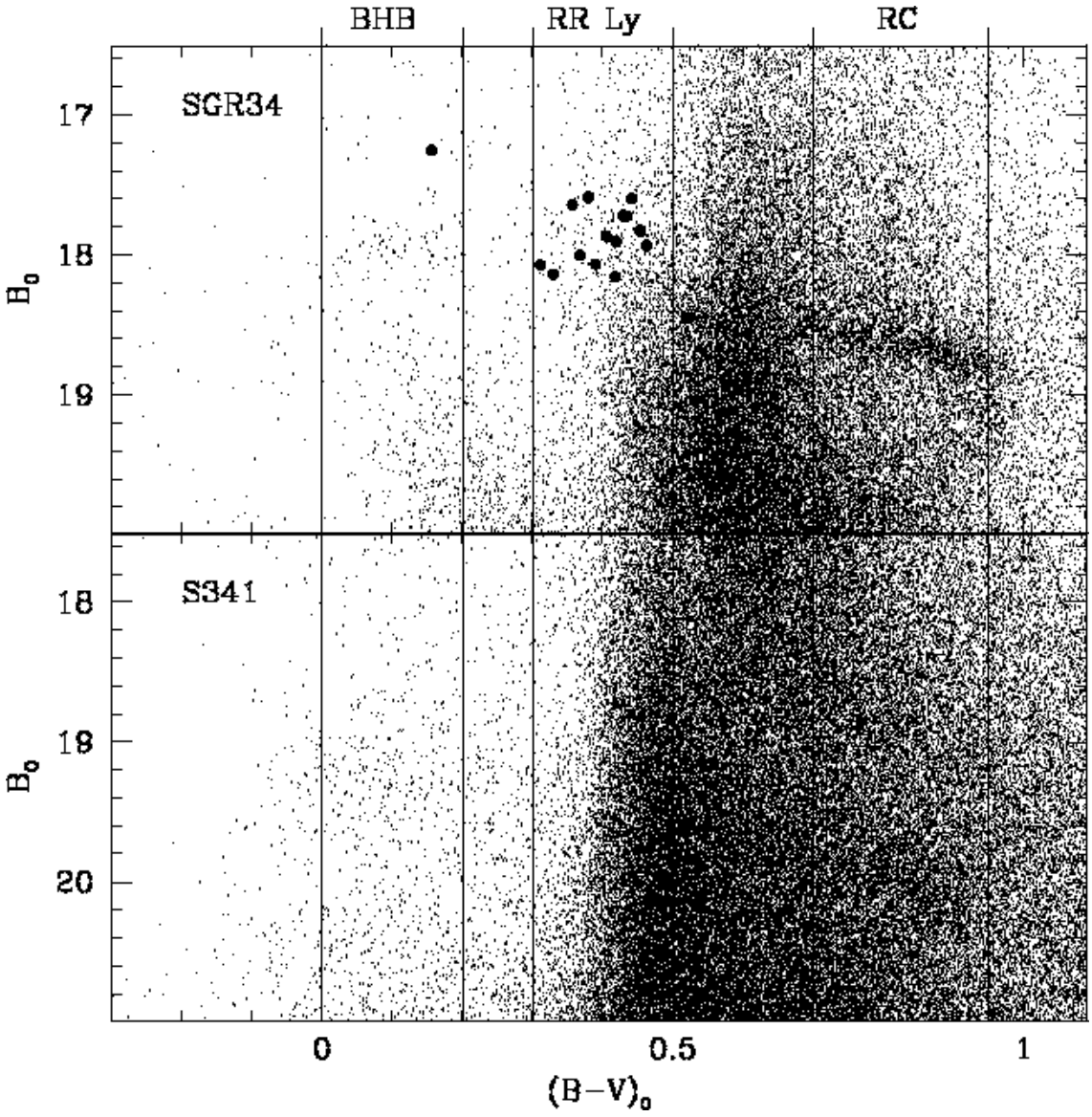

Figure 3.1: CMDs focused on the Horizontal Branch for fields in the core of Sgr (upper panel) and in the Sgr Stream (lower panel). The color strips adopted to select candidate RC and BHB stars are enclosed within vertical lines and labeled. The filled circles in the CMD of *Sgr34* are the ab type RR Lyrae counter-identified in the nearby SGRW field from the catalogue of (Cseresnjes, 2001).

3.1.1 The data

To obtain a representative sample of the stellar population in the core of Sgr we take the photometry of the $1^\circ \times 1^\circ$ wide field located $\sim 2^\circ$ eastward of the galaxy center, recently presented by B06a, i.e. the *Sgr34* field [(l,b) $\simeq (6.5^\circ, -16.5^\circ)$, see B06a for details]. N02 provided two very clear detections of the Sgr Stream in their fields S341+57-22.5 and S167-54-21.5, where the first two numbers of the names are the mean Galactic longitude and latitude. While the BHB is clearly visible in the CMD of S167-54-21.5, the signal of the Stream RC is too weak in this field to derive fully reliable star counts, due to various intrinsic factors that will be discussed elsewhere (Bellazzini et al., in preparation). Hence we exclude this field from the analysis and we focus on S341+57-22.5 (S341 hereafter, for brevity), a ~ 62.5 deg^2 strip enclosed within $200^\circ \leq RA \leq 225^\circ$ and $-1.25^\circ \leq Dec \leq 1.25^\circ$, that samples a portion of the leading arm of the Stream, lying more than 40 kpc away from us in the Northern Galactic hemisphere (N02, Law et al., 2005). The g*,r* photometry by N02 has been transformed into Jonhsons-Cousins B,V according to Smith et al. (2002). The photometry has been corrected for extinction following B06a. Note that the average reddening in the S341 field is $E(B-V) = 0.04$ mag.

SECTION 3.2

HB star counts

In Fig. 3.1 we present reddening-corrected B, B-V CMDs focused on the HB of fields within the main body of Sgr and of the S341 field in the Sgr Stream. We chose the B, $B-V$ CMD because in this plane a larger section of the BHB sequence appears nearly horizontal, with respect to V, $B-V$ diagrams. This will allow a better background subtraction, according to the method that will be described below. Conversely, the RC, that appears tilted in the CMDs of Fig. 3.1, is nearly perfectly horizontal in V, $B-V$ diagrams.
The filled circles superposed in the CMD of *Sgr34* are the ab type RR Lyrae variables we counter-identified in a field located $\sim 2^\circ$ westward of the center of Sgr (SGRW) from the catalogue of Sgr variables by Cseresnjes (2001). The wide area surveyed by Cseresnjes (2001) does not include the *Sgr34* field but has a large overlap with SGRW. The photometry is from the same survey of the *Sgr34* field, the data reduction has been performed as in B06a.
In our dataset the variables are observed at random phase: their color-magnitude distribution is useful here to indicate the position of the instability

strip in our diagrams, that will help in the selection of relatively *pure* BHB and RC samples.
The RC-labeled color strip $0.7 \leq (B-V)_0 \leq 0.95$ encloses the Red Clump population in the main body (at $B_0 \sim 18.7$, upper and middle panel of Fig. 3.1) and in the S341 field (at $B_0 \sim 20.0$, lower panel; the fainter mean magnitude with respect to *Sgr34* is due to a difference in distance between the populations sampled by the two fields, see N02 and Monaco et al., 2004).
The BHB-labeled color strip ($0.0 \leq (B-V)_0 \leq 0.2$), on the other hand, encloses the more populated portion of the BHB, far to the blue of the ab RR Lyrae, at $B_0 \sim 18.0$ in *Sgr34* and at $B_0 \sim 19.3$ in S341.
Obviously there are BHB stars bluer than this limit; the adopted selection is optimally suited for the background subtraction technique described below. Since the comparison is purely differential this does not affect the results discussed below, but the adopted selection does not allow a complete census of BHB stars[1].
It can be seen from Fig. 3.1 that the RC in S341 is slightly bluer than in *Sgr34* (by $\simeq 0.05$ mag). This may be interpreted as a signature of a difference in mean metallicity between the two populations. However, it cannot be excluded that relatively small color differences may be produced by less-than-perfect transformations between the g^*, r^* and B, V, and/or by errors in reddening or calibration, while star counts should be essentially unaffected by these problems (see below).

While clearly visible in all the presented CMDs, both the RC and the BHB features are seriously affected by contamination from unrelated sources, either Sgr stars in different evolutionary phases[2] or foreground stars of our Galaxy. To remove the contribution of this generic "background signal" from star-counts we proceeded as follows: (a) we construct the Luminosity Function (LF) of the stars lying in a given color-strip (RC or BHB), (b) we fit the LF outside the peak associated with the RC and/or BHB features, (c) we subtract the fitted LF to the observed one, and (d) we sum the residuals within the narrow region enclosing the RC or BHB peak. A similar approach has been used before, see, for example, Harbeck et al. (2001). We adopt B_0 LFs for the BHB strip and V_0 LFs for the RC strip to obtain the cleanest signal as possible for the two features that greatly differ in color (temperature). The observed LFs are plotted in Fig. 3.2 for BHB stars, and in Fig.3.3 for the RC stars. RC and BHB peaks are clearly visible in all the presented LFs,

[1]This is why we find a smaller fraction of BHB stars relative to the sum of BHB and RC stars here than in Monaco et al. (2003)). In that paper a more generous selection box was adopted, including also the vertical part of the BHB.

[2]For example, most of the faintest stars in the Fig. 1 CMD within the BHB color strip belong to the Blue Plume population of Sgr (see B06a).

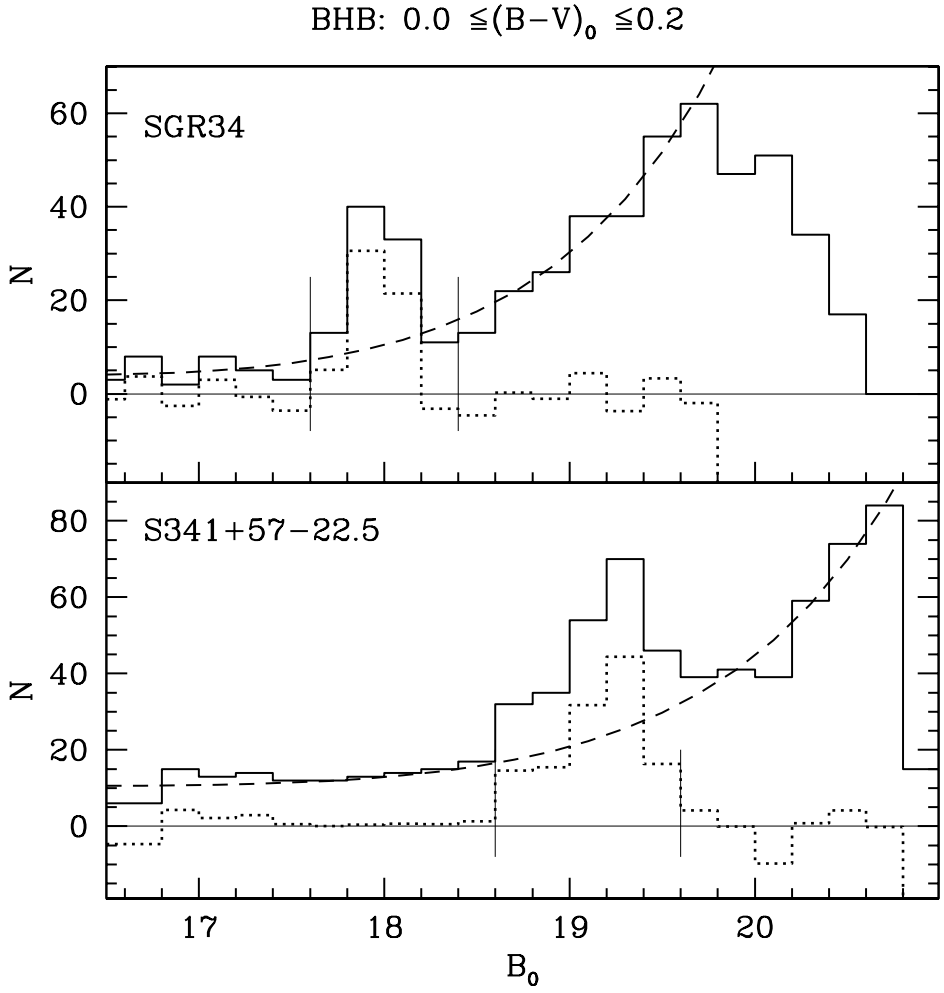

Figure 3.2: LFs of the BHB color strip. The continuous-line histograms are the observed LFs, the long-dashed lines are the best-fit curves to the underlying "background" LF outside the BHB peaks, the dotted-line histograms are the residual of the *observed LF − fitted LF* subtraction. The thin vertical segments enclose the range in which we count BHB stars (the residuals of the fit) to obtain N_{BHB}.

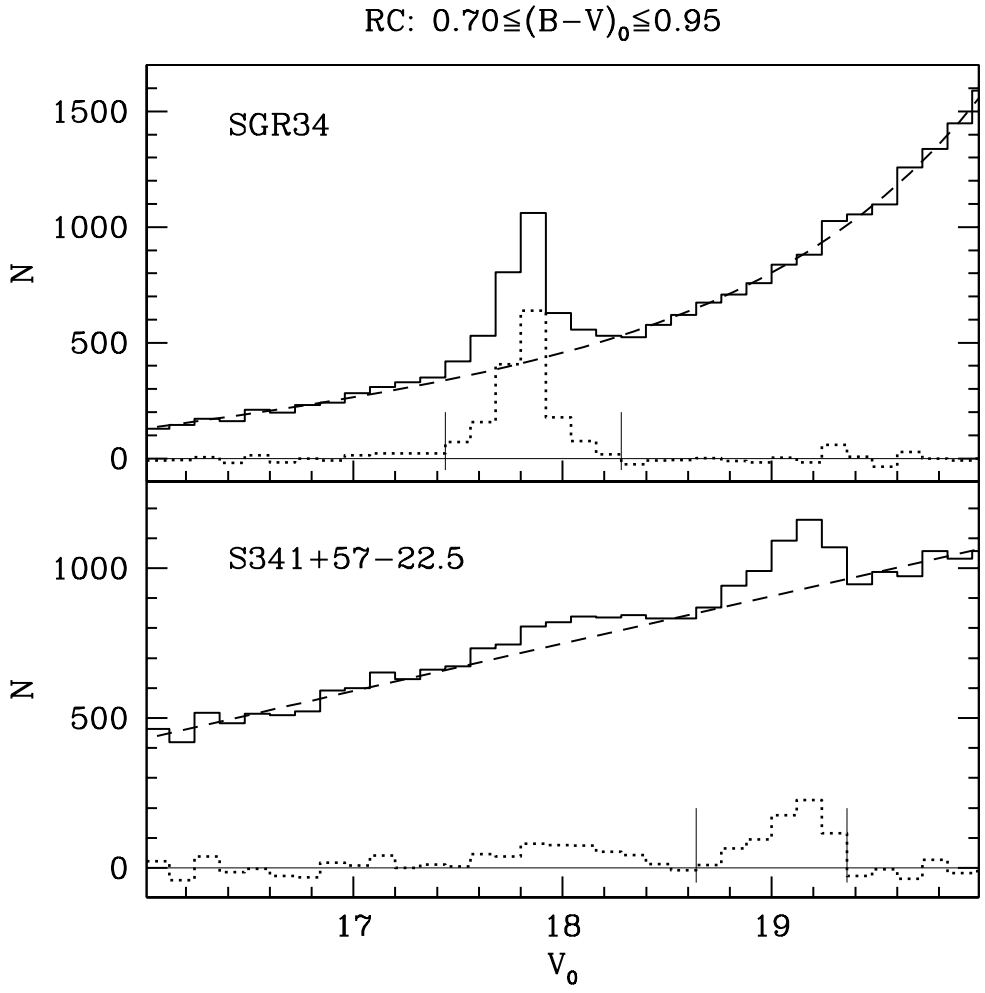

Figure 3.3: LFs of the RC color strip. The symbols are the same as in Fig. 2. The thin vertical segments enclose the range in which we count RC stars.

hence the adopted technique can be reliably used. The fact that the BHB and RC peaks in the S341 LFs are somewhat wider than those in *Sgr34* is probably due to an intrinsic difference in the distance profile along the line of sight of the two considered populations, the core of Sgr being more compact than the considered portion of the Stream. The results of the background-subtracted star counts are summarized in Table 3.1. The square root of the total number of stars counted in the reported magnitude windows (i.e. before subtraction of the background), are adopted as errors on the star counts (N_{BHB}, N_{RC}), according to Poisson's statistic. To check the effects of color shifts (due to metallicity gradients and/or errors in reddening or in the photometric calibration) we repeated the whole procedure after shifting the selection strips by ± 0.03 mag. The resulting N_{BHB}/N_{RC} ratios are unchanged, within the uncertainty, with respect to the values reported in Table 3.1. We also checked the case of a shift of -0.05 mag applied only to the RC strip of S341, to take into account the observed color shift of the Stream RGB in this field, and also in this case the change of N_{BHB}/N_{RC} is smaller that the derived uncertainty.

Table 3.1 shows that the ratio of the number of BHB stars to the number of RC stars (N_{BHB}/N_{RC}) is more than five times larger in the portion of the Stream sampled by the S341 (at $D_{\odot} \simeq 45$ kpc from us, and more than 50 kpc away from the center of the parent galaxy) than within the core of the Sgr galaxy (at $D_{\odot} \simeq 26$ kpc from us). The detected difference between the two fields is significant at the $\geq 4.8\sigma$ level; given the hypothesis that the HB morphology in S341 is the same as in *Sgr34*, we expect $N_{BHB} = 24 \pm 5$ in the Stream field, while we observe $N_{BHB} = 122 \pm 15$. Hence, BHB stars are much more abundant in the Stream (15% of the whole RC+BHB population) than in the main body of Sgr (just 3%, with the adopted selection; see footnote 1). This is a strong indication that old and metal-poor stars are much more represented in the population that was stripped from Sgr in the past than in the presently bound core, providing an independent confirmation and extension of the results by M03 and C07.

The techniques adopted by M03 and C07 may be limited in their application by a low sensitivity (as the infrared colors of M-giants, M03) or by the faintness of targets in distant regions of the Stream (as the high-resolution spectroscopy of individual stars by C07). The approach adopted here cannot provide a direct probe of the metallicity distribution as done by C07, nevertheless it relies on a very sensitive diagnostic (i.e. the HB morphology) that can be successfully measured out to very large distances.

Hence, it may give the opportunity to trace population gradients along the

Table 3.1: Star counts in the BHB and RC

	Sgr34	S341+57-22.5
N_{BHB}	54 ± 10	122 ± 15
N_{RC}	1542 ± 67	686 ± 78
$\frac{N_{BHB}}{N_{RC}}$	0.035 ± 0.007	0.18 ± 0.03
$\frac{N_{BHB}}{N_{RC}+N_{BHB}}$	0.03	0.15

whole extension of the Sgr Stream. Note that the procedure described here and the data reported in Table 3.1 provide the basis (in particular the "Sgr core zero-point" of N_{RC}/N_{BHB}) to measure the population gradient in an homogeneous scale to anyone having access to CMDs of the Stream deep enough to sample the whole HB. This may even allow one to probe differences in stellar populations between wraps of the Stream lying in the same direction but at different distances, such as those seen by Belokurov et al. (2006) and modeled by Fellhauer et al. (2006).
It is apparent from Fig. 3.2 and Fig. 3.3 that the accurate location (in magnitude) of features like the RC and the BHB may provide powerful constraints on the distance and the structure of the Stream, as we will see in next section.

SECTION 3.3

Conclusions

We have detected a $\geq 4.8\sigma$ difference in the ratio of BHB to RC stars between the core of Sgr and a distant portion of its tidal Stream. BHB stars are 5 times more abundant - relative to RC stars - in the considered Stream field than within the main body of the galaxy, a clear signature of the presence of an age/metallicity gradient along the Sgr remnant.
C07 clearly states that the observed metallicity gradient within the Stream cannot be caused by "an intrinsic variation of the instantaneous mean metallicity of Sgr with time", because the chemical enrichment of Sgr was essentially completed much before than the Stream stars that display the gradient effect were stripped from the main body of their parent galaxy (see

also B06a). This leaves the presence of a radial metallicity/age gradient in the progenitor as the only viable explanation for the observed core/Stream gradient (note, however, that the simultaneous presence of stars stripped from Sgr in different peri-Galactic passages in the same portion of the Stream may also play a role; see Fellhauer et al., 2006).

C07 notes also that the implied radial gradient should have been significantly stronger than that typically encountered in dwarf spheroidal galaxies. A comparison with the results by Harbeck et al. (2001) shows that in the galaxies of their sample the N_{BHB}/N_{RC} ratio typically varies by a factor of < 3, over the considered radial range, that is less than the factor of 5 we observe between *Sgr34* and S341.

However changes of a factor of ≥ 8 are observed in Sculptor and Sextans, hence the value found here does not appear exceptional, although the exclusion of the hottest stars from our BHB selection may hide a larger difference.

According to the N-body models by Law et al. (2005) the stars populating the branch of the Stream sampled by the S341 field have been stripped during different orbital revolutions, in the past. Independently of the adopted model (adopting a *spherical*, *oblate* or *prolate* Milky Way halo), only $\sim 30\%$ of the stars in this part of the Stream have been lost from the main body during the current peri-Galactic passage or during the immediately previous one: hence the observed population should be dominated by stars lost more than $\simeq 1.5-2$ Gyr ago (see also Belokurov et al., 2006; Fellhauer et al., 2006). Thus the observed HB morphology should reflect the stellar mix in the outer regions of the Sgr progenitor as it was 2 to 4 peri-Galactic passages ago. We conclude that such a stellar mix was significantly more metal-poor, on average, than that observed in the present-day bound remnant.

CHAPTER 4

The Northern wraps of the Sagittarius Stream as traced by Red Clump stars: distances, intrinsic widths and stellar densities.

We trace the tidal Stream of the Sagittarius dSph galaxy using Red Clump stars from the catalogue of the Sloan Digital Sky Survey - Data Release 6, in the range $150^\circ < RA < 220^\circ$*, corresponding to the range of orbital azimuth* $220^\circ < \Lambda < 290^\circ$*. Substructures along the line of sight are consistently identified as significant peaks superposed to (otherwise smooth) Luminosity Functions, in two different passbands, of colour-selected candidate Red Clump stars. A proper modeling of the LFs allow us to obtain: (a)* $\leq 10\%$ *accurate, purely differential distances with respect to the main body of Sgr, (b) estimates of the FWHM along the line of sight, and (c) estimates of the local density, for each detected substructure. In the range* $255^\circ < \Lambda < 290^\circ$ *we cleanly and continuously trace various coherent structures that can be ascribet to the Stream, in particular: the well known northern portion of the leading arm, running from* $d \simeq 43$ *kpc at* $\Lambda \simeq 290^\circ$ *to* $d \simeq 30$ *kpc at* $\Lambda \simeq 255^\circ$*, and a more nearby coherent series of detections lying a constant distance* $d \simeq 25$ *kpc, that can be identified with a wrap of the trailing arm. The latter structure, predicted by several models of the disruption of Sgr dSph, was never traced before; comparison with existing models indicates that the difference in distance between these portions of the leading and trailing arms may provide a powerful tool to discriminate between theoretical models assuming different shapes of the Galactic potential. A further, more distant wrap in the same portion of the sky is detected only along a couple of lines of sight. For* $\Lambda < 255^\circ$ *the detected structures are more complex and less easily interpreted. We are confident to be able to trace the continuation of the leading arm down to* $\Lambda \simeq 220^\circ$ *and* $d \simeq 20$ *kpc; the trailing arm is seen up to* $\Lambda \simeq 240^\circ$ *where it is replaced by more distant structures. Possible detection of more nearby wraps and of the Virgo Stellar Stream are also discussed. All the performed measures are made publicly available as a coherent set of observational constraints for new generation of theoretical models of the disruption of Sgr.*

SECTION 4.1

Introduction

Stellar tidal streams as well as other substructures in the Milky Way (MW) halo are generally interpreted as the relics of the process of hierarchical formation of the MW, as envisaged by the currently accepted cosmological model (Λ- Cold Dark Matter, Λ-CDM hereafter, see Bullock et al., 2001; Madau et al., 2008, and references therein).
With the advent of large modern surveys, like the 2 Micron All Sky Survey (2MASS, Skrutskie et al., 2006) and the Sloan Digital Sky Survey (SDSS, Adelman-McCarthy et al., 2008, and references therein), our ability to detect stellar systems and/or structures in the halo and in the disc of the MW has incredibly increased and several large-scale likely relics of the build-up of the Galactic halo have been identified (Ibata et al., 2001; Newberg et al., 2002; Yanny et al., 2003; Majewski et al., 2003; Martin et al., 2004; Jurić et al., 2008; Belokurov et al., 2006). Also smaller tidal streams have been found around disrupting globular cluster (see, for example Rockosi et al., 2002; Grillmair & Johnson, 2006) or lacking an evident progenitor (Grillmair & Dionatos, 2006; Belokurov et al., 2006, hereafter Bel06).
The most spectacular example of the process of tidal disruption and accretion of a dwarf satellite into our Galaxy is the Sagittarius dwarf spheroidal galaxy (Sgr dSph), originally discovered by Ibata et al. (1994). The main body of the Sgr galaxy is located at ~ 26 kpc (Monaco et al., 2004) from the Sun, beyond the Galactic bulge (Galactic coordinates $l,b = +5.6^{\circ},-14.0^{\circ}$). The stellar content of Sgr dSph is dominated by an intermediate-age relatively metal-rich population, with distributions peaking at age $\sim$ 6-8 Gyr and $[Fe/H] \sim -0.5$, (see Bellazzini et al., 2006, hereafter B06a, and references therein) but there is also clear evidence for the presence of an older (> 10 Gyr) and more metal-poor population as well, including Blue Horizontal Branch (BHB) (Ibata et al., 1997; Bellazzini et al., 1999a; Monaco et al., 2003) and RR Lyrae stars (Mateo et al., 1995; Alcock et al., 1997; Cseresnjes, 2001). All the available spectroscopic analyses indicates that the Metallicity Distribution (MD) of Sgr stars is characterized by a broad peak in the range $-1.0 \leq [Fe/H] \leq 0.0$, with a weak tail likely extending beyond $[Fe/H] < -2.0$ (see B06a, Cseresnjes, 2001; Monaco et al., 2005; Mc William & Smecker-Hane, 2006; Bonifacio et al., 2006; Sbordone et al., 2007; Bellazzini et al., 2008; Lagadec et al., 2009).
The body of Sgr dSph appears tidally disturbed (Ibata et al., 1995), and, soon after its discovery, it was realized that there was some tidal debris

surrounding the galaxy (Mateo et al., 1996; Fahlman et al., 1996; Alard, 1996; Ibata et al., 1997; Majewski et al., 1999). Indeed, it has been subsequently established that there are two huge tidal tails promanating from the edges of the galaxy and approximately tracing its orbital path, as expected from N-body simulations (Johnston et al., 1995; Ibata & Lewis, 1998). These tails form a coherent and dynamically cold filamentary structure (hereafter Sgr Stream) that extend for tens of kpc from the parent galaxy and has been probed with many different tracers. Yanny et al. (2000) used SDSS first-year commissioning data to identify an overdensity of blue A-type stars in two stripes located at (l, b,D)= ($341^\circ, +57^\circ$,46 kpc) and ($157^\circ, -58^\circ$,33 kpc), which were subsequently found to match with the prediction of the available theoretical models of the Sgr Stream (Ibata et al., 2001). Similarly, (Ivezić et al., 2000) noticed that clumps of RR Lyrae stars in SDSS commissioning data lay along the Sgr orbit. The thorough study of the structure of the halo as traced by F stars from the SDSS, within a strip of $\pm 1.26^\circ$ around the celestial equator, by Newberg et al. (2002) provided the first examples of Colour Magnitude Diagrams (CMD) of the Stream population toward (l, b)= ($350^\circ, 50^\circ$) and (l, b)= ($167^\circ, -54^\circ$). Other detections toward specific directions were provided by Martínez-Delgado et al. (2001, 2004); Bellazzini et al. (2003); Vivas & Zinn (2006).

The first panoramic view of the Sgr Stream was presented by Ibata et al. (2002) using late M giants selected from the Second Incremental Data Release of 2MASS. Subsequently, Majewski et al. (2003, M03 hereafter), having at disposal the final All Sky Data Release of 2MASS, used a larger sample of M giants to provide a clearer view of the whole complex, tracing very neatly the trailing tidal tail all over the Southern Galactic hemisphere, as well as the part of the leading arm closer to the main body of the galaxy, up to $RA \simeq 190^\circ$. In a very recent analysis Yanny et al. (2009) showed that M and K giants can be successfully selected also from the SDSS and SEGUE datasets (Yanny et al., 2009) and used to trace the Stream; one main advantage of using giants as tracers is that they can be (relatively) easily followed-up spectroscopically, thus providing crucial kinematical and chemical informations (Majewski et al., 2004; Monaco et al., 2007; Chou et al., 2007; Yanny et al., 2009).

Bel06 exploited the SDSS data release 5 (DR5) to provide a picture of the leading arm of the Sgr Stream in the vicinity of the North Galactic Cap with remarkable clarity, using tracers (A-F dwarfs) that are intrinsically more numerous than M giants, for a given space density and/or surface brightness[1].

[1]In a stellar population of given age and chemical composition the number of stars per units of sampled (integrated) luminosity in a given evolutionary phase is proportional to the duration of the evolutionary phase (see

In their Fig. 1 they show the density of (candidate) A-F dwarf stars (selected with a simple colour cut, $g-r \leq 0.4$, corresponding to $\sim B-V \leq 0.6$) in the portion of the sky covered by the SDSS. The Sgr Stream emerges very clearly as a broad (and bifurcated) band going from (α, δ) $\simeq (220^\circ, 0^\circ)$ to (α, δ) $\sim (125^\circ, 25^\circ)$, where it plunges into the Galactic Disc. The colour cut adopted by Bel06 is very successful in tracing the Stream structure as it takes advantage of the fact that Sgr stars are younger than typical halo stars, hence they have a bluer Turn Off (TO) colour with respect to the halo population (see Unavane et al., 1996, for another application of the same principle). The density map by Bel06 puts in evidence a clear distance gradient along the Stream, from the nearest part crossing the Disc at $\alpha \approx 120^\circ$, to the the most distant part at $\alpha \approx 210^\circ$, toward the North Galactic Pole (NGP).

More recently, in a pilot project limited to a subsample of the SDSS (the so called Stripe 82) Cole et al. (2008) described a more refined approach to the study of the spatial structure of the Stream, using the same tracers as Newberg et al. (2002). Very recent detections from different data and/or using different models can be found also in de Jong et al. (2009), Prior et al. (2009a), and Keller (2009a).

In Bellazzini et al. (2006, hereafter B06c, presented in Chapter 3) we demonstrated that yet another kind of tracer can be efficiently used to study the Sgr Stream, i.e. core-He-burning stars lying in the well populated Red Clump (RC) of the CMD of Sagittarius dSph. In particular, we showed that it is possible to detect the RC associated with a given sub-structure as a peak in the luminosity function (LF) of sub-samples of stars selected in a relatively narrow colour range including the RC. The spatially localized RC population can be disentangled from the fore/background contaminating population of the MW by subtracting the underlying LF, that is, in general, quite smooth and smoothly varying with position in the sky. In B06c we used this technique to compare the Horizontal Branch (HB) morphology in the Stream and in the main body of Sgr, finding an age/metallicity gradient along the Sgr remnant (see also Monaco et al., 2007; Chou et al., 2007), while in Correnti et al. (2009) we obtained an independent detection of the recently discovered stellar system Boötes III (Grillmair, 2009; Carlin et al., 2009), providing new insight on its nature, structure and stellar populations. Carrell & Wilhelm (2010) recently presented the results of a spectroscopic survey targeting RC stars in the Sgr Stream, selected as in B06c.

Renzini & Buzzoni, 1986; Renzini & Fusi Pecci, 1988; Renzini, 1998, and references therein). A-F stars are evolving along the Main Sequence, a phase lasting several Gyr for these stars, while M giants are in the latest phases of their evolution along the Red Giant Branch, lasting $< 10^8$ yr. Hence in any given field, independently of the absolute density normalization, A-F dwarfs outnumber M giants by a factor of > 10.

The most natural and direct application of this technique is the determination of accurate distance estimates from the magnitude of detected RC peaks, as the RC is well known and widely used as a standard candle since long time (see Paczynski & Stanek, 1998; Stanek & Garnavich, 1998; Girardi & Salaris, 2001; Babusiaux & Gilmore, 2005; Bellazzini et al., 2006, and references therein). For intermediate/old-age populations, the luminosity of the RC peak shows relatively modest variations as a function of age and metallicity, in particular when measured in the reddest optical passband (as Cousins'I, see Girardi & Salaris, 2001). When used differentially, i.e. looking at the same (or very similar) stellar population in different places, the variations in the intrinsic luminosity of the RC due to age/metallicity effects should vanish. Given also the intrinsic narrowness of the feature in Sgr (see below), the RC seems the ideal tool to accurately trace the run of the distance along the orbital azimuth of the Sgr Stream, from the main body of the galaxy all over the portion of the Stream sampled by the SDSS. The other large survey covering all the extent of the Stream, 2MASS, cannot be used in this way as the associated photometry is not sufficiently deep to reach the RC level.
In this paper we will use the RC LF method outlined above to take accurate *purely differential measures* of the distance of the Northern arms of the Sgr Stream with respect to the main body of the galaxy. This will provide strong constraints for the models of the disruption of Sgr within the Galactic (dark) halo, and, in turn on the physical properties of the dark halo itself (Ibata et al., 2001; Helmi, 2004; Johnston et al., 2005). The basic idea is the following: (a) we measure the position of the RC peak in V and I, with independent colour selections using $B-V$ and $V-I$ colours, in the main body of Sgr (from B06a photometry), (b) we select SDSS fields projected onto the Sgr Stream as traced by Bel06, (c) we transform the SDSS photometry into B, V, I magnitudes, (d) we detect the RC peak(s) in V and I LFs from the SDSS on-Stream fields (adopting the same colour selections as in the main body), and (e) we obtain two independent measures of the magnitude differences of the RC peaks between the main body and the considered portion of the Stream. These are fully equivalent to differences in distance modulus, that is differences in distance. The whole set of differential distances can be translated into a set of *absolute* distances by adopting the preferred value of the distance modulus for the main body (see, for example, Alard, 1996; Layden & Sarajedini, 2000; Monaco et al., 2004; Kunder & Chaboyer, 2009). The detection of the same peaks in both V and I LFs provide a useful sanity check on the interpretation of the LFs and on the derived differential distances. As an additional observational constraint to models of the disruption of Sgr

we provide also an estimate of the characteristic width of the Stream section crossed by our fields (see § 4.3.4).
The plan of the paper is the following. In § 2 we present the field of the main body that we used as template and the fields of the Stream used for/in the analysis. In § 3 we describe the method used to analyze the LFs and derive the informations from the peaks. In § 4 we present all the LFs obtained from each fields and we discuss some special cases. In § 5 we compare our results with previous works in literature, with particular emphasis on the different degree of uncertainty related to the distance estimates. In § 6 we compare our distance estimates with models that reproduce the three-dimensional shape of the Stream. Finally, we summarize and discuss our result in § 7.

SECTION 4.2

Data and Observables

As a reference sample for the stellar population in the core of Sgr we take the photometry of a $1^\circ \times 1^\circ$ wide field located $\sim 2^\circ$ eastward of the galaxy center at $(l,b) \simeq (6.5^\circ, -16.5^\circ)$, presented in B06a and named *Sgr34*. This should be considered as fairly representative of the average population of the Sgr galaxy (see Bellazzini et al., 1999a,b), avoiding the youngest and most metal-rich populations that appear to reside in the central nucleus (Siegel et al., 2007; Bellazzini et al., 2008). The strong similarity between the population of the Sgr main body and the Stream has been shown by Newberg et al. (2002) and Bel06, by direct comparison of CMDs[2]. To sample the Galactic population at similar angular distance from the Galactic Center as for *Sgr34* we used the same control field also presented in B06a: a $0.5^\circ \times 0.5^\circ$ field, named *Gal_Field*, at $(l,b) \simeq (-6.0^\circ, -14.5^\circ)$, that was used in B06a to perform the statistical decontamination of the *Sgr34* CMD from the foreground/background Galactic stars. Following B06a we adopted the average reddening values $\langle E(B-V)\rangle = 0.116$ for *Sgr34* and $\langle E(B-V)\rangle = 0.096$ for *Gal_Field*, as derived from the reddening maps of Schlegel et al. (1998, hereafter SFD98).
To study the Stream, we used the SDSS-DR6 photometry of objects classified as stars (extracted from the SDSS CasJobs query system, Adelman-McCarthy et al., 2008) for a series of selected fields along the branch A and B, listed in Tab. 4.1 and plotted in Fig. 4.1. We chose to follow the two branches separately, with non-overlapping fields. These on-Stream fields are similar,

[2] In particular, Bel06 uses as reference, the same photometry of *Sgr34* that is adopted here.

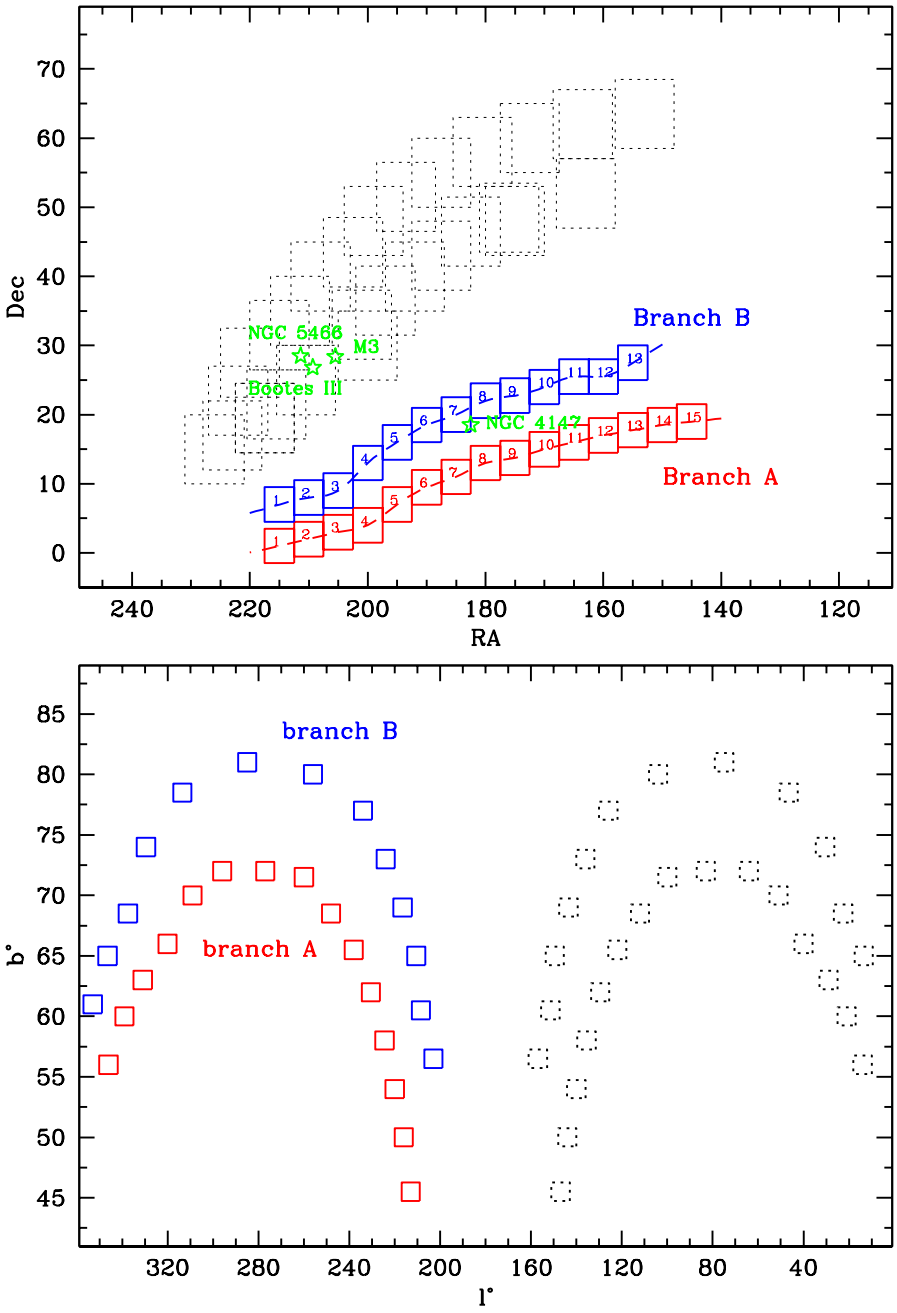

Figure 4.1: Upper panel: Distribution of the on-Stream fields of the branch A (red squares) and the branch B (blue squares) of the Sgr Stream. The control fields of each of them are also reported (black dashed squares). The shape of the two branches is reproduced with a continuous line, following Fig. 1 of Bel06. The position of known stellar system falling into the CFs is indicated in the map with green stars and a label with the name of the object. Bottom panel: The positions of the various fields are reported in Galactic Coordinates, to highlight the symmetry (with respect to the Galactic Center and to the Galactic Plane) of the adopted on-Stream fields and their corresponding Control Fields. The plot is intended to show just the position of the fields and give an rough idea of their dimension, projection effects are not taken into account.

Table 4.1: Equatorial and Galactic coordinates, average E(B-V) and its standard deviation for all the on-Stream fields of branch A and B analyzed. The same quantities are also reported for each control fields.

field	α	δ	l°	b°	$\langle E(B-V)\rangle$	σ	α_c	δ_c	l_c°	b_c°	$\langle E(B-V)\rangle_c$	σ_c
1A	215	1	346	56	0.038	0.007	226	15	14	56	0.034	0.009
2A	210	2	339	60	0.033	0.006	223	17	21	60	0.030	0.008
3A	205	3	331	63	0.026	0.003	222	22	29	63	0.034	0.008
4A	200	4	320	66	0.029	0.004	220	27.5	40	66	0.024	0.010
5A	195	7	309	70	0.031	0.005	215	31.5	51	70	0.015	0.004
6A	190	9.5	296	72	0.024	0.006	211.5	35	64	72	0.013	0.004
7A	185	11	277	72	0.027	0.007	208	40	83	72	0.010	0.004
8A	180	13	260	71.5	0.030	0.006	202.5	43.5	100	71.5	0.014	0.006
9A	175	13.75	248	68.5	0.037	0.007	199	48	112	68.5	0.014	0.005
10A	170	15	238	65.5	0.024	0.006	193.5	51.5	122	65.5	0.014	0.003
11A	165	16	230.5	62	0.022	0.005	187.5	55	129.5	62	0.015	0.004
12A	160	17	224.5	58	0.030	0.006	180.5	58	135.5	58	0.017	0.007
13A	155	17.75	220	54	0.031	0.007	172.5	60	140	54	0.014	0.007
14A	150	18.5	216	50	0.030	0.004	163.5	62	144	50	0.011	0.006
15A	145	19	213	45.5	0.030	0.006	153	63.5	147	45.5	0.017	0.016
1B	215	7	353	61	0.027	0.003	217.5	19.5	13.5	65	0.029	0.008
2B	210	8	346.5	65	0.026	0.003	217.5	19.5	13.5	65	0.029	0.008
3B	205	9	337.5	68.5	0.028	0.004	215.5	21.5	22.5	68.5	0.028	0.008
4B	200	13	329.5	74	0.025	0.004	210.5	25	30.5	74	0.019	0.007
5B	195	16	313.5	78.5	0.027	0.006	200	30	46.5	78.5	0.012	0.002
6B	190	18.5	285	81	0.025	0.005	201	33	75	81	0.012	0.002
7B	185	20	256	80	0.029	0.005	197	36.5	104	80	0.013	0.003
8B	180	22	234	77	0.028	0.006	192	40	126	77	0.016	0.004
9B	175	22.75	224	73	0.023	0.004	187.5	43	136	73	0.017	0.005
10B	170	24	216.5	69	0.017	0.002	182.5	46.5	143.5	69	0.017	0.005
11B	165	25.5	210.5	65	0.022	0.008	176	48.5	149.5	65	0.019	0.005
12B	160	25.5	208.5	60.5	0.025	0.007	175	48	151.5	65	0.018	0.005
13B	155	27.5	203	56.5	0.028	0.007	163	52	157	56.5	0.013	0.004

in position, to those studied by Bel06, but are slightly smaller ($5^\circ \times 5^\circ$ instead of $6^\circ \times 6^\circ$), to avoid overlap between different fields. For each on-Stream field [located, for example, at (l,b)=(l_0,b_0)] we selected also a corresponding *control field* (CF) located at the same latitude and at the same angular distance from the Galactic Center on the other side of the Galaxy [i.e having (l,b)=$(360^0 - l_0, b_0)$][3]. Assuming that the Milky Way is symmetric about its center and its disc mid-plane (that should be a reasonable first-order approximation, at least at the Galactic latitudes considered here, $b \geq 45.5^\circ$; but see Bell et al., 2008), each control field should be fairly representative of the typical Galactic population contaminating our on-Stream fields. Following Bel06, to average out the effects of shot noise, the control fields are larger than the on-Stream fields ($10^\circ \times 10^\circ$). As shown in Fig. 4.1, the globular clusters NGC5466 and M3, and the dwarf galaxy remnant Boötes III are enclosed within some of our control fields (Correnti et al., 2009). To avoid any undesired contamination we excluded from the corresponding samples the stars associated to these stellar systems by excising areas of radius 1° (for the globulars) and 2° (for the dwarf galaxy) around their centers. The only known stellar system that is (partially) enclosed into one of our on-Stream fields is the globular cluster NGC4147 (see Bellazzini et al., 2003, and Bel06). Also in this case we excluded from the adopted sample all the stars within 1° of the cluster center. In the following we will use CFs only as a further observational check that the simple models we adopt to account for the fore/background populations contaminating our LFs are adequate for our purposes (see § 4.8).

For our analysis we adopted the reddening-corrected g,r,i,z magnitudes as provided by CasJobs. Also these corrected magnitudes were obtained using the SFD98 maps, hence the source of the reddening corrections is homogeneous for all the datasets considered in the present analysis. The mean $E(B-V)$ and its standard deviation for each field, averaged over all the stars included in the field, are also reported in Tab. 4.1. It is important to note that the average reddening of our fields is remarkably low ($0.010 \leq E(B-V) \leq 0.038$) and constant within each field ($0.002 \leq \sigma_{E(B-V)} \leq 0.010$), hence any error in the adopted reddening correction would have only a minor impact on our final *differential distance* estimates. For brevity, in the following all the reported magnitudes and colours must be intended as corrected for reddening (i.e., for example, $V = V_0$= extinction corrected V magnitude).

The g,r,i,z magnitudes in the SDSS system have been transformed to the Johnson-Kron-Cousins B,V,I system, as defined by the standard stars by Landolt (1992), using robust empirical transformations that have been

[3]Except in the case of field 1B, for which the CF is the same adopted for the field 2B

checked to be particularly accurate in the colour range typical of RC stars (provided by Lupton 2005[4], derived from large samples of stars in common between SDSS and the extended database of Landolt's standards by Stetson, 2000). In particular, we obtain B and V from g and r, while I is obtained from i and z, adopting the following equations:

$$B = g + 0.3130(g-r) + 0.2271 \qquad \sigma = 0.0107 \tag{4.1}$$

$$V = g - 0.5784(g-r) - 0.0038 \qquad \sigma = 0.0054 \tag{4.2}$$

$$I = i - 0.3780(i-z) - 0.3974 \qquad \sigma = 0.0063 \tag{4.3}$$

Note that the transformed V and I are *fully independent* as they are obtained by independent couples of SDSS magnitudes. Consequently, measures of the position of any significant peak detected in V and I LFs would also be independent, thus providing a powerful cross-check of any detection and distance estimate.

4.2.1 Selections on the colour Magnitude Diagram

In Fig. 4.2 we present reddening-corrected *V,B-V* and *I,V-I* CMDs (focused on the RC features up to the upper region of the Main Sequence, MS) of the main-body field *Sgr34* and of the corresponding control field *Gal_Field*. The comparison between the CMDs of the two fields permits the identification of the main features associated with Sgr and with the fore/background Galactic populations. The RC of Sagittarius dSph is a prominent feature in the CMDs of the *Sgr34* field (upper panels), around $(I, V-I) \simeq (16.9, 0.9)$ and $(V, B-V) \simeq (17.8, 0.8)$. The wide and bended Red Giant Branch (RGB) can be discerned over the background, going from $(I, V-I) \simeq (16.9, 0.9)$ to $(I, V-I) \simeq (14.0, 1.5)$ [$(V, B-V) \simeq (19.5, 0.8)$ to $(V, B-V) \simeq (16.0, 1.4)$], and continuing beyond the limits of the box. The RGB bump is apparent at $V \sim 18.2$ and $I \sim 17.2$, along the RGB (see Monaco et al., 2002). For $V-I < 0.3$ ($B-V < 0.2$) at $I \sim 19.0$ ($V \sim 17.9$) a portion of the Blue Horizontal Branch (BHB) is also visible (Monaco et al., 2003); at $V-I < 0.5$ ($B-V < 0.4$) and $I > 19.5$ ($V > 18.5$) the Blue Plume (BP, Mateo et al., 1995; Bellazzini et al., 1999a, B06a) population is visible. The Sub Giant Branch (SGB, for $V-I > 0.8$ or $B-V > 0.7$) and the upper Main Sequence (MS, to the blue of the above limits) appears for $I > 19.0$ ($V > 20.0$). For a more detailed description of the CMD of Sgr see B06a and Fig. 2.6. The strong vertical band around $V-I \sim 0.7$ ($B-V \sim 0.6$) running over the largest part of the CMD, and bending to the red at $I \sim 19$, $V \sim 20$, is constituted by MS stars of the Milky Way (mostly from the Thick Disc, in this direction,

[4] http://www.sdss.org/dr7/algorithms/sdssUBVRITransform.html

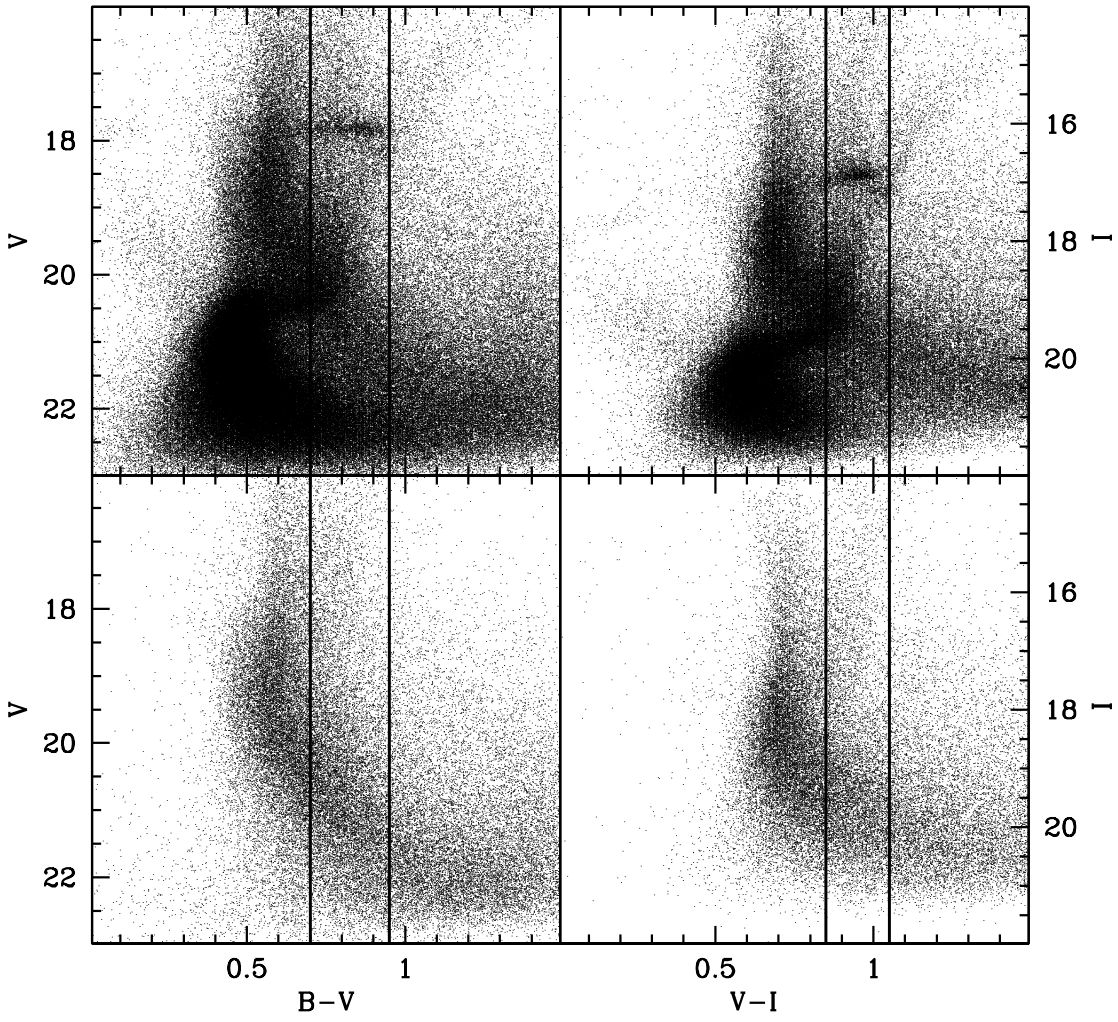

Figure 4.2: Reddening corrected (*V,B-V*) (left panels) and (*I,V-I*) (right panels) CMDs, focused on the RC up to the upper part of the MS, of the Sgr field (*Sgr34*, upper panels) and of the control field (*Gal_Field*, lower panels). The vertical lines enclose the RC populations and are the colour strips used to select the region where build the LFs. The colour range are respectively, $0.70 \leq (B-V) \leq 0.95$ and $0.85 \leq (V-I) \leq 1.05$.

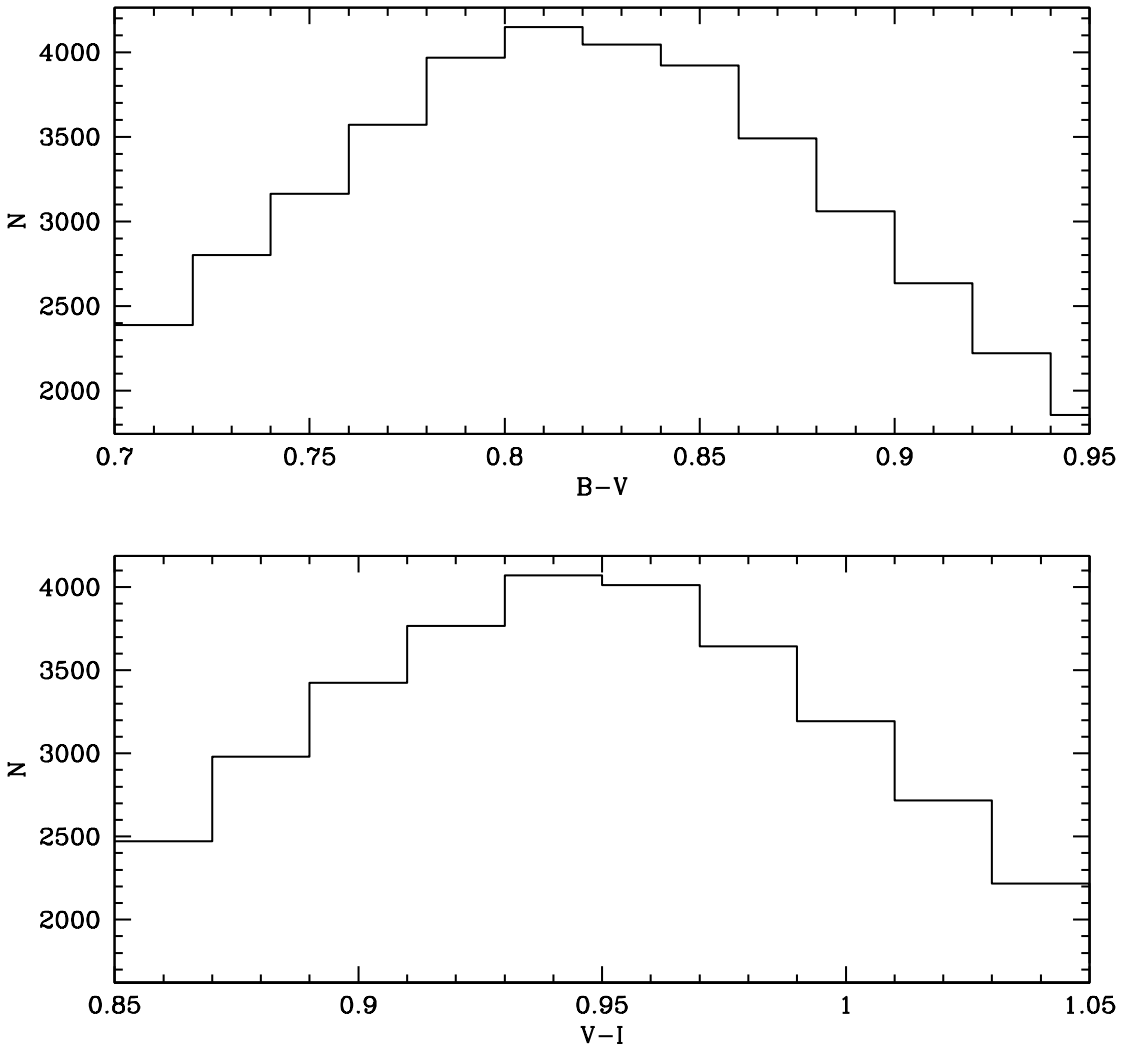

Figure 4.3: Distribution of stars in *B-V* (upper panel) and *V-I* (lower panel) colour strip for the *Sgr34* field. The selection must be optimized in order to contain all the RC stars, but minimizing the presence of contaminating stars. The RC is well confined inside the selected regions and peaks near the middle in both; the magnitude limits of the selection are respectively, $17.3 \leq V \leq 18.3$ and $16.4 \leq I \leq 17.4$.

according to the Galactic model by Robin et al., 2003a); the wide band running parallel, to the red of the vertical portion of this feature is mainly populated by Galactic giants, either in their RGB or RC/HB phase. The majority of the stars redder than $V-I = B-V \sim 1.0$ belong to the vertical plume of local Galactic M dwarfs.

The vertical lines in each panel of Fig. 4.2 enclose the colour stripes that we adopted to select the RC population in the two colours, corresponding to $0.70 \leq B-V \leq 0.95$ and $0.85 \leq V-I \leq 1.05$. The choice of the colour limits was made in order to include the bulk of the RC population even in case of small colour shift due to errors in the adopted reddening corrections and/or population gradients, while keeping the contamination from other sources as low as possible. The distribution in colour within the selection windows (around the magnitude of the observed RC of Sgr) shown in Fig. 4.3 suggests that colour shifts of order ± 0.05 mag would lead just to minor losses of the signal (of the order of 10% respect to the number of stars obtained with our choice in the selection window).

Fig. 4.2 clearly shows that, in addition to Sgr RC stars, several different contaminants are expected to enter the selection window. For $I \leq 18.5$ ($V \leq 19.5$) Galactic giants (mainly RC stars) should be the primary source of contamination, while the sequence of Galactic MS stars crosses the selection stripes at $I > 19$ and $V > 20$, boosting the star counts at faint magnitudes. The RGB of the Sgr population, and in particular the RGB bump, are also selected by the adopted windows. We will show below that this source of contamination has a negligible effect on our LFs. At $I > 19.0$ ($V > 20.0$) the SGB stars of Sgr enter the selection window; as they are much more numerous than RGB and RC stars they may provide a serious contribution to the "background" in our LFs, at faint magnitudes. Finally, the Main Sequence of Sgr crosses the windows at $I > 21$ ($V > 22$). The actual structure of the contamination entering the windows will obviously depend on (a) the Galactic population encountered along the considered line of sight (*los* , hereafter), and (b) the distance of the wrap(s) of the Sgr Stream that is(are) crossed by the considered *los* . However the *los* considered in this study are all at much higher Galactic latitudes than *Sgr34*, hence the degree of contamination per unit area of the sky should be lower, and the average distance of the encountered stars should be higher, hence most of the contamination by Galactic dwarfs should occur at fainter magnitudes than what discussed above for *Sgr34*. Furthermore, all the detections of the Stream presented here are at distances similar or larger than the main body of the galaxy sampled by *Sgr34*; hence, in most cases the contamination by the SGB of the Stream population will occur at fainter

magnitudes than in *Sgr34*[5]. In any case to limit the contribution by dwarf stars, independent of their origin, we limit our analysis to the magnitude ranges $15.0 \leq I \leq 19.5$ and $16.0 \leq V \leq 20.5$[6]. These limits approximately correspond to an accessible range of heliocentric distances 12 kpc $< D <$ 70 kpc (see Fig. 4.5, below).

While the surface brightness of Sgr at *Sgr34* is ~ 25 mag/arcsec^2, typical values for the Stream are > 30 mag/arcsec^2 (Mateo et al., 1998; Bellazzini et al., 2003; Majewski et al., 2003, and references therein). It may be quite hard to identify the feeble signal from such sparse populations even in presence of low background. In fact, even in the most favorable cases, the RC is barely visible in the CMDs of on-Stream Fields (see, f.i. Newberg et al., 2002). The construction and modeling of LFs described below is very effective in extracting the distance information in these cases (B06c, Correnti et al., 2009).

Finally, there are several indications that there is a sizable metallicity (and presumably age) gradient along the Stream, in the sense that the average metallicity is lower in distant portion of the Stream with respect to the main body of Sgr (B06c, Monaco et al., 2007; Chou et al., 2007). This is generally interpreted as due to a pre-existing population gradient within the original body of the Sgr galaxy, as the tidal tails were preferentially populated by stars that resided in the old and metal poor outskirts of Sgr (Chou et al., 2007). It must be stressed that the detected gradient means that the relative proportion of *intermediate-age & metal-rich stars* and of *old-age metal-poor stars* changes along the Stream (and with respect to the main body). This, in turn, changes the HB morphology, i.e. the relative abundance of RC and Blue HB stars (as observed in B06c), but is it not expected to change the intrinsic luminosity of the RC. Indeed, Carrell & Wilhelm (2010) find that the mean metallicity of RC stars along the Stream is very similar to that found in the main body of Sgr. Hence, while the population gradient may bias estimates of the stellar density along the Stream obtained from RC stars, our distance estimates should be unaffected and our characteristic size estimates can be only marginally affected (see § 4.3.4 and Fig. 4.17, below, for further details and discussion).

[5]However it should be noted that the MS of wraps of the Streams that are too nearby to have their RC detected with the present technique may contribute to the contamination of our colour-selected samples of candidate RC stars. Moreover, other unknown substructures may contribute to the contamination (see Correnti et al., 2009, for example).

[6]Except in the case of *Sgr34* where the limits are $15.0 \leq I \leq 18.5$ and $16.0 \leq V \leq 19.5$

4.2.2 Detecting RC peaks in Luminosity Functions

All the LFs of colour-selected RC samples presented in this paper are computed as running histograms (see Bellazzini et al., 2005, and references therein), as these couple the property of collecting the signal from a wide bin with the ability of constraining with great accuracy the location of density maxima, almost independently of the bin width. A bin width of ± 0.2 mag[7] and step of 0.02 mag have been adopted here. After different trials, they have been found to provide a good compromise between the exigence of co-adding all the signal from a given RC population (that requires larger bins) and the ability of distinguishing (resolving) nearby peaks (that is favored by smaller bins). The use of generalized histograms (Laird et al., 1988) would have provided an higher degree of smoothing, possibly making some of our LFs easier to interpret. However we preferred running histograms as they provide the reader a clearer idea of the local noise on the LF as well as a scale in real units ($\frac{stars}{mag\ bin \times FoV}$). The density scales of the various fields have all been reported to unit standard area ($1^\circ \times 1^\circ$) by applying the corrections due to spherical geometry that is inherent to equatorial coordinates.

To illustrate at best the case of the detection of the RC of a spatially confined stellar system in a colour-selected LF, we show in Fig. 4.4 the V and I LFs for the *Sgr34* field (continuous lines), compared with those obtained for the control field *Gal_Field*, normalized by the ratio of background densities between the two fields[8].

The shapes of the *Sgr34* and *Gal_Field* LFs are *remarkably similar*: the only exception is the very strong and well defined peak corresponding to the RC of the Sgr galaxy seen in Fig. 4.2. It is interesting to note that while also other features related to Sgr are visible in the CMDs and (at least partially) included in the selection windows, as for example the RGB bump, in the LFs the RC is the only signal emerging from Sgr population. Independently of the origin of the stellar mix actually selected, the LF of the control field, and, by analogy, the LF of the contaminating population that is superposed to the RC in the *Sgr34* LF, are quite smooth and have a very simple behaviour; in B06c, Correnti et al. (2009) and in § 4.8 we show that this is the general behaviour of the LF of the back/foreground population in the vast majority of

[7] With rare exceptions in which bins of ± 0.25 mag have been adopted to enhance the signal of a weak feature. All these cases are clearly indicated in the following.

[8] This ratio is dominated by the ratio of the areas of the fields, *Sgr34* being $\simeq 4$ times larger than *Gal_Field*. However *Gal_Field* sample a direction $\simeq 2^\circ$ closer to the Galactic Plane and $\simeq 0.5^\circ$ closer to the Galactic Center than *Sgr34*, hence the (column) stellar density is intrinsically larger in the former field. The actual density ratio, computed in selected CMD boxes where the contribution from Sgr dSph stars is negligible, is $\simeq 3$, see Bellazzini et al. (1999b) and B06a.

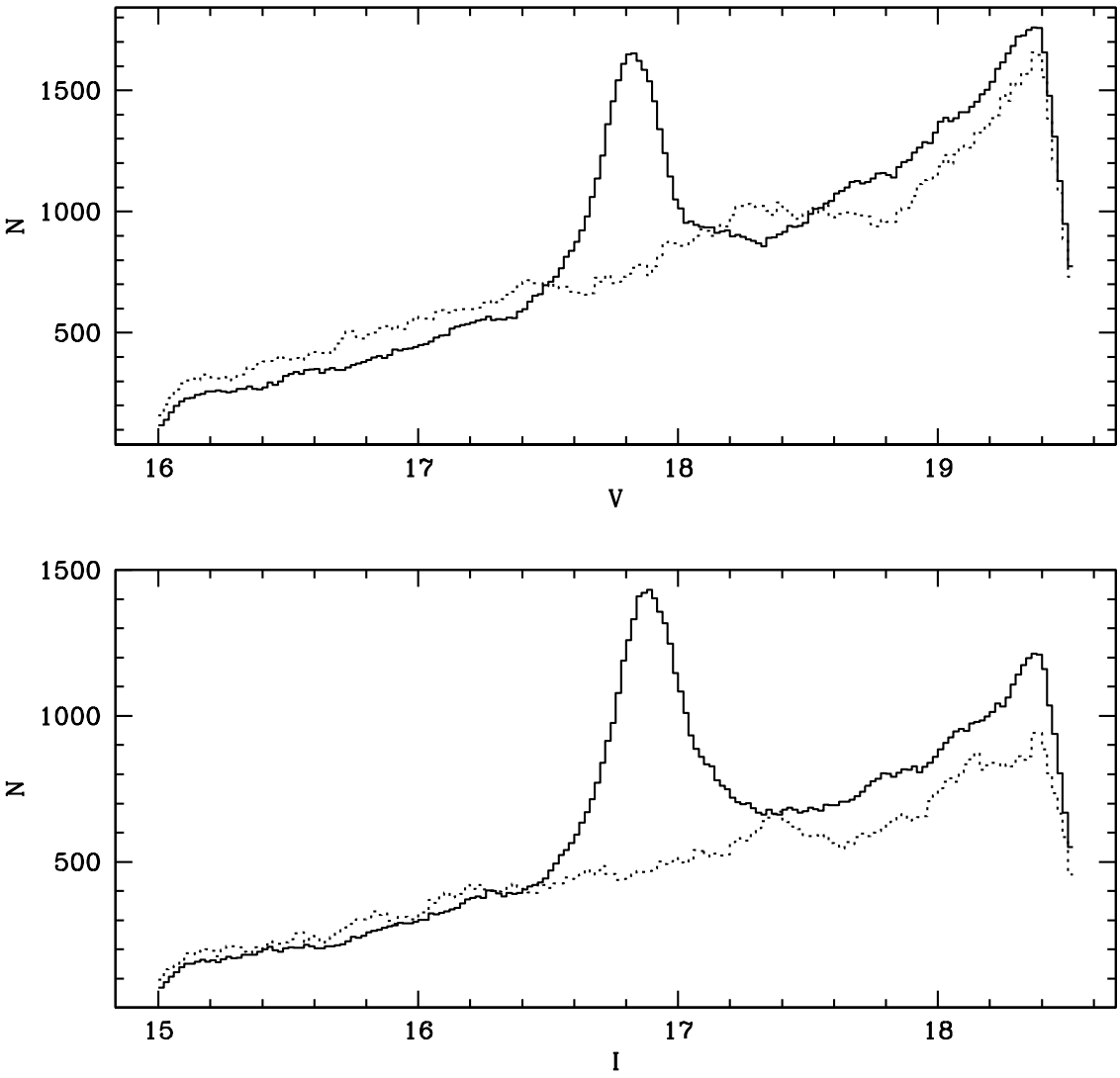

Figure 4.4: De-reddened running histogram LFs of colour-selected RC candidates for *Sgr34* (continuous line) and for the control field *Gal_Field* (dashed line) in V and I magnitude (respectively upper and bottom panel). The shape of the LFs is similar but, as expected, in the *Gal_Field* the peak is completely laking, while in the Sgr field it stands out very clearly.

the considered *los* , thus justifying the choice of a very simple model for them, as described in § 4.3, below.

4.2.3 Sensitivity of the technique

Before proceeding with the description of the method adopted to obtain the actual differential distance estimates, it may be useful to study the sensitivity of our LFs to the various properties of any encountered substructure (distance, density, etc.). To do that we used the dedicated web tool[9] of the BASTI repository of stellar models (Pietrinferni et al., 2004; Cordier et al., 2007) to produce a synthetic population of ~ 45000 stars having age and metallicity similar to the bulk of the Sgr population (age=6 Gyr, $[Fe/H] = -0.5$). The CMD and the colour-selected RC LF of the population are shown in the upper panels of Fig. 4.5. The synthetic stars have been distributed along the line of sight according to gaussian distributions having various mean distances (D=15, 25, 40 and 65 kpc) and Full Width at Half Maximum (FWHM) of 3.3 kpc or 6.6 kpc, to simulate the crossing of a wrap of the Stream at various distances and with different characteristic sizes along the *los* . A $FWHM \simeq 3.3$ kpc is quite typical of sections of Stream wraps crossed perpendicularly by a given *los* , as measured on the models of the distruption of the Sgr galaxy by Law et al. (2005). The $FWHM \simeq 6.6$ kpc has been considered to account for cases of sparser portions of the Stream and/or non-perpendicular intersections with the *los* . The LFs of the resulting colour-selected RC population have been derived (properly including realistic photometric errors) and added to the LF of the background of Fig. 4.4, as modeled in Fig. 4.6, below, to simulate the detection the same structure with the method applied here. The results of this simulation are shown in the bottom panels of Fig. 4.5.

The most obvious effect shown in Fig. 4.5 is the increase of sensitivity with the distance of the structure. This is due to two factors: (1) the inherent "compressive" property of the magnitude scale, by which, for instance, a difference in distance of 3.3 kpc corresponds to a difference in magnitudes of 0.43 mag at D=15 kpc and to just 0.14 mag at D=50 kpc, and (2) the relative dimension of the considered structure and of the *los* cone at the distance of the structure; for nearby structures the fixed FoV adopted here may be smaller than the structure itself, thus missing part of the signal that instead would be included when more distant structures are encountered. This effect illustrates a fundamental property of our method that should be always taken

[9] `http://193.204.1.62/index.html`

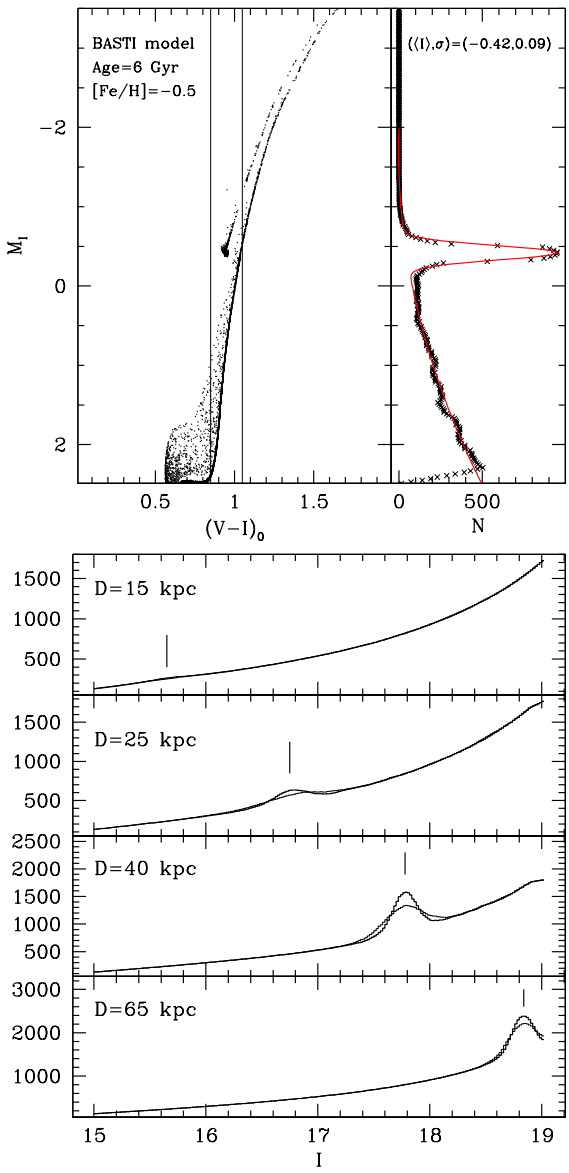

Figure 4.5: *(a).* Upper left panel: CMD of a synthetic population composed of 45953 stars having age=6 Gyr, $[Fe/H] = -0.5$, solar scaled abundance pattern, 10% of binary systems, and Salpeter's Initial Mass Function, from the BASTI database. The colour window adopted to select RC candidates is enclosed within the two thin parallel lines. Upper right panel: LF of the colour-selected RC candidates obtained in the same way as Fig. 4.4($\times$ symbols) and fitted with the same kind of model (red continuous line). The mean and standard deviation of the best-fitting Gaussian are reported within parentheses. *(b).* Bottom panels: the synthetic population shown in panel*(a)* has been distributed along the line of sight according to gaussian distributions having various mean distances (D=15, 25, 40 and 65 kpc, from the upper to the lower panel, respectively) and Full Width at Half Maximum of 3.3 kpc (thick lines) or 6.6 kpc (thin lines). The LF of the resulting colour-selected RC population has been derived and superposed to the (model) LF of the background of Fig. 4.4, to simulate the detection of the same structure at different distances with the method applied here. The vertical segments indicates the positions of the peaks produced by the considered structures.

into account: a structure that is very cleanly detected at, say, D=30 kpc may go completely undetected if located at D=15 kpc, instead. This implies that while significant detections of RC peaks in our LFs are robust and provide accurate distances, the significance of non-detections must be evaluated with great care, on a case by case basis, and, in general cannot be taken as a proof of the *absence* of a given structure (that, for example, may be predicted by some model). One can conceive various different techniques to mitigate this dependence of sensitivity on distance, as, for example, to scale the bin width with magnitude to account for the effect described at point (1), above, or to transform the magnitudes of any colour-selected RC candidate into distances, by assuming template values for M_I and M_V, and then to search for peaks in Distance Functions instead of LFs. However each of these possible solutions would have an impact on the accuracy of the derived distance scale: for this reason we prefer to maintain an approach that derives differential distances from the direct comparison of truly *observable* quantities of strictly the same nature, i.e. the magnitudes of peaks in LFs that can be determined to within a few hundredths of mag, finally providing differential distances with accuracies $<$10%. Other methods to trace structures are intrinsically more powerful for other purposes (like the *detection* of structures, for example; see Bel06). The technique adopted here is best suited for distance measures and we decided to optimize it to this task, at least in the present application.

SECTION 4.3

Modeling observed LFs and measuring differential distances

In the following we will describe the technique that we use to accurately estimate the magnitude (and the statistical significance) of peaks in the LF of on-Stream fields. To illustrate it we recur again to the case of the *Sgr34* field (we will show below also two cases of on-Stream fields). The approach is strictly the same for V and I LFs and it is presented in parallel in the left and right columns of panels of Fig. 4.6:

1. Upper panels: a possible RC peak is detected in both LFs. The underlying smooth LF (the back/foreground component) is fitted with a simple function of the form $f(x) = Ae^x + Bx + C$, once excluded the points in the range enclosing the peak (see also B06a and Correnti et al., 2009). This simple procedure is very effective in all the cases considered here and it

allows a reliable interpolation of the background in the region of the peak. The dotted lines marks the 3,4 and 5σ levels above the background, that are computed including both the Poisson noise and the uncertainty in the fit of the background component. These lines provides a direct scale to evaluate the statistical significance of a detected peak (see Correnti et al., 2009).

2. Middle panels: the model of the background ($f(x)$) is subtracted to the observed LF. The only significant residual is the RC peak that, in general, has a rather symmetrical bell shape. The peak is fitted with a gaussian curve ($G(x)$) by searching for the three parameters of $G(x)$ (mean, σ and normalization factor) that minimize the reduced χ^2. The derived mean is taken as the best estimate for the position of the considered peak. For each peak of the LF that is considered, as the bin of the adopted running histogram are not independent, the resulting χ^2 values can be considered only in a relative sense. After several trials on real cases we found that increases of χ^2 by a factor of 2 with respect to the best solution (having $\chi^2 = \chi^2_{min}$) always correspond to clearly unsatisfying fits (see Fig. 4.9, for an example). For this reason we adopt the difference between the best-fit mean and the mean of the solutions having $\chi^2 = 2\chi^2_{min}$ as a robust and conservative estimate of the accuracy of our measures.

3. Lower panels: the global model, obtained by summing $f(x)$ and $G(x)$, is compared to the observed LFs. This final form of the overall fit is what we will show for all the considered fields in § 4.4, below. In § 4.8 we will show that the adopted model of the fore/background component of the considered LFs ($f(x)$) provides an adequate representation of what observed in actual CF and predicted by current Galactic models.

The application to the *Sgr34* field just described, provides also the Zero Points of our differential distance scale, i.e. the magnitude of the RC in the main body of Sgr, $V = 17.82 \pm 0.02$ and $I = 16.87 \pm 0.02$. As a sanity check, we verify if these numbers are compatible with theoretical stellar model predictions[10]. Adopting the distance modulus $(m-M)_0 = 17.10 \pm 0.15$ for Sgr (Monaco et al., 2004) we obtain $M_I = -0.23 \pm 0.15$ and $M_V = +0.72 \pm 0.15$. These correspond to ages in the range 5-7 Gyr for $[Fe/H] = -0.4$ and 9-11 Gyr for $[Fe/H] = -0.7$ in the models by Girardi & Salaris (2001), in good agreement with all recent

[10]That, however, are quite uncertain and model dependent, in an absolute sense, for stars in this evolutionary phase. For instance the absolute I magnitude of the peak for a age=6 Gyr, $[Fe/H] = -0.5$ model from the BASTI dataset (shown in Fig. 4.5), is matched by a model of age=1.7 Gyr and $[Fe/H] = -0.4$, from the set by Girardi & Salaris (2001).

estimates of the typical age of the bulk of the Sgr stars (see Layden & Sarajedini, 2000; Monaco et al., 2002, B06a).

4.3.1 Examples of on-Stream fits

In Fig. 4.7 and Fig. 4.8 we show two examples of application to on-Stream fields, the fields 7A and 5A, respectively. In the first case a broad peak with significance above 4 σ is detected in both the V and I LFs. The derived differential distances with respect to the main body are in good agreement, within the uncertainties. The $f(x)+G(x)$ model provides an excellent description of the observed LFs.
Two significant peaks are detected in the LFs of the field 5A (Fig. 4.8), thus, in this case, we need a model with two gaussian components. Both peaks are significantly narrower that that found in field 7A. Nevertheless the model $f(x)+G_1(x)+G_2(x)$ provides an excellent representation of the observed LFs. The differential distances obtained from the V and I LFs are in good agreement: there is no doubt that we are detecting *the same structures in both LFs*.

To place the results shown in Fig. 4.7 and Fig. 4.8 into the proper context, we plot the positions of the detected peaks into the $X_{\odot,Sgr}Y_{\odot,Sgr}$ plane of the heliocentric Sgr coordinates as defined by Majewski et al. (2003), in Fig. 4.10. This plane is defined to coincide with the plane of the orbit of Sgr, hence the Stream is expected to be confined within a few kpc about it. We compare our detection with one of the N-body models of the tidal disruption of Sgr by Law et al. (2005). In particular we plot in Fig. 4.10 the results of the evolution of the N-body model of Sgr within a Galactic DM halo of prolate shape (flatness q=1.25, see Law et al., 2005; Johnston et al., 2005, for further details on the models). To compare observations and model in a consistent way we transformed our relative distances into absolute values by adopting the same distance modulus for Sgr as Law et al. (2005), i.e. $(m-M)_0 = 16.9$ (Mateo et al., 1995). The points of the model that are encountered by the considered F.o.V.s along the *los* (F7A and F5A, from left to right, respectively) are plotted as heavier dots.
Taking the considered model as a realistic representation of the actual Sgr relic (a very reasonable assumption, in first approximation; Law et al., 2005), it is clear that any *los* around the considered plane would cross one or more different wraps of the Stream, at different distances (see Fig. 4.10,). The peak from F7A and the most distant peak from F5A seem to match a distant portion of the leading arm. The nearest peak from F5A matches very well with a wrap of the trailing arm that appears narrow and well defined and

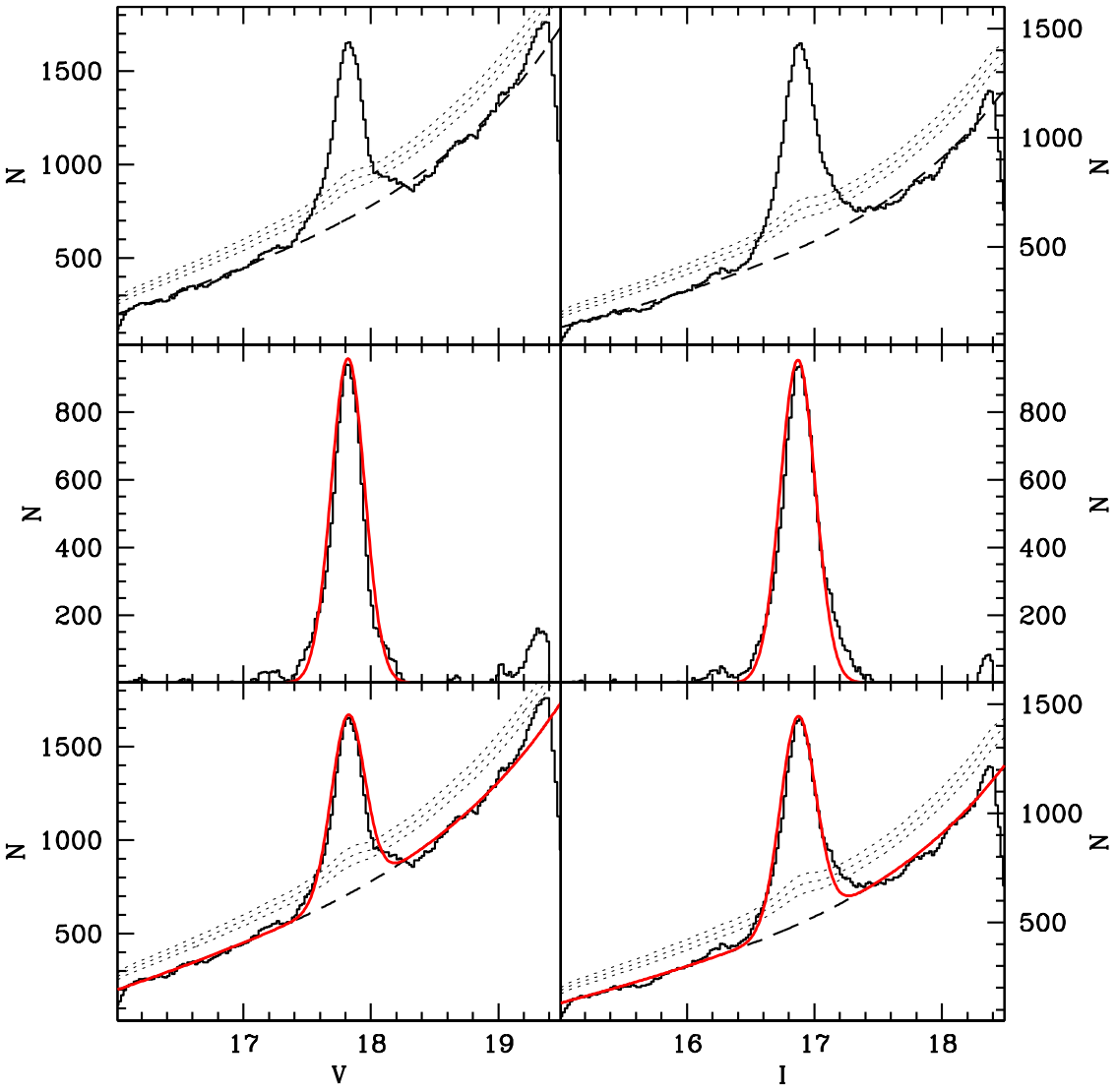

Figure 4.6: Upper panels: de-reddened running histogram LFs of colour-selected RC candidates for the *Sgr34* field (continuous line) in V and I magnitude (left and right panel, respectively); the dashed line represents the polynomial fit of the background ($f(x)$). The dotted lines marks the 3,4 and 5σ levels above the background, that is computed including both the Poisson noise and the uncertainty in the fit. Middle panels: Residuals of the subtraction between the observed LFs and the fit of the LFs without the peaks; in red we plotted the fit of the peaks, obtained with a gaussian ($G(x)$). Bottom panels: same as the first one, with added in red the total fit of the LFs (polynomial for the bkg + gaussian for the peaks, $f(x)+G(x)$).

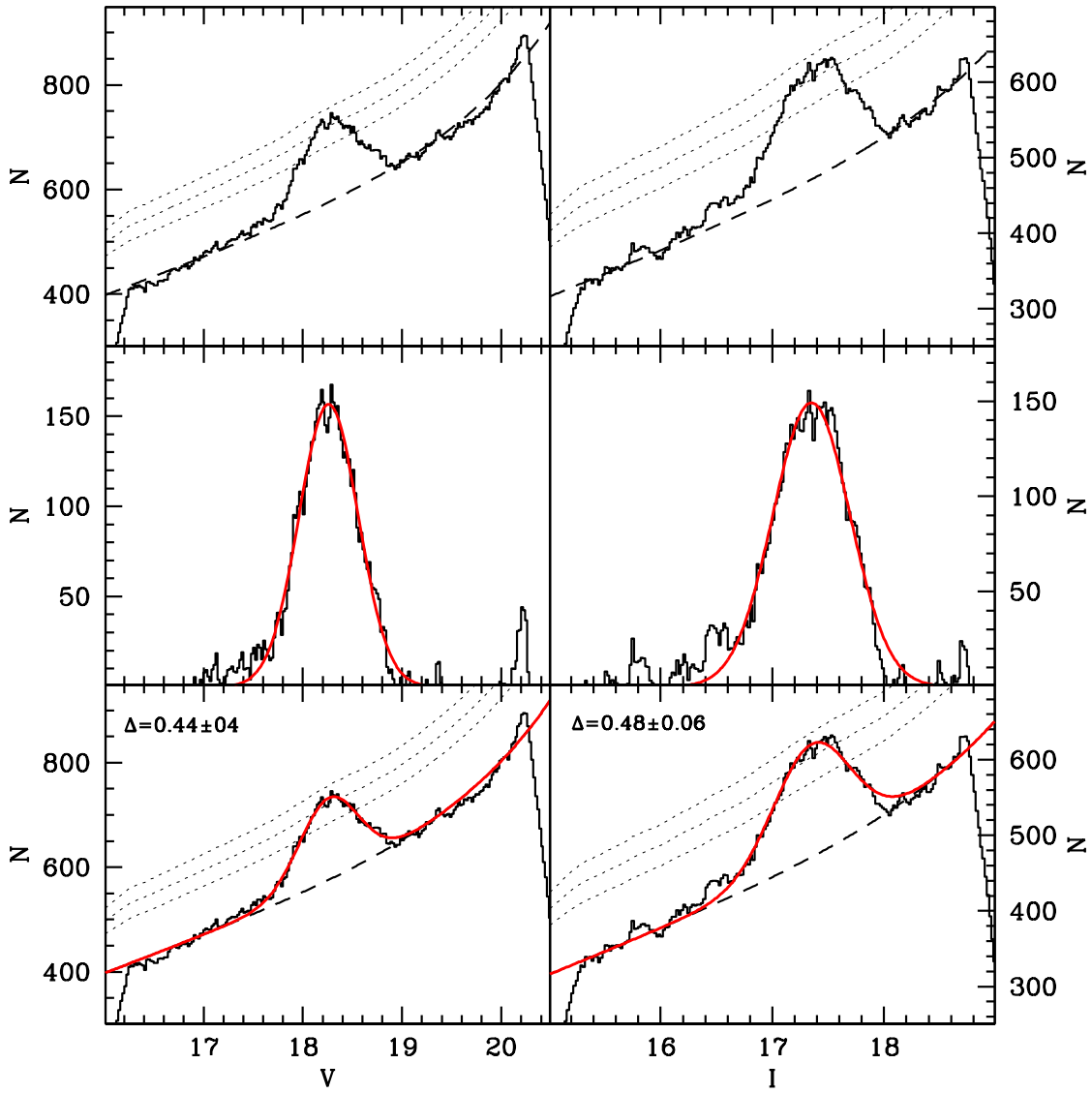

Figure 4.7: Upper panels: de-reddened running histogram LFs of colour-selected RC candidates for a Stream field (field 7A, continuous line) in V and I magnitude (left and right panel, respectively); the dashed line represents the polynomial fit of the background ($f(x)$). The dotted lines marks the 3,4 and 5σ levels above the background, that is computed including both the Poisson noise and the uncertainty in the fit. Middle panels: Residuals of the subtraction between the observed LFs and the fit of the LFs without the peaks; in red we plotted the fit of the peaks, obtained with a gaussian ($G(x)$). Bottom panels: same as the first one, with added in red the total fit of the LFs (polynomial for the bkg + gaussian for the peaks, $f(x)+G(x)$).

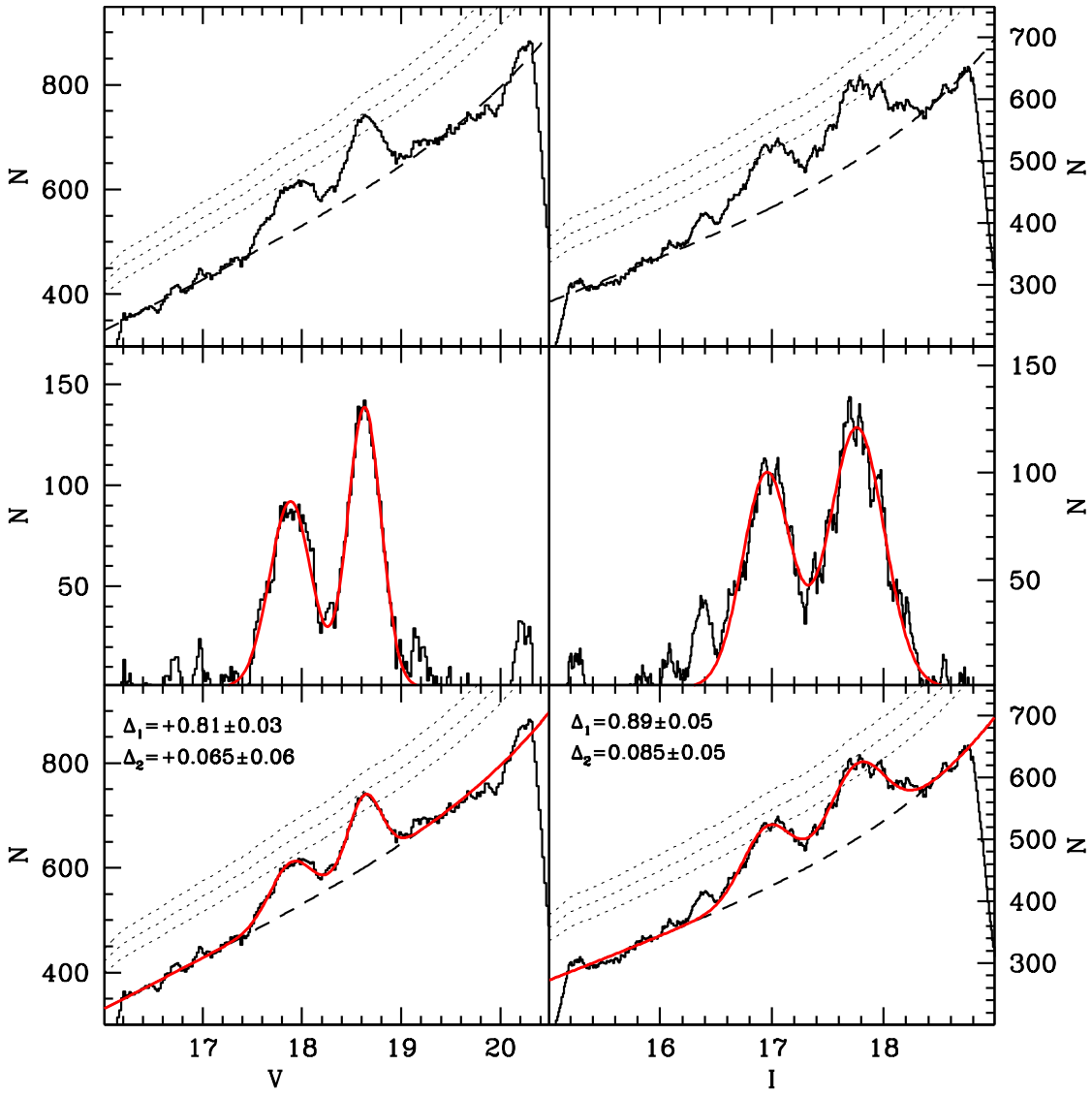

Figure 4.8: As Fig. 4.7, but for a different field (F5A). The method is the same altough this field shows more than one peak.

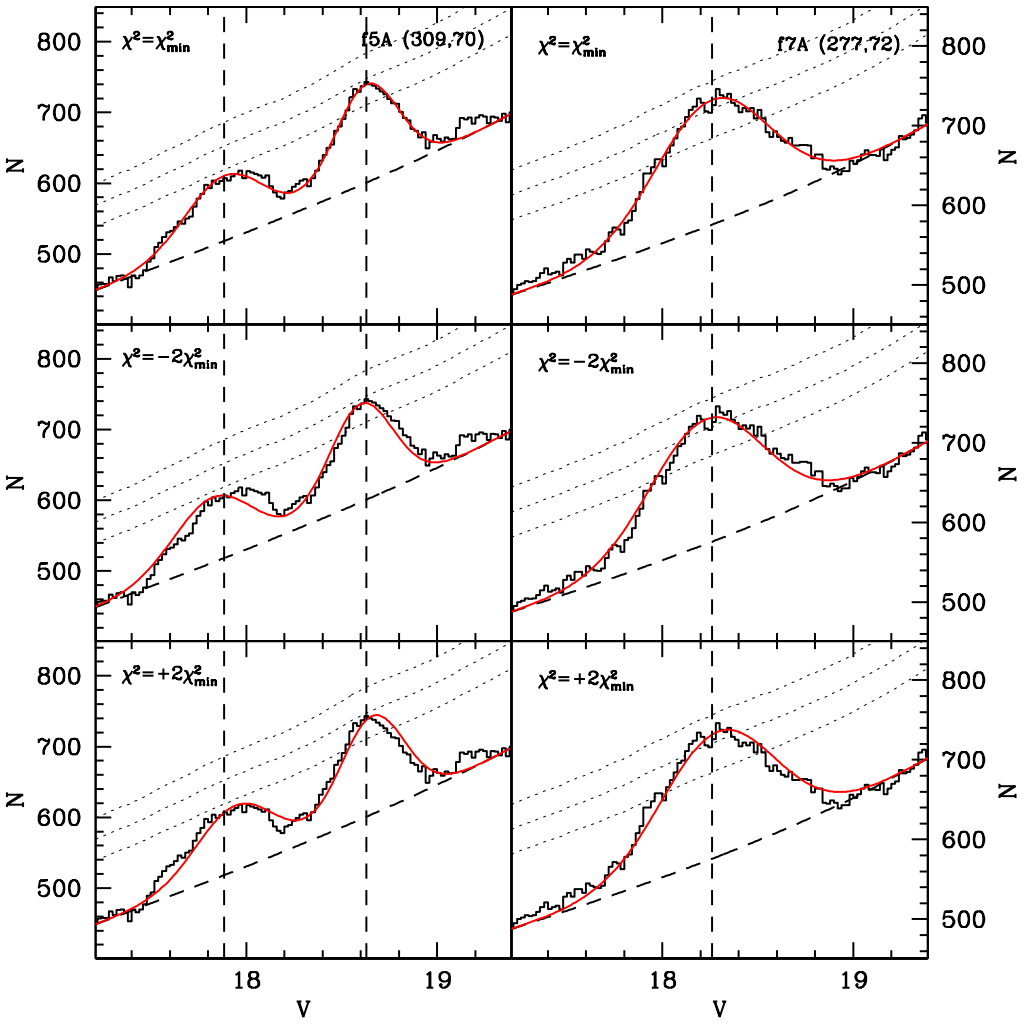

Figure 4.9: Upper panels: de-reddened running histogram LFs, zoomed in the region of the peak(s), of colour-selected RC candidates for the Stream field F5A (left panels) and F7A (right panels). The meaning of the symbol are the same as Fig. 4.7, the red line represents the global model, $f(x)+G(x)$, with the best fit value of $G(x)$ mean (value for which $\chi^2=\chi^2_{min}$). Middle and lower panels: as upper ones, with the exception that the values of the $G(x)$ means are those that have $\chi^2=\pm\chi^2_{min}$ ($\chi^2=-2\chi^2_{min}$, middle panels and $\chi^2=+2\chi^2_{min}$, lower panels, respectively). It is clearly visible that in these last two cases the fit is totally unsatisfying.

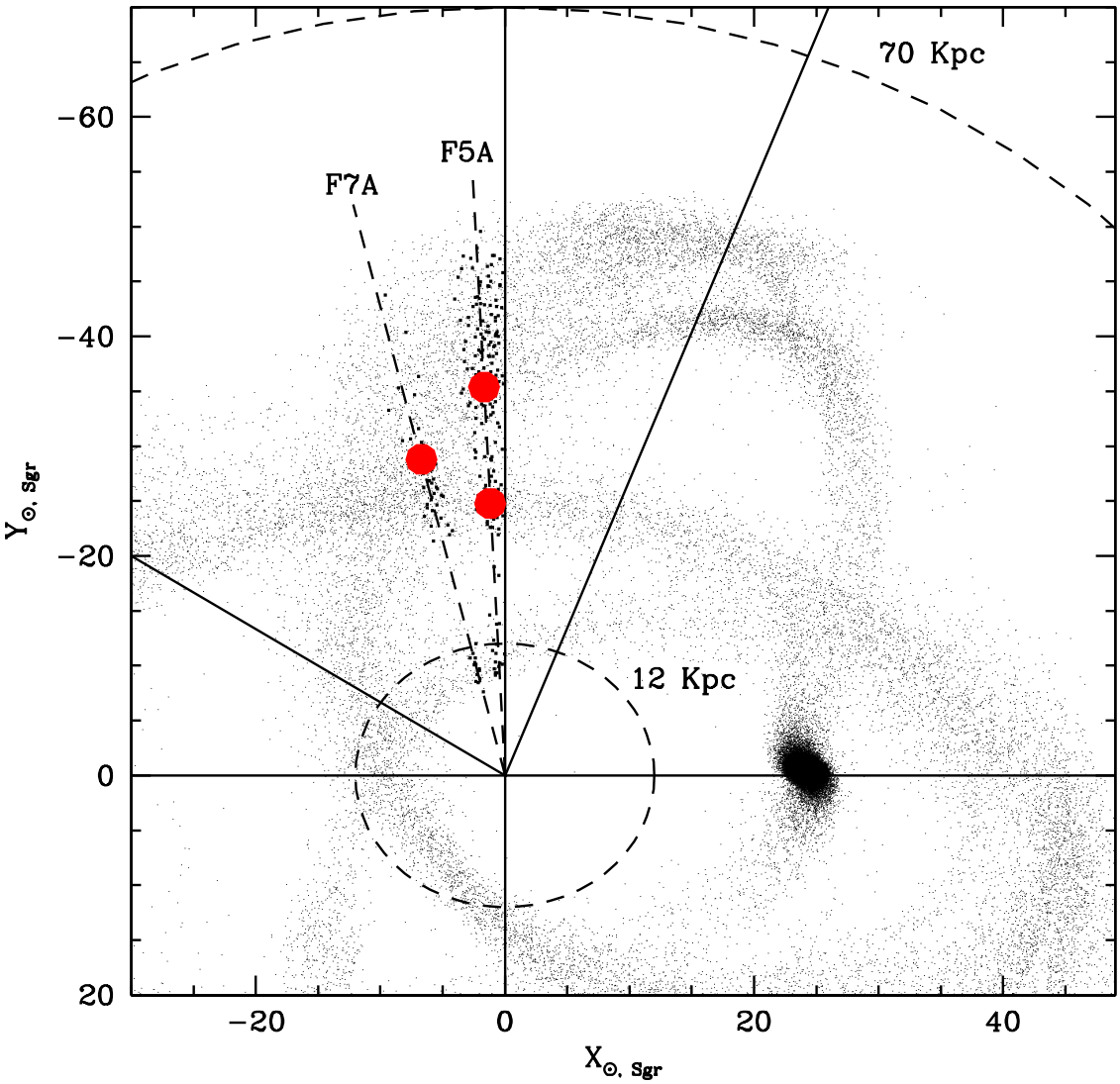

Figure 4.10: N-body model of the disruption of Sgr by Law et al. (2005, prolate Dark Matter halo case) in heliocentric Sgr coordinates (see Majewski et al., 2003). The heavily printed dots are the subset of the model particles that are enclosed in the two observed fields considered here (f5A and f7A). The observed position of the Stream in these fields, as estimated from the position of the RC peak in our LFs, are plotted as filled (red) circles.

that is crossed nearly perpendicular by the considered *los* . According to the considered model, both *los* should also cross a nearby wrap at a distance not enclosed in our range of sensitivity, that is delimitated by the two dashed circles in Fig. 4.10. No wrap is expected to lie outside D=60 kpc in the region sampled by our fields.

Both the more distant F5A detection and the single F7A detection occur in regions where the model predicts the confluence and crossing of different wraps. At a first glance to Fig. 4.10 it may appear that the constraining power of a single "mean position" of a Stream wrap, as derived with our method, is not sufficient to describe the complex structure of the Sgr remnant along a given *los* . In Fig. 4.11 we compare the observed RC peaks of F5A and F7A (and their best-fit gaussian models) with the peaks derived from the N-body model shown in Fig. 4.10 and from the oblate-halo model from the same set (Law et al., 2005) by (a) selecting the model particles encountered by the FoV cone, (b) assigning to each of them the absolute magnitude of the RC ($M_V^{RC} = +0.72$ and $M_I^{RC} = -0.23$, according to § 4.3) and deriving their apparent magnitude according to their distance, (c) adding gaussian photometric errors as a function of the apparent magnitude similar to the observed ones, and (d) producing the running histogram of the derived magnitudes with the same settings adopted for the observed LFs. To make easier the comparisons shown in Fig. 4.11, the synthetic LFs have been multiplied by an arbitrary normalization factor. The qualitative resemblance of the observed and predicted structures for the prolate-halo model is striking. On the other hand the oblate-halo model is clearly unable to reproduce the observations, even in terms of number of Stream wraps encountered by the considered *los* .

A more thorough comparison of our observations with theoretical models of the disruption of Sgr will be presented in § 4.6. Here we are just interested to demonstrate that our method allows a detailed comparison between models and observations not only in term of mean distances, but also in terms of the actual *shape* of the structures along the *los* (see Fig. 4.11, left panels, in particular). In other words a fully successful model of the Sgr Stream must reproduce the correct position *and shape* of the observed peaks: this provides the opportunity for a fruitful detailed comparison between models and observations also in regions were different Stream wraps cross each other. In the present study we provide the position and the FWHM of the peaks (as the most basic shape parameter, see § 4.3.4) but anyone interested to more detailed comparisons can easily reproduce our results and obtain plots like Fig. 4.11.

In § 4.4 the LFs of all the considered on-Stream fields, with the associated detections will be presented and briefly discussed. In agreement with the qualitative predictions of the model shown in Fig. 4.10, in most cases we will detect two peaks at different distances.

4.3.2 Classification of the detections

We divided the detections in three categories, assigning a *flag* to each of them, according to the following prescriptions:

- $flag = 1$: peaks that are above the 3σ threshold both in the V and I LFs, and having the same $\Delta(Mag)$ in both passbands, within the errors. These are called *primary* peaks.
- $flag = 2$: peaks having the same $\Delta(Mag)$ in both passbands, within the errors, but reaching the 3σ threshold only in one of the two LFs. In all the $flag = 2$ cases described in the following, the weaker peak is always just below 3σ. These are called *secondary* peaks.
- $flag = 3$: clearly visible peaks having the same $\Delta(Mag)$ in both passbands, within the errors but not reaching the 3σ threshold in both the LFs. These correspond to uncertain detections that we report just for completeness. In some case a weak peak in the LF in one band is tentatively identified as it corresponds to a stronger peak in the other LF. These peaks are called also *tertiary* peaks.

The observed LFs and the detected peaks will be briefly described and discussed in § 4.4.

4.3.3 Number of RC stars associated to each peak

Our modeling of the observed LF automatically provides also an estimate of the total number of stars associated to any given peak. This gives a useful additional constraint for theoretical models; we will illustrate this possibility with an example in § 4.6.2. In Tab. 4.2 we provide the number of stars associated to a given peak normalized to an area of 25 deg^2 (quite similar to the actual area of our fields). This number is the weighted mean of the estimates obtained from the V and I LFs, where the assumed error on the estimate from each LF is just the square root of the observed number (hence it should be considered as a lower limit to the real error).
Adopting the *Sgr34* field as a baseline (having $N^{RC}_{Sgr34} \simeq 1500$ stars/deg^2, and $mu_V \simeq 25.5$ mag/arcsec^2; Monaco et al., 2005), and translating our on-Stream estimates into stars/deg^2 units (N^{RC}_i, for the field i) we can transform our

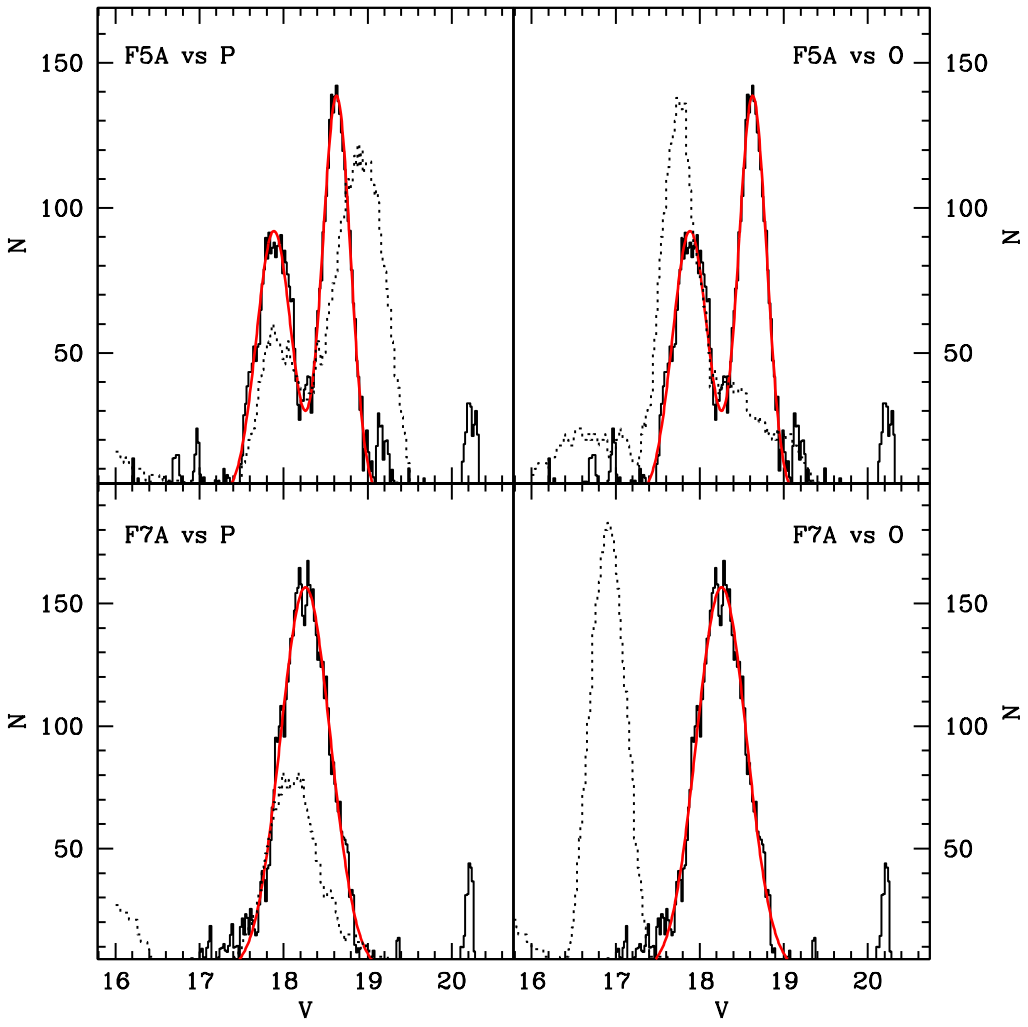

Figure 4.11: Comparison between the observed field-subtracted RC LFs from F5A (upper panels) and F7A (lower panels) and the predictions of the N-body models by Law et al. (2005) in the same directions (left panels: prolate-halo model, the same as Fig. 4.10; right panels: oblate halo model). The observed LFs are the continuous running histograms, the red continuous curves are the best-fit gaussians, the dotted running histograms are the predictions of the models, including the photometric errors. The histograms from the N-body models have been multiplied by arbitrary normalization factors ($2\times$ and $3\times$, for the left and right panels, respectively) to make the plots more readable.

numbers into surface brightness, according to the same formula used in Bellazzini et al. (2006):

$$\mu_{V,i} = \mu_{V,Sgr34} - 2.5log(\frac{N_i^{RC}}{N_{Sgr34}^{RC}}) + \Delta(m-M)_0 \quad (4.4)$$

derived from Renzini (1998), where $\Delta(m-M)_0 = (m-M)_0^i - (m-M)_0^{Sgr34} = \Delta V = \Delta I$. Using this equation we find that the V surface brightness of the portions of the Sgr Stream studied in the present paper range between 30.6 mag/arcsec^2 and 33.6 mag/arcsec^2, quite typical of tidal tails and in good agreement with previous results (see, for example, Bellazzini et al., 2003, and references therein).

It is important to recall that the measured densities refers only to RC stars: in presence of a population gradient (as is likely the case in the Stream, Bellazzini et al., 2006; Chou et al., 2007) they would trace a different fraction of the total stellar content at different positions along the Stream. Analogously, the derived surface brightness estimates have been rescaled assuming the stellar mix of *Sgr34* for all the considered portions of the Stream. For this reason these estimates should be considered with caution: given the sense of the gradient it is expected that they provide lower (faint) limits when converted into luminosity or surface brightness. In this context, it is interesting to note that if we convert our surface brightness into the same density units adopted by Niederste-Ostholt et al. (2010, $L_\odot$/kpc) we find that our results are fully compatible with the trend of density as a function of RA derived by these authors (see their Fig. 7), for both branches. On the other hand our densities are lower than their by a factor of $\sim 4-5$. It is reasonable to assume that part of the difference may be accounted for by the effect of the population gradient described above.

4.3.4 Depth along the *los* of the Stream wraps

Fig. 4.11 shows that the observed RC peaks contains also valuable information on the characteristic size of the section of the Stream branches crossed by our *los*, as peaks at similar distances display different widths. To obtain a quantitative estimate of the linear width along the *los* of the structures identified here, we recurred to the synthetic population described in § 4.2.3. In particular we tried to reproduce the *models* of the observed peaks[11] with smoothed histograms of the synthetic RC population, properly

[11] In this way we avoid any problem associated with the (partial) overlap of *observed* peaks; adjacent overlapping peaks are disentangled by our models as Point Spread Function -fitting photometric packages disentangle the fluxes from two partially overlapping stars on an image.

including the effects of photometric errors. As done in § 4.2.3, we assign a distance along the *los* to each star of the synthetic RC population according to a gaussian distribution having the same mean and normalization as the observed peak, and we search for the value of σ_d giving the best match between the two models. In Tab. 4.2 we report the Full Width at Half Maximum (in kpc) of the adopted distributions, FWHM=$2.35\sigma_d$. The best match is judged by eye, typical uncertainties are $\sim 20\%$. The adopted procedure get rid of the effects of the distance on the width of the LF peaks discussed in § 4.2.3.

Since the synthetic population that we adopt is strictly single-age and single-metallicity, the intrinsic luminosity width of its RC should be smaller than the actual width of the RC of Sgr, as the latter hosts stars spanning a range of ages and metallicities (B06a, Girardi & Salaris, 2001; Siegel et al., 2007; Bellazzini et al., 2008). For this reason the FWHM values we obtain in this way must be considered as strong *upper limits* to the real values. Moreover, it has to be recalled that we report FWHM along a given *los* , that may have various incidence angles with respect to the encountered Stream wraps. Applying the method to the *Sgr34* field we obtain $FWHM \simeq 3$ kpc, not too far from the minor-axis FWHM in the plane of the sky as obtained from the best-fit King (1962) model by Majewski et al. (2003), i.e. $FWHM \simeq 1.1$ kpc, in particular if we take into account that the *los* toward the core of Sgr is (likely) not exactly perpendicular to the major axis of the dwarf galaxy (see Fig. 4.10). Based on this test, it is reasonable to assume that our FWHM overestimates the true values by a factor of > 2.

In any case, the ratio between the FWHM of two different *los* /locations in the Stream, or, equivalently, the differential trend of the FWHM as a function of orbital azimuth along a given Stream wrap, can be directly compared to the predictions of theoretical models of the disruption of Sgr.

SECTION 4.4

On-Stream detections

In this section we present all the LFs obtained from each field analyzed of the branch A and B; we plot the LFs from magnitude V and I as showed in Fig. 4.14, for the branch A, and Fig. 4.15, for the branch B. Together with the observed LFs, we plot also the background model ($f(x)$, dashed lines), the threshold limits for the detections (dotted lines, respectively $3, 4, 5\sigma$), that, as

already said, include both the Poisson noise and the uncertainty in the fit, and the global model that fit the observed LFs ($f(x)+G(x)$, red lines). Each field is labeled according to the names assigned in Tab. 4.1 and with its Galactic coordinates (l,b).

In summary, we detect 25 *primary* (flag=1) peaks, 10 *secondary* (flag=2), and 15 tertiary (flag=3) peaks. Most of the considered LFs show two significant peaks, corresponding to subsequent crossing of different wraps of the Stream along the *los* . The trend of peaks distance as a function of Sgr longitude (Λ_{Sgr}) shown in Fig. 4.12 can be useful to better understand the morphology of the various LFs presented below. Most primary peaks appear to trace a wrap of the leading arm whose distance from the Sun steadily decreases from $D \simeq 45$ kpc at $\Lambda_{Sgr} \simeq 290^\circ$ to $D \simeq 20$ kpc at $\Lambda_{Sgr} \simeq 230^\circ$. Both primary and secondary peaks traces a more nearby filamentary structure at constant distance $D \simeq 25$ kpc, from $\Lambda_{Sgr} \simeq 290^\circ$ to $\Lambda_{Sgr} \simeq 260^\circ$, then bending toward larger distances, reaching $D \simeq 40$ kpc at $\Lambda_{Sgr} \simeq 230^\circ$. This feature is tentatively identified as a wrap of the trailing arm (see § 4.6). The two wraps crosses at $\Lambda_{Sgr} \sim 245^\circ$ (see § 4.6). Some secondary and tertiary peaks seem to trace more feeble distant or nearby wraps (see § 4.6 for a deeper discussion). The comparison with the considered model suggests that most of the detected peaks can be associated with the Sgr Stream. The tertiary peak at $\lambda_{Sgr} \sim 263^\circ$ and $d \simeq 18$ kpc, and the primary peak at $\lambda_{Sgr} \sim 280^\circ$ and $d \simeq 19.5$ kpc, are possibly associated to other overdensities in the Virgo constellation (see Duffau et al., 2006; Jurić et al., 2008; Newberg et al., 2007, and references therein), as discussed in some detail in § 4.6. Before proceeding in the description of the various detections, we anticipate that the differential distance moduli ($\Delta V = V_{RC}^{Field} - V_{RC}^{Sgr34}$; the analogous definition being valid also for ΔI), reported in Tab. 4.2, obtained from primary and secondary peaks detected in the V and I LFs are in *excellent* agreement, as shown in Fig. 4.13. This confirms the reliability of our detections and distance estimates. For this reason, from § 6.8 on and in Fig. 4.12 we adopt the mean of ΔV and ΔI as our final differential distance moduli estimates.

4.4.1 Branch A detections

In the branch A we analyzed 15 fields, the corresponding observed LFs and the adopted best-fit models are shown in Fig. 4.14 We obtained a total of 24 peak detections, with the following classification: 10 primary peaks, 5 secondary peaks and 9 tertiary peaks. The LFs of the first five fields (from F1A to F5A, upper left panel and first two rows of the upper right panel of Fig. 4.14) display a common general behaviour: they present two

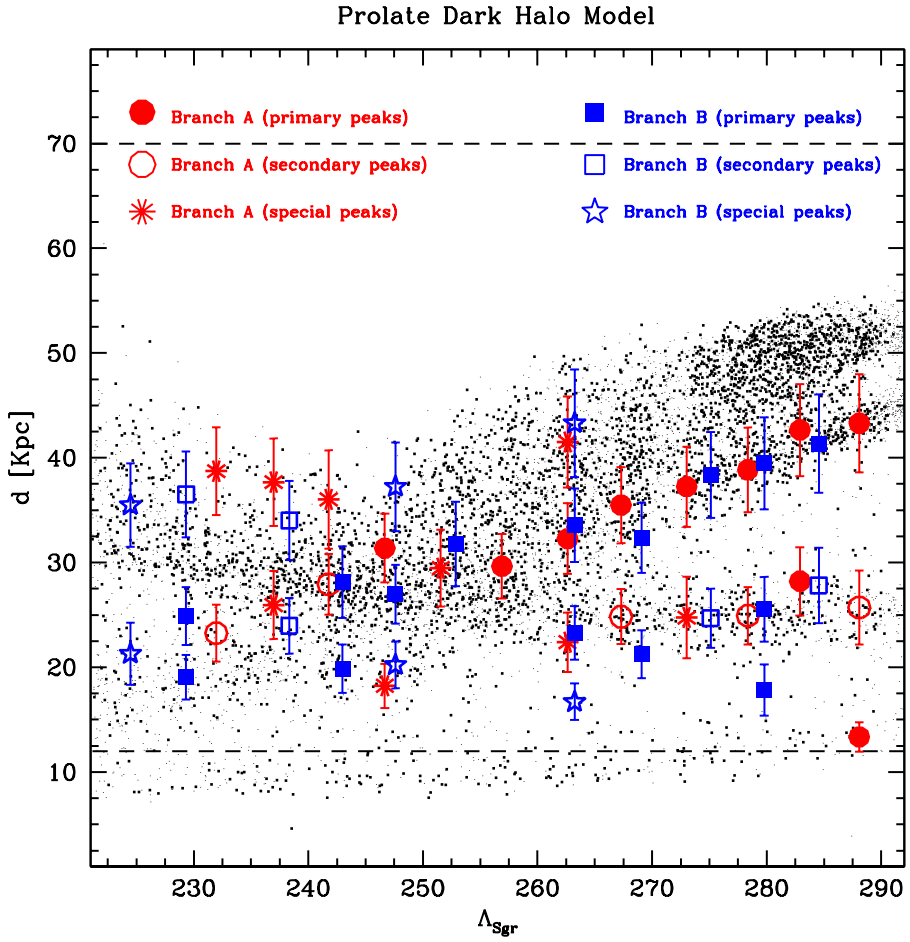

Figure 4.12: Distribution of the primary (red filled circles - branch A -, and blue filled squares - branch B), secondary (red open circles - branch A -, and blue open squares - branch B) and *tertiary* detections (red starred symbols - branch A, and blue stars - branch B) in the Λ_{Sgr} vs. heliocentric distance plane (a true distance modulus of 16.90 has been adopted here). The horizontal dashed lines enclose the range of sensitivity of our method. The prolate-halo N-body model by Law et al. (2005) is also reported (small dots) as an aid for the interpretation of the plot. The heavier dots are those enclosed in the cones of the considered FoVs.

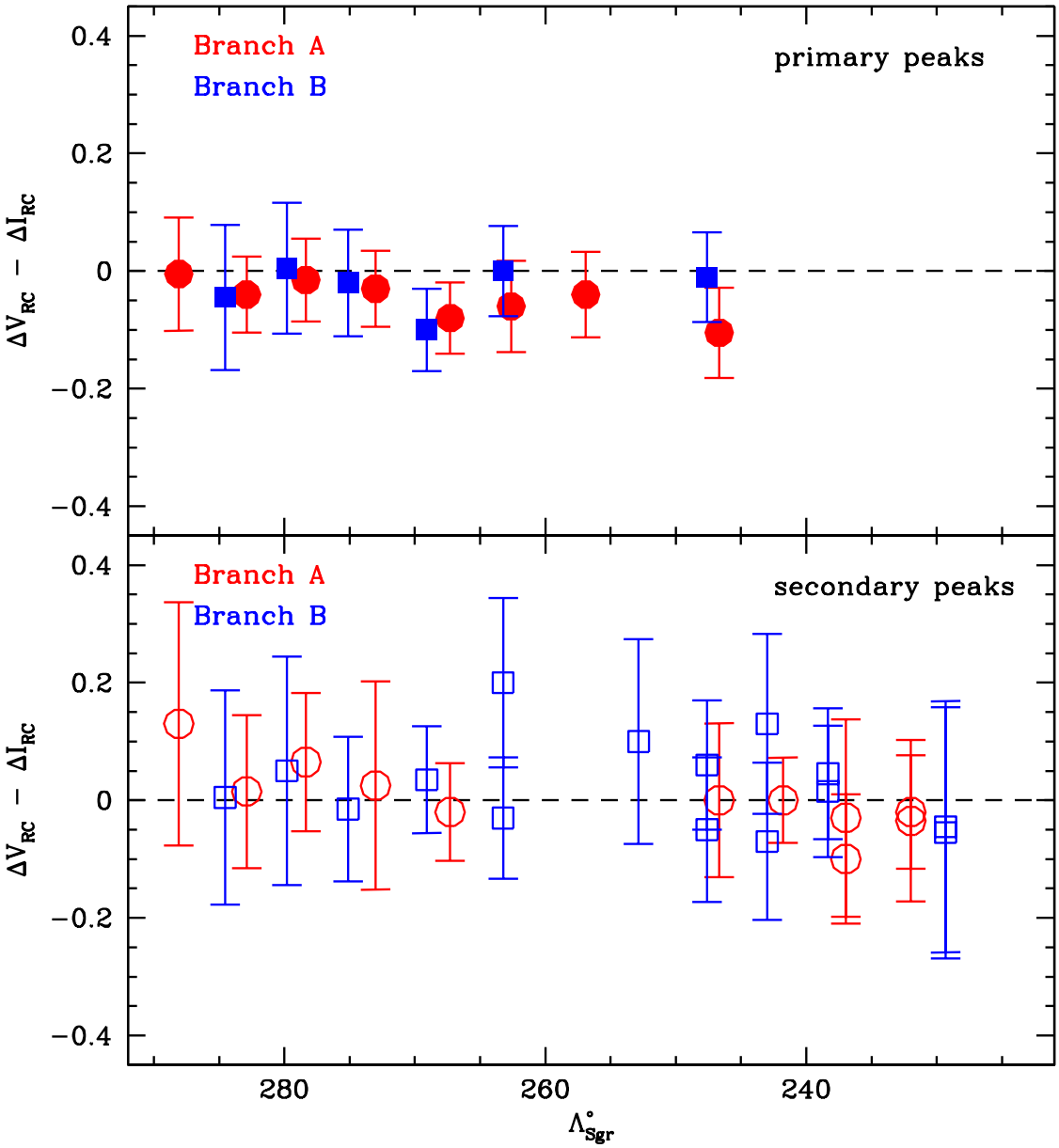

Figure 4.13: Comparison between the differential distance moduli obtained from peaks in the V and I LFs for primary (upper panel) and secondary (lower panel) peaks.

Table 4.2: Distances, FWHM and density for the detected peaks.

field	l°	b°	ΔV	$d\Delta V$	ΔI	$d\Delta I$	D [kpc]	dD [kpc]	sign. (V)	sign. (I)	FWHM [kpc]	N_{RC} [stars / 25 deg^2]	dN	flag
1A	346	56	1.280	0.073	1.285	0.063	47.48	5.13	$\geq 5\sigma$	5σ	9.8	241.0	10.6	1
			0.215	0.141	0.085	0.151	28.20	3.86	4σ	$< 3\sigma$	7.1	353.1	9.2	2
			-1.270	0.054	-1.270	0.054	14.65	1.08	3σ	3σ	1.3	79.0	6.4	1
2A	339	60	1.230	0.054	1.270	0.036	46.77	4.81	$\geq 5\sigma$	$\geq 5\sigma$	4.2	227.1	9.2	1
			0.360	0.092	0.345	0.092	30.94	3.57	4σ	3σ	9.5	303.2	10.6	1
3A	331	63	1.040	0.045	1.055	0.054	42.61	4.42	$> 5\sigma$	$\geq 5\sigma$	11.3	345.5	12.7	1
			0.060	0.073	-0.005	0.092	26.64	2.99	4σ	$< 3\sigma$	6.2	327.5	9.9	2
4A	320	66	0.940	0.036	0.970	0.054	40.83	4.21	$\geq 5\sigma$	5σ	7.5	158.4	7.8	1
			0.080	0.092	0.055	0.151	27.13	4.27	$< 3\sigma$	$< 3\sigma$	14.6	225.6	9.9	3
5A	309	70	0.810	0.028	0.890	0.054	38.91	3.99	4σ	4σ	8.6	113.9	8.5	1
			0.065	0.063	0.085	0.054	27.23	2.88	$< 3\sigma$	$\geq 3\sigma$	5.1	115.9	7.1	2
6A	296	72	0.620	0.045	0.670	0.063	35.98	3.77	4σ	4σ	7.0	171.4	10.8	1
			-0.080	0.122	-0.220	0.122	24.56	3.11	$< 3\sigma$	$< 3\sigma$	3.9	65.9	7.2	3
			1.180	0.054	1.200	0.054	45.50	4.76	$< 3\sigma$	$< 3\sigma$	1.4	48.7	6.5	3
7A	277	72	0.440	0.036	0.480	0.063	32.51	3.38	$\geq 4\sigma$	$\geq 4\sigma$	10.9	188.5	10.1	1
8A	260	71.5	0.530	0.102	0.360	0.131	32.31	4.02	$< 3\sigma$	$< 3\sigma$	3.9	122.1	5.8	3
9A	248	68.5	0.530	0.054	0.635	0.054	34.40	3.60	5σ	5σ	17.0	230.6	10.2	1
			-0.595	0.082	-0.595	0.102	20.00	2.31	$< 3\sigma$	$< 3\sigma$	2.6	71.0	5.8	3
10A	238	65.5	0.330	0.063	0.330	0.036	30.62	3.19	3σ	$< 3\sigma$	5.3	90.1	5.1	2
			0.945	0.151	0.845	0.102	39.51	5.14	$< 3\sigma$	$< 3\sigma$	3.0	64.2	4.4	3
11A	230.5	62	0.930	0.082	1.030	0.073	41.31	4.57	$< 3\sigma$	$< 3\sigma$	9.5	41.6	5.9	3
			0.155	0.151	0.185	0.073	28.44	3.56	$< 3\sigma$	$< 3\sigma$	6.2	37.5	5.1	3
12A	224.5	58	1.030	0.063	1.050	0.073	42.46	4.59	$> 3\sigma$	$< 3\sigma$	4.2	103.5	6.7	3
			-0.085	0.092	-0.050	0.102	25.500	2.99	$> 3\sigma$	3σ	9.8	167.3	9.6	2
1B	353	61	1.160	0.082	1.205	0.092	45.34	5.16	3σ	3σ	6.9	172.3	8.5	1
			0.325	0.102	0.320	0.151	30.51	3.95	3σ	$< 3\sigma$	12.5	351.6	10.7	2
2B	346.5	65	1.085	0.092	1.080	0.063	43.30	4.81	$\geq 5\sigma$	$\geq 5\sigma$	9.3	186.8	10.0	1
			0.180	0.122	0.090	0.092	28.00	3.40	5σ	5σ	8.8	373.7	10.7	1
			-0.650	0.141	-0.640	0.151	19.54	2.68	3σ	3σ	3.5	124.2	7.9	1
3B	337.5	68.5	1.010	0.073	1.030	0.054	42.07	4.50	$> 3\sigma$	$> 3\sigma$	6.8	233.9	7.9	1
			0.055	0.082	0.070	0.092	27.07	3.08	3σ	$< 3\sigma$	6.8	170.1	7.9	2
4B	329.5	74	0.600	0.045	0.700	0.054	35.49	3.68	$> 5\sigma$	5σ	15.0	271.0	10.9	1
			-0.245	0.054	-0.280	0.073	23.31	2.49	$> 4\sigma$	3σ	3.1	160.1	6.5	1
5B	313.5	78.5	0.730	0.054	0.730	0.054	36.81	3.85	5σ	5σ	6.5	124.8	7.4	1
			-0.080	0.073	-0.050	0.073	25.53	2.79	4σ	3σ	4.1	133.2	6.6	1
			1.380	0.102	1.180	0.102	47.47	5.47	$> 3\sigma$	$< 3\sigma$	6.9	56.2	7.4	3
			-0.800	0.054	-0.770	0.054	18.32	1.92	$< 3\sigma$	$< 3\sigma$	2.2	61.4	5.1	3
7B	256	80	0.660	0.102	0.560	0.141	34.84	4.41	3σ	$> 3\sigma$	~ 20.0	201.1	9.8	1
8B	234	77	0.250	0.054	0.260	0.054	29.58	3.09	4σ	$> 4\sigma$	6.5	115.4	6.9	1
			-0.340	0.073	-0.400	0.082	22.18	2.46	$< 3\sigma$	$< 3\sigma$	3.3	92.8	5.3	3
			0.930	0.082	0.980	0.092	40.83	4.65	$< 3\sigma$	$< 3\sigma$	9.2	89.5	6.9	3
9B	224	73	0.410	0.092	0.280	0.122	30.85	3.73	$\geq 3\sigma$	3σ	12.0	189.8	8.4	1
			-0.445	0.073	-0.375	0.112	21.78	2.54	$> 3\sigma$	3σ	3.1	58.6	6.1	1
10B	216.5	69	0.765	0.102	0.750	0.045	37.28	4.14	$< 3\sigma$	$> 3\sigma$	7.0	110.6	7.7	2
			0.020	0.102	-0.025	0.045	26.27	2.92	$< 3\sigma$	$> 3\sigma$	4.4	74.4	7.7	2
12B	208.5	60.5	0.885	0.151	0.940	0.151	40.04	5.57	$< 3\sigma$	3σ	8.1	92.0	6.3	2
			0.070	0.082	0.090	0.073	27.29	3.02	3σ	3σ	4.0	78.7	6.3	1
			-0.500	0.073	-0.500	0.082	20.89	2.31	3σ	3σ	2.4	75.3	6.3	1
13B	203	56.5	0.890	0.082	0.810	0.082	38.91	4.36	$< 3\sigma$	$< 3\sigma$	7.2	81.2	6.4	3
			-0.200	0.151	-0.320	0.151	23.34	3.25	$< 3\sigma$	$< 3\sigma$	6.7	142.1	6.4	3

main peaks, the one at fainter magnitudes always being the strongest (a *primary* peak in all cases), while the brighter ones are wider and span all the classes from flag=1 to flag=3, depending on the specific field. It is quite clear that this series of peaks traces two coherent structures placed at different distances along the *los* . The I LF of F4A may suggest a splitting of the brighter/weaker peak into two separate components: we consider this interpretation as unlikely, nevertheless the result obtained with a three peaks model is briefly discussed in § 4.4.3. The only exception is a primary peak detected at $V \sim 16.5$ in F1A: this likely corresponds to the nearest wrap of the Stream that emerges from the $d < 12$ kpc circle (where our method is blind) only in this field, that correspond to the most Eastern of all the considered *los* (see § 4.6).

The LFs of F6A (second upper right panel of Fig. 4.14) present an overall structure similar to those described above. However we identified an additional (fainter), and finally we adopted a three peaks solution, whose validity is confirmed by the inspection of LFs obtained with reduced bin width (i.e., higher resolution[12]; see § 4.4.3 for an alternative). The newly resolved third peak, at magnitude $V \sim 19$ ($I \sim 18$), corresponds to a distance $D \simeq 42$ kpc at $\Lambda_{Sgr} \simeq 265°$; this detection seems related to a very distant wrap of the leading arm (see for example Fig.4.21). F6A is the only branch-A field in which we detect a peak related to this distant wrap of the leading arm, that was observed also by Bel06 (see § 6.8); the same structure is detected in branch B along the same *los* , as well as along an additional one (F8B).

F7A is one of the two fields in the branch A that present only one detection: LFs (third upper right panels of Fig. 4.14) show a single, very prominent *primary* peak . As said, this *los* intercepts a region where two/three the wraps of the Stream cross each other. Fig. 4.11 shows that the presence of a single peak is in good agreement with the models predictions. In both the LFs of the adjacent field F8A, a remarkably weak peak appears at similar position as in F7A, hence we obtain only a tentative flag=3 detection. We have no convincing explanation for the weakness of the peak detected in this field: it may be related to the complex structure of the various Stream wraps or to a local dip in the density along the Stream. However, the derived distance is in good agreement with the trend observed in others Branch-A fields. In the LFs of F9A field we identify again two peaks, the faintest one being very prominent and wide; also this *los* intercept a region of crossing wraps, thus superposed structures may contribute to the production of a strong and remarkably wide

[12]We note that this is the only case in which a change in the bin width produced a change in the interpretation of the LFs.

primary peak. The weaker/brighter peak is more interesting: it is clearly identified in both LFs, even if below the 3σ threshold, at $V \sim 17.20$ ($I \sim 16.30$): as discussed later in § 4.6 this feature may trace a near wrap of the Stream that was never detected before.
LFs of fields from F10A to F12A show two peaks at similar positions, with a remarkable variety of absolute and relative strenghts. This may reflect the highly structured morphology that is suggested by models in this region (see § 4.6). F11A is crossed by the Orphan Stream (Belokurov et al., 2007a). While the distance of this structure (~ 30 kpc toward this *los*) does not match with the detected peaks we cannot rule out some contamination from Orphan Stream stars in this field.
We did not find any convincing signal in F13A, F14A and F15A; the overall shape of the LFs appear quite different from the other cases and, in the case of F15A, the polynomial model do not appear to provide a satisfactory fit to the background population. In particular the LFs present a strong excess at bright magnitudes ($V < 18$, $I < 17$) with respect to those in the previously discussed fields, such that they appear flat or even decreasing with increasing magnitude. These are the fields with the lowest Galactic latitude, hence we attribute these feature to contamination by (relatively) nearby stars from the Galactic thick disc (and, possibly, the Monoceros structure, see Fig. 1 of Bel06) that overwhelms the signal from the Sgr Stream RC. This seems confirmed by the comparison with the corresponding CFs (the case of F15A is shown in Fig. 4.28, in § 4.8), that display LFs essentially indistinguishable from those of the on-Stream fields. This implies that the adopted technique can be used successfully only at large distances from the Galactic plane. Given the above reasons we preferred not to consider for further analysis the possible peaks at $V(I) \sim 16(15)$ and $V(I) \sim 17.5(16.5)$ in F14A.

4.4.2 Branch B detections

In the branch B we analyzed 13 fields, obtaining a total number of 26 detections, with the following classification: 15 primary, 5 secondary and 6 tertiary peaks. The main structures found in branch A are mirrored also in branch B, as clearly shown in Fig. 4.12. In all the fields (except F7B) we detect at least two peaks; in two cases (F8B and F12B) we also detect a third peak; in F8B this is likely tracing the more distant Stream wrap running nearly parallel to the main wrap of the leading arm (see above and Fig. 4.12); in another case (F5B), in addition to three peaks analogous to those in F8B, we found an additional nearby peak (see § 4.6 for a discussion). An alternative interpretation for the LFs of F12B is presented in § 4.4.3. Quite suprisingly,

Table 4.3: Alternative solutions for three *los* .

field	l°	b°	ΔV	$d\Delta V$	ΔI	$d\Delta I$	D [kpc]	dD [kpc]	sign. (V)	sign. (I)	FWHM [kpc]	N_{RC} [stars/25 deg^2]	dN	flag
4A	320	66	0.940	0.036	0.970	0.054	40.83	4.21	$\geq 5\sigma$	5σ	7.5	158.4	7.8	1
			0.280	0.073	0.360	0.102	30.48	3.49	$< 3\sigma$	$< 3\sigma$	3.2	119.3	7.1	3
			-0.160	0.092	-0.170	0.092	24.38	2.81	$< 3\sigma$	$< 3\sigma$	1.9	107.3	6.4	3
2B	346.5	65	1.085	0.092	1.080	0.063	43.30	4.81	$\geq 5\sigma$	$\geq 5\sigma$	9.3	186.8	10.0	1
			0.130	0.151	0.080	0.122	27.61	3.68	5σ	5σ	14.0	498.9	13.6	1
12B	208.5	60.5	0.885	0.151	0.940	0.151	40.04	5.57	$< 3\sigma$	3σ	8.1	92.0	6.3	2
			-0.215	0.151	-0.170	0.151	24.07	3.35	3σ	3σ	12.0	155.1	8.6	1

the LFs of F6B appear completely smooth and featureless. In this case we were not able to find out an explanation for this behaviour (but see above for the discussion of the similar case of F8A).
In analogy with F7A (and F8A) F7B is the only case of a branch B LFs fitted with a single peak model. The morphology of the I LF and the comparison with the adjacent F8B field suggest that two, or possibly three peaks may be merged together in this LF. However we were unable to resolve the peak into separate components even in LFs with smaller bin width (as for the case of F6A). We caution the reader that this primary detection is likely concealing significant - but undetected -substructure.

4.4.3 A few special cases

There are a few cases in which the observed LFs do not provide unequivocal indications for the model to be adopted, in particular concerning the number of $G_i(x)$ functions to be included in the model, i.e. the number of detected peaks. F7B, briefly discussed above, is the only case in which we feel that the observed peak is due to the merging of two (or, more likely, three) adjacent peak that we cannot resolve. In Fig. 4.16 we present acceptable alternative models (with respect to the solutions shown in Figg. 4.14 and 4.15 and listed in Tab. 4.2) for the three cases in which our preference for the adopted models (Tab. 4.2) is only marginal, and is also supported by the continuity within a large scale structure (a Stream wrap). In Tab. 4.3 we report the corresponding alternative solutions, that can be replaced to that of Tab. 4.2 by scientists that will use our number to constrain models of Sgr, if they judge them more appropriate, for some reason.

4.4.4 Intra-Branch fields

In the present analysis we do not consider the structure of the Stream in the Dec direction. We fully adopted the view of Belokurov et al. (2006), where the leading arm of the Stream as seen from TO stars in the SDSS bifurcates into branch A and branch B around RA=220° and the separation between the branches increases with decreasing RA. We proceeded to a basic verification

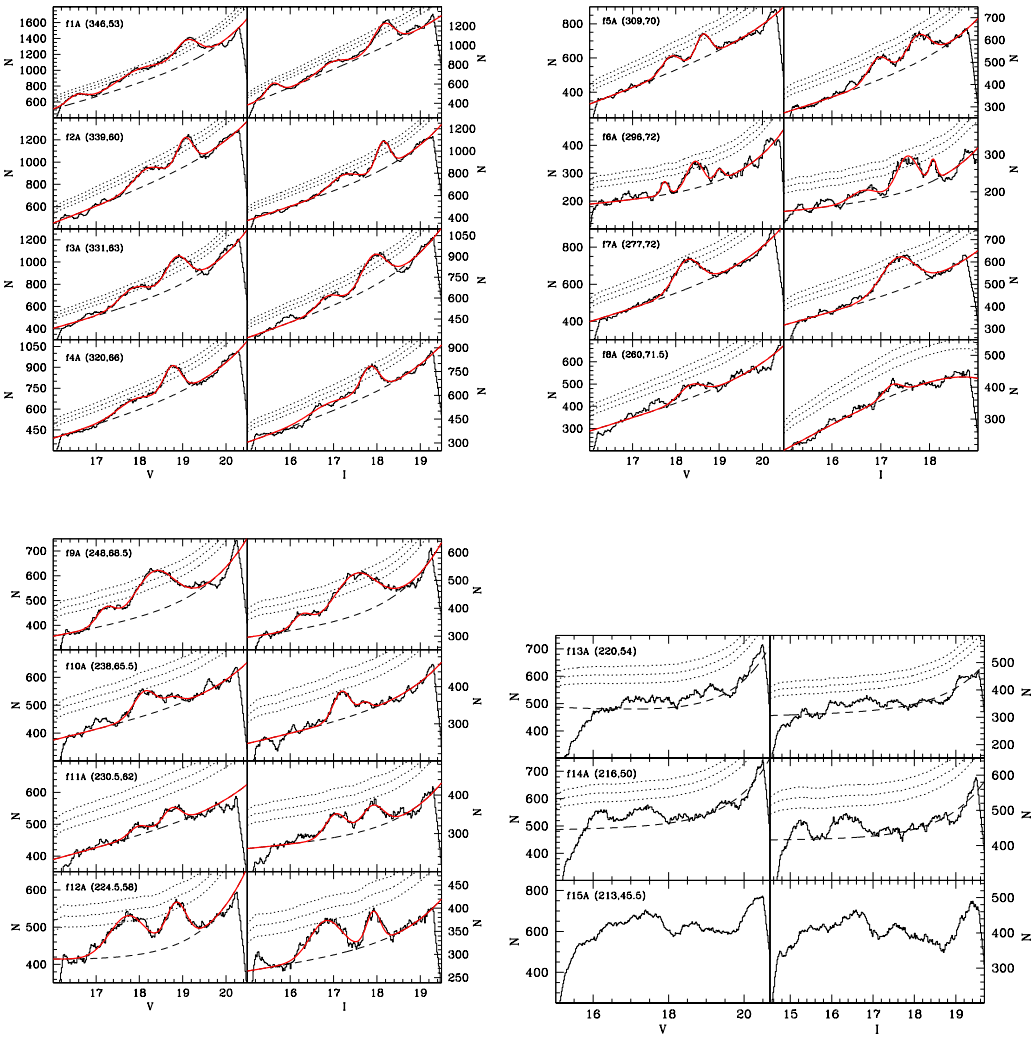

Figure 4.14: Fits of the observed LFs (in V and I) for fields on Branch A of the Sgr Stream. The numbers in parentheses are the Galactic longitude and latitude of the center of the field, in degrees. The meaning of the symbols is the same as in Figg. 4.7 and 4.8, above. No global fit has been attempted for LFs that did not show significant RC peaks (F8A, F13A, F14A, F15A).

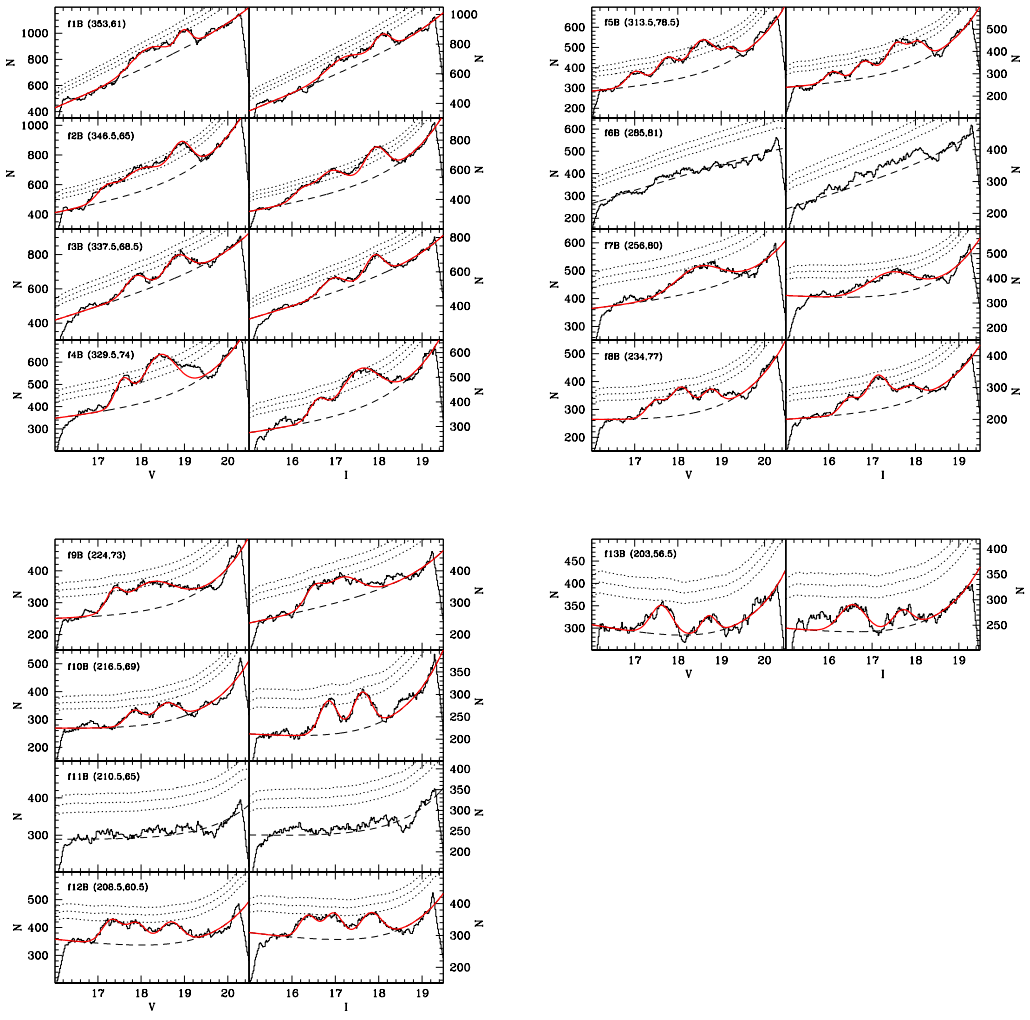

Figure 4.15: The same as Fig. 4.14 but for fields on Branch B of the Sgr Stream. No global fit has been attempted for LFs that did not show significant RC peaks (F6B, F11B).

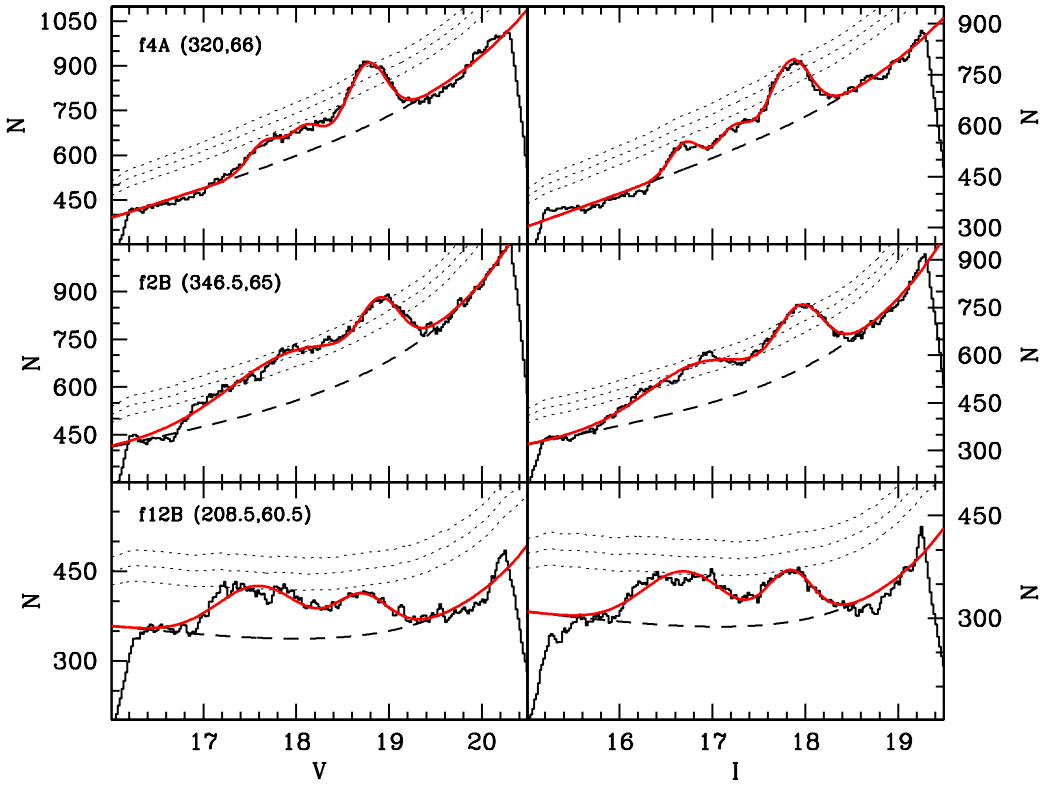

Figure 4.16: Fits of the observed LFs (in V and I) for fields on branch A and B of the Stream, obtained using the alternative solutions reported in Tab. 4.3. The meaning of the symbols is the same as in Figg. 4.7 and 4.8, above.

of this scenario by looking at the LFs of a few Intra-Branches (I) fields (not shown here, for brevity), located at intermediate Dec with respect to the A and B fields F5, F7, F10 and F12. In agreement with the results of Belokurov et al. (2006), we find that the LFs F5I and F7I mimic the structure of the LFs of the corresponding A and B fields, showing peaks at the same position and with similar shape, but weaker than in the on-Stream field (i.e. tracing a lower stellar density). In the LFs of F10I the peaks seen in the A and B LFs are just barely visible and they are completely disappeared in F12I. Hence, these limited set of tests confirms the reality and the morphology of the Stream bifurcation as observed by Belokurov et al. (2006).

4.4.5 The colour of the RC peaks

The colour of the RC peak is known to be very sensitive to metallicity and weakly sensitive to age, in the range of ages relevant for the present study (4-12 Gyr Girardi & Salaris, 2001). As our procedure of independent peak detections in V and I LFs automatically provides the colours of the RC peaks, it is worth to check if there is some hint of a colour (metallicity) gradient along the Stream. In Fig. 4.17 the colours of the observed peaks are compared to the theoretical models by Girardi & Salaris (2001). All of the peak detections shown in Fig. 4.17 are compatible with having the same colour within the uncertainties (that are quite large for some non-primary peak). It is interesting to note that the large majority of points clusters around the $[M/H] = -0.7$ model, in good agreement with the results by Bellazzini et al. (2006) and Carrell & Wilhelm (2010) (see also § 4.2.1). No significant trend of colour (metallicity) of the RC population with orbital azimuth is apparent and the few points showing the larger colour difference from the mean locus are always among those having the most uncertain colour estimates.

SECTION 4.5

Comparison with previous analyses

Before discussing in detail the comparison between our distance estimates and the findings from previous works, it is worth to consider the difference between the performances of the various adopted tracers. The intrinsic stability (and ubiquity along the Stream) of our standard candle (RC stars), the adopted approach to the analysis, best suited for the detection and location of RC peaks, and the purely differential nature (Stream vs. main

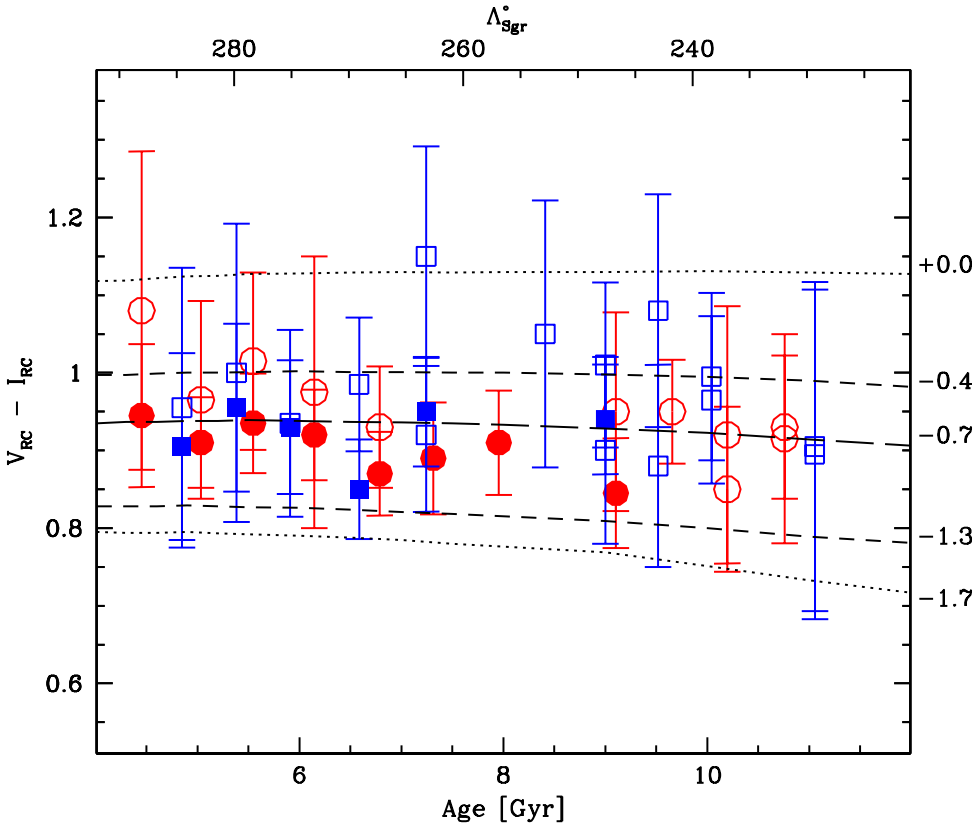

Figure 4.17: De-reddened colour of the observed RC peaks as a function of Λ_{Sgr}. The observed points are compared with the predictions of the Girardi & Salaris (2001) theoretical models for different metallicities, plotted as a function of age of the population in the range 4-12 Gyr. The scale on the lower horizontal axis (age) refers to models, that on the upper horizontal axis (Λ_{Sgr}) refers to observed points.

body) of our measures, make our distance estimates the more comprehensive, accurate and *homogeneous* set publicly available (even if limited to the region of sensitivity described above). The uncertainties associated to our estimates are lower than any previous work, with a typical value of $\leq 5\%$, raising to $\leq 10\%$ in the worst cases. For example, Majewski et al. (2003) reports that the characteristic uncertainty of their photometric parallaxes based on M-giant is $\simeq 20\%$; Martin et al. (2004) showed that uncertainties in the age/metallicity of the considered populations may lead to systematics of order $\sim 30\%$ in the distance scale based on M giants. F stars (assumed to be TO stars of Sgr) proved to be an excellent mean to trace even very feeble substructures (Belokurov et al., 2006; Newberg et al., 2007). However the assumption of a common absolute magnitude for all colour-selected F stars imply large uncertainties, as these stars span a range of luminosities much larger than RC stars. For example, if we consider the distribution in V magnitude of (a) the RC selected with our colour window, and (b) the MSTO stars selected in colour as done by Bel06 (and limited to $V > 20.0$ in the photometry of the *Sgr34* field), we found two obvious single peaked distributions, but while the FWHM of the RC peak is $\simeq 0.3$ mag, the MSTO stars peak has $FWHM \simeq 2$ mag. Indeed, Cole et al. (2008), in their pilot project on stripe 82, showed that the assumption of a fixed magnitude for these stars may lead to very large errors. Blue Horizontal Branch stars are easier to select against the Galactic fore/background, but are rarer than RC stars. Moreover, even if selected in a colour range where the Horizontal Branch is really nearly horizontal, the distribution in magnitude of these stars is not expected to be as clearly peaked as the RC (see B06c). In this sense, the Sub Giant Branch (SGB), used by Bel06 and Keller (2009b), is more promising, as it is a very narrow feature in CMDs of metal rich populations. However it should be much more sensitive to metallicity and age variations than the RC (see, for example, B06a, and references and discussion therein), and being much (intrinsically) fainter, its use is limited to a lower distance range, for any given dataset. Finally, RR Lyrae stars (Ivezić et al., 2000; Vivas & Zinn, 2006; Prior et al., 2009b; Keller et al., 2008) can provide distances with even superior accuracy with respect to our method; well sampled light curves can also give indications on physical properties of individual stars (metallicity, for example) that cannot be obtained from RC stars. However RR Lyrae are (likely) less frequent than RC stars over most of the Stream extension and, above all, they need time series to be safely identified and to obtain a reliable apparent magnitude averaged over the pulsation period: for this reason the available data cover a much smaller region of the sky with respect to generic "single epoch" standard

candles.

4.5.1 Comparison with specific detections

Yanny et al. (2000) were the first to interpret a stellar over-density in the halo as possibly due to the Sgr Stream. In the first available (equatorial) stripe of the SDSS they identified an excess of A-type stars around $\Lambda_{\odot} \sim 295°$, adjacent to our field F1A. The heliocentric distance inferred is of 48 kpc, in good agreement with our estimate for the main wrap of the leading arm in this direction ($D \simeq 45$ kpc at $\Lambda_{Sgr} \simeq 290°$). This results will be later confirmed by the more thorough study by Newberg et al. (2002), that used F stars as main tracers. Altough they do not comment on it, Yanny et al. (2000) data also shown an excess of A-type stars less than 20 kpc away along the same *los* (see their Fig. 18 and 19). This may be more easily associated to the constant distance coherent structure we see at $d \simeq 25$ kpc than to the nearest wrap that we (possibly) detect at $\Lambda \simeq 287°$ and $d \simeq 13$ kpc.
A similar detection of two density enhancements toward the Northern Loop was reported by Ivezić et al. (2000), from the study of RR Lyrae in the same SDSS stripe studied by Yanny et al. (2000), and by Vivas & Zinn (2006), also using RR Lyrae from the QUEST RR survey, which explored nearly the same region of sky ($\Lambda_{\odot} \sim 270° - 290°$). Both studies comment primarily on an excess of RR Lyrae stars at 45-50 kpc (corresponding to the main wrap of the leading arm); however a structure around ~ 20 kpc is also noted.
Majewski et al. (2003), provided a clear panoramic view of the Sgr Stream using M giants as standard candles; they were able to trace very neatly the trailing tail all over the Southern Galactic hemisphere, as well as part of the leading arm closer to the main body of the galaxy, up to $RA \simeq 190°$. They report two cases of M giants excess along the *los* in common with the present analysis. The most evident at a distance $D \sim 45$ kpc, compatible with our estimates, and the other one, less pronounced, at a distance $D \sim 20 - 25$ kpc, for which the interpetation is not so clear as in the case of A stars and RR Lyrae detections.
All the detections mentioned above, as well as others toward specific directions, also not included in the range considered here (Martínez-Delgado et al., 2001, 2004; Bellazzini et al., 2003; Vivas & Zinn, 2006), are collected and reported in Fig. 17 of M03. This figure, as well as Fig. 19 in Law & Majewski (2010), clearly illustrates how it may be difficult and misleading to put results from different sources (and on different distance scales) all together. In this sense, it is more fruitful to compare our results with other data set providing homogeneous distance estimates for significant portions of

some wrap in common with those detected here.
For instance, Bel06, that used A-F dwarf stars from the SDSS to trace the Stream, detected a distant gradient along the main wrap of the leading arm that is in good agreement with our results (for both branches). More interestingly, Bel06 found a double detection in a couple branch A *los* (from F5A to F7A): in addition to the main wrap of the leading arm, they found also a more distant structure, ~ 15 kpc behind. This finding is also in excellent agreement with our results (see § 4.4.1). The only difference is that we detect this structure, at similar distance, also in the corresponding branch B fields.
Newberg et al. (2007) investigated the relationship between several previously identified substructures in the direction of Virgo and the Sgr Stream using imaging and spectroscopic observations of F stars and BHB stars from SDSS and SEGUE. In their Tab. 1, they reported the detections associated to the Sgr Stream, providing also estimates of the distance of these structures. This allowed us to perform the direct comparison with our results that is presented in Fig. 4.18. The agreement for the structure detected in both studies (main wrap of the leading arm) is very good, both for branch A and B.
Niederste-Ostholt et al. (2010) investigated the leading arm of Sgr Stream in the same region of the "field of Stream" analyzed by Bel06, using BHB candidates from the SDSS. The distances to BHBs are calculated assuming an absolute magnitude $M_g = 0.7$ and are in good agreement with the results of Bel06. In Fig. 4.18 we compare our estimates with those obtained by Niederste-Ostholt et al. (2010), reported in their Tab. 1, in the region of sky going from $RA \geq 160^\circ$ to $RA \leq 220^\circ$. Our distances are calculated using a true distance modulus of $(m-M)_0 = 17.10$, roughly the same adopted by Niederste-Ostholt et al. (2010, the g magnitude of the BHB in the main body is $g \sim 17.80$). In all the regions of data-sets overlap the match is very good, both for branch A and B detections. The trailing arm of Sgr Stream is not sampled by Niederste-Ostholt et al. (2010) that concentrated their analysis on the detection of the leading arm and on an accurate distance estimate for this wrap of the Stream.
In conclusion, the overall agreement with previous detections of the leading arm is very good. The situation for the other coherent structures detected here is more difficult to judge; in our view the only firm conclusion that can be drawn is that several independent studies found evidences for some structure located in front to the main wrap of the leading arm, in the considered range of Λ. It is unclear if some of these detections can be associated with the constant distant (putative) wrap of the trailing arm detected here or to even more

nearby wraps. In this dense it is interesting to note that a similar coherent structure, at a similar distance, is detected also by Keller (2009b), using SGB stars (see his Fig. 7).

SECTION 4.6

Comparison with models

As soon as it was realized that Sgr was likely undergoing tidal disruption, several authors attempted to model the process by means of N-body simulations, to establish the plausibility of proposed models and to infer the properties (mass, orbit) of the original system (Velazquez & White, 1995; Johnston et al., 1995; Ibata et al., 1997; Edelsohn & Elmegreen, 1997; Ibata et al., 2001; Gómez-Flechoso et al., 1999; Johnston et al., 1999; Jiang & Binney, 2000; Helmi & White, 2001). It is interesting to note that Velazquez & White (1995) were able to provide estimates of perigalactic and apogalactic distances and orbital period remarkably similar to those obtained in the most recent studies, just one year after the discovery of Sgr ($R_{peri} \simeq 10$ kpc, $R_{apo} \simeq 52$ kpc and $P_{orb} \simeq 0.76$ Gyr, to compare, for instance, with $R_{peri} \simeq 15$ kpc, $R_{apo} \simeq 60$ kpc and $P_{orb} \simeq 0.85$ Gyr, from Law et al., 2005). The possible rôle of Sgr in the formation of the Galactic Disc warp was studied by Ibata & Razoumov (1998) and Bailin (2003).

However, since the Sgr Stream appears as a remarkably coherent structure crossing large part of the Galactic halo on a nearly-polar orbit, it seems the ideal tracer to study the overall shape and the degree of clumping of the Galactic halo as a whole. For this reason, the most recent N-body modeling efforts have focused on constraining the shape of the DM halo of the Milky Way (Ibata et al., 2001; Martínez-Delgado et al., 2004; Helmi, 2004; Law et al., 2005; Johnston et al., 2005; Fellhauer et al., 2006; Law et al., 2009; Law & Majewski, 2010). However it turned out that the conclusions of these studies depended on the specific set of observational constraints considered, and it is now generally accepted the idea that none of the static-potential axisymmetric halo models considered is able to reproduce simultaneously all the available positional and kinematic data (see Yanny et al., 2009; Law et al., 2009, for references and discussion). In a recent contribution Law et al. (2009) anticipated that the adoption of triaxial halo models can help to solve this problem: in § 4.6.3 we briefly consider the N-body model they produced as a follow-up of that analysis (Law & Majewski, 2010). In any

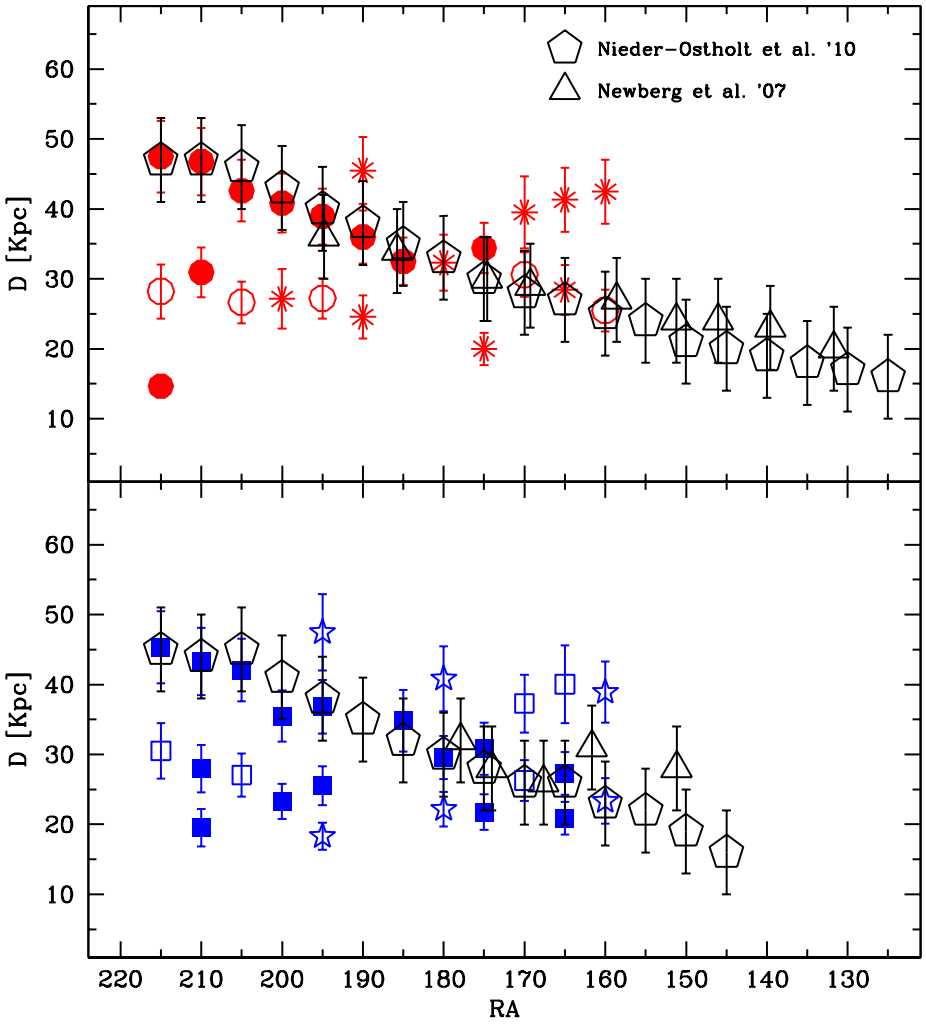

Figure 4.18: Comparison between our distance estimates (same symbols as in Fig. 4.12) and those by Newberg et al. (2007, open triangles) and by Niederste-Ostholt et al. (2010, open diamonds) The match between the different indicators is remarkably good, for the portions of the leading arm considered by the three studies. The trailing arm is detected only in the present study.

case, it is quite clear that currently available models are far from perfect, and more detailed simulations are needed to extract all the possible information on the Galactic DM halo from the Sgr Stream, as more (and more accurate) observational constraints become available. For example, Fellhauer et al. (2006) interpreted the bifurcation of the trailing arm giving rise to the A and B branches considered here as produced by the precession between two subsequent orbits. As the implied amount of precession is relatively small, this, in turn, requires that the potential felt by Sgr should be nearly spherical. However the similarity between the two branches (in terms of distance, kinematics and stellar content) led Yanny et al. (2009) to suggest that in fact the two branches are composed by stars lost at the same epoch, i.e. they are in the same orbital phase. In this case the separation between the two branches would not be related to orbital precession and would have nothing to say about the shape of the potential. In their recent analysis, Niederste-Ostholt et al. (2010) adopt the same view of Yanny et al. (2009)[13].

In the present contribution we provide very accurate distance estimates along the northern branches of the Sgr Stream as powerful constraints for future generations of Sgr disruption models that will include effects like halo triaxiality, dynamical friction, time-evolving Galactic potential etc. In this section we discuss our findings in comparisons with the predictions of the three models by Law et al. (2005, L05 hereafter), just to show how powerful accurate distance constraints can be in distinguishing between different models (some examples of such comparisons have already been presented in § 4.3.1 and Fig. 4.12). One of the main aims of the studies by L05 and Johnston et al. (2005), was to use the existing observations on the Sgr Stream to constrain the shape of the Galactic halo. For this reason the three models they provide[14] describe the final state of the evolution of a realistic progenitor of Sgr after a few orbits within a Galactic potential having a *prolate*, *spherical*, or *oblate* DM halo. For sake of semplicity, in the following we will refer to these models as to the Oblate (O), Spherical (S) and Prolate (P) models, respectively. In all the models, each particle is flagged according to the peri-galactic passage in wich it become unbound from the main body of the galaxy. Here we refer to stars still bound or lost during the current peri-galactic passage as having $p = 0$; $p = -1, -2, -3, -4$ refers to particles lost one, two, three and four peri-galactic passages ago, respectively. $p = 0$ stars are out of the range accessible with the fields considered here, according to the L05 models. When we speak of "young" and "old" wraps of the Stream we refer to

[13] See also the discussion in Law & Majewski (2010).

[14] Publicly available at `http://www.astro.virginia.edu/ srm4n/Sgr`

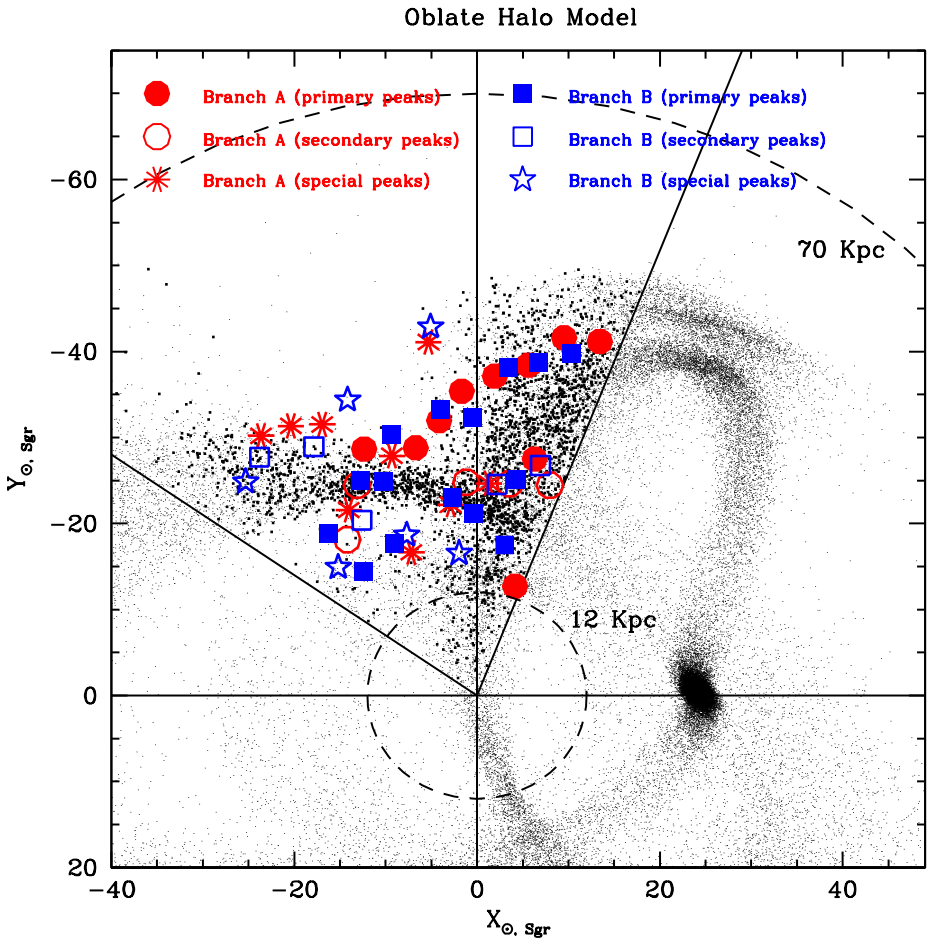

Figure 4.19: Comparison between the positions of the observed RC peaks and the predictions of Law et al.'s (2005) N-body model of the disruption of Sgr within an *oblate* DM halo in the $X_{\odot,Sgr}$ vs. $Y_{\odot,Sgr}$ plane (i.e. the approximate plane of Sgr orbit seen face-on). Heavier dots indicate model particles enclosed in our FoVs cones. To be consistent with Law et al. (2005) we converted our differential distances into absolute ones by assuming a true distance modulus of 16.90 for the main body of Sgr.

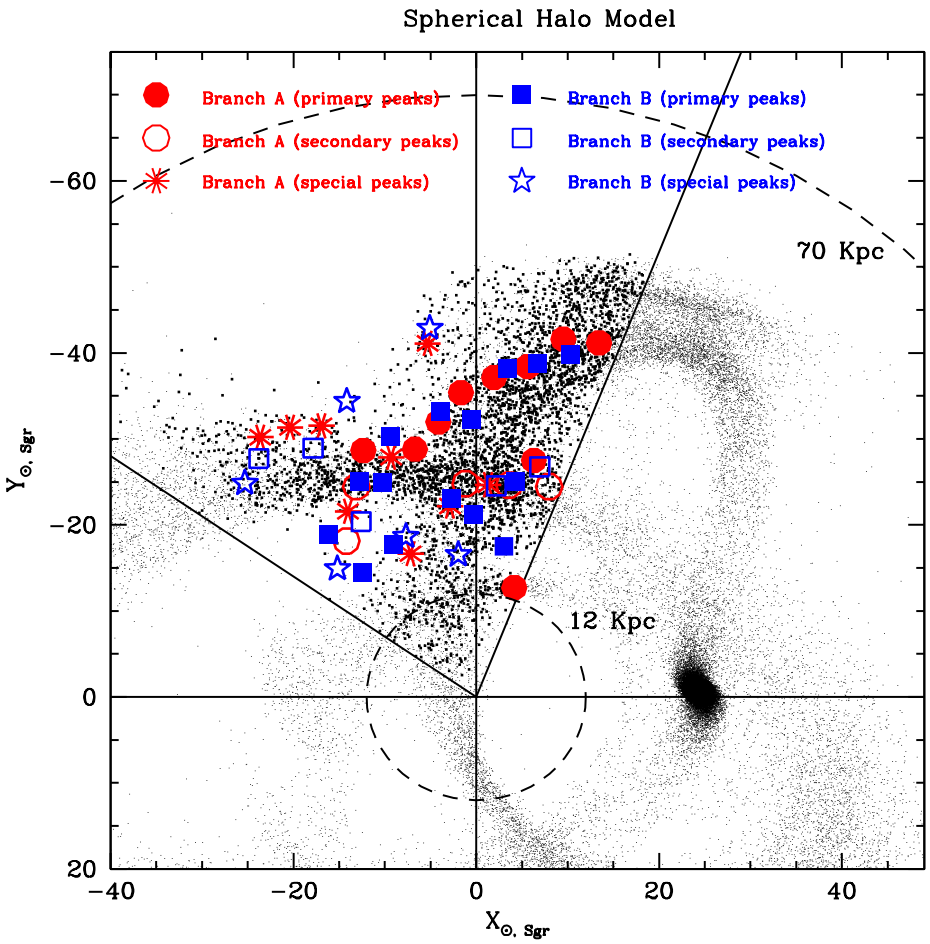

Figure 4.20: The same as Fig. 4.19, but for a N-body model within a *spherical* DM halo.

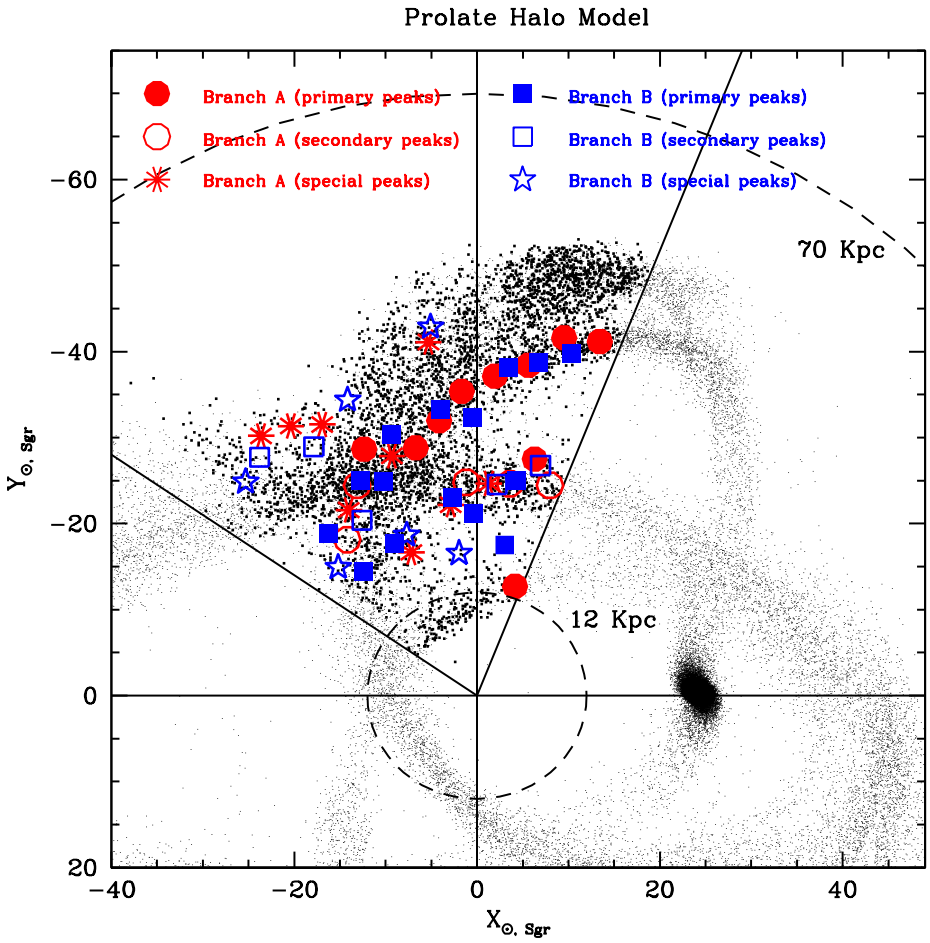

Figure 4.21: The same as Fig. 4.19 and 4.20, but for a N-body model within a *prolate* DM halo.

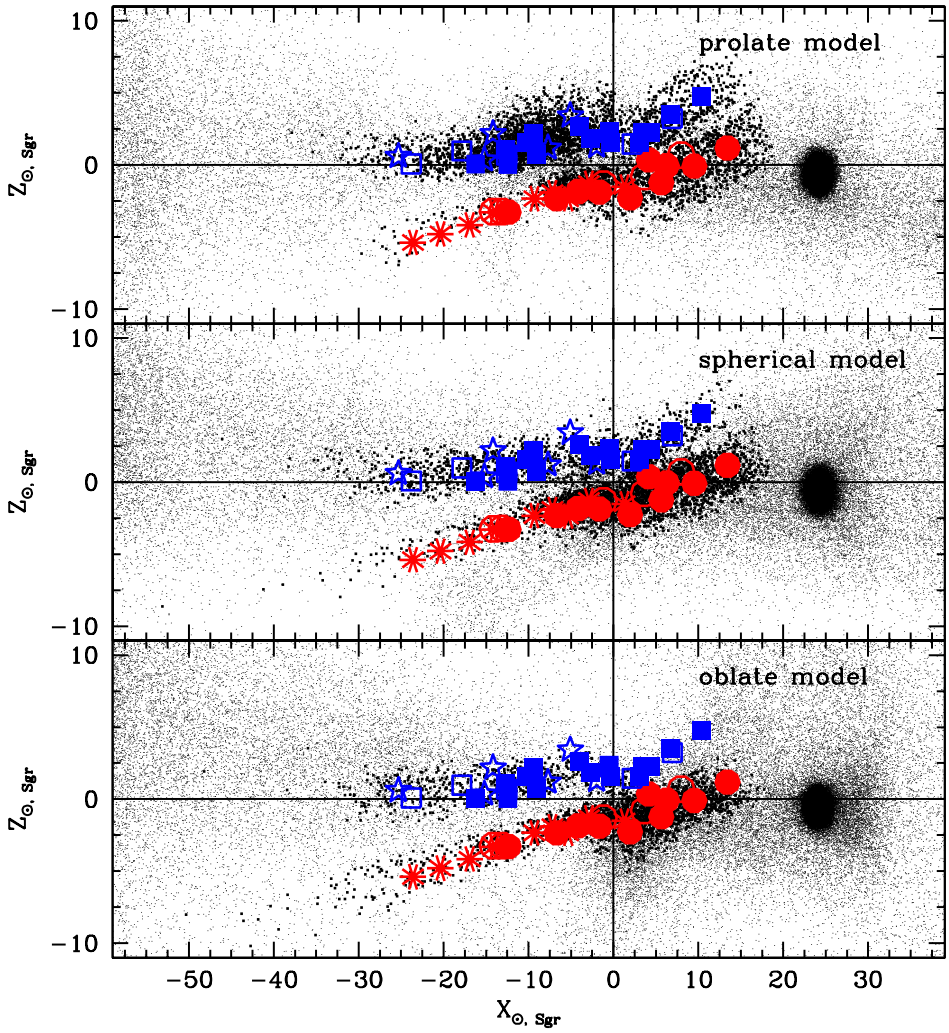

Figure 4.22: Comparison of observed peaks positions with Law et al.'s (2005) models in the $X_{\odot,Sgr}$ vs. $Z_{\odot,Sgr}$ plane (i.e. perpendicular to the orbital plane of Sgr, that is seen edge-on). The symbols are the same as in Fig. 4.19.

portions of the Stream whose population is dominated by particles lost in the most recent or less recent peri-galactic passages, respectively, on an age-scale encompassing the last ~ 5 orbits, i.e. $\sim 3-4$ Gyr.
In Figg. 4.19, 4.20 and 4.21 the three models are compared with the positions of the observed RC peaks in the $X_{\odot,Sgr}$ vs. $Y_{\odot,Sgr}$ plane[15], as in Fig. 4.10, above. It is immediately apparent from Fig. 4.19 that the trend traced by our primary peaks rules out the O model, that fails to reproduce the most prominent branch of the Stream seen in SDSS data, i.e. the portion of the leading arm descending from the North Galactic Pole (while there is some agreement for the - putative - nearby portion of the trailing arm). The case of the spherical model is similar, even if the disagreement between observations and model prediction is less severe (Fig. 4.20).
The comparison with the prolate model is the most interesting and we take it also as the occasion to describe the trends found in our data in a deeper detail. It should be stressed that, in the following, we interpret the coherent structures we have detected using this specific model as a guideline. For an example of a different interpretation see § 4.6.3, below. There are several worth noticing features in Fig. 4.21:

1. For $X_{\odot,Sgr} > -7$ kpc the agreement between the positions of our primary branch-A peaks and the portion of the leading arm going from $(X,Y) \simeq (16,-40)$[16] to $(X,Y) \simeq (-7,-28)$ is *excellent*. Also primary branch-B peaks follow the same trend thus confirming that the two structures lie at *the same distance* (see also Fig. 4.12, and Belokurov et al., 2006; Fellhauer et al., 2006; Yanny et al., 2009). According to the considered model, this part of the leading arm is dominated by $p = -1$ particles up to $X_{\odot,Sgr} \simeq 0$, and by a mix of $p = -2$ and $p = -3$ particles for $X_{\odot,Sgr} < 0$.

2. Several detections seem to extend the path of the arm down to (X,Y)=(-15,-15), possibly suggesting a slightly less elongated shape of the arm with respect to the model predictions. The coherence of the structure is less clear in this region: the model predicts that various wraps cross here and this may be source of some confusion.

3. The model predicts the presence of a more ancient (mostly populated by $p = -2$ and $p = -3$ particles) and wider wrap running nearly parallel to the portion of the leading arm described above, but behind it. This structure has been detected in branch-B, where we obtain two flag=3

[15] For brevity, in the following we will drop the $\odot,Sgr$ index any time we found this convenient; $X_{\odot,Sgr}$, $Y_{\odot,Sgr}$ and X, Y are interchangeable. For the same reason, the values of X, Y must be always intended as expressed in kpc, even if not explicitly stated.

[16] In the following we drop the $\odot,Sgr$ indices, for brevity. The unity is always kpc.

points, at $(X,Y) \sim (-5,-44)$, in coincidence with a branch-A detection, and at $(X,Y) \sim (-14,-35)$. These points appear to trace the outer edge of this wrap , as depicted by the considered model. On the other hand, there is no detection (in any branch) for $X > 0$, i.e. where the detection of the second wrap should be easier, according to the model, as the separation from the inner wrap increase with X and the feature is denser and narrower in that region. This lack of detection seems confirmed by the independent results of Belokurov et al. (2006), that, however, detect the most distant wrap at $X < 0$ only in the direction of Branch A. To have a deeper insight into this problem in Fig. 4.23 we provide a direct comparison between observations and model at the LF level, as done in Fig.. 4.11. Here we compare the observed LF of the F1A, F2A and F3A fields with the LFs obtained from the model in the considered *los* for particles lost one, two, three and four peri-galactics ago. From the upper-right panel it is clear that the dense $X > 0$ part of the outer wrap, produced by $p = -2$ particles in the model, has no counterpart in the observed LFs and would be easily detected if actually there. On the other hand the sum of the relics having $p = -1,-3$, and $p = -4$ provide a satisfactory match to all the observed peaks. This suggest that there is a real mismatch between the L05 P model predictions and our observations in this part of the halo. We note that the spherical model suffer from the same problem, while the oblate model do not predict a strong signal at that position, but it fails to match all the observations at $X < 0$ for this wrap.

4. A coherent series of detections lying at nearly constant $Y \sim 25$ kpc, traced from $X \sim 8$ to $X \sim -14$ in both branches, traces a filamentary structure that is identified here for the first time. Isolated detections with M giants and RR Lyrae were previously reported at $\Lambda \sim 295^\circ$ (Ivezić et al., 2000; Majewski et al., 2003; Vivas & Zinn, 2006). This feature matches quite well a wrap of the trailing arm that is present in all the L05 models; it can be appreciated from Fig. 4.12 and Fig. 4.21 that the agreement with the P model is very good. For $X < -14$ however the positions of the peaks do not trace the model prediction anymore. This apparent discontinuity along this branch cannot be (only) due to the distance effects discussed in § 4.2.3 as the distance is expected to increase and the sensitivity of the method should increase accordingly. Moreover we are able to detect peaks both more and less distant than the position predicted by the model along these *los*. This feature has no counterpart in the triaxial halo model discussed in § 4.6.3, below. It is clear that additional information is

needed to understand better the nature of this structure, as, for example, the kinematics of member stars.

5. There are a primary and a tertiary branch-B detections, plus one tertiary branch-A detections, tracing a feeble (but coherent) spur from an ancient ($p = -3, -4$) wrap, predicted by the model to arch between $(X,Y) \sim (-10,-15)$ and $(X,Y) \sim (-3,-22)$. As far as we know this is the first detection of this nearby portion of the Stream. A couple of primary branch-B detection (and a tertiary Branch-A one) may trace similar substructures on the near side of the constant distant portion of the trailing arm (see § 4.6.3 for an alternative interpretation).

6. There are a couple of other cases of slight distance mismatch between branch-A and branch-B detections, occurring, however in the region around $(X,Y) \sim (-10,-25)$ where different wraps of the Stream cross each other and it may be really difficult to disentangle the various contribution based on distances alone. A more interesting case is provided by the two pairs of detections around $(X,Y) \sim (-23,-30)$, a region where the model predicts only feeble structures and branch-B detections are clearly more nearby than branch-A ones. It is intriguing to note that the few particles of the model lying in this region are not uniformly distributed but appear to form two approximately parallel tiny bridges that reasonably reproduce the observed pattern. Also in this case this is the first detection of such structures.

7. Both the P and S models by L05 predicts the presence of a pretty dense and narrow wrap composed by $p = -3$ and $p = -4$ particles crossing the accessible range of the X,Y plane from $(X,Y) \sim (-7,-7)$ to $(X,Y) \sim (5,-12)$, where it emerges from the $d < 12$ kpc zone of insensitivity of our method (the triaxial model briefly discussed in § 4.6.3 also display a similar feature). Here we have a primary detection from the LF of F1A, that currently is the first detection of this nearby wrap of the leading arm[17]. A detailed exploration of the $d < 12$ kpc zone would require a different kind of analysis, hence it is postponed to a future contribution.

8. Two Branch-B detections, located at $(X,Y) \sim (-3,-16)$ and $(X,Y) \sim (+3,-18)$, F5B and F2B, respectively, do not seem to match any significant structure of the spherical and prolate L05 models; the primary

[17] While the distinction between *leading* and *trailing* arms is easy and sensible for particles lost in the latest two peri-galactic passages, it becomes increasingly blurred for Stream wraps dominated by more ancient relics, as a particle can reach the same position in these parts of the Stream both from the leading and from the trailing sides of the tidal tails.

one (that with positive X) is marginally consistent with the part of the leading arm plunging toward the Sun of the oblate model (but see § 4.6.3, below). As anticipated in § 4.4.1, their position [(RA,Dec)=($195^\circ, +16^\circ$, $d \sim 18$ kpc, and (RA,Dec)=($190^\circ, +18.5^\circ$, $d \sim 19.5$ kpc, respectively] is fully compatible with the outer fringes (i.e. the high Galactic latitude edge) of the nearby overdensity S297+63-20.5, discovered by Newberg et al. (2002) and discussed in detail in Newberg et al. (2007). It is unclear why we do not detect the structure in other adjacent fields, or in the corresponding Branch A fields. This may be due to the intrinsic weakness of the RC signal from these nearby features, or it may reflect a high degree of complexity of the sub-structures, as suggested in the analysis by Keller et al. (2009); Vivas et al. (2008). Newberg et al. (2007) provided positional and kinematical evidences arguing against the association of S297+63-20.5 with the Sgr Stream, that was originally proposed by Martínez-Delgado et al. (2007) and cannot be completely ruled out at the present stage (see also the discussion in Law & Majewski, 2010). However Fig. 4.21 provide further support to the conclusions by Newberg et al. (2007): the peaks detected here do not present any continuity with the main branches of the leading and trailing arms of the Stream as traced in the present analysis (but see also § 4.6.3, below). Our data suggest that the leading arm crosses the Galactic plane at ~ 10 kpc from the Sun, toward the Anticenter, in agreement with Newberg et al. (2007) and Seabroke et al. (2008). On the other hand, the identification of S297+63-20.5 with the Virgo Stellar Stream (VSS, Duffau et al., 2006; Vivas et al., 2008) seems likely, while the relationship between VSS and the Virgo Over Density (VOD, Newberg et al., 2007; Keller et al., 2009) is less certain (see Newberg et al., 2007; Keller, 2009b). We are currently following up these possible detections of S297+63-20.5/VSS in F5B and F6B (also looking for the structure at lower latitudes). If confirmed, they would provide the first detection of RC stars in these structures, in analogy with the cases of Boo III discussed in Correnti et al. (2009). RC stars may provide new insights on the nature of complex series of structures recently identified in the direction of Virgo (Keller et al., 2009; Keller, 2009b).

All the features and correlations with the P model described above can be seen even more clearly and directly in Fig. 4.12, that provides the most natural way to compare our measures with models. For example, the match between two weak model structures described at point 6, above, and our detections can be very clearly appreciated in that plot, at $230^\circ < \Lambda < 245^\circ$ and $d \simeq 37$ kpc. The

linear trend of increasing distance with decreasing Λ of the two parallel sets of observed points is very nicely matched by corresponding filaments of particles in the model. Fig. 4.22 shows that the overall morphology of the three models is remarkably similar in the $X_{\odot,Sgr}$ vs $Z_{\odot,Sgr}$ plane and reproduce the general trends of the data (except for the Oblate model, that predicts a total lack of particles for branch-B detections at $X_{\odot,Sgr} > 0$, at odds with observations). A more detailed analysis in this plane is beyond the scope of the present paper. On the other hand, we must conclude, from the results summarized above, that the *prolate* model by Law et al. (2005) is the one (among those considered here) providing the best match to the positional data considered here. It should be stressed that with this *we do not intend to say that a prolate halo model is favoured by our data*, as the comparison was limited to just three very specific models that are already known to not be able to fit all the positional and kinematical observational constraints available (Law et al., 2009).
In particular it should be recalled that the available radial velocities of Stream stars seems to favor prolate models (Helmi, 2004), while the angular precession of the leading arm with respect to the trailing arm favor spherical or slightly oblate models (L05, Johnston et al., 2005; Newberg et al., 2007; Prior et al., 2009b, and references therein). We simply note that any future model intended to fit all the observed characteristic of the Sgr Stream must have a spatial structure *very* similar to that of the *prolate* model by Law et al. (2005), at least in the portion of space sampled by our study, unless an alternative origin is assumed for the $d \sim 25$ kpc structure we tentatively interpreted as the trailing arm.

4.6.1 Trends of depth as a function of orbital azimuth

In line with the above discussion, in Fig. 4.24 we compare the FWHM along the *los* described in § 4.3.4 with those measured from the distribution of particles of the Prolate model of L05, along the same *los* . The following discussion is mainly intended to illustrate the possible use of the derived FWHM. It should be considered that there are additional sources of uncertainty affecting this comparison, associated with the the measure of FWHM in models. For example, the measured width depend on the actual number of particles of the model, the limited number of particle may lead to underestimates of the actual width. This expected effect is clearly confirmed in Fig. 4.24, where observed FWHM are always equal or larger than their model couterparts. The disentanglement of overlapping structure may be also problematic, as it is unavoidably performed in different ways in the observed

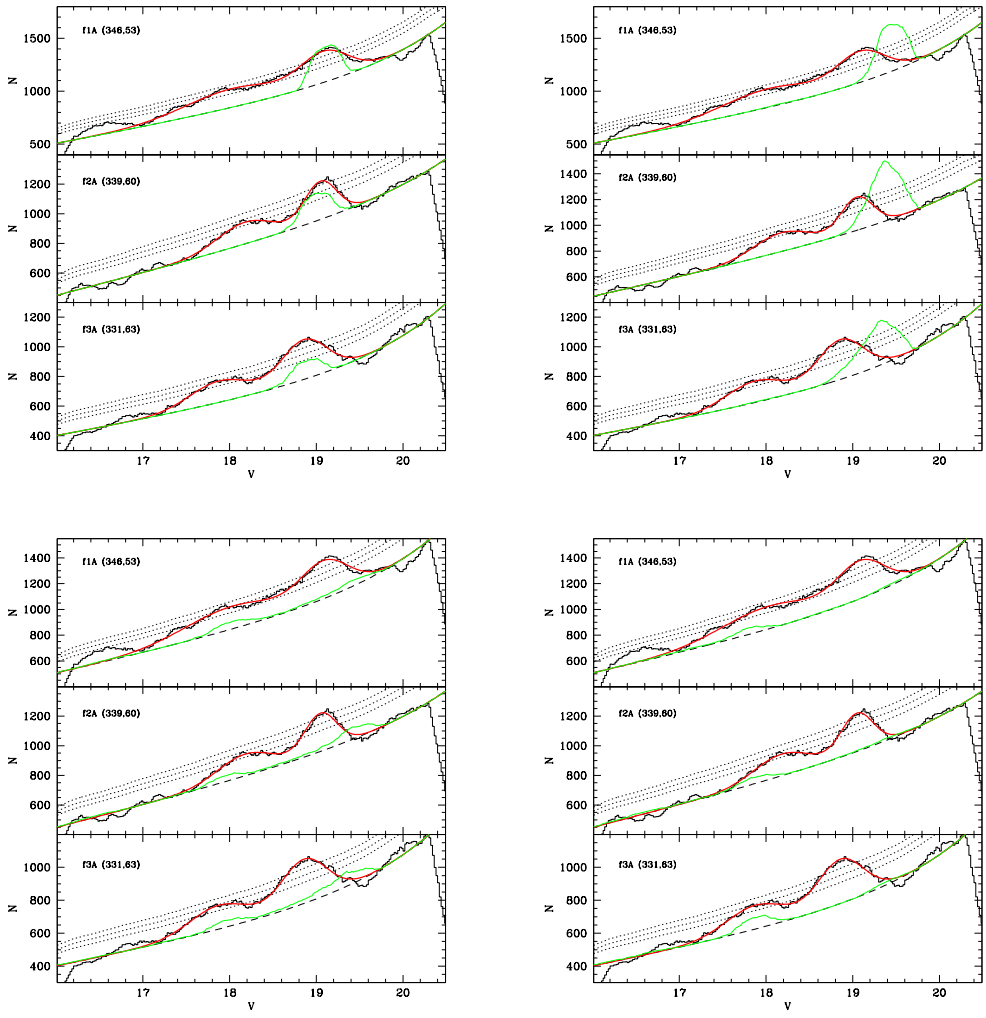

Figure 4.23: Comparison of the observed LFs in the field F1A, F2A, F3A with the synthetic LF obtained by adding the (arbitrarily normalized) *los* histogram from the prolate N-body model (as in Fig. 4.11 above) to the best-fit background model of the considered field. Each of the four (triple) panels report the synthetic LF including only N-Body debris stripped from the main body one, two, three or four orbits ago, going from the upper left, to the upper right, to the lower left and to the lower right panels, respectively.

LFs and in the N-body models.
To minimize the possible ambiguities associated with the collapse of complex structures along the *los* into a single FWHM measure (see § 4.3), especially in regions where different wraps cross one another, in Fig. 4.24 we limit our comparison to $X > -10$ kpc peaks tracing the two main wraps (leading and trailing arms) that are 30 kpc apart at $\Lambda_{Sgr} = 290^\circ$ and cross each other at $\Lambda_{Sgr} = 265^\circ$, and we consider only primary and secondary peaks. The most interesting and sensible comparison is between the trends of the FWHM as a function of orbital azimuth. The upper panels of Fig. 4.24 show that the observed and predicted trends for the leading arm are indeed similar, both in direction and in amplitude, for both branches. The agreement of the absolute values of the FWHM is also satisfying (within a factor of ~ 2), with four Branch A and one Branch B detections closely matching the model predictions. The FWHM of the considered detections from F1A and F3A give some reason of concern, as they break the continuity of the observed trend: this may suggest that there may be some unresolved structure in these peaks. Alternatively we have to accept variations of a factor of ~ 2 as due to the uncertainty inherent to the adopted method of estimating FWHM. The overall agreement is reasonable also for the putative trailing arm.
It is interesting to note that the different trends observed in the two branches of the leading arm are reproduced by the P model that do not present any bifurcation (see also Fig. 4.25, for a similar behaviour in the Λ vs. density trend in the leading arm).

4.6.2 Trends of density as a function of orbital azimuth

In strict analogy with the analysis described in the previous subsection, in Fig. 4.25 we present the comparison of the observed and predicted trends of the stellar density (see § 4.3.3) as a function of Λ. The measured density is compared with the density of particles in the same wrap of the P model. The density scale of the model has been multiplied by the arbitrary factor 2.5, to achieve a reasonable normalization with the observed values. As in § 4.6.1 the comparison presented is just intended as illustrative of the possible use of these numbers, and it is limited to the cleanest portions of the leading and trailing arms, at $X > -10$ kpc.

For the leading arm the match between the overall observations and the models is acceptable, in particular for the branch A. The highly discrepant point at $\Lambda \sim 263^\circ$ is associated with an especially complex LF model, with three overlapping peaks (F5B): for this reason we are inclined to ascribe the discrepancy to an erroneous density estimate.

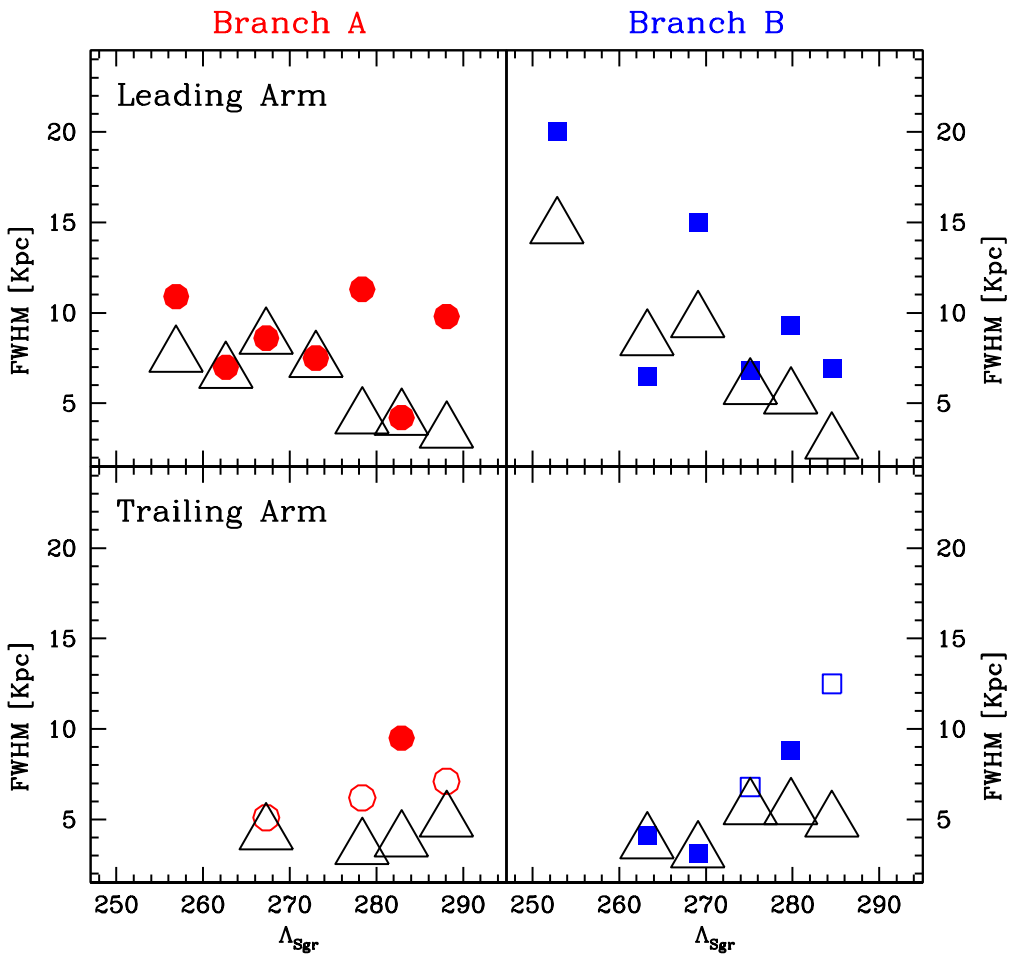

Figure 4.24: Comparison between the trends with Λ_{Sgr} of the observed FWHM along the *los* (the same symbols as Figg. 4.19, 4.20, 4.21, above, and the predictions of the Prolate model by L05, open triangles). The comparison is limited to the *los* from F1 to F7 (i.e., those providing the cleanest tracing of the leading and trailing arms). The upper row of panels refers to detections in the leading arm, the lower row to detections in the trailing arm. The left and right rows of panels refer to branch A and branch B, respectively. The field number increases (from F1 to F7) from right to left, as in Fig. 4.12 and Figg. 4.19, 4.20, 4.21.

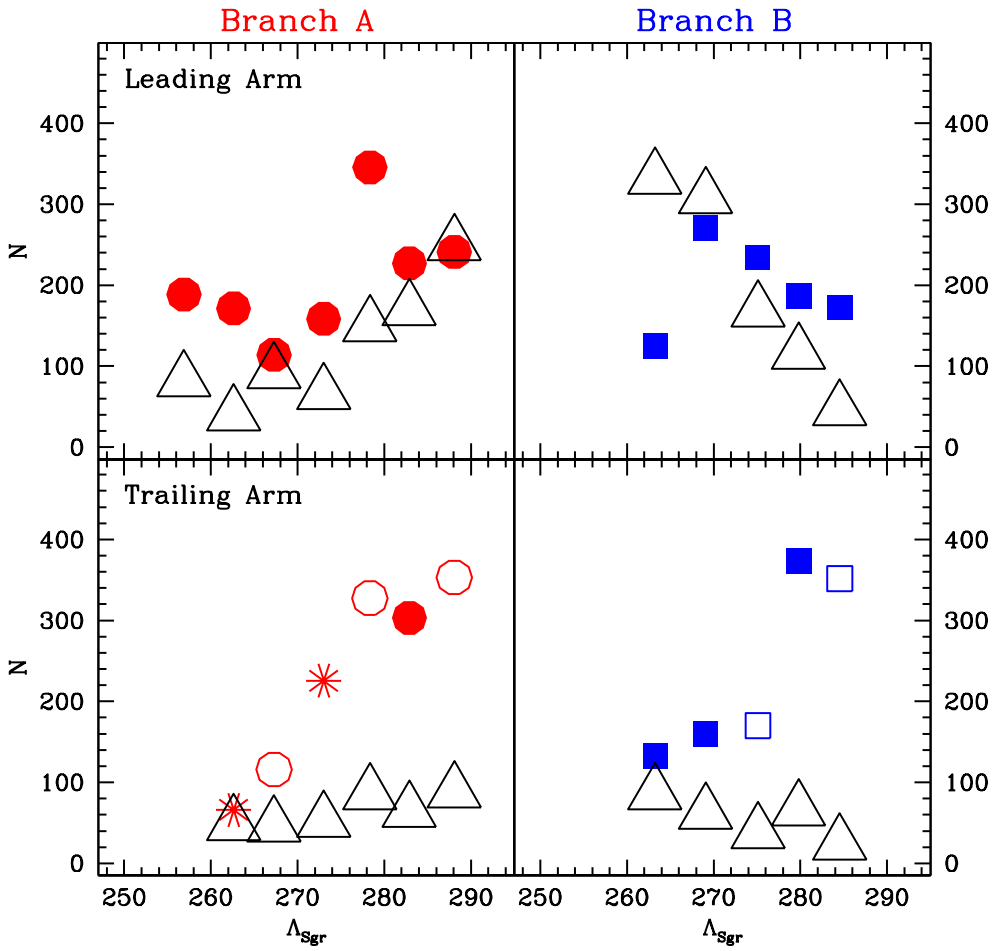

Figure 4.25: The same as Fig. 4.24 for the density of RC stars as a function of Λ. An arbitrary normalization factor of 2.5 is applied to all the density values from the theoretical model.

On the other hand, while the model predicts low or even negative gradients of density with increasing Λ, the observations show a very strong positive gradient, similar in both branches[18]. This is an obvious example of the kind of constraints that can be achieved with these data: in principle, any fully successful model of the disruption of Sgr must also reproduce a density gradient similar to the observed one. However it has to be taken into account that the available models are intended to describe the dark matter halo in which the baryonic part of the galaxy is embedded. While, for example, stars and DM particles in the Stream should not greatly differ in their kinematical and positional properties, their density would follow the same trends only if mass strictly follows light also in tidal tails, that is very unlikely to be the case (see Peñarrubia et al., 2008, and references therein)

4.6.3 The triaxial model by Law & Majewski 2010

When the present manuscript was ready for submission, a preprint was posted (Law & Majewski, 2010) where, following up the preliminary analysis by Law et al. (2009), a new N-body model of the disruption of Sgr within a triaxial Galactic potential, is shown to provide a reasonable match to most of the existing observational constraints. In particular, the new model reproduces the distance *vs.* Λ trend reported by Bel06 for the main wrap of the leading arm, the precession between the leading and trailing arms, and it matches the existing sets of kinematical measures. As said, it is far beyond the scope of the present analysis to find out which is the best available model. However it is worth to show the comparison between our results and this new model, for completeness and (above all) as a very instructive example of how the interpretation of observed features may depend on the considered model (see § 4.7 for discussion). From the inspection of Fig. 4.26 and Fig. 4.27 it can be concluded that the triaxial halo model provides a reasonable match to distance gradient of the main wrap of the leading arm, over the whole range of Λ covered by our data. This is not unexpected as the model is found to fit the observations by Bel06 in this regard, and we are in good agreement with these authors. The same is true for the sparse detections behind the main wrap, that were also found by Bel06. It is interesting to note that, similarly to the P and S models, the T models predicts a remarkable increase of the density of this wrap for $\Lambda > 275^\circ$ ($X > 0$) that is not observed, neither by us or by Bel06. Moreover the T model does not seem to display the narrow

[18] It has to be recalled that the bifurcation in two branches is an observed property of the main wrap of the leading arm. There is no reason to discuss other wraps as divided into two branches: here this is merely incidental, due to adopted distribution of the observed fields that were chosen to trace the bifurcation.

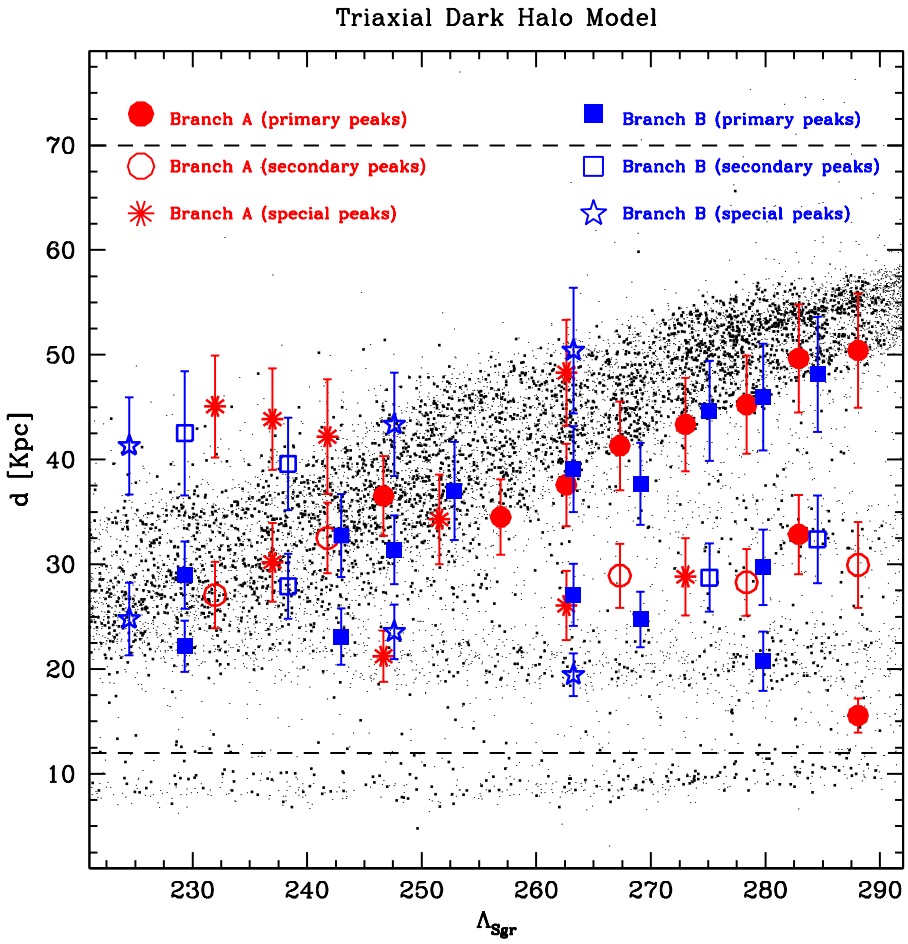

Figure 4.26: Comparison with the new "triaxial halo" (T) model by Law & Majewski (2010): distance vs. orbital azimuth. Symbols are the same as in Figg. 4.19, 4.20 and 4.21. Our measures have been rescaled to match the distance scale adopted by Law & Majewski (2010), that implies a distance to the main body of Sgr $d = 28$ kpc (i.e. $(m-M)_0 = 17.23$, instead of $(m-M)_0 = 16.90$, as adopted by L05).

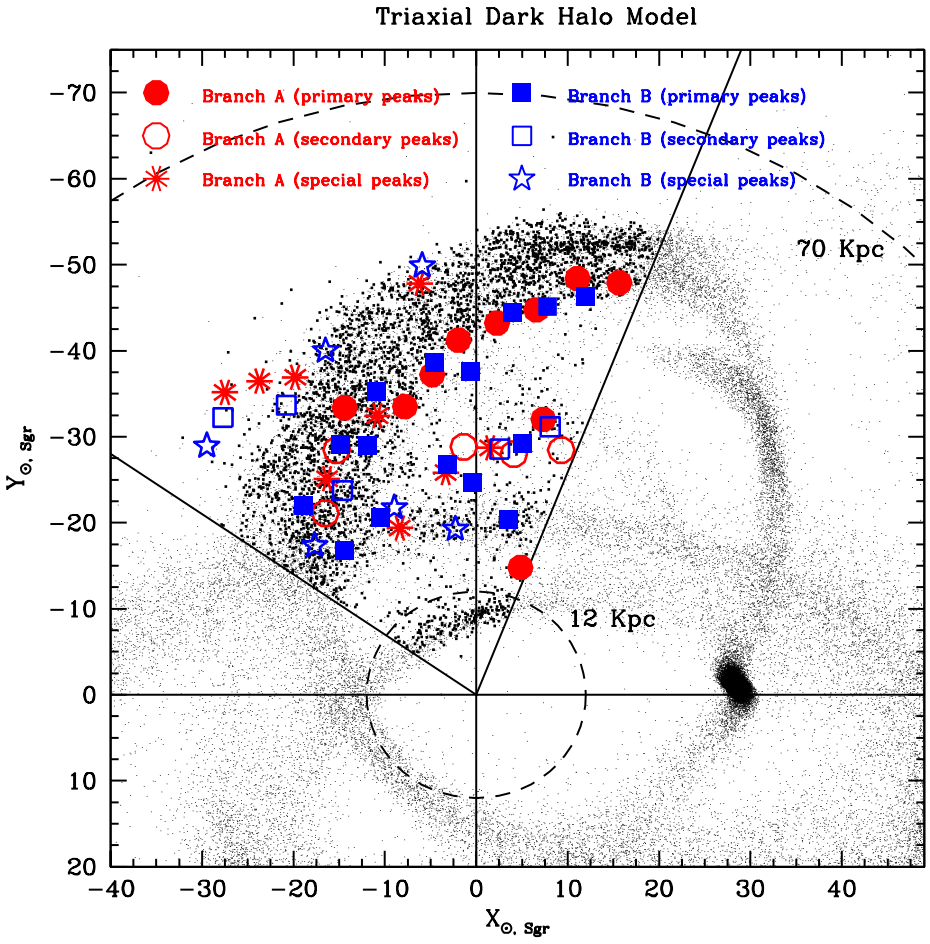

Figure 4.27: Comparison with the new "triaxial halo" (T) model by Law & Majewski (2010): the $X_{\odot,Sgr}$ vs. $Y_{\odot,Sgr}$ plane, with the same assumptions and symbols as Fig. 4.6.3.

and dense structure of the main wrap of the leading arm that in the P model appears to match so well our coherent set of primary detections in that region. We postpone a detailed comparison between the observed structures along the *los* and the predictions of the P and T model to a future contribution: here we limit the discussion to the main features of the models (i.e. trends of distance with orbital azimuth). The new model makes predictions very similar to those of the P and O models also regarding the nearest wrap of the Stream, running across the whole range of Λ sampled by our data.

The T model presents a very coherent narrow wrap of the trailing arm running at nearly constant $d \simeq 20$ kpc from $\Lambda \simeq 290^\circ$ to $\Lambda \simeq 250^\circ$, then it begins to bend gently toward $d \simeq 25$ kpc from $\Lambda \simeq 235^\circ$ where it crosses with the leading arm. This feature matches *very nicely* the nearby ($d \leq 25$ kpc) detections that we tentatively attributed to S297+63-20.5/VSS and to an ancient spur of the leading arm, in the comparison with the P model described in detail in § 4.6, above.

On the other hand, the coherent structure we detect from $\Lambda \simeq 260^\circ$ to $\Lambda \simeq 250^\circ$, that we interpreted as a wrap of the trailing arm, is not present in the T model. The same is true for the $d \geq 40$ kpc structures at $\Lambda \leq 245^\circ$. The orbital path of the simulated Sgr galaxy matches also these structures, so it is not excluded that they may correspond to very ancient wraps. However, it has to be noted that the T model is the remnant of the evolution of a Sgr progenitor for $\simeq 8$ orbits (not just ~ 4 as for S,O, and P) models, thus it should include wraps populated from more ancient stripping events than the S, O, and P models.

In conclusion, while the P model still appears to provide a more thorough match of the observed structures, the T model provides a promising alternative that deserve to be investigated in further detail. Not surprisingly, the mere comparison with our own (limited) data-set shows that both models need to be refined.

SECTION 4.7

Summary and conclusions

We have used RC stars to trace the long tidal tail of the Sgr dSph galaxy in the portion of the Northern sky sampled by the SDSS-DR6. Structures along the line-of-sight are identified as peaks in the (otherwise smoothly increasing) I and V LFs of colour-selected samples of candidate RC stars, from $\sim 5^\circ \times 5^\circ$ fields covering the whole extension of the two main branches (A and B) of

the Sgr Stream identified by Belokurov et al. (2006) in the same dataset. Any other part of the Stream in addition to these branches is expected to lie (approximately) in the same plane, i.e. it should be visible in the considered fields. The analysis has been focused to get the most accurate and reliable distances to all the wraps of the Stream that we were able to detect.
Many significant peaks were consistently found in both the LFs of several fields. The observed LFs were modeled as a series of Gauss curves (one for each peak) superposed to a polynomial accounting for the smooth fore/background population. For each significant peak we derived a purely differential estimate of its distance (with uncertainties $\leq 10\%$), an estimate of the FWHM along the *los* , and an estimate of the associated density of RC stars attributable to the considered structure. All the derived quantities are provided in Tab. 4.2 as powerful constraints for the new generations of models of the disruption of the progenitor of Sgr dSph within the Milky Way halo.
To illustrate the potential of our measures in that context we compared them with the three models made publicly available by Law et al. (2005). These provide a realistic realization of the present epoch configuration of particles that were originally bound to a progenitor similar to Sgr that was evolved for $\simeq 4$ orbital periods within a static Galactic potential with different degrees of flattenting (a spherical, oblate and prolate halo, respectively). The models (and in particular the Prolate halo one, that matches pretty well most of our observations) are also used as guidelines for the interpretation of our results. The great complexity of a structure like the Sgr Stream, multiply wrapped around the Galaxy, requires a process of convergency between models and observations: the latter must constraint models but the former are indispensable to re-conduce such a complexity to a single structure (see § 4.6.3).
Our technique resulted in higher-accuracy distance estimates with respect to previous studies, and demonstrated to be quite sensitive to feeble structures. However, the sensitivity is easily destroyed by contamination from Galactic sources: for these reasons we had to limit our survey to $b > 50^\circ$, while other (more abundant) tracers are able to follow the Stream down to $b > 30^\circ$. The overall agreement with previous analyses is good (see § 6.8). Finally, and most important, our method proved especially efficient in the detection of (relatively) nearby structures. In the following we summarize and briefly discuss the main conclusions of the present study, taking Fig. 4.12 and Fig. 4.21, as references.

- For $\Lambda > 255^\circ$ ($X > -10$ kpc) the leading arm of the Stream is cleanly and coherently detected in both branches, going from $d = 43$ kpc at $\Lambda \simeq 290^\circ$ to

$d = 30$ kpc at $\Lambda \simeq 255^\circ$. This is in full agreement with the results obtained with other tracers (Newberg et al., 2007; Niederste-Ostholt et al., 2010). This portion of the leading arm is the most unambiguous and robustly constrained.

- In the same range of Λ (and X) a remarkably coherent structure is also very clearly detected at nearly constant distance from us, $d \simeq 25$ kpc. According to the S and P models by L05 this can be interpreted as a wrap of the trailing arm, while it has no obvious counterpart in the recently presented T model (Law & Majewski, 2010). The P model matches the observed structure very well. As said, previous detections of this wrap were previously reported only around $\Lambda = 295^\circ$ (see Majewski et al., 2003, for discussion and references).

- The comparison with the L05 models strongly suggest that the run of the relative distance as a function of Λ of the two wraps described above has a strong power in discriminating between different models of the Stream. In particular the S and O models by L05 clearly fails to reproduce the observed trends. On the other hand the P model reproduces the trend nearly perfectly.

- Weak detections of a further, more distant wrap (running parallel to the leading arm, in the same range of Λ as above) were also obtained. These support similar results by Belokurov et al. (2006). An enhancement of the density of this wrap at $\Lambda > 275^\circ$, predicted by the S, P and T models, seems to be excluded by the present analysis (in agreement with Bel06).

- Turning to the $\Lambda < 255^\circ$ ($X < -10$ kpc) portion of the survey, this is characterized by a very complex structure, partly due to the crossing of multiple wraps predicted to occur in this region by all the models. Hence the interpretation of these structure is less straightforward, and must be considered as tentative. However, the P model appear to provide a reasonable match to all the detections in this region: for these reason we adopt it as a guideline for our best-effort interpretation of the data (see § 4.6.3 for an alternative view).

- The leading arm seems to be traced beyond $\Lambda \simeq 255^\circ$, continuing its trend of linear decrease of its distance down to $d \simeq 20$ kpc at $\Lambda \simeq 220^\circ$. Extrapolating from the observed trend one would expect the arm to cross the Galactic disc at ~ 10 kpc from the Sun, in agreement with the conclusions by Newberg et al. (2007); Seabroke et al. (2008); Law & Majewski (2010). The degree of coherence of the detections of this portion

of the leading arm is lower, suggesting the possible presence of further (unresolved) substructure or due to higher uncertainties associated to weaker and overlapped structures .

- In the same region, the continuation of the trailing arm is coherently traced where predicted by the P model up to $\Lambda > 240^\circ$ ($X > -15$ kpc). For $\Lambda < 235^\circ$, in particular, we lack any detection corresponding to the well defined structure predicted by the model (the same is true for the T model). On the other hand, coherent detections are obtained *behind* the main wrap of the trailing arm as predicted by the P model for $\Lambda < 240^\circ$. These detections may indicate a different shape for that portion of the trailing arm. However, as discussed above, they match two more feeble structures running parallel to the main arm. It is obvious that the P model is not adequate to fit all our observations, in spite of the good overall match.

- The most nearby detections are the more difficult to be firmly interpreted. However the single primary detection at $d \simeq 13$ kpc and $\lambda \simeq 287^\circ$ (just beyond the $d \leq 12$ kpc "zone of avoidance" of our thechnique) matches the prediction of all the three L05 models, as well as for the model by Law & Majewski (2010). For this reason we are quite confident to have detected for the first time the nearest wrap of the leading arm. We are currently following up this finding, to check if the predicted $d \sim 10$ kpc wrap can be detected also in other *los* .

- The three detections at $d \sim 20$ kpc and $\lambda \simeq 245^\circ$ are matched by a spur of the P model. The two detections at $d \simeq 18$ kpc and $\lambda > 260^\circ$ have been tentatively ascribed to the S297+63-20.5/VSS overdensity. The T model matches very well *all* of these detections with a single narrow wrap of the Sgr trailing arm. However Law & Majewski (2010) confirm that the kinematic predicted by their model toward VSS is markedly different from what observed by Duffau et al. (2006) and Newberg et al. (2007).

- The overall trends of FWHM along the *los* as a function of Λ of the P model provide a reasonable match to our primary detections of the leading arm. It is especially interesting to note that the model reproduces the different trends encountered in the two branches, even if it does not produce the observed bifurcation. This seems to provide further support to the view (adopted by Yanny et al., 2009; Niederste-Ostholt et al., 2010) that branch A and branch B are substructures within the same wrap of the Stream, and not different wraps as proposed by Fellhauer et al.

(2006). However, a limited set of tests performed on intra-branches fields suggests that the bifurcation in the Dec direction shown by Belokurov et al. (2006) is real. Probably a deeper, thorough and independent analysis of the Dec structure of this wrap of the Stream is deserved (see Law & Majewski, 2010, for possible alternative explanations).

- The observed trends of density as a function of RA along the leading arm (branches A and B) are in fair agreement with those by Niederste-Ostholt et al. (2010). Our estimates of the total luminosity per kpc at any given RA are lower than their by a factor of $\sim 4-5$.
- Kinematical follow up of the newly identified structures is clearly urged. Carrell & Wilhelm (2010) recently demonstrated that this can be carried on using exactly the same tracer stars, i.e. RC stars.

SECTION 4.8

Appendix - The LFs of Control Fields

To verify empirically that the peaks we interpret as due to intersections of the condidered *los* with Stream wraps, we have inspected all the colour-selected LFs of the Control Fields described in § 4.2. The overall conclusion is that there is nothing similar to the peaks we observe in the LF of our on-Stream fields in generic Galactic fields at similar distances from the plane and the center of the Galaxy.
In Fig. 4.28 we show various examples: the LFs of six on-Stream fields (continuous lines) are compared to the LFs of their corresponding CFs (dotted lines, see Fig. 4.1). The best-fit models for the on-Stream LFs, together with the background and the 3σ levels are also reported, using the same symbols as in § 4.3 and § 4.4, above. The two LFs are normalized by the ratio of the sampled areas, but any other reasonable normalization (for example, by the ratio between the number of stars that fall inside our colour selection) does not significantly change the results.
The shapes of the LFs are very similar in the range not affected by the peaks associated with the Stream, as already observed when we have done the same comparison in the main body (Fig. 4.6). It is quite clear that peaks attributed to the Sgr Stream are completely lacking in the LFs of Control Fields. It is also reassuring to note that the models for the LFs of the contaminating back/foreground population we have adopted for the on-Stream fields provide a good description also of the CF LFs, at least out to $V \simeq 18.5$. Beyond this

limit it is quite clear that in the on-Stream fields there is an additional source of contamination, that has to be ascribed to RGB, SGB and MS stars from the Stream population itself, as discussed in § 4.2.1. This provides further support to the idea that the adopted approach of fitting the back/foreground component directly on on-Stream LFs is the most effective way to get rid of this kind of self-containation from other species of Stream stars, that would not have been possible if we merely subtracted the CF LFs to the on-Stream ones. In the lower right panel we present the case of F15A, discussed in § 4.4.1. It is interesting to note the great similarity between the two considered LFs for this field, where we do not detected any signal from the Stream, and therefore are expected to be (both) dominated by the generic halo/thick disc Galactic population.

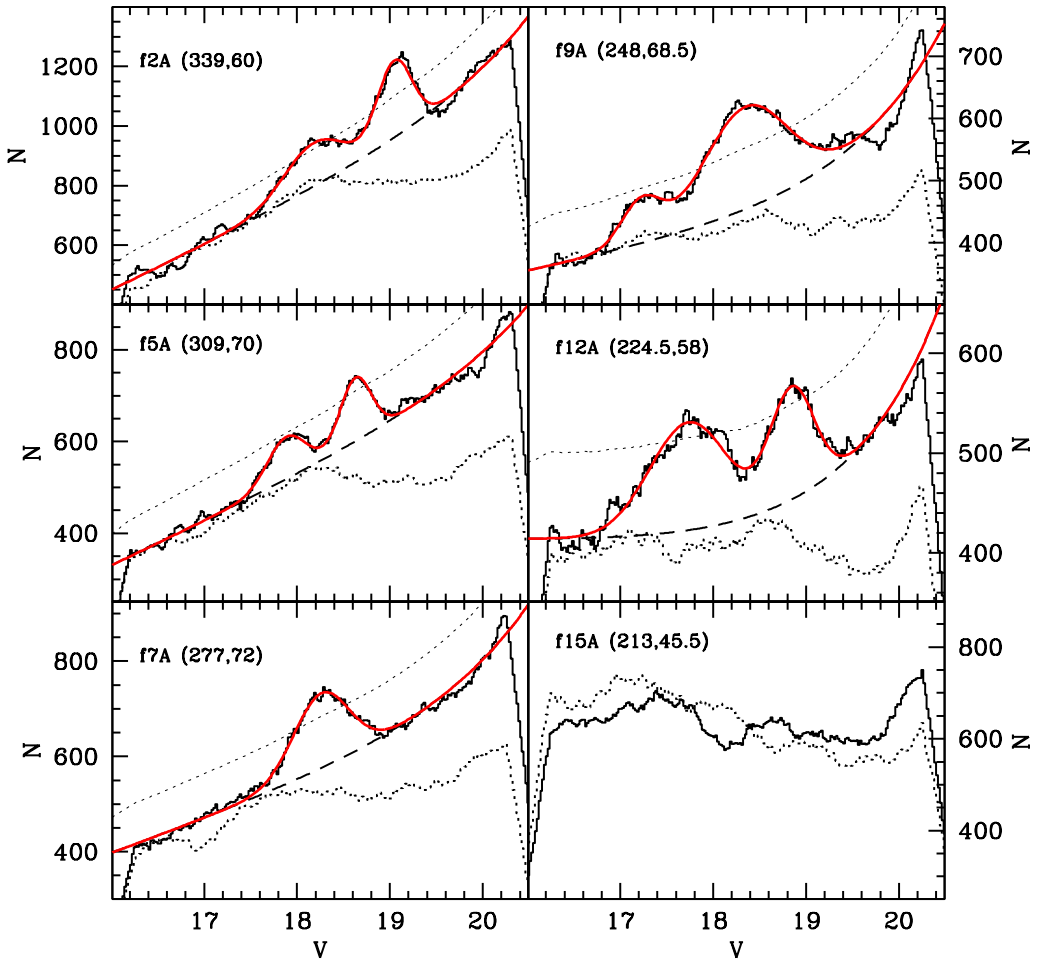

Figure 4.28: Comparison between a sample of the on-Stream LFs studied in this paper (continuous histogram; best-fit model in red) and the LF of the corresponding Control Fields.

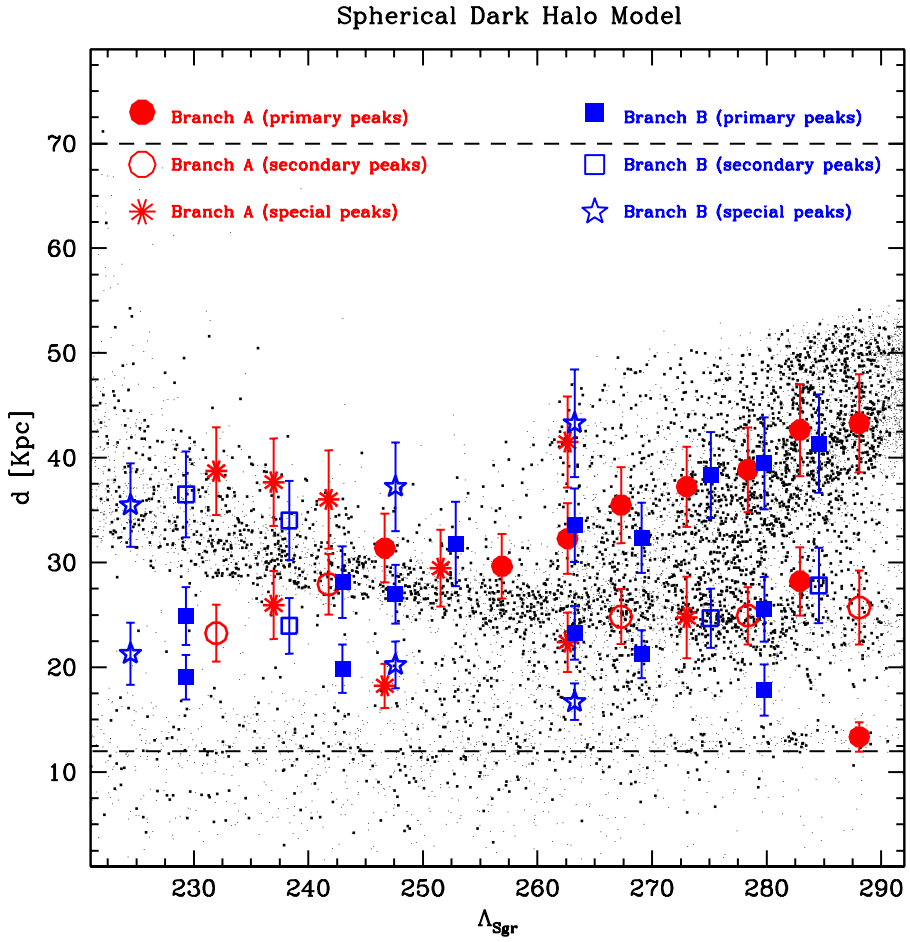

Figure 4.29: Distribution of the primary (red filled circles - branch A -, and blue filled squares - branch B), secondary (red open circles - branch A -, and blue open squares - branch B) and special detections (red starred symbols - branch A, and blue stars - branch B) in the Λ_{Sgr} vs. heliocentric distance plane (a true distance modulus of 16.90 has been adopted here). The horizontal dashed lines enclose the range of sensitivity of our method. The spherical-halo N-body model by Law et al. (2005) is also reported (small dots) as an aid for the interpretation of the plot. The heavier dots are those enclosed in the cones of the considered FoVs.

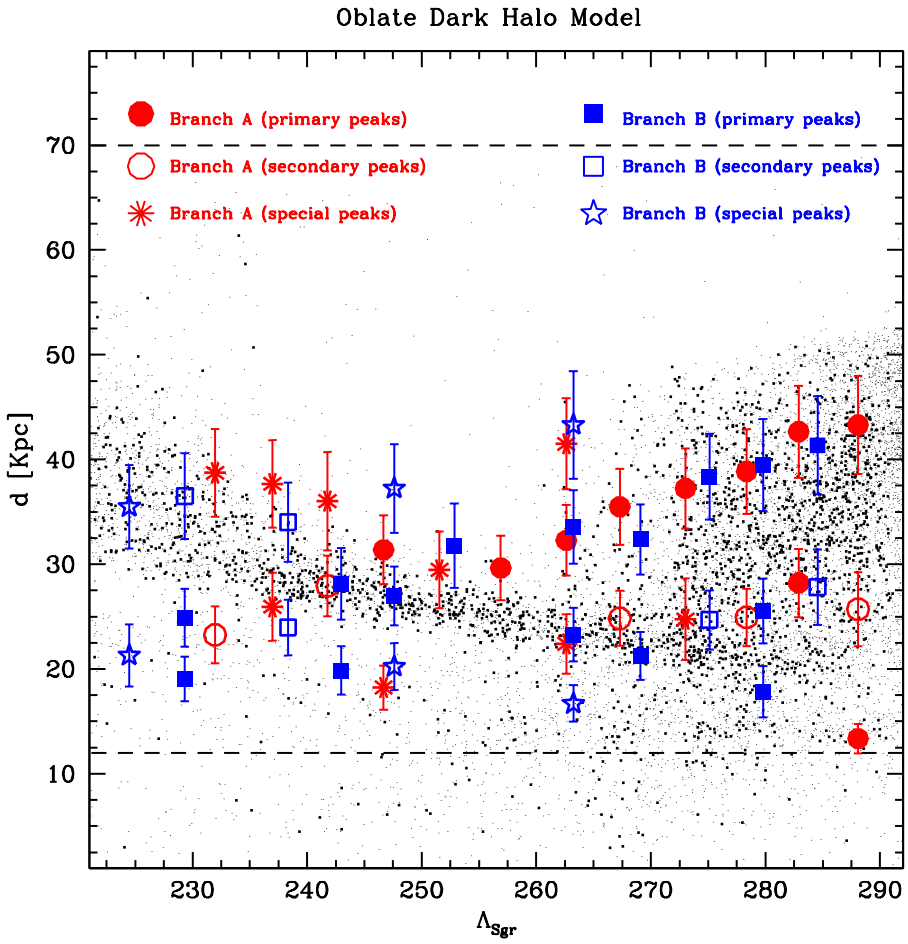

Figure 4.30: Same as fig. 4.29 but in this case our detections are compared with the oblate-halo N body model by Law et al. (2005).

CHAPTER 5

Red Clump stars in the Boötes III stellar system

We report on the detection of a population of Red Clump (RC) stars probably associated with the recently discovered stellar system Boötes III. The RC is identified as a 3σ *peak in the Luminosity Function (LF) of colour-selected stars extracted from the SDSS database. The peak is consistently detected in the* g, r, i *and* z *LFs at the expected luminosity of a typical RC at the distance of Boötes III. Moreover the stars around the LF peak show a maximum of surface density nearly coincident with the reported center of the system. Assuming that the detected feature is the genuine RC of Boötes III, we find that the system has the HB morphology typical of old and metal-poor dwarf spheroidals, it has an integrated magnitude* $M_V \simeq -5.8 \pm 0.5$ *and an ellipticity* $\varepsilon \sim 0.5$*, quite typical of the recently identified new class of very faint dwarf galaxies.*

SECTION 5.1

Introduction

The advent of large modern surveys, like the 2 Micron All Sky Survey (2MASS, Skrutskie et al., 2006) and the Sloan Digital Sky Survey (SDSS, Adelman-McCarthy et al., 2008, and references therein), has greatly increased our ability to detect stellar systems and/or structures of very low surface brightness in the halo and the disc(s) of the Milky Way (MW). Large scale sub-structures have been traced over huge portions of the sky (Newberg et al., 2002; Yanny et al., 2003; Majewski et al., 2003; Martin et al., 2004; Jurić et al., 2008), but also feeble tidal streams have been found around disrupting globular clusters (see, for example Rockosi et al., 2002; Grillmair & Johnson,

2006) or lacking an evident progenitor (Belokurov et al., 2006; Grillmair, 2009). Moreover, a completely new class of very faint dwarf galaxies ($0 < M_V < -8.5$; Martin et al., 2008, hereafter MJR08) have been discovered (see Belokurov et al., 2007b; Zucker et al., 2006a,b; Irwin et al., 2007; Liu et al., 2008, and references therein). These substructures are generally interpreted as the relics of the process of hierarchical assembly of the MW, as predicted by galaxy formation models within the current cosmological scenario (see Bullock et al., 2001; Madau et al., 2008, and references therein).

In Bellazzini et al. (2006, hereafter B06, presented in Chapter 3) we used SDSS data to study the stellar content of the largest tidal stream in the halo of the MW, the one produced by the disruption of the Sagittarius dwarf spheroidal (Sgr dSph) galaxy (Ibata et al., 1994; Majewski et al., 2003; Belokurov et al., 2006). In particular, we showed that it is possible to detect the Red Clump (RC) of core-He-burning stars associated with a given sub-structure as a peak in the Luminosity Function (LF) of sub-samples of stars selected in a relatively narrow colour range including the RC. The RC peak of the sub-structure can be disentangled from the fore/background contaminating population of the MW by subtracting the underlying LF, that is, in general, quite smooth and smoothly varying with position in the sky. In B06 we used this technique to compare the Horizontal Branch (HB) morphology in the stream and in the main body of Sgr. However, it was pointed out that the most natural and direct application would be the determination of accurate distances from the magnitude of the detected RC peaks, as the RC is well known and widely used as a standard candle (see Paczynski & Stanek, 1998; Stanek & Garnavich, 1998; Girardi & Salaris, 2001; Babusiaux & Gilmore, 2005; Bellazzini et al., 2006, and references therein). For intermediate-old age populations, the luminosity of the RC peak shows relatively modest variations as a function of age and metallicity, in particular when measured in the reddest optical passbands (as Cousins' I, see Girardi & Salaris, 2001). We have used theoretical isochrones from the Girardi et al. (2004) set to verify that this is true also for the r,i,z SDSS passbands. We found that the magnitude of the RC peak varies by $\simeq 0.55$ mag, $\simeq 0.43$ mag, and $\simeq 0.34$ mag, in r, i and z, respectively, for ages between 4 and 12.5 Gyr over the metallicity range $-1.8 \leq [M/H] \leq 0.0$.

We have started an extensive search and analysis of the RC peak along the portion of Sgr stream that is enclosed in the SDSS, a study that is now almost completed (see Correnti et al., 2008, and Chapter. 4). During the analysis, while looking at the LF of a control field outside the Sgr stream, we noticed a relatively weak but well defined peak where a smooth LF was

expected instead. Following up this finding, we realized that the considered field enclosed a faint stellar system that was very recently discovered with a different technique by Grillmair (2009, hereafter G09), i.e. the possible dwarf galaxy (or relic dwarf galaxy) Boötes III.

G09 detected Boo III as a weak overdensity centered at (RA, Dec)=(209.3°,26.8°) and extending for $\sim 1.5°$ from the center (but most of the signal is detected within $R \sim 0.8°$), at a mean heliocentric distance $D \sim 46$ kpc. The system has been detected with the *matched filter* technique (Rockosi et al., 2002) that allows the maximization of the signal from the filtered population over the strong Galactic fore/background. The filter adopted by G09 was mostly sensitive to the blue side of the Main Sequence (MS) and Turn Off (TO) region of a typical old and metal-poor population. G09 concluded that "the galaxy is revealed almost entirely by subgiant and TO stars...". No significant correlation of the new system with structures in the interstellar extinction maps (Schlegel et al., 1998, hereafter SFD98) was found, and indeed the reddening is quite low in all the (large) area explored by G09. The cluster of galaxies Abell 1824, having a radius of $R \simeq 13'$, was noted to lie within $3'$ from the object, but G09 showed that the density map obtained from the objects classified as galaxies in the SDSS does not present any obvious correlation with Boo III. The field-subtracted CMD (G09 Fig. 12) shows upper MS, TO and SGB features that are reasonably bracketed by the ridge lines of the globular clusters M13 and M15, having [Fe/H]$= -1.54$ and [Fe/H]$= -2.26$, respectively. The RGB and (possible) RC remain buried in the subtraction noise, that dominates the plot for $r < 20.5$. However the inspection of the un-subtracted CMD allowed G09 to identify a population of likely BHB stars (at $(g-i)_0 < 0.0$, where the contamination is very low) probably associated with Boo III. Matching the observed BHB with empirical templates, he found $(m-M)_0 = 18.35$. Boo III is very sparse and appears significantly elongated in the E-W direction. G09 finds it immersed into a very faint stellar stream, dubbed *Styx*. Since he found that the populations in the two substructures appear similar he concluded that Boo III is (very likely) a disrupting dwarf galaxy physically associated with the stream and that it is its most probable progenitor.

In this letter we report on the detection of Boötes III (Boo III) from RC stars and on the new insight on the stellar content of this system obtained from this population.

SECTION 5.2

The Red Clump of Boötes III

To trace the RC population of Boo III, that was not detected by G09, we will adopt the technique developed by B06. The technique used by G09 (and many others, see Rockosi et al., 2002; Newberg et al., 2002; Yanny et al., 2003; Belokurov et al., 2006, 2007b) is optimized for the detection of new structures, as it maximizes the contrast over the background. It uses mainly MS stars - the most abundant stars in any stellar system - thus reaching very low surface brightness levels and allowing the efficient surveying of large areas of the sky. On the other hand, our approach is best suited for a more accurate localization of detected structures. The method collapses all the information from colour-selected candidate RC stars into a mono-dimensional histogram, where any statistically significant peak provides a direct estimate of the distance. The RC stars are much less numerous than MS stars but, in general, are tightly *clumped*, both in colour and in magnitude, when placed at the same distance. In the following we will consider the SDSS-DR6 photometry of objects classified as stars (extracted from the SDSS CasJobs query system, Adelman-McCarthy et al., 2008) from two fields: (a) F1, a circular field centered on the center of Boo III (as determined by G09) and with radius $R = 0.8^\circ$, (b) CF, a square $8^\circ \times 8^\circ$ Control Field with the same center as F1 but with the inner $R \leq 2^\circ$ circle removed. To average out statistic noise in the fore/background population, CF has much lager area than F1 (by a factor of ~ 20). As the two globular clusters NGC5466 and M3 were included in CF, we excised from it two circular areas centered on the clusters and having radius $R = 1^\circ$, i.e. much larger than their limiting radii (Harris, 1996, hereafter H96).
All the stars are corrected for reddening using the SFD98 maps. The average and standard deviation in $E(B-V)$ is 0.019 ± 0.003 in F1 and 0.015 ± 0.003 in CF. In the following all the reported colours and magnitudes must be intended as corrected for reddening. The LFs in r, i, and z of F1 and CF stars, lying in the colour range that is expected to enclose the RC, are compared in the right panels of Fig. 5.1. The independent colour selections adopted in $(g-r)$, $(g-i)$ and $(g-z)$ are shown in the corresponding CMDs in the left panels of Fig. 5.1. The LFs are computed as running histograms having bin width of ± 0.3 mag and step of 0.01 mag, as this approach allows the best determination of the position of peaks (see Bellazzini et al., 2005, and references therein). It seems quite clear that the LFs of F1 present additional structures with respect to CF, for $r, i, z < 19$. In particular, all the LFs show a clear peak around $r, i, z \sim 18.5$

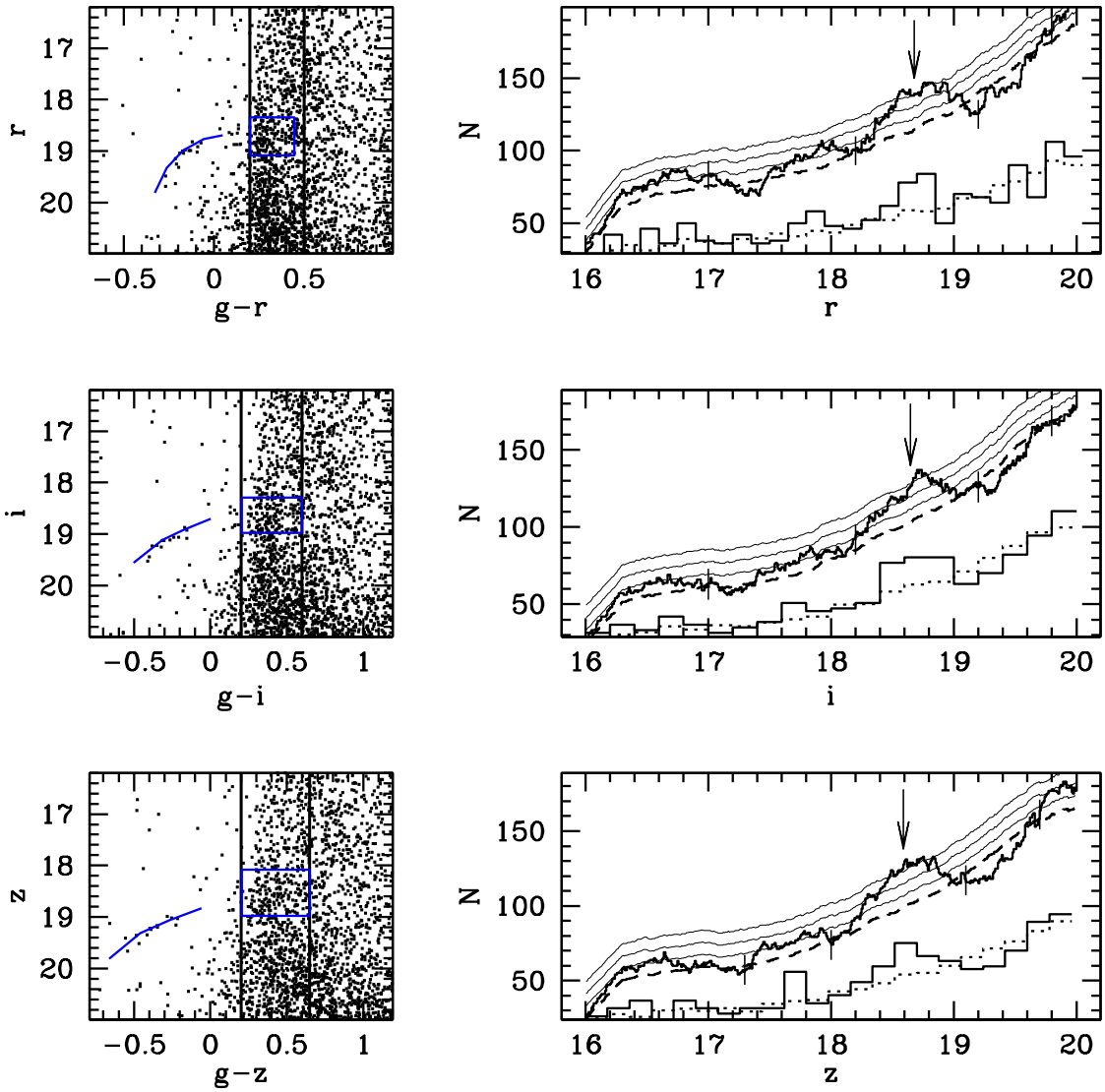

Figure 5.1: Left panels: CMDs of F1 in various combinations of magnitudes and colours. The vertical lines enclose the adopted colour-selection windows. The boxes and the ridge-lines are the templates for Draco RC and BHB, respectively, as derived in Fig. 5.2, below, corrected for the distance of Boo III derived here. Right panels: de-reddened running-histogram LFs of colour-selected RC candidates for F1 (continuous line) and CF (dashed line) in r, i and z. The thin lines marks the 1, 2, and 3σ levels above the background, including all the sources of uncertainty. The estimated positions of the peaks are indicated by arrows, the ranges over which we have performed the normalization are indicated by thin vertical segments. The LFs represented as ordinary histograms are also reported for comparison (F1: thin continuous histogram, CF: thin dotted histogram), after being multiplied by a factor of $\simeq 2$ to fit into the limits of the plots.

that is hardly compatible with a chance fluctuation of star counts. The peak is detected also in the g LF but it is not shown if Fig. 5.1 for reasons of space. The LFs of the CF have been normalized to the F1 ones by minimizing the average difference over large intervals around the main peak, i.e. $17.0 < r,i < 18.2$ and $19.2 < r,i \leq 19.8$, $17.3 < z < 18.0$ and $19.1 < z \leq 19.7$. In all the considered cases the peaks reach the 3σ level above the background, that includes both the Poisson noise and the uncertainty in the adopted normalization.

We estimated the position of the peaks by fitting Gauss curves to the residuals of the subtraction between the LFs of F1 and CF. We obtain $g = 19.05$, $r = 18.68$, $i = 18.65$, and $z = 18.59$, with a typical uncertainty of ± 0.05 mag. If interpreted as genuine Red Clump peaks, these would imply a distance very similar to Boo III. For instance, transforming the theoretical absolute V and I magnitudes of the RC for a Z=0.001, age=10 Gyr population provided by Girardi & Salaris (2001) into $M_r^{RC} = 0.40$ and $M_i^{RC} = 0.23$[1], we find $(m-M)_0 = 18.28$ and 18.42, to be compared with $(m-M)_0 = 18.35$ (G09). The coincidence calls for a common origin of the MS + SGB + BHB populations found by G09 and the possible RC detected here.

When dealing with such distant, ghostly systems, with very low surface brightness and luminosity, like Boo III (or Boo II, CV II, etc., see MJR08, Liu et al., 2008), we may face the possibility that the proof of their existence and their characterization can be obtained only by painstaking accumulation of many - sometime weak, but consistent - clues. While the evidence presented here is not sufficient in itself to confirm the presence of a stellar system, we think that it provides strong support to the findings by G09 and it may allow a further insight on the nature of Boo III. In the following we will show that even if the statistical significance of the detected peak is not very strong (3σ), the interpretation of this feature as the RC population of Boo III has an excellent degree of consistency with the known properties of the stellar system.

Even if in Fig. 5.1 we adopted the intervals that maximize the signal of the RC peak, the feature is well detected for a range of colour selections. On the other hand the colour of the RC is mostly sensitive to the chemical composition (Girardi & Salaris, 2001) and can provide useful indications on the metallicity of the detected population. To allow a direct comparison with empirical templates we studied the RC population of the two old clusters displaying an RC in the SDSS sample by An et al. (2008, i.e., Pal 4, M71). The colour of the putative RC of Boo III ($g-r = 0.37$) is much bluer than

[1]Using transformations derived from the comparison between 713 stars in common between the SDSS and Stetson (2000) photometry of NGC 2419.

that of M71 ($g-r=0.62$ and $[Fe/H]=-0.73$), and even bluer than that of Pal 4 ($g-r=0.48$ and $[Fe/H]=-1.48$), suggesting that these stars belongs to a population more metal-poor than $[Fe/H]\sim-1.5$, in agreement with the independent results by G09. If Boo III is a new stellar system and the LF peak detected here is indeed its RC population, we are facing an old metal-poor system that displays a complex (bi-modal?) HB morphology, having both a BHB and a RC. This is very reminiscent of classical dwarf spheroidal satellites of the MW dominated by old and metal-poor populations like, for example, Sculptor, Sextans, Leo II, Tucana, Ursa Minor and Draco (see Harbeck et al., 2001, and references therein). Since Draco is included in the SDSS it may provide the ideal template for a simultaneous fit of the RC and BHB of Boo III. In Fig. 5.2 we present a determination of the r, i, and z absolute magnitudes of the RC in Draco, obtained from the peak of colour-selected LFs, as above, from SDSS-DR6 photometry. The adopted reddening and distance are from Bellazzini et al. (2002, hereafter B02), the RR Lyrae are identified from the list by Bonanos et al. (2004). We have also plotted rectangles that approximately comprise the RC in the various CMDs, as well as ridge lines fitting the mean loci of the BHB. With these tools in hand we can attempt a simultaneous fit of the RC and BHB of Boo III. In case of success this will lend strong support to the association of the two features and, in turn, to the interpretation of Boo III as a dwarf galaxy (or relic of). Coupling the apparent magnitudes of Boo III RC from Fig. 5.1 with the absolute magnitudes of Draco RC from Fig. 5.2 we obtain $(m-M)_0=18.46$, 18.59 and 18.59, from r, i, and z, respectively. Averaging these value we obtain a final estimate of $(m-M)_0=18.58\pm0.05$ (internal) ±0.14(external), in good agreement with G09, once taken into account that his estimate is based on the H96 distance scale that is $\simeq0.2$ shorter than the scale adopted in B06 (from Ferraro et al., 1999). Accounting for this systematic the two estimates differ by only 0.03 mag. Shifting the Draco RC+BHB templates by $(m-M)_0=18.58$ in the Boo III CMDs we achieve the matches of the BHB shown in the left panels of Fig. 5.1, that can be considered as very satisfactory. Hence the BHB and the putative RC of Boo III can be simultaneously fitted by the respective Draco templates. Fig. 5.2 also indicates that (a) our colour-selected RC samples may be contaminated by type ab RR Lyrae observed at random phase, that may partially blur the actual RC signal, and (b) the weak features in the F1 LFs, brighter than the RC peak, may be due to Asymptotic Giant Branch stars falling into the selection window. In the upper panels of Fig. 5.3 we show the running histograms of RA and Dec for stars in the RC peak. The two distributions have clear maxima nearly coinciding with the

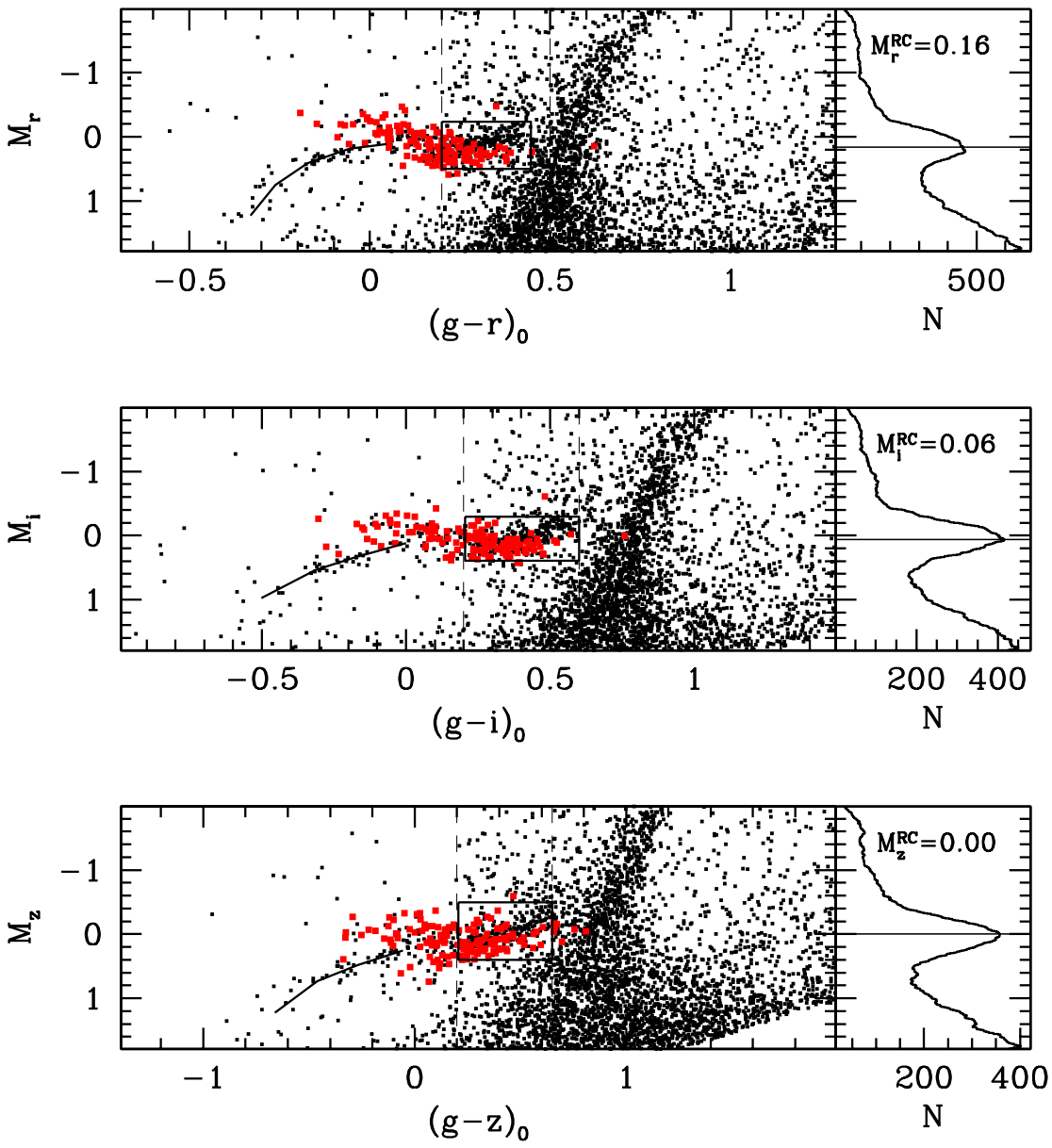

Figure 5.2: CMDs of the innermost $R = 15'$ of the Draco dSph from photometry extracted from the SDSS-DR6. The heavier (red) points are RR Lyrae counter-identified from the set by Bonanos et al. (2004). The rectangles that approximately enclose the RC in the various CMDs, and the BHB ridge lines have been drawn by eye. The thin dashed lines show the same colour windows adopted in Fig. 5.1 to select candidate RC stars. The same is also adopted for the LFs shown in the right panels, with the same step and bin width as in Fig. 5.1.

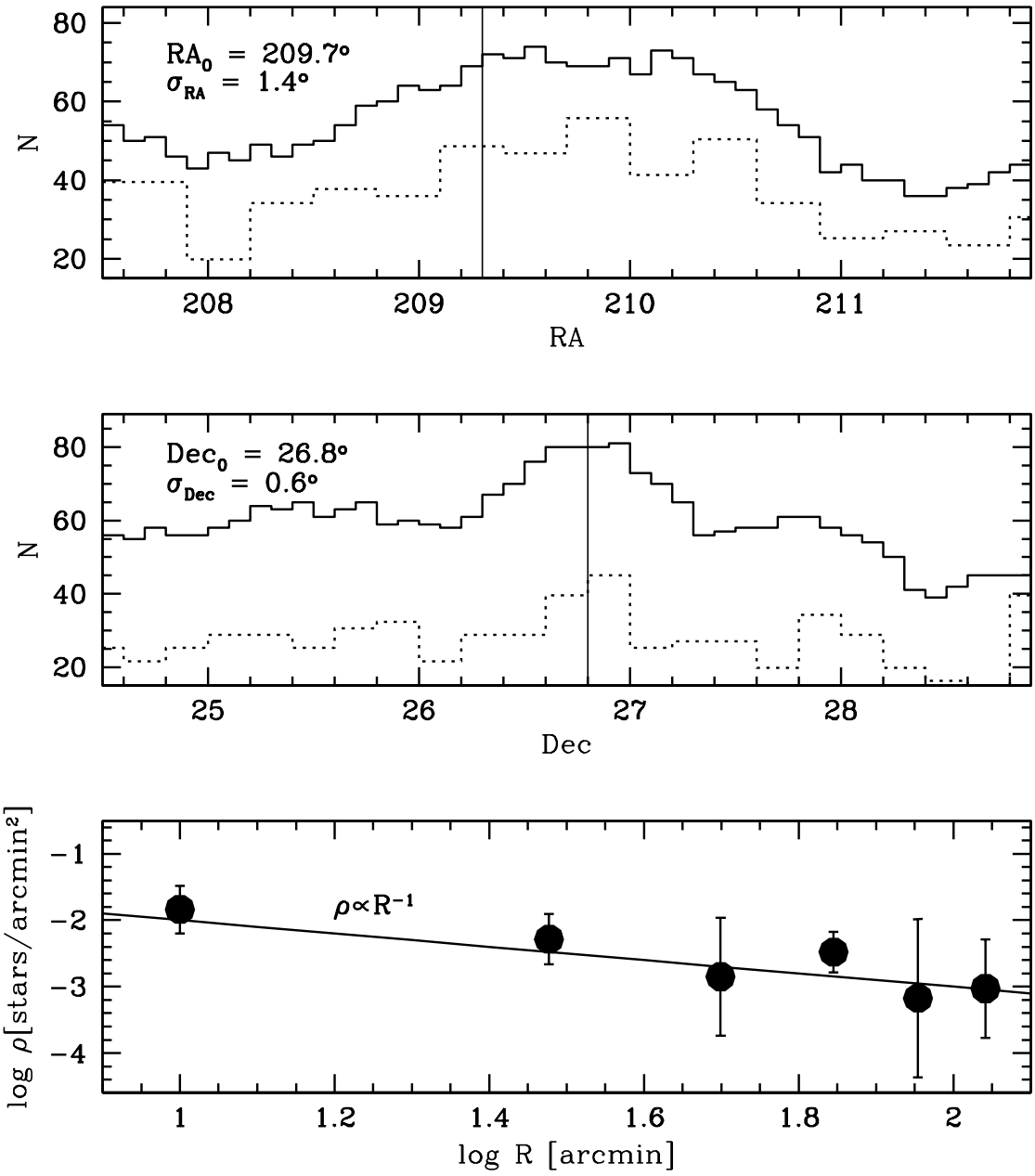

Figure 5.3: Spatial distribution of stars around the RC peak (colour selections as in Fig. 5.1 and $18.5 \leq r \leq 18.8$). Upper panel: distribution in RA within a 2° wide strip enclosing Boo III (Dec=$26.8^\circ \pm 1^\circ$). Middle panel: distribution in Dec within a 2° wide strip enclosing Boo III (RA=$209.3^\circ \pm 1^\circ$). The horizontal scale is the same in the two panels. The adopted bin width and step of the running histograms (continuous lines) are $\pm 0.4^\circ$ and 0.1°, respectively. The ordinary histograms (dotted lines, rescaled by a factor of $\times 1.8$) are also reported, as a reference. The vertical thin lines marks the position of the center of Boo III estimated by G09. The mean and σ of the Gauss curves best fitting our distributions are reported in the upper-left corners. Lower panel: the background-subtracted azymutally-averaged density profile is compared with a R^{-1} profile.

position of Boo III estimated by G09. Moreover the Gauss curve that best fits the peak in the RA direction has a $\sigma \sim 2$ times larger than its counterpart in Dec, nicely confirming the strong E-W elongation found by G09. Finally, the plot in the lower panel of Fig. 5.3 shows that the surface density profile of RC peak stars displays a radial decline from the center of Boo III, with a slope fully consistent with what found by G09.

SECTION 5.3

Discussion

We have detected a peak in the LFs of colour-selected candidate RC stars in a circular $R \leq 0.8^{\circ}$ field centered on the newly proposed dwarf galaxy Boo III (G09). Even if the statistical significancy of the peak is not particularly strong (3σ), the detection (a) has been consistently obtained in the g, r, i, and z LFs, (b) in all cases it is located at the expected luminosity of Boo III RC, (c) a simultaneous fit of the putative RC and BHB of Boo III has been obtained with RC+BHB templates of Draco dSph, (d) the stars located in the RC peak have a maximum in surface density at the same position in the sky as Boo III, and (e) their radial surface-density profile is fully consistent with that found by G09 for MS stars of Boo III. Hence, it is extremely likely that the detected signal is due to a population that is physically associated with the newly discovered system. This results lend support to the G09 interpretation of Boo III as a new stellar system, possibly a disrupting dwarf spheroidal galaxy, even if a final verdict must wait for spectroscopy of a sizable sample of member stars. If we accept the hypothesis that Boötes III is a genuine stellar system, from the present analysis we can draw the following conclusions:

1. The system has a composite HB morphology very typical of dSph galaxies dominated by old and metal-poor populations (but having a spread in age and metallicity, like Scu, Sex, UMi, Dra). All of these galaxies contains also RR Lyrae variables. By analogy some RR Ly could be present also in Boo III. Re-scaling the population of Draco to the total luminosity of Boo III, ~ 10 RR Ly are expected.

2. The average distance modulus from the RC is $(m-M)_0 = 18.58 \pm 0.15$ corresponding to $D \simeq 52.0 \pm 3.6$ kpc. The difference with respect to G09 is completely accounted for by the different distance scales adopted. The detected signal is too weak to look for the difference in distance between the Eastern and Western lobes of the galaxy claimed by G09. For the

same reason we were unable to find any detectable RC signal from the much fainter *Styx* stream that was claimed to be associated with the galaxy (G09). [2]

3. The technique adopted here allows us to count the RC stars (B06). Adding also the BHB we obtain a rough estimate of the number of core-He-burning stars ($N_{Hb} \simeq 38$) that can be directly converted into a distance-independent estimate of the absolute integrated V magnitude by means of the Evolutionary Flux Theorem (Renzini & Buzzoni, 1986), as done in Bellazzini et al. (2006). Using Eq. 1 of Renzini (1998), adopting the parameters appropriate for a population with [M/H]$= -1.35$ and age=10 Gyr from Maraston (2005), and $t_{Hb} = 9 \times 10^7$ yr from the BASTI database (canonical Z=0.01 models of age=8.2 Gyr; Cordier et al., 2007), we get $M_V \simeq -5.8 \pm 0.5$, very weakly depending on the assumed age and metallicity. This value is straight in the middle of the range covered by the new class of faint dwarf galaxies and in agreement with their distribution in the half-light radius r_h vs. M_V plane, for any reasonable choice of r_h in the range between 0.1 kpc and 0.7 kpc, corresponding to $\sim 0.1^\circ$ and 0.8° (see MJR08, and references therein). From N_{Hb} we also estimated an average surface brightness within $R \leq 0.8^\circ$ of $\mu_V \simeq 31.3 \pm 0.3$ mag/arcsec^2. Finally, estimating the ellipticity as $\varepsilon = 1 - \sigma_{Dec}/\sigma_{RA}$ (thanks to the E-W orientation of the major axis, see G08 and Fig. 5.3) we find $\varepsilon \sim 0.5$, also in agreement with the other newly discovered faint dwarfs (MJR08).

NOTE: in a successive paper, Carlin et al. (2009) reported the results of a spectroscopy study of Boötes III. They measured radial velocities for 193 Boo III candidate stars, selected to have magnitudes and colours consistent with its upper main sequence and lower red giant branch, as well as a number of horizontal branch candidates. From 20 identified candidate Boo III members, they measure a system velocity of $V_\odot = 197.5 \pm 3.8$ $km\ s^{-1}$ and a velocity dispersion of $\sigma_o = 14.0 \pm 3.2$ $km\ s^{-1}$. They used the somewhat large velocity dispersion and the implied highly radial orbit, along with morphological evidence from G09 and our paper, to argue that Boo III is likely the first known object observed in a transitional state between being a bound dwarf galaxy and a completely unbound tidal stream. In conclusion, they spectroscopically confirmed the *discovery* if this system.

[2] On the other hand, the LFs of sources, colour-selected as in Fig. 5.1 and classified as "galaxies" in the SDSS do not show any peak over the whole considered range and lie much below than the level reached by stellar LFs around $r, i, z \simeq 18.5$ (by a factor of ~ 2), thus confirming the conclusion by G09 that the Boo III overdensity is not associated with the A1824 cluster of galaxies.

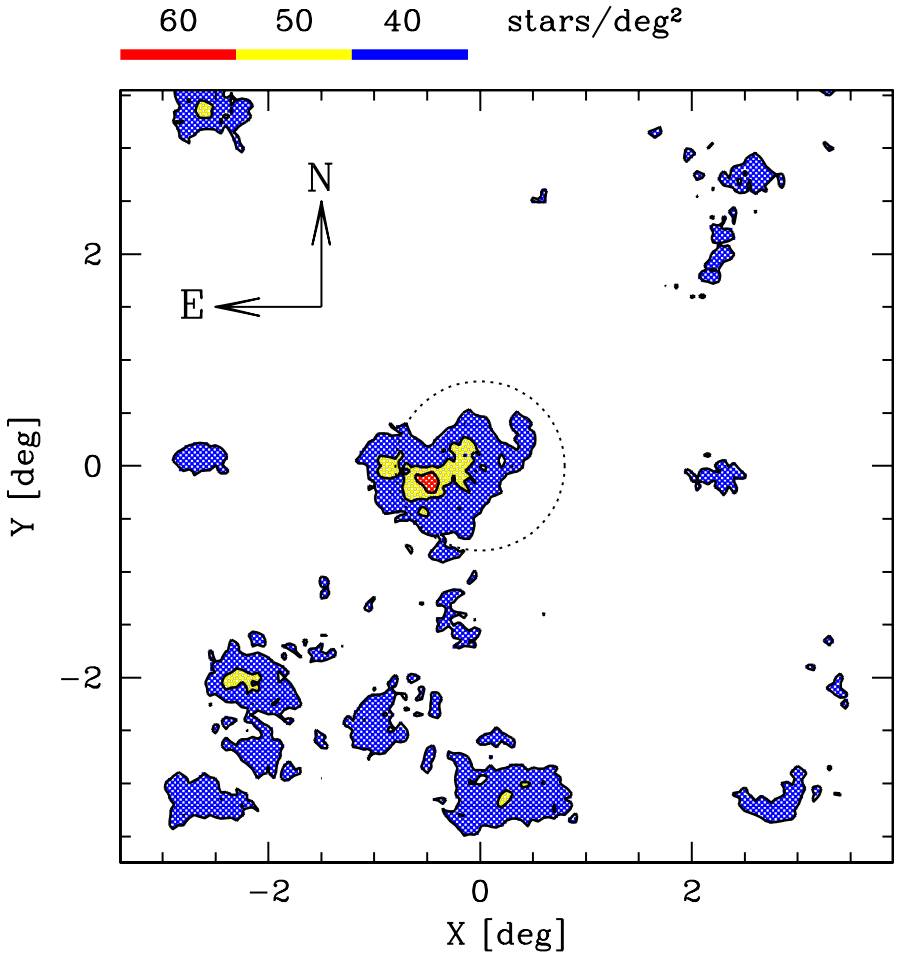

Figure 5.4: Spatial distribution of RC stars in an area of 30′, centered on the center of Boötes III (as determined by G09). The colour selection is the same of Fig. 5.1 and $18.5 < r < 18.6$; the colour code representing the number density of RC stars is shown in the top part of the figure, the red colour indicating the denser region (i.e. 60 stars/deg^2) while the blue the sparser (i.e. 40 stars/deg^2). The resulting density map is very similar to the one presented in G09.

CHAPTER 6

The non-peculiar velocity dispersion profile of the stellar system ω Centauri

We present the results of a survey of radial velocities over a wide region extending from $r \simeq 10'$ out to $r \simeq 80'$ (∼1.5 tidal radii) within the massive star cluster ω Centauri. The survey was performed with FLAMES@VLT, to study the velocity dispersion profile in the outer regions of this stellar system. We derived accurate radial velocities for a sample of 2557 newly observed stars, identifying 318 bona-fide cluster red giants. Merging our data with those provided by Pancino et al. (2007), we assembled a final homogeneous sample of 946 cluster members that allowed us to trace the velocity dispersion profile from the center out to r ∼32 arcmin. The velocity dispersion appears to decrease monotonically over this range, from a central value of $\sigma_v \sim 17.2$ Km s^{-1} down to a minimum value of $\sigma_v \sim 5.2$ Km s^{-1}. The observed surface brightness profile, rotation curve, velocity dispersion profile and ellipticity profile are simultaneously well reproduced by a simple dynamical model in which mass follows light, within the classical Newtonian theory of gravitation. The comparison with an N-body model of the evolution of a system mimicking ω Cen during the last 10 orbits into the Galactic potential suggests that (a) the rotation of stars lying in the inner $\simeq 20'$ of the clusters is not due to the effects of the tidal field of the Milky Way, as hypothized by other authors, and (b) the overall observational scenario is still compatible with the possibility that the outer regions of the cluster are subject to some tidal stirring.

SECTION 6.1

Introduction

ω Centauri is the most massive and luminous globular cluster (GC) of the Milky Way ($M \sim 2.5\ 10^6\ M_\odot$ van de Ven et al., 2006). It is the only known Galactic GC which shows clear star-to-star variations in the abundance of iron-peak elements (Freeman & Rodgers, 1975; Norris et al., 1996) and indication exists for possible helium abundance variation among its stellar populations (Norris, 2004; Piotto et al., 2005). Together with a few other clusters (like M54 and NGC2419, for example), ω Cen fall well above the sharp upper envelope of the main distribution of GCs on the size-luminosity plane (Mackey & van den Bergh, 2005; Federici et al., 2007). These (and other) evidences suggest that ω Cen could be not a "genuine" GC but more likely the nuclear remnant of a dwarf galaxy that merged in the past with the Milky Way (see Freeman, 1993; Bellazzini et al., 2008, for a discussion of the analogy with the case of M54 within the disrupting Sgr dwarf galaxy).

From the dynamical point of view, ω Cen is one of the most flattened among Galactic GCs (Meylan, 1987). The flattening is generally interpreted as due to the observed rotation, as the variations of ellipticity with distance from the cluster center correlates with the amplitude of the rotation curve (Merritt et al., 1997; Meylan & Mayor, 1986). Merritt et al. (1997) found that ω Cen can be well described as an isotropic oblate rotator in which the mass is distributed as the light. In a recent study van de Ven et al. (2006) modelled ω Cen with an axisymmetric implementation of Schwarzschild's orbit superposition method. They found that the system is close to isotropic inside a radius of about 10 arcmin and becomes increasingly tangentially anisotropic in the outer region, which displays significant mean rotation. These authors suggested that this phase-space structure could be caused by the effects of the tidal field of the Milky Way, as kinematical gradients are a typical outcome of tidal stresses (see Muñoz et al., 2008, and references therein).

A number of studies on the kinematics of the cluster have been performed in the recent past (Meylan et al., 1995; Mayor et al., 1997; Norris et al., 1997; Reijns et al., 2006; van de Ven et al., 2006), particularly focused on the innermost $r < 20'$ region. Recently, Scarpa et al. (2003, hereafter SC03) measured the velocity dispersion profile of ω Cen at larger distances ($20' < r < 28'$) using UVES spectra of 75 candidate cluster members. They found that the velocity dispersion profile remains constant at large radii rather than

decrease monotonically, as expected for systems in which mass follows light. These authors suggested that this behaviour could be due to a breakdown of Newton's law in the weak acceleration regime, as proposed in the popular Modified Newtonian Dynamics framework (MOND, Milgrom, 1983, 2008). However, it has been noted that actually this cannot be the case, as a flat velocity profile at large radii is predicted by MOND only for clusters in the deepest MOND regime, i.e. where both the internal accelleration and that due to the gravitational field of the Milky Way are significantly lower that the MOND scale accelleration, $a_0 \simeq 1.2 \times 10^{-8}$ cm/s^2 (Baumgardt et al., 2005; Moffat & Toth, 2008). On the contrary, at the position of ω Cen the external accelleration due to the Milky Way is $> a_0$. In this regime, the predictions of MOND are similar to the Newtonian behaviour (see also Moffat & Toth, 2008; Haghi et al., 2009).

Nevertheless, a flat velocity dispersion profile over a large radial range would be uncompatible with a mass-follow-light model (Gilmore et al., 2007) and may suggest the presence of a halo of Dark matter (DM) embedding the star cluster and driving the kinematics of the stars in the outer regions (Carraro & Lia, 2000; Mashchenko & Sills, 2005). In any case the available evidences are not sufficient to support the case of DM: as McLaughlin & Meylan (2003) demonstrated, SC03 data could be well described by simple, self-consistent dynamical models without the need of MOND and/or dark matter. A larger kinematic survey in the region $r > 20'$ is overdue to assess the behaviour of the dispersion profile in this range.

A controversial issue is also represented by the possible presence of signatures of tidal effects in the outskirts of this stellar system. If the present-day cluster is just the nuclear remnant of a larger system, it is reasonable to expect some observable overdensity of stripped stars in the surroundings, if the latest phase of disruption occurred in the recent past (up to a few orbital period ago; see Combes et al., 1999; Dinescu, 2002; Tsuchiya et al., 2004; Mizutani et al., 2003; Ideta & Makino, 2004; Bekki & Freeman, 2003). Leon et al. (2000) studied the 2-D structures of the distribution of stars around ω Cen from $5.5^\circ \times 5.5^\circ$ photographic films obtained with the ESO Schmidt telescope. This analysis evidenced the presence of a pair of tidal tails approximately oriented in the direction of the Galactic center, in projection. This result has been questioned by Law et al. (2003) who found that *a)* Leon et al. (2000) tidal tails were strongly correlated with unhomogeneities in the reddening distribution and *b)* no extra-tidal component can be detected using the homogeneous near-infrared photometry of the 2MASS survey. In a recent dedicated survey, Da Costa & Coleman (2008) derived the radial velocities

(with an accuracy of ~ 10 $Km\ s^{-1}$) of 4105 stars located on a wide region out to a distance of 2 tidal radii from the cluster center. They estimated that less than 0.7% of the total cluster mass is comprised between 1 and 2 tidal radii, implying that the stripping process on the progenitor (if any) must have been largely completed at early epochs.
In this paper we present the results of a survey of radial velocities in ω Cen performed with FLAMES@VLT, focused on the radial range $10' < r < 30'$ and aimed at the assessment of the kinematical properties in the outskirts of the cluster. The new dataset, combined with the homogeneous sample of Pancino et al. (2007) allowed us to derive a robust velocity dispersion profile from the center to a distance of $32'$ with an accuracy ≤ 1 $Km\ s^{-1}$. In § 2 we describe the observations and the data reduction techniques. In § 3 we present the metallicity and the velocity distributions. § 4 is devoted to the description of the method used to derive the velocity dispersion profile of ω Cen. In § 5 we compare the observed kinematics of this stellar system with a set of dynamical models and N-body simulations. § 6 is devoted to the analysis of the sample of stars located in the outer region of ω Cen. Finally, we summarize and discuss our results in § 7.

SECTION 6.2

Observations and Data reduction

The analysis presented here is based on two spectroscopic datasets: *i)* the *inner sample*: constituted of a sample of ~ 700 red giants selected from the photometry by Pancino et al. (2000) in the magnitude range $13 < B < 16$ lying within $15'$ from the cluster center and presented in Pancino et al. (2007, hereafter P07) and *ii)* the *outer sample*: constituted of a sample of 2557 red giants selected from the 2MASS catalogue Skrutskie et al. (2006) between $6.0 < K < 13.0$, observed in 28 pointings at distances $10' < r < 80'$ from the cluster center (see Fig. 6.1).
At $r \sim 20'$ from the cluster center, the surface brightness is already $\mu_V > 22.0$ mag/arcsec^2, implying that Red Giant Branch (RGB) stars of ω Cen should be relatively rare and indeed not numerous enough to fill all the fibers of a single FLAMES plate. To achieve the maximum efficiency in selecting cluster members for the *outer sample* we gave the highest priority for fiber allocation to stars (a) lying within a selection box in colour-magnitude diagram broadly enclosing the cluster RGB (see Fig. 6.5), defined from the accurate infrared

photometry by Sollima et al. (2004) and (b) with UCAC2 (Zacharias et al., 2004) proper motions differing by less than $\pm$ 8 *mas* yr^{-1} from the bulk proper motion of the cluster, as determined by van Leeuwen et al. (2000). These "a priori" criteria allowed to select some hundreds high-confidence target stars. The remaining fibers were positioned on other stars selected from the 2MASS catalogue in the same magnitude range, as shown in Fig. 6.5, below.
Observations have been done with FLAMES (Pasquini et al., 2002) at the ESO VLT in Paranal, Chile, between 2003 May 22 and 28 (*inner sample*, P07) and between 2008 July 13 and August 20 (*outer sample*). In both cases, FLAMES has been used in GIRAFFE mode, using the high-resolution (R $\sim$ 22,500) grating HR13 (6120-6395 Å) and reaching a signal-to-noise ratio of $50-300$ $pixel^{-1}$, depending on the star magnitude. The *inner sample* has been already used by P07 to study the rotation pattern of the stellar populations of ω Cen. The data reduction and calibration procedure is very similar to that adopted here for the *outer sample* (see below), and is described in detail in P07.
The *outer sample* data have been reduced with the GIRAFFE BLDRS (Base-Line Data Reduction Software) 4 which includes cosmic-ray removal, bias subtraction, flat-field correction, wavelength calibration, and pixel resampling. Sixteen fibers have been dedicated to sky observations in each exposure. An average sky spectrum has been obtained and subtracted from the object spectra by taking into account the different fiber transmission. The spectra have been then continuum-normalized and corrected for telluric absorption bands with IRAF. The spectra of three program stars are shown in Fig. 6.2 to illustrate the quality of our data.
Radial velocities have been derived through Fourier cross-correlation, using the *fxcor* task in the radial velocity IRAF package. The spectrum of each object has been correlated with a high signal-to-noise template spectrum of the Geneva radial velocity standard star HD42807, retrived from the ELODIE archive (Moultaka et al., 2004). All spectra have been corrected for heliocentric velocity[1]. The average error on the derived radial velocity is $\sigma_v \sim 0.5$ Km s^{-1}. Nine stars are in common between the *inner* and the *outer* samples: the average difference in radial velocity is $\Delta\, v_r = -0.09 \pm 0.16$, fully consistent with no systematic shift between the two samples. Star by star comparisons with other datasets are also very satisfying. The average radial velocity difference of the 278 stars in common with Reijns et al. (2006) is $\Delta\, v_r = 1.48 \pm 1.76$, while for the 36 stars in common with Johnson et al.

[1]The derived radial velocities of the *outer sample* stars are available in electronic form at the CDS (http://cdsweb.u-strasbg.fr/).

(2008) is $\Delta\ v_r = 1.62 \pm 1.47$, i.e., consistent with null difference within the uncertainties. Reijns et al. (2006) velocities were derived from spectra of resolution $8500 < R < 17000$; the resolution of Johnson et al. (2008) spectra was $R = 13000$; in both cases the typical uncertainty is $\sim 1.5\ Km\ s^{-1}$.
In addition, metallicities have been also derived for the *outer sample* stars. A set of 15 iron lines has been selected from the database of Kurucz & Bell (1995) in the spectral range covered by our spectra. These lines have been identified, whenever possible, on each spectrum and have been fitted with Gaussian functions. The integral of the difference between the continuum and the line profile provided the equivalent width (EW) of each line. The abundance analysis has been performed using the latest version of the Kurucz (1979) model atmospheres and the MOOG line analysis code (Sneden, 1973) to compute LTE abundances from individual EWs. The abundance has been derived from the model that best reproduced the observed EWs, for assumed values of temperature, gravity, and microturbulence velocity. Temperatures have been derived from $J-K$ colours adopting the colour-temperature transformations by Montegriffo et al. (1998) a reddening $E(B-V) = 0.11$ (Lub, 2002) and the extinction coefficients by Savage & Mathis (1979). The gravity parameter *log g* has been then computed assuming a distance modulus to ω Cen of $(m-M)_0 = 13.70$ (Bellazzini et al., 2004; Del Principe et al., 2006). The microturbulence velocity has been initially set as $2\ Km\ s^{-1}$ and then adjusted within a range of about $1\ Km\ s^{-1}$ by minimizing the trend in the deduced abundances with EWs for Fe I lines. The average error on the derived metallicities is $\sigma_{[Fe/H]} \sim 0.2$ *dex*. The comparison with the metallicity determinations by Johnson et al. (2008) for the 36 stars in common indicates a difference of $\Delta[Fe/H]_{our-J} = -0.21 \pm 0.25$, indicating an acceptable agreement for the purposes of the present study, that is focused on the kinematics in the outer regions of ω Cen. Here we derived metallicities of our stars to have an independent sanity check of the selection criteria adopted in §3 to identify cluster members. A full analysis of the abundance pattern of the selected stars will be the subject of a more detailed dedicated analysis, that will be presented in a forthcoming paper.

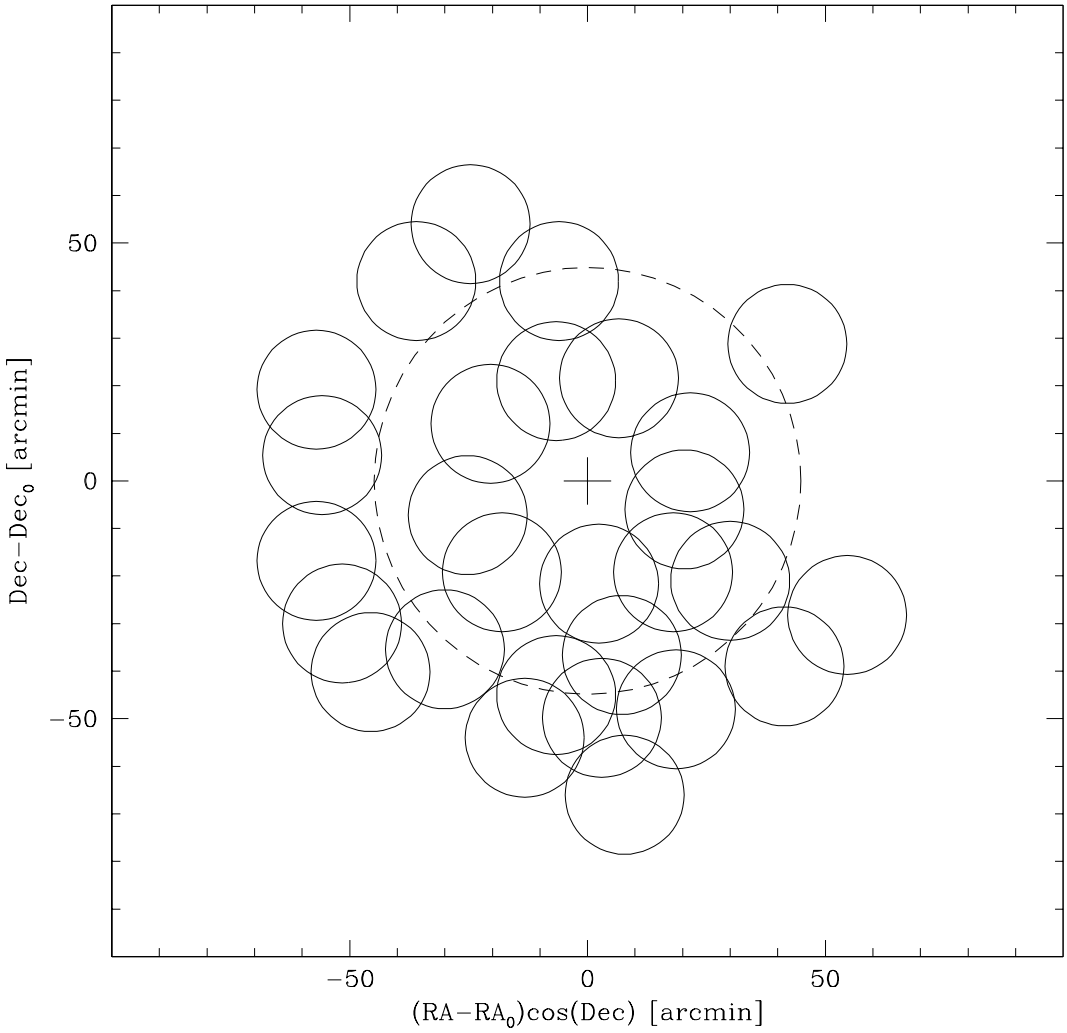

Figure 6.1: Map of the region sampled by the FLAMES observations. North is up, east towards the right-hand side. The 28 fields observed with FLAMES (*outer sample*) are shown as continuous circles. The cluster center and tidal radius (from Trager et al., 1995) are indicated by the black cross and the dashed line, respectively.

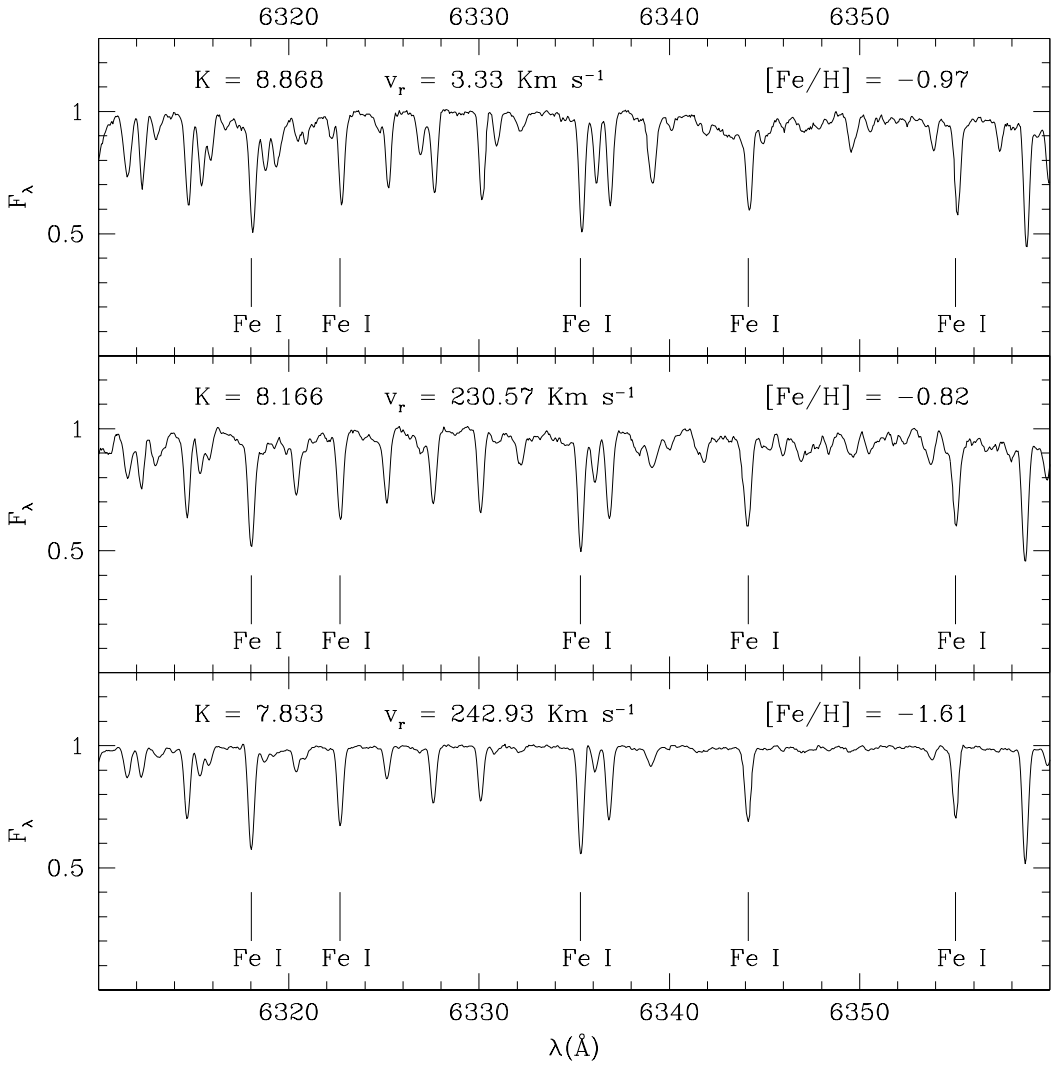

Figure 6.2: Spectra of the field star 2MASS13331099-4749262 (top panel), and of the ω Cen stars 2MASS13262366-4742424 (middle panel) and 2MASS13283381-4732055 (bottom panel). A sample of iron lines used in the analysis are also indicated.

SECTION 6.3

Radial velocity and Metallicity distribution

In Fig. 6.3 the radial velocities of the entire sample are plotted as a function of the distance from the cluster center. To calculate distances we deprojected right ascension and declination into X and Y coordinates with the following relations, suited for extended objects that are not close to the celestial equator (from van de Ven et al., 2006):

$$X = -r_0 \; cos \; \delta_0 sin(RA - RA_0)$$

$$Y = r_0[sin \; \delta \; cos \; \delta_0 - cos \; \delta \; sin \; \delta_0 \; cos(RA - RA_0)]$$

where RA_0 and δ_0 are the coordinate of the cluster center and $r_0 = 10800/\pi$ is the scale factor to have X and Y in arcmin. At the adopted distance, 1 arcmin corresponds to 1.6 pc. As can be noted, the clump of ω Cen stars is clearly visible at large positive velocities ($v_r > 190 \; Km \; s^{-1}$) while field stars are broadly distributed around the average velocity $< v_r >= -8.0 \pm 30.2 \; Km \; s^{-1}$, in good agreement with the predictions of the Galactic model by Robin et al. (2003b, hereafter R03) for thin disc and thick disc stars in this direction, and very different from the typical velocity of ω Cen ($< v_r >= 233.2 \pm 0.4 \; Km \; s^{-1}$). Fig. 6.4 shows the metallicity distribution obtained for the 338 stars belonging to the *outer sample* and with radial velocity $190 < v_r < 290 \; Km \; s^{-1}$. A sharp and asymmetric peak at $[Fe/H] \sim -1.8$ can be seen, with a long tail extending toward higher metallicity ($[Fe/H] > -1.4$). Secondary peaks are also visible at metallicity $[Fe/H] \sim -1.3$ and $[Fe/H] \sim -0.85$, in agreement with the previous spectroscopic determinations by Norris et al. (1996); Suntzeff & Kraft (1996); Johnson et al. (2008).

SECTION 6.4

Velocity dispersion

6.4.1 Selection criteria

In order to construct the velocity dispersion profile of ω Cen we need to distinguish the bona-fide cluster stars from the Galactic field contamination. In fact, although the field population and ω Cen stars have very different bulk velocities, a small (but non neglibible) fraction of stars belonging to the Galactic halo could lie in the same velocity range of genuine cluster stars.

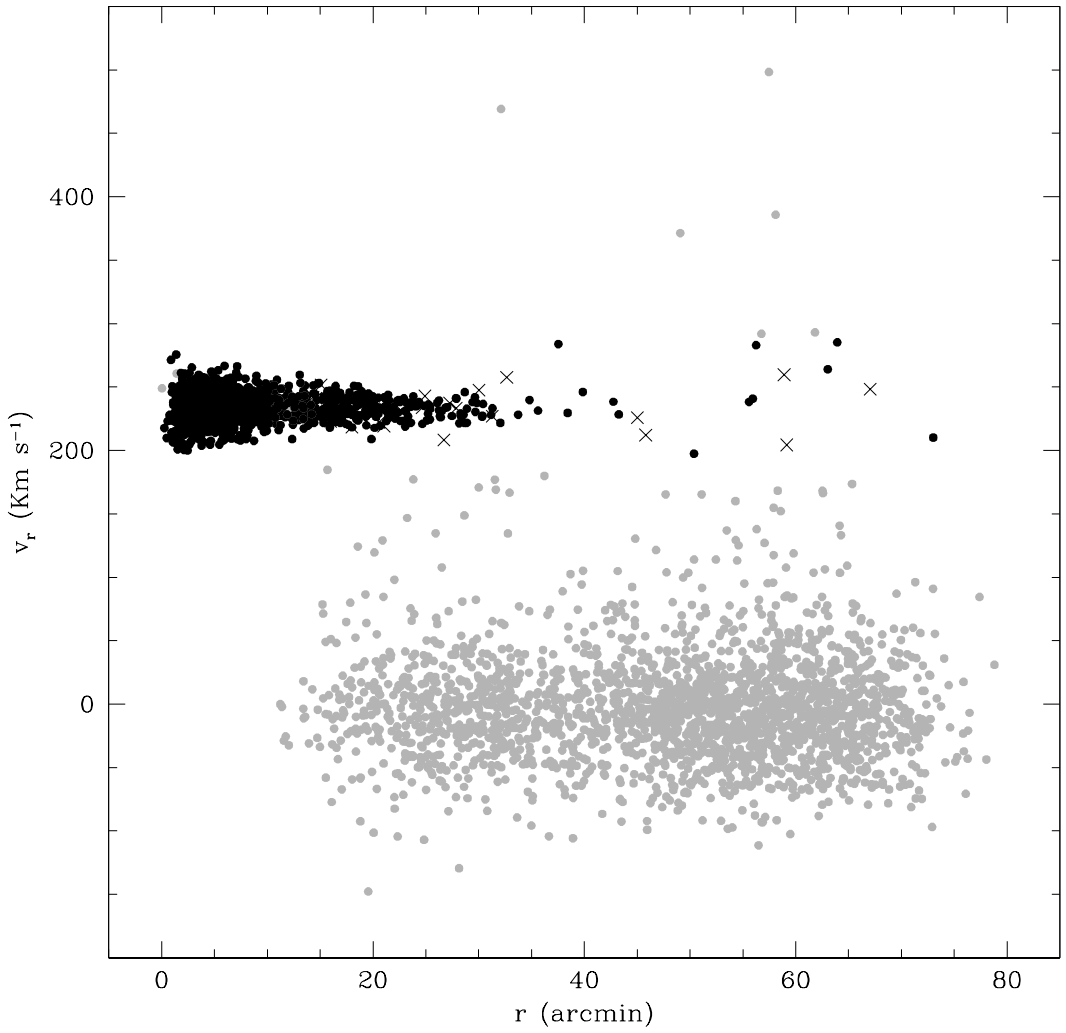

Figure 6.3: The radial velocities of the entire sample are plotted as a function of the distance from the cluster center. Grey points represent object rejected by the radial velocity selection criterion (*i*) defined in § 6.4.1. Crosses represent object rejected by the other selection criteria.

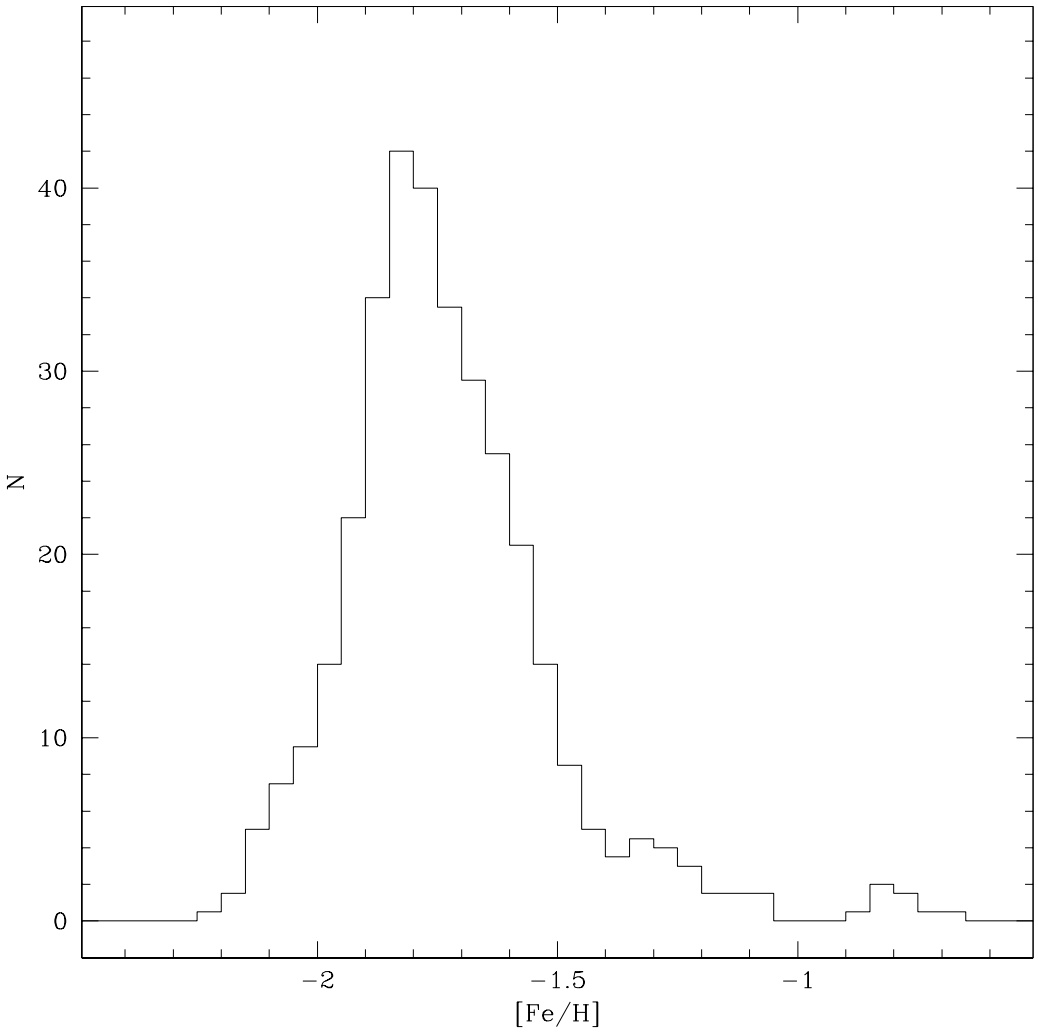

Figure 6.4: Metallicity distribution of the 338 stars belonging to the *outer sample* with radial velocity $190 < v_r < 290$ $Km\ s^{-1}$. The distribution is obtained using a running box of 0.1 dex width and a step size of 0.05 dex.

This is particularly important in the external region where the cluster density drops quickly with radius, while the density of the field population remains constant (see §6.6).
To this aim, we excluded from the *inner sample* all the stars with radial velocity $v_r < 190\ Km\ s^{-1}$ (see P07) and adopted three different selection criteria for the *outer sample*:

- *i) Radial velocity:* The bulk radial velocity of ω Cen has been estimated to be $< v_r >= 233.2 \pm 0.4\ Km\ s^{-1}$ with a maximum velocity dispersion at the center of $\sigma_v \simeq 20\ Km\ s^{-1}$ (Meylan et al., 1995). Therefore, a first selection has been made by taking as possible members only stars with $190 < v_r < 290\ Km\ s^{-1}$[2]. Note that this selection is safe since the velocity dispersion is expected to decrease significantly at large distances from the center. Therefore this criterion is not expected to introduce any bias in the selected sample.

- *ii) Position in the CMD:* Fig. 6.5 shows the K *vs* $(J-K)$ CMD of the *outer sample* stars. We considered as cluster members only the stars lying within the selection box enclosing the cluster RGB that we have originally adopted to chose high-priority targets, that is shown in Fig. 6.5.

- *iii) Proper motions:* We identified 245 stars in common with the proper motion catalogue by van Leeuwen et al. (2000). These authors provide for each star a membership probability calculated according to its position in the proper motions plane. On the basis of this additional information, we excluded all the 20 stars with a membership probability smaller than 50%.

A total of 946 stars passed the above selection criteria, 628 belonging to the *inner sample* and 318 belonging to the *outer sample*. In Fig. 6.3 the accepted and rejected stars are clearly indicated. The adopted approach is rather conservative as our aim is to obtain the most reliable sample of cluster members to study the kinematics in the outer regions where the velocity dispersion is low and can be biased by a limited number of spurious sources. On the other hand, while the second and, in particular, the third criterion listed above may exclude from the sample some genuine member, this cannot bias our results as these selections are independent of the radial velocity of the stars. Nevertheless, is interesting to note that using the R03 Galactic model as decribed in §6.6, below, we expect a very low degree of

[2]The choice of an asymmetric range has been performed to minimize the field contamination in the region where the bulk of the field stars are located.

contamination. In particular, the predicted number of Galactic stars with $190 < v_r < 290$ $Km\ s^{-1}$ in our sample is 2.2 ± 0.5 for $r \leq 15'$, 1.4 ± 0.3 for $15' < r \leq 28'$, and 1.4 ± 0.3 in the range $28 < r \leq 44$ (see §6.6 for a discussion of the $r > 44'$ region).

Another potential selection criterion is based on the metallicity. Note, however, that only Galactic halo stars are expected to contaminate the sample at velocities $190\ Km\ s^{-1} < v_r < 290\ Km\ s^{-1}$. This Galactic component have a metallicity distribution ranging between $-2.2 < [Fe/H] < -0.8$ with a peak at $[Fe/H] = -1.6$ (Ivezić et al., 2008). Moreover, the contaminating halo stars lie in the foreground and background of ω Cen. Their different distances translate into a wrong determination of their surface gravities and, consequently, spread out their original metallicity distribution. As a consequence, the resulting metallicity distribution of the halo population largely overlaps the metallicity distribution of the ω Cen stars. Therefore, this selection criterion is poorly efficient in discriminating the cluster membership. However, we considered also a sample retaining only the stars whose metallicity is close to the main peak of the metallicity distribution shown in Fig. 6.4 ($-1.95 < [Fe/H] < -1.55$). In the following paragraph we calculated the velocity dispersion profile of ω Cen with and without adopting this last criterion, as a further check of our results.

6.4.2 Method

Once selected the bona-fide cluster member stars, as a first step we corrected for perspective rotation. In fact, since ω Cen has a large extension on the plane of the sky (with a diameter about twice that of the full moon), its systemic motion produces a non-negligible amount of apparent rotation (Feast, 1961). We corrected for this effect using the following correction (see van de Ven et al., 2006):

$$\Delta v_r = 0.001379\ (X\mu_X + Y\mu_Y) D\ Km\ s^{-1}$$

to be subtracted to the observed v_r. $\mu_X = 3.88$ and $\mu_Y = -4.44$ are the systemic proper motions in units of $mas\ yr^{-1}$ (van Leeuwen et al., 2000) and $D = 5.5$ is the distance to ω Cen in kpc (Bellazzini et al., 2004; Del Principe et al., 2006).

As a second step, we divided the sampled area in a set of concentric annuli at various distances from the cluster center, searching for the best compromise to have well populated and compact radial bins (except for the innermost $r < 1'$ bin that is not relevant in this context). Within each annulus we calculated

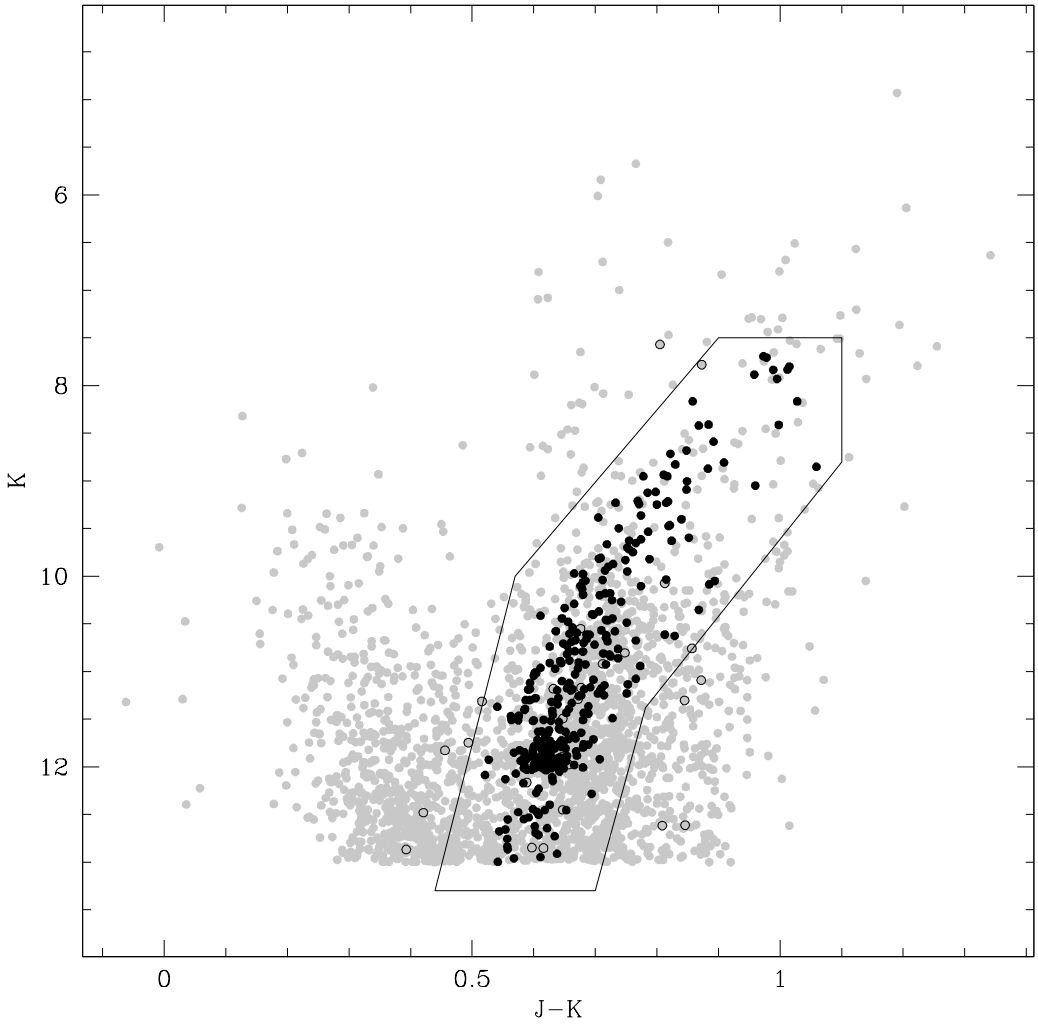

Figure 6.5: K *vs.* $(J-K)$ CMD of ω Cen. Grey points represent the stars rejected by the radial velocity selection criterion (i) defined in § 6.4.1. Open points represent stars rejected by the other selection criteria. The adopted selection box is also shown. The clump of member stars around $K \simeq 11.7$ is the RGB bump of the cluster (see Sollima et al., 2004).

the value of σ_v that maximize the log-likelihood

$$L(\sigma_v) = \sum_{i=1}^{N} log \int_{-\infty}^{+\infty} \frac{e^{-\frac{(v_i - <v>)^2}{2\sigma_v^2}} e^{-\frac{(v_i - <v>)^2}{2\sigma_i^2}}}{2\pi\ \sigma_v\ \sigma_i} dv$$

where v_i and σ_i are the radial velocity and its corresponding error for the N stars contained in the annulus and $< v >$ the average cluster velocity (Walker et al., 2006). As a further selection, in each annulus we excluded the outliers stars whose radial velocity differs more than 3 times the *local* σ_v from the cluster bulk velocity (see Fig. 6.6; Bellazzini et al., 2008).

The derived velocity dispersion profile is listed in Table 1 and shown in Fig. 6.7 for the case of the sample selected with (filled points) and without (open points) the metallicity selection criterion. As can be noted, no significant differences are evident between the two profiles. For this reason, in the following we refer always to the sample not selected in metallicity. The obtained profile shows a central velocity dispersion of $\sigma_v = 17.2^{+4.6}_{-3.0} Km\ s^{-1}$ in agreement with the previous estimates by Meylan et al. (1995); Mayor et al. (1997); Norris et al. (1997); van de Ven et al. (2006). The measured velocity dispersion appears to decrease monotonically with distance out to $r \simeq 26'$ from the cluster center, where it reaches a minimum of $\sigma_v = 5.2^{+0.80}_{-0.65} Km\ s^{-1}$. A small, non statistically significant, increase of the velocity dispersion is noticeable in the last bin, at a distance of $\sim 32'$.

In Fig. 6.8 the obtained velocity dispersion profile is compared with the profiles obtained by van de Ven et al. (2006) and SC03. Note that our profile agree very well with that obtained by van de Ven et al. (2006) in the overlapping region $r \leq 20'$. At distances $r > 24'$ the behaviour of our profile differs from that obtained by SC03. In particular, while the profile by SC03 flattens around a value of $\sigma_v \sim 8\ Km\ s^{-1}$, our profile continues to decrease. The statistical disagreement between the two profiles is $\sim 2\sigma$, hence it cannot be considered as statistically significant. The number of target stars in range $20' < r < 28'$ and the accuracy of the radial velocity estimates of the present study is similar to SC03. However, SC03 do not report (a) if their velocities have been corrected for perspective rotation (§4.2) and (b) the details of the adopted selection criteria; in particular it is not said if the selection in v_r takes into account the *local* value of the velocity dispersion at the considered radius. In any case, our results indicate that the flattening of the velocity dispersion curve shown by SC03 may not reflect a real kinematic feature of the cluster but a chance fluctuation, instead. The (doubtful) increase of the dispersion in the $< r > \simeq 32'$ bin observed here, if real, would be more compatible with the onset of tidal heating that with the effects of MOND or DM (see §6.5.2;

Table 6.1: Velocity dispersion profile of ω Cen.

r	$< r >$	N	σ_v	$\Delta\,\sigma_v$
arcmin	arcmin		Kms^{-1}	Kms^{-1}
0 - 1	0.75	10	17.20	$^{+4.60}_{-3.00}$
1 - 2	1.51	50	16.66	$^{+1.80}_{-1.50}$
2 - 3	2.50	80	15.16	$^{+1.30}_{-1.10}$
3 - 4	3.49	91	14.32	$^{+1.20}_{-0.95}$
4 - 6	5.04	151	13.34	$^{+0.80}_{-0.70}$
6 - 8	6.99	112	12.17	$^{+0.85}_{-0.80}$
8 - 12	9.63	150	10.15	$^{+0.60}_{-0.60}$
12 - 16	14.01	98	9.19	$^{+0.70}_{-0.60}$
16 - 20	17.75	99	8.28	$^{+0.65}_{-0.55}$
20 - 24	21.79	48	6.39	$^{+0.70}_{-0.55}$
24 - 28	25.71	24	5.21	$^{+0.80}_{-0.65}$
28 - 44	32.25	26	7.01	$^{+1.10}_{-0.90}$

see also Muñoz et al., 2008, and references therein). Note that this last bin is located outside the radial range covered by SC03 data.

SECTION 6.5

Comparison with Theoretical Models

To check if canonical dynamical models are able to reproduce the observed kinematics of ω Cen, in the following sections we compare our data with a set of analytical models (Wilson, 1975). N-body simulations have also been performed to study the effects of the tidal field of the Milky Way on different models of the cluster.

6.5.1 Analytical models

We attempt to reproduce our observations using Wilson (1975) models. These models have the advantage of taking into account the cluster rotation, predicting simultaneously the surface brightness, the velocity dispersion, the rotation, and the ellipticity profiles. These models adopt the distribution function

$$f(E,J) = \begin{cases} (e^{-E} - 1 + E)e^{\beta J - \frac{1}{2}\zeta^2 J^2} & \text{if } E < 0 \\ 0 & \text{if } E \geq 0 \end{cases}$$

Any choice of the a-dimensional central potential U_0, and of the two free parameters of the above equation (β and ζ), yelds a different rotating model in virial equilibrium. The adoption of a core radius r_c and of the inclination angle

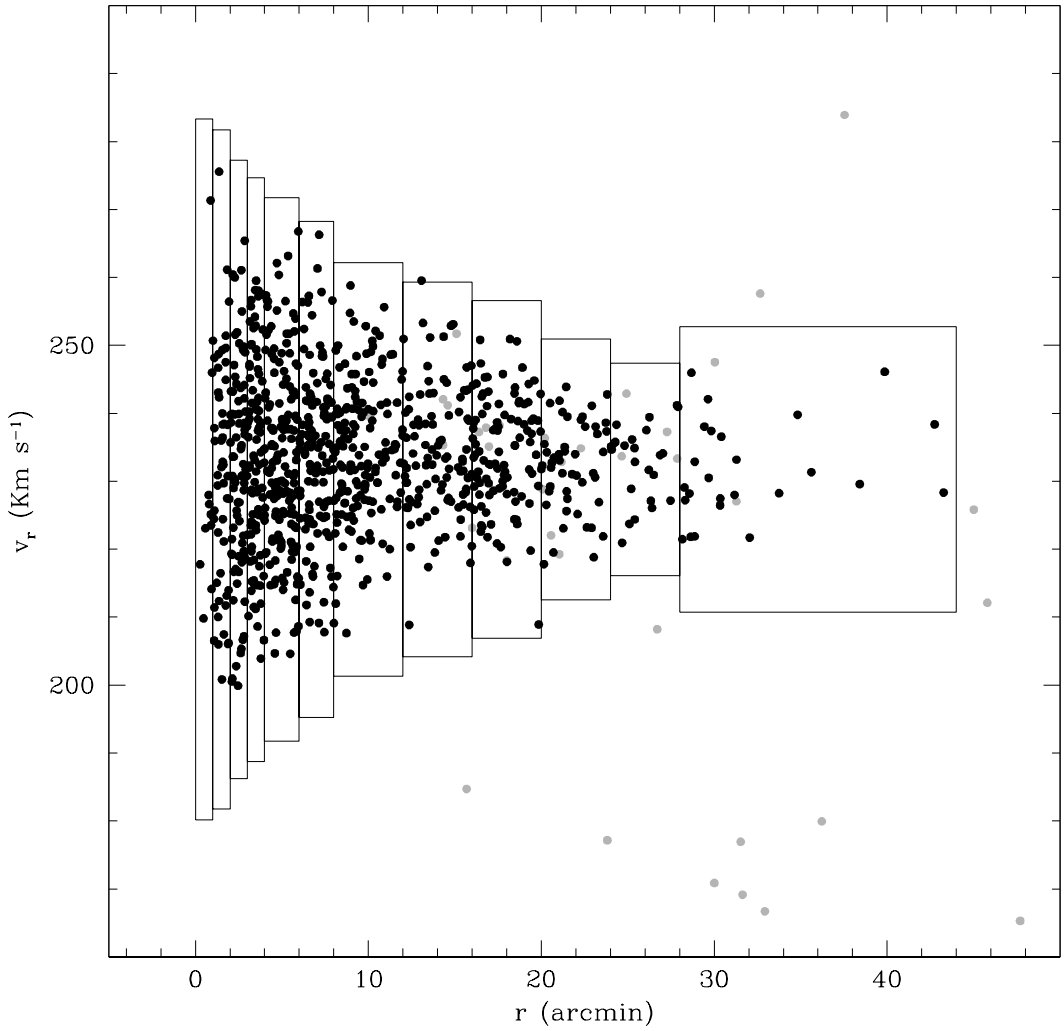

Figure 6.6: Radial velocity distribution as a function of the distance from the cluster center for stars with $190 < v_r < 290$ $Km\ s^{-1}$. The adopted bins of variable size are indicated together with the local 3σ range. Grey points represent the object rejected by the selection criteria defined in § 6.4.1

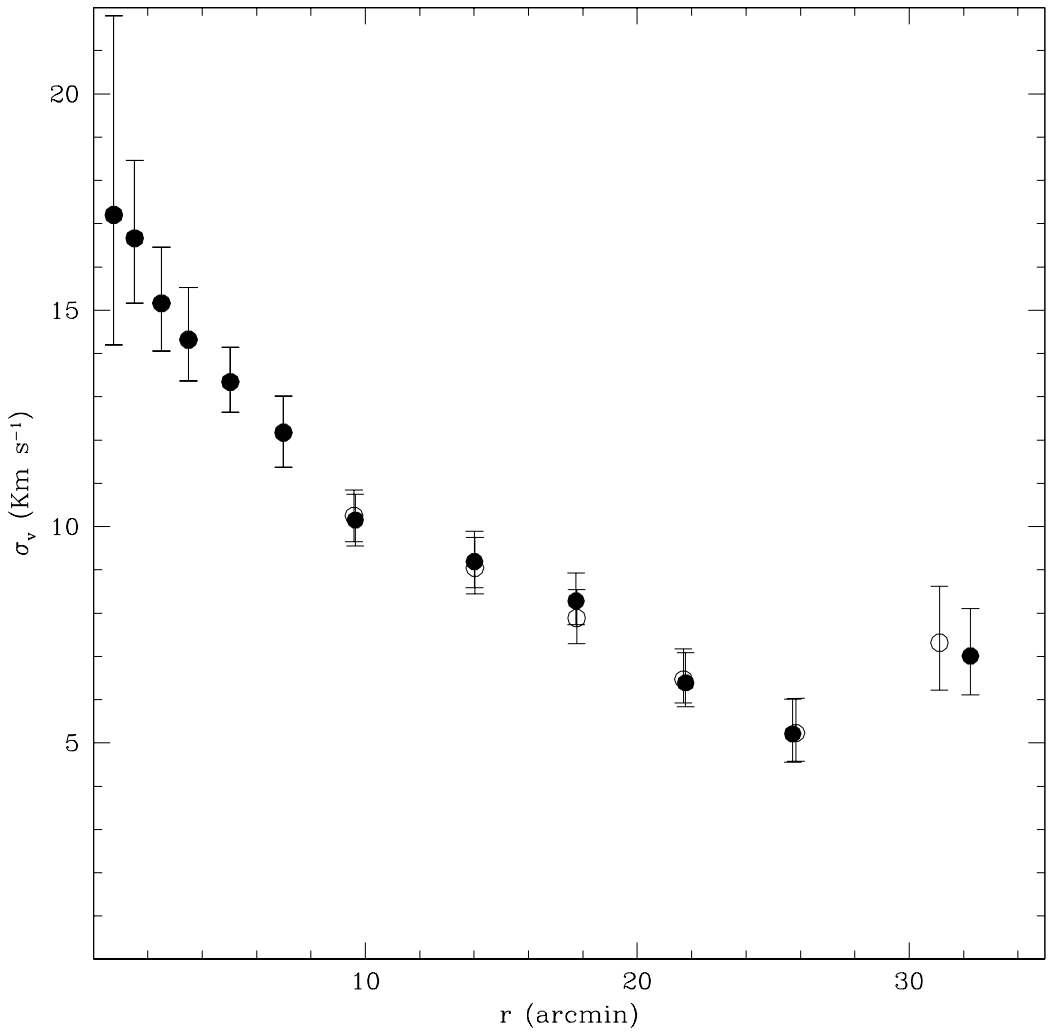

Figure 6.7: Velocity dispersion profile of ω Cen. Open and filled points refers to the sample selected and not selected in metallicity, respectively.

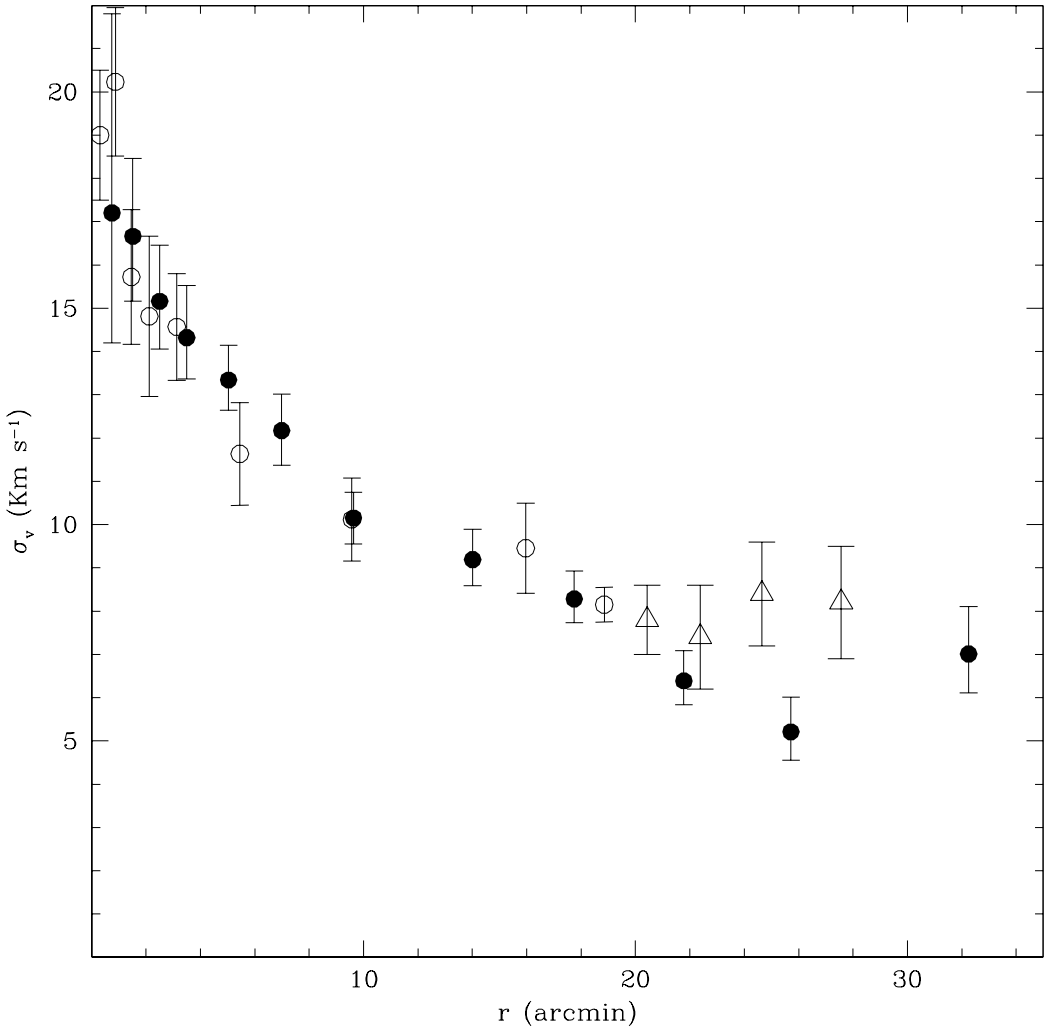

Figure 6.8: Comparison between the velocity dispersion profile presented in this paper (filled points) with those by van de Ven et al. (2006, open points) and by SC03, open triangles).

respect to the plane of the sky *i* provide an actual realization of the model that can be compared with observations. We explored the parameter space to find out one set reproducing simultaneously *i)* the surface brightness profile, *ii)* the velocity dispersion profile, *iii)* the rotation curve and *iv)* the ellipticity profile, giving lower weight to this last item. We adopt the velocity dispersion profile derived in § 6.4.2, the surface brightness profile by Trager et al. (1995) and the ellipticity profile by Geyer et al. (1983). Since the angle of rotation in the plane of the sky of ω Cen is $\phi \sim 0^\circ$, the rotation curve corresponds to the $X - v_r$ diagram.

The best-fit model has been found by fixing the inclination angle $i = 48^\circ$ (van de Ven et al., 2006) and assuming $U_0 = -6.3$, $\beta = 0.8$, $\zeta = 0.4$ and $r_c = 2.8'$. The ratio between the rotational kinetic energy and the absolute value of the potential energy of this model is $T/|W| = 0.09$, indicating that it is stable against non-axisymmetric perturbations (Ostriker & Peebles, 1973). The fit of the observational data with this model is shown in Fig. 6.9. As can be noted, the agreement is good in all the four diagrams. In particular, the model well reproduces all the observed kinematic properties of the cluster (rotation and dispersion) over the entire radial range covered by our data[3].

This means that *the velocity dispersion and rotation profiles of* ω *Cen are fully consistent with an equilibrium model in which the mass distribution follows the light, in the framework of classical Newtonian gravitation.* This is in good agreement with the results by McLaughlin & Meylan (2003), that were limited to the velocity dispersion profile.

6.5.2 N-body simulations

As described in § 6.1, there is no strong evidence for the presence of a significant population of tidally stripped stars around ω Cen. The most thorough study in this sense is the one by Da Costa & Coleman (2008) that, from their extensive radial velocity survey, concluded that less than 0.7% of the total cluster mass is comprised between 1 and 2 tidal radii. This result implies that the stripping process must have been largely completed at early epochs. Therefore, if ω Cen is indeed the remnant of a larger system destroyed long time ago, it must have lost a large part of its stars in a orbit with a larger apogalacticon with respect to the present day, because of orbital decay due to dynamical friction (Zhao, 2002; Bekki & Freeman, 2003; Tsuchiya et al., 2004; Mizutani et al., 2003; Ideta & Makino, 2004). This implies that the present-

[3]The marginal disagreement between the predicted and observed velocity dispersion profile in the innermost region could be induced by many second-order effects in modelling the shape of the velocity distribution in the internal cluster region (e.g. non-rotational anisotropy) and/or by the possible presence of an intermediate-mass black hole object in the center of ω Cen (as proposed by Noyola et al., 2008)

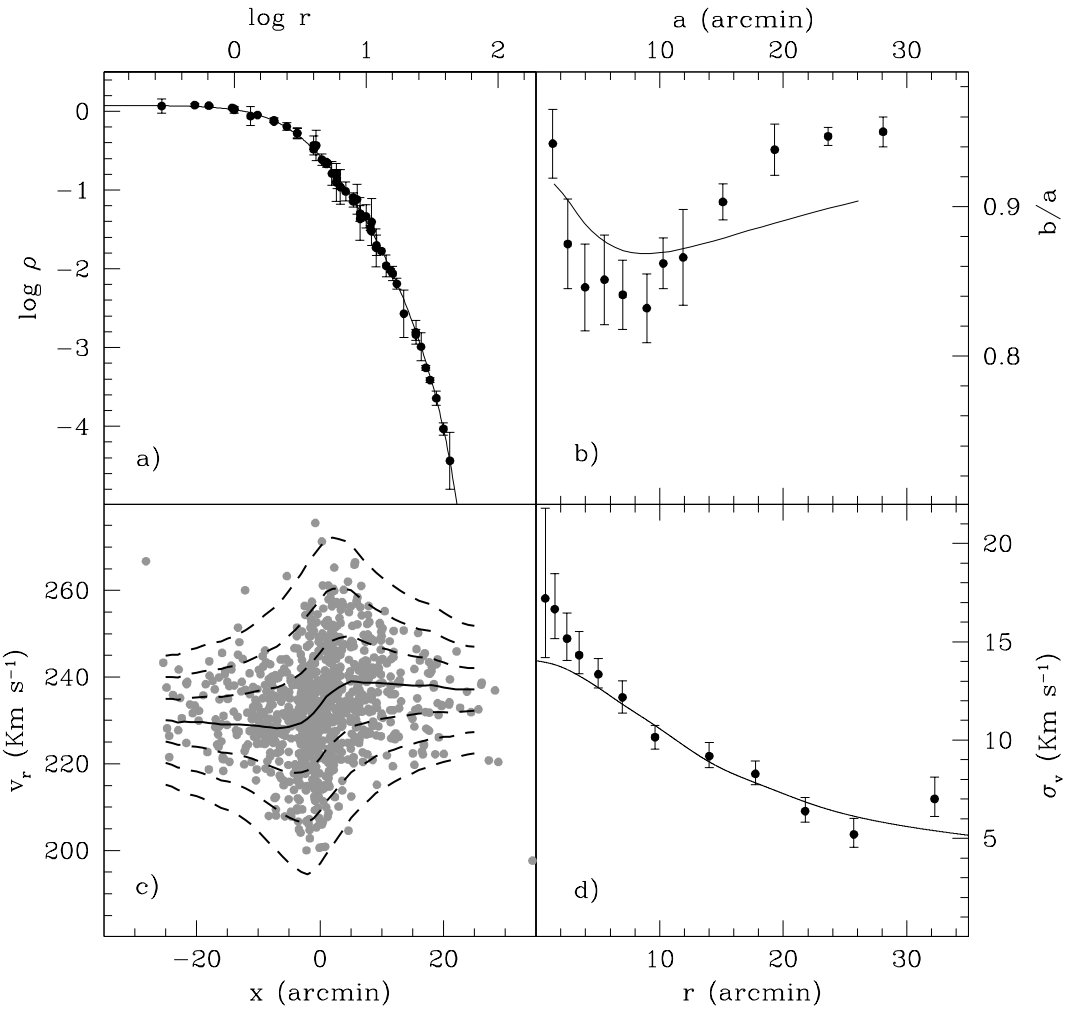

Figure 6.9: Comparison between the best-fit Wilson (1975) model (solid lines) and a) the projected surface brightness (from Trager et al., 1995) b) the ellipticity profile (from Geyer et al., 1983) c) the rotation curve and d) the velocity dispersion profile presented in this paper. In panel c) the 1σ,2σ and 3σ contours predicted by the model are also shown as dashed lines.

day system should be approximately in equilibrium with the tidal field of the Milky Way and lies on a stable orbit, as its mass is now sufficently low to make the effect of dinamical friction negligible.
We adopt this view as a working hypothesis for a simple N-body simulation aimed at studying the spatial distribution and the kinematical properties of the stars eventually stripped from the cluster by the tidal field of the Galaxy while the system is in the present-day stable orbit (see Ideta & Makino, 2004). The very good knowledge of the distance and 3-D motion of ω Cen (van Leeuwen et al., 2000) gives a high predictive power, under the limitations of the assumed hypothesis (for more detailed and extensive studies see Bekki & Freeman, 2003; Tsuchiya et al., 2004; Ideta & Makino, 2004, and references therein). The simulation was performed with `falcON`, a fast and momentum-conserving tree-code (Dehnen, 2000, 2002), within the NEMO environment (Teuben, 1995). Gravity was softened with the kernel 'P_2' of Dehnen (2000), with a softening length of 2 pc. The model cluster was let to evolve within the three-component (bulge+disc+halo) static Galactic potential 2b of Dehnen & Binney (1998), which has $v_{rot}(R_\odot) = 231\ Km\ s^{-1}$ and a total mass within 100 kpc of $\simeq 1 \times 10^{12} M_\odot$. ω Cen was represented by 50000 particles distributed according to an equilibrium (King, 1966) model having $W_0 = 6.0$, $r_t = 100$ pc and $M = 5 \times 10^6\ M_\odot$. This model has concentration (c) and tidal radius (r_t) values similar to the real cluster; the central velocity dispersion is also very similar, $\sigma \simeq 17.0\ Km\ s^{-1}$, but it should be recalled that the initial velocity distribution is completely isotropic, lacking any intrinsic rotation.
`falcON` is best suited to follow the evolution of non-collisional systems. While the effects of two-body encounters have been shown to be negligible in ω Cen (Ferraro et al., 2006; Sollima et al., 2007), this may not be the case in the innermost region of our model. To minimize undesired effects due to two-body encounters in the densest part of the model we have adopted a softening length approximately as large as the cluster core radius. For this reason the evolution in the innermost few r_c of the model should not be considered as a good representation of the evolution of the real cluster. On the other hand our model is fully adequate to study the reaction of the outer regions to the tidal strain of the Galactic potential, i.e. the morphology and the kinematics of possible tidal tails, that is what we are interested into. Note also that the 2-body relaxation time at the half-mass radius of our model (Binney & Tremaine, 1987, their Eq. 4-9) is a factor of $\simeq 4$ larger than the duration of our simulation, hence, in any case, the effects of particle encounters on the global properties of the model should be negligible.
First of all we integrated backward in time, within the adopted potential, the

orbit of a test particle whose initial position and 3-D velocity coincide with those of ω Cen at the present epoch - positions from Bellazzini et al. (2004) and velocity from van Leeuwen et al. (2000). The orbit has a period of $\simeq 80$ Myr, pericentric and apocentric distances of 1.5 kpc and 6.5 kpc, respectively, very similar to the orbits derived by Mizutani et al. (2003) and Ideta & Makino (2004).

We launched our N=50000 particle model from the apocenter at the epoch t=0.972 Gyr in the past. With this assumption the cluster evolves within the adopted potential for more than 10 orbits from that time to the present epoch (t=0). At the end of the simulation the model is within 40 pc of the current position of ω Cen, and the 3-D velocity is within 5% of the real cluster velocity. The distribution of the particles at the end of the simulation (see Fig. 6.10) is in good agreement with the results by Mizutani et al. (2003) and (Ideta & Makino, 2004). The remnant have developed two tidal tails extending over the whole orbital path. However, the tidal radius of the bound remnant is only 10% smaller than the initial model and there is a mere 8% of the particles that lie outside that radius after 10 perigalactic passages. This confirms that ω Cen is currently nearly at equilibrium with the tidal field of the Milky Way and that any tidal tail originating from the present day cluster should be very weak and hard to detect. In particular, it is interesting to note that only 0.4% of the particles are found in the annulus between 1 r_t and 2 r_t, in excellent agreement with the results of Da Costa & Coleman (2008). Rescaling to the observed total luminosity of the cluster the average surface brightness in that annulus due to tidally stripped stars is $\mu_V \sim 30.0$ mag/arcsec^2. In Fig. 6.11 the final surface brightness and the velocity dispersion profiles of the simulated satellite are shown. As can be noted, the surface brightness profile deviates from the King profile at $r > 40'$, following the power-law trend typical of tidally stripped stars (see Johnston et al., 1999; Muñoz et al., 2008, and references therein). This deviation occurs at a very low surface density level (about 3.5 orders of magnitude lower than the center), just outside the limit reached so far by any photometric investigation. Note that neither King models nor Wilson's ones can reproduce this external behaviour.

Also the velocity dispersion profile shows a departure from the predicted King profile. However, in this case the drift already occurs at $r \sim 25'$ yielding a flatter profile at larger distances. In any case, the derived profile is compatible with the observed one , within the uncertainties. Hence, the available observations appear still compatible with the tidal stripping scenario described by our N-body model. Fig. 6.11 suggests that the "easiest" way to look for the observational signatures of the ongoing formation of tidal

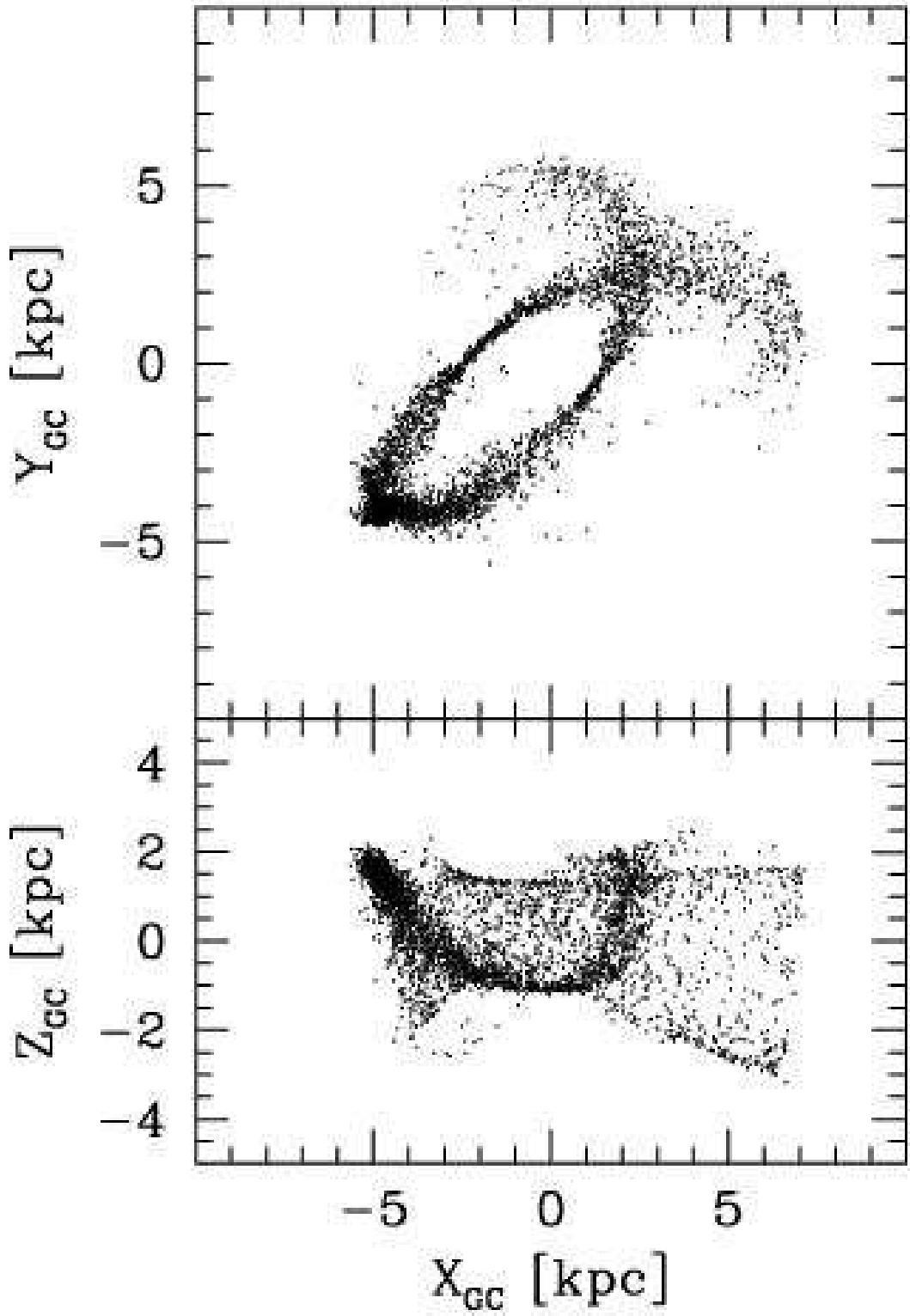

Figure 6.10: Position of the particles at the end of the N-body simulation A (present epoch) in galactocentric coordinates. The X-Y plane coincides with the Galactic Plane, the X-Z plane is perpendicular to it and passes through the Sun. Note the excellent agreement with the much finer simulation by Ideta & Makino (2004, , the upper right panel of their Fig. 2).

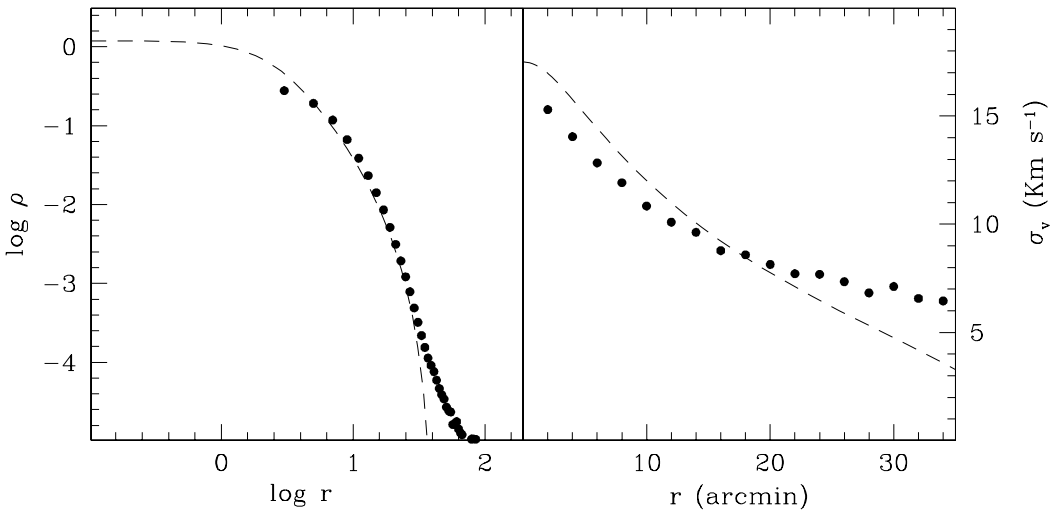

Figure 6.11: Surface brightness (left panel) and velocity dispersion (right panel) profiles for the bound remnant at the end of the N-body simulation A (filled circles). The dashed lines are from the King (1966) model that best fits the final surface brightness profile.

tails would be to reliably extend the surface brightness profile using abundant and easy-to-select tracers as Main Sequence stars, searching for the power-law branch of the profile.

SECTION 6.6

The outer region

In § 6.4 we presented the velocity dispersion profile of ω Cen calculated out to a distance of $\sim 32'$, and comprising stars out to $r = 44'$ from the cluster center. A more careful analysis is needed when considering the region at $r > 44'$ i.e. close to the cluster tidal radius. In this region, only seven stars passed the selection criteria defined in § 6.4.1. The resulting velocity dispersion of this sample is $\sigma_v = 36.0^{+12.5}_{-7.5}$ $Km\ s^{-1}$, about a factor of 2 larger than the central value, and a factor of 5 larger than the outermost point of the profile, at $< r > \simeq 32$. It is worth noticing that although the adopted selection criteria are efficient in eliminating the contaminating field stars in the inner region of the system, their efficiency decrease at larger distances, as the surface density of ω Cen stars plunges below the background level due to

Galactic field stars.
To check the membership of these sample of stars we performed various tests. First, we compared our sample with the predictions of the R03 Galactic model. Although this model is only a statistical representation of the Galactic field population (see Drimmel et al., 2005), it gives a good estimate of the order of magnitude of the field contamination. To minimize the effect due to small number statistics, we retrived (and merged together) two simulated catalogue covering an area of 5 sqare degrees each, in the direction of ω Cen. The v_r distributions of simulated stars approximately lying in the same magnitude and colour range of the observed stars is well fitted by a sum of two Gaussian distributions, one for the main peak of thin disc + thick disc Galactic stars at $-150 < v_r < 150\ Km\ s^{-1}$, the other for the Halo population. Once fixed the density normalization of the two components, the number of stars expected in our sample, in any given range of r and v_r is easily obtained by re-normalizing the Gaussian of the main component to the number of observed stars having $-150 < v_r < 150\ Km\ s^{-1}$ in that range. Adopting this procedure, the expected number of field stars with $190 < v_r < 290\ Km\ s^{-1}$ at distances $r > 44'$ turns out to be $N_{field} = 4.0 \pm 0.9$. Therefore, according to this test, about half of the outermost stars are likely non-members, Galactic Halo stars.
Another possibility is to estimate the number of cluster stars expected at such distance by means of the cluster density profile. Indeed, in a given radial bin (defined between r_1 and r_2) the expected ratio between the number of cluster stars (N_{mem}) and field stars (N_{field}) can be written as

$$\frac{N_{mem}}{N_{field}} = \frac{\int_{r_1}^{r_2} 2\pi r \rho_{mem} dr}{\int_{r_1}^{r_2} 2\pi r \rho_{field} dr} = C\ \frac{\int_{r_1}^{r_2} r \rho_{mem} dr}{\int_{r_1}^{r_2} r\ dr} \tag{6.1}$$

where ρ_{mem} and ρ_{field} represent the projected surface density of member stars and field stars, respectively. In the above equation the density of field stars has been assumed to be constant over the field of view of the cluster. We counted N_{field} as the number of stars with $190\ Km\ s^{-1} < v_r < 290\ Km\ s^{-1}$ in each radial bin and estimated the constant C by best-fitting the ratio N_{mem}/N_{field} measured in the innermost bins (at $r < 44'$) with the prediction of the best-fit Wilson model described in § 6.5.1. Then, we estimated the number of cluster members stars in the most external bin by using eq. 6.1 and N_{field} measured in this bin. Following this procedure we estimated $N_{mem} = 0.4$ at $r > 44'$. However, as shown in § 6.5.2, the interaction between ω Cen and the Milky Way would produce a departure from the King profile in the external region of the cluster, implying a higher surface density. Therefore, the number of cluster members stars in the external region is expected to be larger than this estimate. We

performed the above procedure also assuming at $r > 40'$ a power-law density profile with index $\alpha = -3.8$ (i.e. the slope predicted by our N-body simulation). Also in this case, the expected number of cluster members results $N_{mem} = 1.5$. Thus, according to this test, the majority of the high-velocity external stars should be field stars. It is interesting to note that none of the seven considered stars pass the metallicity selection criterion defined in § 6.4.1. A Kolmogorov-Smirnov test gives a probability smaller than 0.2% that the metallicity of these stars can be randomly extracted from the metallicity distribution of the entire sample of cluster members stars shown in Fig. 6.4. Given all the results above we can safely conclude that most of (if not all) the seven stars passing our selection criteria at $r > 44'$ are likely not member of the cluster.

Having established that, we draw the attention of the reader on a curious occurrence. In Fig. 6.12 the radial velocities of the stars with $190 < v_r < 290$ $Km\ s^{-1}$ is shown as a function of the right ascension for the observed sample and for the particles of the N-body model described in § 6.5.2. Note that the most external stars are not evenly distributed in the considered plane. Most of the $r > 44'$ stars lying to the West of the cluster have v_r larger that the systemic cluster velocity, while the opposite is true for $r > 44'$ Eastern stars. This apparent trend of mean v_r with RA is in the same sense as that expected to be imprinted by the Galactic tidal field on stripped stars, clearly visible in the N-body model (lower panel of Fig. 6.12). By means of Monte-Carlo extractions from the synthetic R03 catalogue described above, we estimated that the chance occurrence of such an asimmetry in Halo stars is lower than 5%. If the observed gradient would be revealed as real using a much larger sample of stars in this range of distances, this would make very difficult to interpret most of these stars as belonging to the Galactic Halo and the hypothesis of a tidal tail must be reconsidered.

Another interesting issue emerges from this comparison: in the innermost region of the cluster ($201.0^\circ < RA < 202.3^\circ$ in Fig 6.12), the clear S-shaped trend due to the cluster rotation is clearly visible In particular, in this case the Eastern branch of the rotation curve has larger average v_r with respect to the Western branch. This trend is just in the opposite direction of what produced in the N-body simulation by the Galactic tidal strain. This strongly suggests that the rotation in the inner $30'$ of ω Cen is not induced by the interaction with the Milky Way, as previously suggested by van de Ven et al. (2006), but it is an intrinsic property of the system, instead.

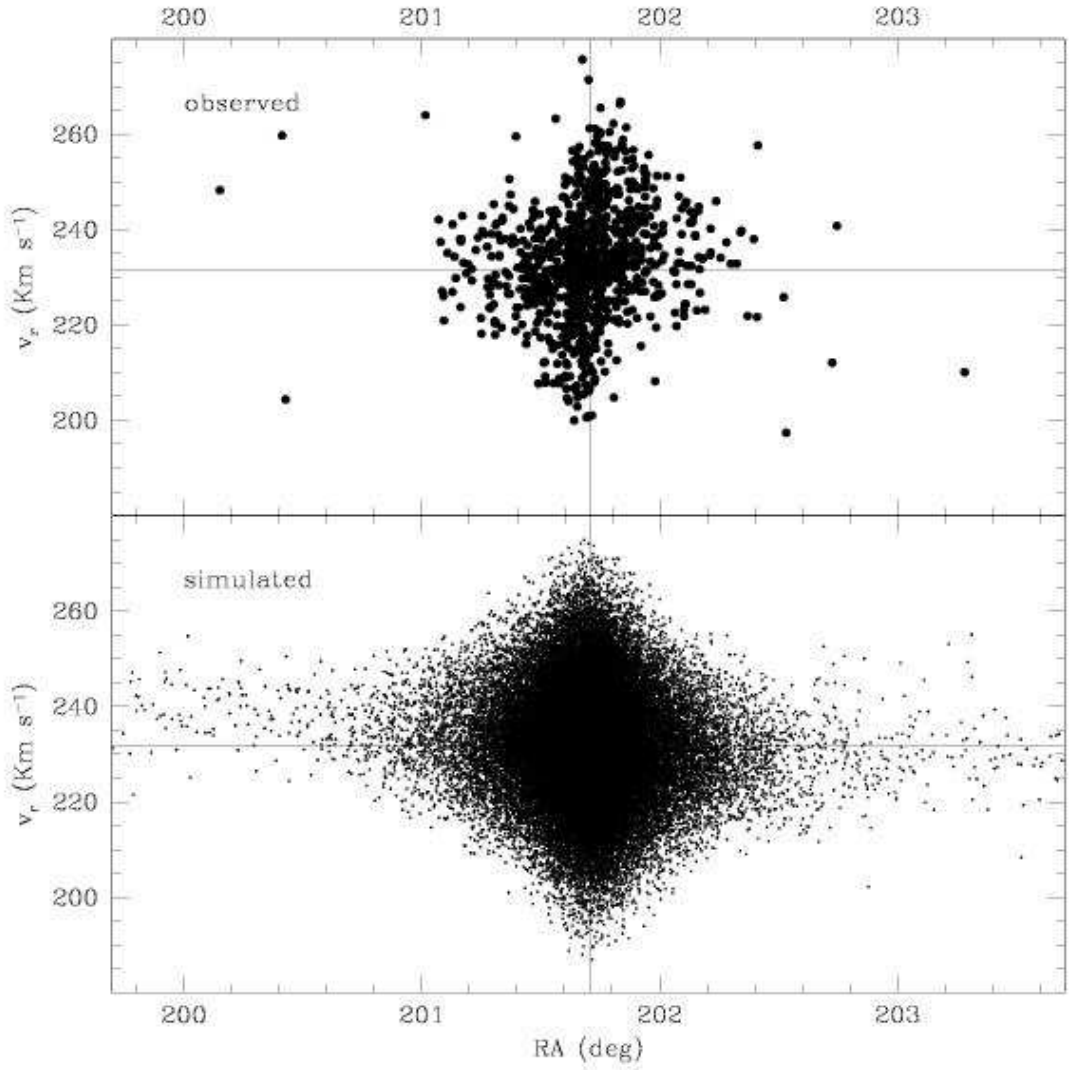

Figure 6.12: The radial velocities of the stars with $190 < v_r < 290\ Km\ s^{-1}$ is shown as a function of the right ascension for the observed sample (top panel) and for the N-body simulation described in § 6.5.2 (bottom panel).

SECTION 6.7

Summary and conclusions

In this paper we present high accuracy radial velocities for a sample of more than 2500 stars in the direction of ω Cen. Adding the homogeneous sample by P07 and applying various un-biased selection criteria, we selected a sample of 946 bona-fide cluster's members displaced over a wide region up to a distance of $\sim 80'$ from the cluster center.
We derived a very reliable velocity dispersion profile in the range $1.5' \leq r \leq 28'$. In this range the velocity dispersion appears to decrease monotonically from a central value of $\sigma_v \sim 17.2\ Km\ s^{-1}$ down to a minimum value of $\sigma_v \sim 5.2\ Km\ s^{-1}$. A non-statistically significant raise to $\sigma_v \simeq 7.0 \pm 1.0\ Km\ s^{-1}$ is observed in an outer extended radial bin ($28' \leq r < 44'$), that must be considered with great caution because of the uneven radial distribution of the 26 candidate member stars included. The obtained profile is consistent with those obtained by previous authors within $r \simeq 20'$ (Meylan et al., 1995; Mayor et al., 1997; van de Ven et al., 2006) but differs from that derived by Scarpa et al. (2003) in the most external region of the cluster. In particular, at odds with the SC03 analysis, we did not find any sign of flattening of the velocity dispersion profile in the region between $20' < r < 28'$. The observed velocity dispersion profile of ω Cen, as well as its structural and kinematical properties is well reproduced by a Wilson (1975) equilibrium model in which mass follows light. Therefore, with the present data we find no evidences of neither the presence of dark matter nor MOND effects, at least in the inner $30'$ from the center. The majority of the seven candidate members we found at $r > 44'$ are consistent with being iterlopers from the Galactic Halo. The only piece of evidence that is in marginal contrast with this view is that they seem to display a velocity gradient similar to that expected for star tidally stripped from ω Cen, according to the prediction of a simple N-body model. The comparison with the same N-body model suggests that the well-known rotation pattern observed in the inner $30'$ of ω Cen is not produced by the Galactic tidal strain, but it should be intrinsical to the stellar system, instead. The present study, mainly focused on the kinematics in the range $20' < r < 30'$, as well as that performed by Da Costa & Coleman (2008), focused on the search of extra-tidal stars ($60' < r < 120'$), reached the limits that can be achieved using RGB stars as tracers. Future studies aimed at assessing the shape of the velocity dispersion profile in the range $30' < r < 60'$ and trying to identify extra-tidal stars must rely on much more abundant Main Sequence stars.

Bibliography

Abadi M. G., Navarro J. F., Steinmetz M., Eke V. R., 2003, ApJ, 591, 499

Abazajian K., et al., 2003, AJ, 126, 2081

Adelman-McCarthy J. K., et al., 2008, ApJS, 175, 297

Alard C., 1996, ApJ, 458, L17+

Alcock C., et al., 1997, ApJ, 474, 217

An D., et al., 2008, ApJS, 179, 326

Baade W., 1944, ApJ, 100, 137

Babusiaux C., Gilmore G., 2005, MNRAS, 358, 1309

Bahcall J. N., Soneira R. M., 1980, ApJS, 44, 73

Bailin J., 2003, ApJ, 583, L79

Baumgardt H., Grebel E. K., Kroupa P., 2005, MNRAS, 359, L1

Bekki K., Chiba M., 2005, MNRAS, 356, 680

Bekki K., Freeman K. C., 2003, MNRAS, 346, L11

Bell E. F., Zucker D. B., Belokurov V., Sharma S., Johnston K. V., Bullock J. S., Hogg D. W., Jahnke K., de Jong J. T. A., Beers T. C., Evans N. W., Grebel E. K., Ivezić Ž., Koposov S. E., Rix H., Schneider D. P., Steinmetz M., Zolotov A., 2008, ApJ, 680, 295

Bellazzini M., Correnti M., Ferraro F. R., Monaco L., Montegriffo P., 2006, A&A, 446, L1

Bellazzini M., Ferraro F. R., Buonanno R., 1999a, MNRAS, 304, 633

Bellazzini M., Ferraro F. R., Buonanno R., 1999b, MNRAS, 307, 619

Bellazzini M., Ferraro F. R., Ibata R., 2003, AJ, 125, 188

Bellazzini M., Ferraro F. R., Origlia L., Pancino E., Monaco L., Oliva E., 2002, AJ, 124, 3222

Bellazzini M., Ferraro F. R., Sollima A., Pancino E., Origlia L., 2004, A&A, 424, 199

Bellazzini M., Gennari N., Ferraro F. R., 2005, MNRAS, 360, 185

Bellazzini M., Ibata R., Ferraro F. R., Testa V., 2003, A&A, 405, 577

Bellazzini M., Ibata R., Martin N., Lewis G. F., Conn B., Irwin M. J., 2006, MNRAS, 366, 865

Bellazzini M., Ibata R. A., Chapman S. C., Mackey A. D., Monaco L., Irwin M. J., Martin N. F., Lewis G. F., Dalessandro E., 2008, AJ, 136, 1147

Bellazzini M., Newberg H. J., Correnti M., Ferraro F. R., Monaco L., 2006, A&A, 457, L21

Belokurov V., et al., 2006, ApJ, 642, L137

Belokurov V., et al., 2007a, ApJ, 658, 337

Belokurov V., et al., 2007b, ApJ, 654, 897

Binney J., Tremaine S., 1987, Galactic dynamics

Bonanos A. Z., Stanek K. Z., Szentgyorgyi A. H., Sasselov D. D., Bakos G. Á., 2004, AJ, 127, 861

Bonifacio P., Zaggia S., Sbordone L., Santin P., Monaco L., Monai S., Molaro P., Marconi G., Girardi L., Ferraro F. R., di Marcantonio P., Caffau E., Bellazzini M., 2006, in Hill V., Pasquini L., eds, The Milky Way and its Satellites Vol. 000 of ESO Astrophysics Symposium, Abundances in Sagittarius Stars. pp 232–235

Bullock J. S., Johnston K. V., 2005, ApJ, 635, 931

Bullock J. S., Kravtsov A. V., Weinberg D. H., 2001, ApJ, 548, 33

Carlin J. L., Grillmair C. J., Muñoz R. R., Nidever D. L., Majewski S. R., 2009, ApJ, 702, L9

Carraro G., Lia C., 2000, A&A, 357, 977

Carraro G., Zinn R., Moni Bidin C., 2007, A&A, 466, 181

Carrell K., Wilhelm R., 2010, ArXiv e-prints

Chou M.-Y., Majewski S. R., Cunha K., Smith V. V., Patterson R. J., Martínez-Delgado D., Law D. R., Crane J. D., Muñoz R. R., Garcia López R., Geisler D., Skrutskie M. F., 2007, ApJ, 670, 346

Cole N., et al., 2008, ApJ, 683, 750

Combes F., Leon S., Meylan G., 1999, A&A, 352, 149

Cordier D., Pietrinferni A., Cassisi S., Salaris M., 2007, AJ, 133, 468

Correnti M., Bellazzini M., Ferraro F. R., 2009, MNRAS, 397, L26

Correnti M., Bellazzini M., Ferraro F. R., Monaco L., 2008, Memorie della Societa Astronomica Italiana, 79, 692

Cseresnjes P., 2001, A&A, 375, 909

Da Costa G. S., Coleman M. G., 2008, AJ, 136, 506

de Jong J. T. A., Yanny B., Rix H., Dolphin A. E., Martin N. F., Beers T. C., 2009, ArXiv e-prints

Dehnen W., 2000, ApJ, 536, L39

Dehnen W., 2002, Journal of Computational Physics, 179, 27

Dehnen W., Binney J., 1998, MNRAS, 294, 429

Del Principe M., et al., 2006, ApJ, 652, 362

Diemand J., Zemp M., Moore B., Stadel J., Carollo C. M., 2005, MNRAS, 364, 665

Dinescu D. I., 2002, in F. van Leeuwen, J. D. Hughes, & G. Piotto ed., Omega Centauri, A Unique Window into Astrophysics Vol. 265 of Astronomical Society of the Pacific Conference Series, A Solar Neighborhood Search for Tidal Debris from ω Centauri's Hypothetical Parent Galaxy. pp 365–+

D'Onghia E., Lake G., 2008, ApJ, 686, L61

Drimmel R., Bucciarelli B., Lattanzi M. G., Spagna A., Jordi C., Robin A. C., Reylé C., Luri X., 2005, in C. Turon, K. S. O'Flaherty, & M. A. C. Perryman ed., The Three-Dimensional Universe with Gaia Vol. 576 of ESA Special Publication, What Gaia Will See: All-Sky Source Counts from the GSC2. pp 163–+

Duffau S., Zinn R., Vivas A. K., Carraro G., Méndez R. A., Winnick R., Gallart C., 2006, ApJ, 636, L97

Edelsohn D. J., Elmegreen B. G., 1997, MNRAS, 290, 7

Eggen O. J., Lynden-Bell D., Sandage A. R., 1962, ApJ, 136, 748

Fahlman G. G., Mandushev G., Richer H. B., Thompson I. B., Sivaramakrishnan A., 1996, ApJ, 459, L65+

Feast M. W., 1961, MNRAS, 122, 1

Federici L., Bellazzini M., Galleti S., Fusi Pecci F., Buzzoni A., Parmeggiani G., 2007, A&A, 473, 429

Fellhauer M., Belokurov V., Evans N. W., Wilkinson M. I., Zucker D. B., Gilmore G., Irwin M. J., Bramich D. M., Vidrih S., Wyse R. F. G., Beers T. C., Brinkmann J., 2006, ApJ, 651, 167

Ferraro F. R., Dalessandro E., Mucciarelli A., Beccari G., Rich R. M., Origlia L., Lanzoni B., Rood R. T., Valenti E., Bellazzini M., Ransom S. M., Cocozza G., 2009, Nat, 462, 483

Ferraro F. R., Messineo M., Fusi Pecci F., de Palo M. A., Straniero O., Chieffi A., Limongi M., 1999, AJ, 118, 1738

Ferraro F. R., Sollima A., Rood R. T., Origlia L., Pancino E., Bellazzini M., 2006, ApJ, 638, 433

Freeman K., Bland-Hawthorn J., 2002, ARA&A, 40, 487

Freeman K. C., 1993, in G. H. Smith & J. P. Brodie ed., The Globular Cluster-Galaxy Connection Vol. 48 of Astronomical Society of the Pacific Conference Series, Globular Clusters and Nucleated Dwarf Ellipticals. pp 608–+

Freeman K. C., Rodgers A. W., 1975, ApJ, 201, L71+

Fukugita M., Ichikawa T., Gunn J. E., Doi M., Shimasaku K., Schneider D. P., 1996, AJ, 111, 1748

Fusi Pecci F., Bellazzini M., Cacciari C., Ferraro F. R., 1995, AJ, 110, 1664

Fusi Pecci F., Ferraro F. R., Bellazzini M., Djorgovski S., Piotto G., Buonanno R., 1993, AJ, 105, 1145

Geyer E. H., Nelles B., Hopp U., 1983, A&A, 125, 359

Gilmore G., Reid N., 1983, MNRAS, 202, 1025

Gilmore G., Wilkinson M. I., Wyse R. F. G., Kleyna J. T., Koch A., Evans N. W., Grebel E. K., 2007, ApJ, 663, 948

Gilmore G., Wyse R. F. G., Kuijken K., 1989, ARA&A, 27, 555

Girardi L., Grebel E. K., Odenkirchen M., Chiosi C., 2004, A&A, 422, 205

Girardi L., Salaris M., 2001, MNRAS, 323, 109

Gómez-Flechoso M. A., Fux R., Martinet L., 1999, A&A, 347, 77

Grebel E. K., 2005, in H. Jerjen & B. Binggeli ed., IAU Colloq. 198: Near-fields cosmology with dwarf elliptical galaxies Near-field cosmology with Local Group dwarf spheroidals. pp 1–10

Grillmair C. J., 2009, ApJ, 693, 1118

Grillmair C. J., Dionatos O., 2006, ApJ, 643, L17

Grillmair C. J., Johnson R., 2006, ApJ, 639, L17

Gunn J. E., et al., 1998, AJ, 116, 3040

Gunn J. E., et al., 2006, AJ, 131, 2332

Haghi H., Baumgardt H., Kroupa P., Grebel E. K., Hilker M., Jordi K., 2009, MNRAS, 395, 1549

Harbeck D., Grebel E. K., Holtzman J., Guhathakurta P., Brandner W., Geisler D., Sarajedini A., Dolphin A., Hurley-Keller D., Mateo M., 2001, AJ, 122, 3092

Harris W. E., 1996, AJ, 112, 1487

Helmi A., 2004, ApJ, 610, L97

Helmi A., White S. D. M., 2001, MNRAS, 323, 529

Hogg D. W., Finkbeiner D. P., Schlegel D. J., Gunn J. E., 2001, AJ, 122, 2129

Ibata R., Bellazzini M., Chapman S. C., Dalessandro E., Ferraro F., Irwin M., Lanzoni B., Lewis G. F., Mackey A. D., Miocchi P., Varghese A., 2009, ApJ, 699, L169

Ibata R., Irwin M., Lewis G. F., Stolte A., 2001, ApJ, 547, L133

Ibata R., Lewis G. F., Irwin M., Totten E., Quinn T., 2001, ApJ, 551, 294

Ibata R., Martin N. F., Irwin M., Chapman S., Ferguson A. M. N., Lewis G. F., McConnachie A. W., 2007, ApJ, 671, 1591

Ibata R. A., Gilmore G., Irwin M. J., 1994, Nat, 370, 194

Ibata R. A., Gilmore G., Irwin M. J., 1995, MNRAS, 277, 781

Ibata R. A., Lewis G. F., 1998, ApJ, 500, 575

Ibata R. A., Lewis G. F., Irwin M. J., Cambrésy L., 2002, MNRAS, 332, 921

Ibata R. A., Razoumov A. O., 1998, A&A, 336, 130

Ibata R. A., Wyse R. F. G., Gilmore G., Irwin M. J., Suntzeff N. B., 1997, AJ, 113, 634

Ideta M., Makino J., 2004, ApJ, 616, L107

Irwin M. J., et al., 2007, ApJ, 656, L13

Ivezić Ž., et al., 2000, AJ, 120, 963

Ivezić Ž., et al., 2008, ApJ, 684, 287

Ivezić Ž., Lupton R., Schlegel D., Smolčić V., Johnston D., Gunn J., Knapp J., Strauss M., Rockosi C., The SDSS Collaboration 2004, in F. Prada, D. Martinez Delgado, & T. J. Mahoney ed., Satellites and Tidal Streams Vol. 327 of Astronomical Society of the Pacific Conference Series, Halo Structure Traced by SDSS RR Lyrae. pp 104–+

Jiang I., Binney J., 2000, MNRAS, 314, 468

Johnson C. I., Pilachowski C. A., Simmerer J., Schwenk D., 2008, ApJ, 681, 1505

Johnston K. V., Bullock J. S., Sharma S., Font A., Robertson B. E., Leitner S. N., 2008, ApJ, 689, 936

Johnston K. V., Law D. R., Majewski S. R., 2005, ApJ, 619, 800

Johnston K. V., Majewski S. R., Siegel M. H., Reid I. N., Kunkel W. E., 1999, AJ, 118, 1719

Johnston K. V., Sigurdsson S., Hernquist L., 1999, MNRAS, 302, 771

Johnston K. V., Spergel D. N., Hernquist L., 1995, ApJ, 451, 598

Jurić M., et al., 2008, ApJ, 673, 864

Kang X., Mao S., Gao L., Jing Y. P., 2005, A&A, 437, 383

Keller S. C., 2009a, ArXiv e-prints

Keller S. C., 2009b, ArXiv e-prints

Keller S. C., da Costa G. S., Prior S. L., 2009, MNRAS, 394, 1045

Keller S. C., Murphy S., Prior S., Da Costa G., Schmidt B., 2008, ApJ, 678, 851

King I. R., 1966, AJ, 71, 64

Klypin A., Kravtsov A. V., Valenzuela O., Prada F., 1999, ApJ, 522, 82

Knebe A., Gill S. P. D., Gibson B. K., Lewis G. F., Ibata R. A., Dopita M. A., 2004, ApJ, 603, 7

Kroupa P., Theis C., Boily C. M., 2005, A&A, 431, 517

Kunder A., Chaboyer B., 2009, AJ, 137, 4478

Kunkel W. E., 1979, ApJ, 228, 718

Kurucz R., Bell B., 1995, Atomic Line Data (R.L. Kurucz and B. Bell) Kurucz CD-ROM No. 23. Cambridge, Mass.: Smithsonian Astrophysical Observatory, 1995., 23

Kurucz R. L., 1979, ApJS, 40, 1

Lagadec E., Zijlstra A. A., Sloan G. C., Wood P. R., Matsuura M., Bernard-Salas J., Blommaert J. A. D. L., Cioni M.-R. L., Feast M. W., Groenewegen M. A. T., Hony S., Menzies J. W., van Loon J. T., Whitelock P. A., 2009, MNRAS, 396, 598

Laird J. B., Carney B. W., Rupen M. P., Latham D. W., 1988, AJ, 96, 1908

Landolt A. U., 1992, AJ, 104, 340

Larsen J. A., Humphreys R. M., 1996, ApJ, 468, L99+

Law D. R., Johnston K. V., Majewski S. R., 2005, ApJ, 619, 807

Law D. R., Majewski S. R., 2010, ArXiv e-prints

Law D. R., Majewski S. R., Johnston K. V., 2009, ApJ, 703, L67

Law D. R., Majewski S. R., Skrutskie M. F., Carpenter J. M., Ayub H. F., 2003, AJ, 126, 1871

Layden A. C., Sarajedini A., 2000, AJ, 119, 1760

Leon S., Meylan G., Combes F., 2000, A&A, 359, 907

Li Y., Helmi A., 2008, MNRAS, 385, 1365

Liu C., Hu J., Newberg H., Zhao Y., 2008, A&A, 477, 139

Lub J., 2002, in F. van Leeuwen, J. D. Hughes, & G. Piotto ed., Omega Centauri, A Unique Window into Astrophysics Vol. 265 of Astronomical Society of the Pacific Conference Series, The Reddening of ω Centauri: E(B-V) = 0.11. pp 95–+

Lynden-Bell D., 1982, The Observatory, 102, 202

Mackey A. D., van den Bergh S., 2005, MNRAS, 360, 631

Madau P., Kuhlen M., Diemand J., Moore B., Zemp M., Potter D., Stadel J., 2008, ApJ, 689, L41

Majewski S. R., 1993, ARA&A, 31, 575

Majewski S. R., 1994, ApJ, 431, L17

Majewski S. R., 2004, Publications of the Astronomical Society of Australia, 21, 197

Majewski S. R., 2010, ArXiv e-prints

Majewski S. R., Kunkel W. E., Law D. R., Patterson R. J., Polak A. A., Rocha-Pinto H. J., Crane J. D., Frinchaboy P. M., Hummels C. B., Johnston K. V., Rhee J., Skrutskie M. F., Weinberg M., 2004, AJ, 128, 245

Majewski S. R., Siegel M. H., Kunkel W. E., Reid I. N., Johnston K. V., Thompson I. B., Landolt A. U., Palma C., 1999, AJ, 118, 1709

Majewski S. R., Skrutskie M. F., Weinberg M. D., Ostheimer J. C., 2003, ApJ, 599, 1082

Maraston C., 2005, MNRAS, 362, 799

Martin N. F., de Jong J. T. A., Rix H., 2008, ApJ, 684, 1075

Martin N. F., Ibata R. A., Bellazzini M., Irwin M. J., Lewis G. F., Dehnen W., 2004, MNRAS, 348, 12

Martínez-Delgado D., Aparicio A., Gómez-Flechoso M. Á., Carrera R., 2001, ApJ, 549, L199

Martínez-Delgado D., Gómez-Flechoso M. Á., Aparicio A., Carrera R., 2004, ApJ, 601, 242

Martínez-Delgado D., Peñarrubia J., Gabany R. J., Trujillo I., Majewski S. R., Pohlen M., 2008, ApJ, 689, 184

Martínez-Delgado D., Peñarrubia J., Jurić M., Alfaro E. J., Ivezić Z., 2007, ApJ, 660, 1264

Martínez-Delgado D., Pohlen M., Gabany R. J., Majewski S. R., Peñarrubia J., Palma C., 2009, ApJ, 692, 955

Marulli F., Bonoli S., Branchini E., Gilli R., Moscardini L., Springel V., 2009, MNRAS, 396, 1404

Mashchenko S., Sills A., 2005, ApJ, 619, 243

Mateo M., Kubiak M., Szymanski M., Kaluzny J., Krzeminski W., Udalski A., 1995, AJ, 110, 1141

Mateo M., Mirabal N., Udalski A., Szymanski M., Kaluzny J., Kubiak M., Krzeminski W., Stanek K. Z., 1996, ApJ, 458, L13+

Mateo M., Olszewski E. W., Morrison H. L., 1998, ApJ, 508, L55

Mateo M., Udalski A., Szymanski M., Kaluzny J., Kubiak M., Krzeminski W., 1995, AJ, 109, 588

Mayor M., Meylan G., Udry S., Duquennoy A., Andersen J., Nordstrom B., Imbert M., Maurice E., Prevot L., Ardeberg A., Lindgren H., 1997, AJ, 114, 1087

Mc William A., Smecker-Hane T., 2006, in Hill V., Pasquini L., eds, The Milky Way and its Satellites Vol. 000 of ESO Astrophysics Symposium, The Composition of the Sagittarius Dwarf Spheroidal Galaxy and Implications for Nucleosynthesis and Chemical Evolution. pp 236–239

McLaughlin D. E., Meylan G., 2003, in G. Piotto, G. Meylan, S. G. Djorgovski, & M. Riello ed., New Horizons in Globular Cluster Astronomy Vol. 296 of Astronomical Society of the Pacific Conference Series, Velocity Dispersion in the Halo of ω Centauri: No Need for MOND Given the Present Data. pp 153–+

Merrifield M. R., 2005, in N. J. C. Spooner & V. Kudryavtsev ed., The Identification of Dark Matter Dark Matter on Galactic Scales (Or the Lack Thereof). pp 49–+

Merritt D., Meylan G., Mayor M., 1997, AJ, 114, 1074

Metz M., Kroupa P., Jerjen H., 2009, MNRAS, 394, 2223

Metz M., Kroupa P., Libeskind N. I., 2008, ApJ, 680, 287

Metz M., Kroupa P., Theis C., Hensler G., Jerjen H., 2009, ApJ, 697, 269

Meylan G., 1987, A&A, 184, 144

Meylan G., Mayor M., 1986, A&A, 166, 122

Meylan G., Mayor M., Duquennoy A., Dubath P., 1995, A&A, 303, 761

Milgrom M., 1983, ApJ, 270, 365

Milgrom M., 2008, ArXiv e-prints

Mizutani A., Chiba M., Sakamoto T., 2003, ApJ, 589, L89

Moffat J. W., Toth V. T., 2008, ApJ, 680, 1158

Monaco L., Bellazzini M., Bonifacio P., Buzzoni A., Ferraro F. R., Marconi G., Sbordone L., Zaggia S., 2007, A&A, 464, 201

Monaco L., Bellazzini M., Bonifacio P., Ferraro F. R., Marconi G., Pancino E., Sbordone L., Zaggia S., 2005, A&A, 441, 141

Monaco L., Bellazzini M., Ferraro F. R., Pancino E., 2003, ApJ, 597, L25

Monaco L., Bellazzini M., Ferraro F. R., Pancino E., 2004, MNRAS, 353, 874

Monaco L., Bellazzini M., Ferraro F. R., Pancino E., 2005, MNRAS, 356, 1396

Monaco L., Ferraro F. R., Bellazzini M., Pancino E., 2002, ApJ, 578, L47

Montegriffo P., Ferraro F. R., Origlia L., Fusi Pecci F., 1998, MNRAS, 297, 872

Moultaka J., Ilovaisky S. A., Prugniel P., Soubiran C., 2004, PASP, 116, 693

Muñoz R. R., Carlin J. L., Frinchaboy P. M., Nidever D. L., Majewski S. R., Patterson R. J., 2006, ApJ, 650, L51

Muñoz R. R., Majewski S. R., Johnston K. V., 2008, ApJ, 679, 346

Navarro J. F., Frenk C. S., White S. D. M., 1997, ApJ, 490, 493

Navarro J. F., Helmi A., Freeman K. C., 2004, ApJ, 601, L43

Newberg H. J., Yanny B., Cole N., Beers T. C., Re Fiorentin P., Schneider D. P., Wilhelm R., 2007, ApJ, 668, 221

Newberg H. J., Yanny B., Rockosi C., Grebel E. K., Rix H.-W., Brinkmann J., Csabai I., Hennessy G., Hindsley R. B., Ibata R., Ivezić Z., Lamb D., Nash E. T., Odenkirchen M., Rave H. A., Schneider D. P., Smith J. A., Stolte A., York D. G., 2002, ApJ, 569, 245

Niederste-Ostholt M., Belokurov V., Evans N. W., Penarrubia J., 2010, ArXiv e-prints

Norris J. E., 2004, ApJ, 612, L25

Norris J. E., Freeman K. C., Mayor M., Seitzer P., 1997, ApJ, 487, L187+

Norris J. E., Freeman K. C., Mighell K. J., 1996, ApJ, 462, 241

Noyola E., Gebhardt K., Bergmann M., 2008, ApJ, 676, 1008

O'Connell D. J. K., 1958, Ricerche Astronomiche, 5

Olszewski E. W., Suntzeff N. B., Mateo M., 1996, ARA&A, 34, 511

Ostriker J. P., Peebles P. J. E., 1973, ApJ, 186, 467

Paczynski B., Stanek K. Z., 1998, ApJ, 494, L219+

Pancino E., Ferraro F. R., Bellazzini M., Piotto G., Zoccali M., 2000, ApJ, 534, L83

Pancino E., Galfo A., Ferraro F. R., Bellazzini M., 2007, ApJ, 661, L155

Pasquini L., et al., 2002, The Messenger, 110, 1

Peñarrubia J., Navarro J. F., McConnachie A. W., 2008, ApJ, 673, 226

Peebles P. J. E., 1971, Physical cosmology

Pietrinferni A., Cassisi S., Salaris M., Castelli F., 2004, ApJ, 612, 168

Piotto G., Villanova S., Bedin L. R., Gratton R., Cassisi S., Momany Y., Recio-Blanco A., Lucatello S., Anderson J., King I. R., Pietrinferni A., Carraro G., 2005, ApJ, 621, 777

Press W. H., Schechter P., 1974, ApJ, 187, 425

Prior S. L., Da Costa G. S., Keller S. C., 2009a, ApJ, 704, 1327

Prior S. L., Da Costa G. S., Keller S. C., 2009b, ApJ, 704, 1327

Reijns R. A., Seitzer P., Arnold R., Freeman K. C., Ingerson T., van den Bosch R. C. E., van de Ven G., de Zeeuw P. T., 2006, A&A, 445, 503

Renzini A., 1998, AJ, 115, 2459

Renzini A., Buzzoni A., 1986, in Chiosi C., Renzini A., eds, Spectral Evolution of Galaxies Vol. 122 of Astrophysics and Space Science Library, Global properties of stellar populations and the spectral evolution of galaxies. pp 195–231

Renzini A., Fusi Pecci F., 1988, ARA&A, 26, 199

Robin A. C., Reylé C., Derrière S., Picaud S., 2003a, A&A, 409, 523

Robin A. C., Reylé C., Derrière S., Picaud S., 2003b, A&A, 409, 523

Rockosi C. M., Odenkirchen M., Grebel E. K., Dehnen W., Cudworth K. M., Gunn J. E., York D. G., Brinkmann J., Hennessy G. S., Ivezić Ž., 2002, AJ, 124, 349

Savage B. D., Mathis J. S., 1979, ARA&A, 17, 73

Sbordone L., Bonifacio P., Buonanno R., Marconi G., Monaco L., Zaggia S., 2007, A&A, 465, 815

Scarpa R., Marconi G., Gilmozzi R., 2003, A&A, 405, L15

Schlegel D. J., Finkbeiner D. P., Davis M., 1998, ApJ, 500, 525

Seabroke G. M., et al., 2008, MNRAS, 384, 11

Searle L., Zinn R., 1978, ApJ, 225, 357

Siegel M. H., Dotter A., Majewski S. R., Sarajedini A., Chaboyer B., Nidever D. L., Anderson J., Marín-Franch A., Rosenberg A., Bedin L. R., Aparicio A., King I., Piotto G., Reid I. N., 2007, ApJ, 667, L57

Simon J. D., Geha M., 2007, ApJ, 670, 313

Skrutskie M. F., et al., 2006, AJ, 131, 1163

Smith J. A., et al., 2002, AJ, 123, 2121

Sneden C., 1973, ApJ, 184, 839

Sollima A., Ferraro F. R., Bellazzini M., 2007, MNRAS, 381, 1575

Sollima A., Ferraro F. R., Origlia L., Pancino E., Bellazzini M., 2004, A&A, 420, 173

Stanek K. Z., Garnavich P. M., 1998, ApJ, 503, L131+

Stetson P. B., 2000, PASP, 112, 925

Stoughton C., et al., 2002, AJ, 123, 485

Strigari L. E., Bullock J. S., Kaplinghat M., Simon J. D., Geha M., Willman B., Walker M. G., 2008, Nat, 454, 1096

Suntzeff N. B., Kraft R. P., 1996, AJ, 111, 1913

Tegmark M., et al., 2004, PhRvD, 69, 103501

Teuben P., 1995, in R. A. Shaw, H. E. Payne, & J. J. E. Hayes ed., Astronomical Data Analysis Software and Systems IV Vol. 77 of Astronomical Society of the Pacific Conference Series, The Stellar Dynamics Toolbox NEMO. pp 398–+

Trager S. C., King I. R., Djorgovski S., 1995, AJ, 109, 218

Tsuchiya T., Korchagin V. I., Dinescu D. I., 2004, MNRAS, 350, 1141

Tucker D. L., et al., 2006, Astronomische Nachrichten, 327, 821

Unavane M., Wyse R. F. G., Gilmore G., 1996, MNRAS, 278, 727

van de Ven G., van den Bosch R. C. E., Verolme E. K., de Zeeuw P. T., 2006, A&A, 445, 513

van Leeuwen F., Le Poole R. S., Reijns R. A., Freeman K. C., de Zeeuw P. T., 2000, A&A, 360, 472

Velazquez H., White S. D. M., 1995, MNRAS, 275, L23

Vivas A. K., Jaffé Y. L., Zinn R., Winnick R., Duffau S., Mateu C., 2008, AJ, 136, 1645

Vivas A. K., Zinn R., 2006, AJ, 132, 714

Vivas A. K., Zinn R., Gallart C., 2005, AJ, 129, 189

Walker M. G., Mateo M., Olszewski E. W., Bernstein R., Wang X., Woodroofe M., 2006, AJ, 131, 2114

Watkins L. L., Evans N. W., Belokurov V., Smith M. C., Hewett P. C., Bramich D. M., Gilmore G. F., Irwin M. J., Vidrih S., Wyrzykowski Ł., Zucker D. B., 2009, MNRAS, 398, 1757

White S. D. M., Frenk C. S., 1991, ApJ, 379, 52

White S. D. M., Rees M. J., 1978, MNRAS, 183, 341

Willman B., Dalcanton J. J., Martinez-Delgado D., West A. A., Blanton M. R., Hogg D. W., Barentine J. C., Brewington H. J., Harvanek M., Kleinman S. J., Krzesinski J., Long D., Neilsen Jr. E. H., Nitta A., Snedden S. A., 2005, ApJ, 626, L85

Wilson C. P., 1975, AJ, 80, 175

Wyse R. F. G., Gilmore G., 1989, Comments on Astrophysics, 13, 135

Yanny B., et al., 2000, ApJ, 540, 825

Yanny B., et al., 2009, AJ, 137, 4377

Yanny B., Newberg H. J., Grebel E. K., Kent S., Odenkirchen M., Rockosi C. M., Schlegel D., Subbarao M., Brinkmann J., Fukugita M., Ivezic Ž., Lamb D. Q., Schneider D. P., York D. G., 2003, ApJ, 588, 824

Yanny B., Newberg H. J., Johnson J. A., Lee Y. S., Beers T. C., Bizyaev D., Brewington H., Fiorentin P. R., Harding P., Malanushenko E., Malanushenko V., Oravetz D., Pan K., Simmons A., Snedden S., 2009, ApJ, 700, 1282

York D. G., et al., 2000, AJ, 120, 1579

Zacharias N., Urban S. E., Zacharias M. I., Wycoff G. L., Hall D. M., Monet D. G., Rafferty T. J., 2004, AJ, 127, 3043

Zentner A. R., Bullock J. S., 2003, ApJ, 598, 49

Zentner A. R., Kravtsov A. V., Gnedin O. Y., Klypin A. A., 2005, ApJ, 629, 219

Zhao H. S., 2002, in F. van Leeuwen, J. D. Hughes, & G. Piotto ed., Omega Centauri, A Unique Window into Astrophysics Vol. 265 of Astronomical Society of the Pacific Conference Series, Are ω Centauri and G1 Like Massive Globular Glusters the Remnant Cores of Infalling Dwarf Galaxies? - Dynamical Constraints. pp 391–+

Zucker D. B., et al., 2006a, ApJ, 650, L41

Zucker D. B., et al., 2006b, ApJ, 643, L103